

Optimization of the Probe Placement for Radiofrequency Ablation

Dissertation

zur Erlangung des akademischen Grades
eines Doktors der Naturwissenschaften

Dem Fachbereich 3 der Universität Bremen
vorgelegt von

Inga Altrogge

Bremen, 2. Februar 2009

Datum des Promotionskolloquiums: 27. April 2009

Gutachter: Prof. Dr. Heinz-Otto Peitgen (CeVis, Universität Bremen)
Prof. Dr. Christof Büskens (ZeTeM, Universität Bremen)
Prof. Dr. Tobias Preusser (Jacobs University Bremen)

Acknowledgements

I would like to thank my supervisor Prof. Dr. Tobias Preusser and my colleague Dr. Tim Kröger for answering all my questions and giving me support and ideas during this PhD thesis work. Moreover, I would like to thank Prof. Dr. Heinz-Otto Peitgen for enabling this work and for fruitful discussions on the topic. I would also like to thank Prof. Dr. Christof Büskens, Dr. Caroline Böß , Hanne Tiesler and Sabrina Haase for their participation in my committee. Further, I am grateful to Thomas Stein from Celon AG for providing me with the figures shown in the introduction of this work. Special thanks goes to all my colleagues from CeVis and Fraunhofer MEVIS, who mainly contributed to a likable working atmosphere. Also, I would like to thank my family for all their patience and belief in my work.

Finally, I want to thank my boyfriend Thomas Werner for all his encouragement, patience and love, as well as for reading and commenting on this work.

Abstract

Radiofrequency (RF) ablation is a widely used, minimally invasive technique for the treatment of liver cancer. Within this method, an RF current is used to heat the tumor tissue up to high temperatures which are lethal to the tissue. The RF current is generated by a high frequency generator and induced into the tissue via so-called needle- or umbrella probes, which contain one or more electrodes. Especially, in situations where a surgical resection is not possible due to the patient's physical condition and state of the tumors, the RF ablation technique offers a powerful but less invasive alternative. However, the success of an RF ablation, i. e. the completeness of tumor destruction with minimum amount of effected native tissue, considerably depends on the accuracy of needle insertion and control of the energy supply, as well as on the cooling effects of blood perfusion.

The aim of this work is to develop a three-dimensional model for the optimization of the RF probe placement. The model is based on a numerical finite element computation of the electric potential and heat distribution inside the malignant and surrounding native tissue during an RF ablation. The optimization is performed by minimizing a temperature based objective functional under these constraining equations. Moreover, since the tissue properties of the individual patient cannot be determined exactly in advance, also a model based on stochastically distributed tissue parameters is developed, in order to investigate the sensitivity of an optimal probe placement found by the presented algorithm, with respect to changes in these quantities. A further well-known difficulty associated with RF ablation is the cooling influence of blood perfusion on the ablation result. For this reason, a method to quickly estimate the cooling effect of large blood vessels based on a precalculation of all patient-independent quantities, is introduced. Finally, a first approach towards an optimal control of the electric energy which is induced into the tissue via the RF generator, is presented and discussed. The results show that the simulation and optimization of an RF ablation is of essential importance to yield the best possible outcome and thus present a helpful tool for assisting the interventional radiologist.

Contents

1	Introduction	1
2	Simulation of Radiofrequency Ablation - Forward Modeling	7
2.1	Problem Formulation	7
2.2	Mathematical Modeling	9
2.3	A Simplified Model for the Optimization of the Probe Placement . . .	15
2.4	Solution of the Potential- and Heat Equation	17
2.4.1	An Analytical Solution to the Potential Equation (Approximation by a Concatenation of Balls)	18
2.4.2	Numerical Solution with Finite Elements	21
3	Optimal Probe Placement for Radiofrequency Ablation	24
3.1	Introduction of Two Basic Optimization Methods	24
3.1.1	Gradient Descent Method	25
3.1.2	Lagrange-Newton (SQP) Method	27
3.2	A First Approach in 2D	30
3.2.1	First Results	31
3.3	Formulation and Comparison of Different Objective Functionals for the Optimization in 3D	33
3.3.1	Numerical Integration	37
3.4	An Algorithm for the Optimization	38
3.4.1	Descent Direction	41
3.4.2	Step Size	43
3.4.3	Stopping Criterion	43
3.4.4	Optimization Algorithm	44
3.5	Results Obtained with a Monopolar Probe	45
3.6	Application of Multiple Coupled Probes	48
3.7	Multi-Level Optimization on Coarse Grids	49
3.7.1	The Multi-Level Optimization Algorithm	52
3.8	Results Obtained with the Multi-Level Optimization	52
3.9	Conclusions and Discussion	57
4	Analysis of Material Parameter Uncertainty	59
4.1	Problem Formulation	59
4.2	A Stochastic Model for RF Ablation	62
4.3	Generalized Polynomial Chaos and Stochastic Collocation	64

4.4	Sensitivity Analysis	66
4.4.1	Local Sensitivity Analysis	66
4.4.2	Probability Density of Joint Distribution	66
4.4.3	Covariance of Joint Distribution	67
4.5	Optimizing the Probe Location in the Presence of Uncertain Material Parameters	68
4.6	Optimality System and Stochastic Gradient Descent	69
4.6.1	The Stochastic Multi-Level Optimization Algorithm	71
4.7	Results	72
4.7.1	Artificial Scenario	73
4.7.2	Real RF Scenario	77
4.7.3	Probe Placement for Expected Maximal Volume of Destroyed Tumor Tissue	83
4.8	Conclusions and Discussion	85
5	Fast Estimation of the Heat Sink Effect of Large Blood Vessels	90
5.1	Problem Formulation	90
5.2	Mathematical Modeling	91
5.3	Completion of the Single-Vessel-Model to a Model for a Complex Vascular Tree	100
5.4	Results	102
5.5	Discussion and Outlook	108
6	Further Extensions and Improvements	111
6.1	Coupled Optimization of Bipolar Probe Placement and Setup Power .	111
6.1.1	Results and Conclusion	118
6.2	Optimization of the Number and Placement of Uncoupled Probes . .	121
6.2.1	Results and Discussion	123
7	Ongoing Work	128
7.1	Optimal Control of the Generator Power	128
7.1.1	Problem Formulation	128
7.1.2	Modeling of the Time-Dependent Problem and Numerical So- lution with Finite Elements	129
7.1.3	Modeling and Comparison of Different Objective Functionals .	132
7.1.4	An Algorithm for Solving the Optimal Control Problem	138
7.1.5	Results and Discussion	144
7.2	Miscellaneous	148
8	Summary and Future Work	150
	List of Figures	158
	List of Tables and Algorithms	167
	Bibliography	168

1 Introduction

“Cancer is a leading cause of death worldwide: it accounted for 7.9 million deaths (around 13 % of all deaths) in 2007” [89]. In Europe, there are estimated over 3 million new cases of cancer and about 1.7 million deaths from the disease per year [33]. Thereby, the second most common cancer (after breast cancer) is *colorectal cancer* (CRC), i. e. cancer located in colon or rectum. Even in Germany there are over 300000 new cases of cancer per year [33, 13], where again colorectal cancer is the second most common cancer site among both women and men. Moreover, colorectal cancer is the second major cause of death due to cancer [33, 13] and the main cause of *liver metastases*. Approximately 50 – 60 % of all patients with colorectal cancer also develop liver metastases during the course of the disease [70, 80]. But also other tumors, like for example mamma carcinoma and bronchial carcinoma may spread into the liver. Altogether, more than 50 % of all patients suffering from cancer also develop hepatic metastases with high morbidity and mortality [70]. The reason for this is that the liver is the largest blood-filtering organ, such that via the bloodstream cancer cells are transported into the liver, where they cause malignant growth. The median survival of patients with untreated colorectal liver metastases ranges between 6 – 12 months [70, 80]. Although the surgical resection yields an improved survival and counts as gold standard in the treatment of resectable colorectal liver metastases, only about 10 – 25 % of the patients are suitable for resection [80, 70, 32].

Another type of tumorous disease of the human liver are *hepatocellular carcinoma* (HCC), which are primary liver carcinoma. Hepatocellular carcinoma in most cases are caused by a viral hepate infection (hepatitis B or C), or a liver cirrhosis which often results from a chronic hepatitis or alcoholism. In more detail, among the industrialized countries about 60 % of all hepatocellular carcinoma are caused by a chronic hepatitis, where the viral hepatitis C infection becomes chronic in 60 – 80 % of cases [75]. Furthermore, persons with hepatitis C caused liver cirrhosis are of exceedingly high risk to develop a hepatocellular carcinoma. In addition, additional consumption of alcohol in the case of a chronic hepatitis C, significantly increases the probability to develop a hepatocellular carcinoma. The 5 year survival rate of patients with liver cirrhosis is stated with 50 – 80 %, while the time of survival after the initial diagnosis of a hepatocellular carcinoma often only lies in a range of months, depending on the stage of the tumor and the chosen form of therapy [75]. A healing can be achieved only by a complete tumor removal or -destruction. However, the requirements for a surgical resection are only rarely given, since surgery is eligible only for patients with single, early stage HCC and well-preserved liver function [75, 60]. In particular among patients with cirrhotic HCC, only less than 5 % come into question for resection [60, 24] due to the risk of liver failure.

1 Introduction

For the treatment of both, liver metastases and primary liver carcinoma, surgical resection currently counts as gold standard. But, since the resection of liver carcinoma is limited to patients with sufficiently good medical condition (in particular well-preserved liver function) and moreover is restricted by the number, size and location of the tumors, thermal ablation and especially percutaneous *radiofrequency*



(*RF*) ablation has become a widely used, minimally invasive alternative. In more detail, RF ablation offers effective local tumor destruction by using a high-frequency current (typically at about 500 kHz) which is induced into the tissue by one or more RF probes, such that the tissue around the probe is heated up to temperatures at which tissue cells and in particular tumor cells die. The figure on the left shows a typical setup for RF ablation. More precisely, we see a generator system (CelonPOWER-System™) including the power control unit and a triple peristaltic pump for internal probe cooling. Further, on top of the control unit we see a laptop for the medical imaging of the tumor and the applied RF probe. In addition, the figure down right shows a bipolar RF needle probe that is used in connection with the generator system depicted on the left.

Besides RF ablation, also some other minimally invasive techniques have been developed during the last decades in order to provide a better treatment especially for those patients who are excluded from surgery. Among these procedures are e.g. further thermal ablation techniques such as laser ablation and focused ultrasound. Other minimally invasive procedures are e.g. cryoablation which uses low temperatures of about -190°C to destroy the tumor by freezing the tissue, percutaneous ethanol injection which destroys tumor cells by dehydrating them, as well as chemoembolization, where tumor destruction is achieved by stopping the blood supply through the hepatic arteries and additionally applying anti-cancer drugs.



However, percutaneous RF ablation is considered to be one of the most promising minimally invasive alternatives to surgical resection for the treatment of liver cancer (especially in cases, where an open surgery is not possible) [11, 59, 80, 84]. It is regarded to be safer than e.g. cryoablation [70, 84], more practicable versus laser ablation [70] and more effective than ethanol injection or chemoembolization [70, 43]. Moreover, in recent years an increasing number of interventional radiologists apply percutaneous RF ablation not only in cancer cases which are excluded from surgery, but also in cases of resectable liver metastases (though adequate randomized clinical trials supporting whether RF ablation can replace open surgery in selected cases of resectable liver metastases still have to be performed [67]). Further, not only liver tumors, but also other tumor sites, such as kidney, lung, bone, prostate and breast,

are treated by RF ablation by now [29, 14].

The success of an RF ablation mainly depends on the completeness of tumor destruction and enduring absence of recrudescences, while damages on internal organs or large blood vessels have to be avoided. An incomplete coagulation of tumor cells naturally results in new tumor growth, where surviving tumor cells can alter their biological activities. More precisely, these tumor cells can show a higher malignancy than before and become more resistant to thermal ablation [67]. The reason for this, is that a tissue heating up to high temperatures which are insufficient for cell destruction, stimulates the expression of so-called heat shock proteins, which play an important role in protein-protein interactions, such as folding and unfolding, and in particular increase the thermotolerance of cells on exposure to heat stress. Moreover, not only an incomplete tumor destruction, but also a too fast coagulation process can jeopardize the success of an RF ablation. In more detail, a too fast tumor heating can effect an intratumoral steam production with a steep buildup of intratumoral pressure. As result the tumor may burst which then leads to an explosive intravascular spread of the tumor cells into the portal or arterial branches, such that scattered recurrences are the consequence [67].

All this shows that in order to yield the best oncologic outcomes, a thorough planning of the RF therapy is of essential importance. Thereto, the numerical simulation of this treatment is an indispensable tool [84, 51, 56]. Moreover, since the completeness of tumor destruction without injury of internal organs or key vessels mainly depends on the accuracy of the needle insertion and the control of the electric energy, which is induced into the tissue, a thorough planning of the probe's positioning as well as a determination of the optimal generator power are highly recommendable to assert a successful treatment. The modeling and simulation of RF ablation has been investigated by several authors [79, 28, 47, 43, 84, 85, 87, 56]. A recent overview on the state-of-the-art and future challenges is given by Berjano [14]. Moreover, some authors already have focussed on the improvement of needle insertion for thermal ablation techniques: For interstitial ultrasound thermo-therapy, a two-dimensional optimization model has been presented by Khalil-Bustany et al. [52]. Furthermore, Villard et al. [86, 85] presented a three-dimensional optimization of the needle insertion based on a heuristic approach, where the volume of coagulated tissue is approximated by ellipsoids.

The aim of this work is to develop a model for the optimization of the placement of mono- and bipolar RF (needle) probes based on a finite element simulation of the underlying physical processes. Also the development of an approach for calculating an optimal control of the electric energy which is induced into the tissue during an RF ablation, is a desirable objective which already is considered here in a first preliminary approach and thus is part of current and ongoing work.

Related Work and State of the Art

In [70] Pereira refers to RF ablation as one of the most promising minimally invasive techniques for the treatment of small-sized, unresectable liver metastases. At the same time, he considers percutaneous RF ablation not to be an equivalent al-

ternative to surgical resection at the present time. Only solitary, small-sized and deep-seated metastases are excluded from this opinion. In addition, Suppiah et al. [80] argue for percutaneous RF ablation in the case of unresectable colorectal hepatic metastases. In their experiments they find out that “percutaneous RF ablation is well tolerated and provides an effective means of prolonging disease-free and overall survival” in patients with unresectable colorectal hepatic metastases. The application of RF ablation to unresectable hepatocellular carcinoma (HCC) e.g. is considered in the work of Lencioni et al. [58]. They mainly compare RF ablation with percutaneous ethanol injection (PEI), but also discuss other methods of percutaneous ablation such as percutaneous acetic acid injection, percutaneous microwave coagulation and percutaneous cryosurgery. From their studies, they conclude that RF ablation can be considered as treatment of choice for patients with unresectable, early-stage HCC.

Besides the application of RF ablation to different types of unresectable liver cancer, however also the application of this method to resectable liver metastases is subject of the literature. In his current work [67], Mulier points out that, though RF ablation already is performed in cases of resectable liver metastases, no final proof, whether RF ablation is equivalent to resection for these cancer cases, exists up to now. Hence, he calls for a randomized trial that shows, which of both techniques (surgical resection or RF ablation) is better suited for the treatment of resectable colorectal liver metastases and which are the conditions that have to be fulfilled. Moreover, he discusses several advantages and disadvantages of resection and RF ablation, respectively.

In order to achieve the best possible ablation results, several authors have mathematically modeled and simulated RF ablation: In his dissertation [79], Stein develops a two-dimensional model for the simulation of RF ablation (based on the assumption of cylindrical symmetry around the probe), which he solves by using finite differences. Haemmerich with Tungjitkusolmun et al. [43, 84] and also Welp [87] consider a three-dimensional model for RF ablation. They solve the forward problem numerically with help of commercial finite element software (such as ABAQUS, PATRAN and ANSYS) on unstructured grids which inevitably is time consuming. Deuffhard et al. [28] consider a finite element model for simulating hyperthermia which is a related form of therapy. With this technique, the whole organ is heated by e.g. microwaves up to temperatures of 40–44 °C. Obviously, for the mathematical modeling of this method the heat equation plays a major role. However, an essential difference to RF ablation appears in the heat supply: With hyperthermia the heat is not induced into the tissue by a probe (i.e. the heat does not propagate into the tissue from a small local region), but instead all parts of the tissue are simultaneously heated. Moreover, the modeling of tissue dehydration is rather insignificant for hyperthermia due to the lower temperature values used within this method.

An investigation of the blood flow during RF ablation is focussed e.g. in the work of Jain and Wolf [47]. More precisely, in contrast to earlier models their approach aims at a more realistic blood flow simulation, where more detailed information such as different flow velocities and the viscosity of blood are taken into account. Also

Crezee and Legendijk [23] developed a complex model for simulating the cooling effects of large blood vessels, but for the method of hyperthermia. Various influencing factors such as thermal equilibration effects and the type of blood flow are considered in their model. However, the calculation of such complex models inevitably is associated with high computational costs. In contrast to that, Yim et al. [95] developed a simple distance measurement between the tumors and large vessels, which can be performed quite faster, but still has to be interpreted (in terms of e.g. an optimal probe placement) by the user.

Another known difficulty in the modeling of RF ablation is the identification of the individual state-dependent tissue properties. Hence, in some approaches such as the two-dimensional model presented by Stein [79], the tissue parameters have been modeled time-dependent. Further, in [37] Geneser et al. used a generalized Polynomial Chaos - Stochastic Galerkin (gPC-SG) approach (see Chapt. 4 and [49], Sect. 6.4) to evaluate the effects of variations and uncertainty in the conductivity values assigned to organs in a two-dimensional electrocardiograph simulation of the human thorax.

A common property of all of the approaches mentioned above is that they deal with the forward problem of simulating RF ablation or related thermo-therapies. However, none of these approaches aims at an optimization of the probe placement. In [52], Khalil-Bustany et al. developed a two-dimensional optimization model for interstitial ultrasound thermo-therapy. Their approach is based on a minimax-optimization, the idea of which is to predefine a range of desired temperature values and to minimize the maximal deviation from this interval. A three-dimensional optimization of the probe placement for RF ablation has been presented by Villard and Baegert et al. [86, 85, 12, 10]. In contrast to the methods developed in the current work, their optimization is based on a heuristic modeling of the underlying physical process in order to reduce the computational time. More precisely, they use a simple geometric optimization, where the region of coagulated tissue is approximated by ellipsoids.

In [74], Schmidt et al. compare the efficacy of an impedance controlled power supply with a manual power control during RF ablation. Their results show that an impedance controlled power supply (which allows for considerably longer ablation times without an essential increase of the impedance) significantly enlarges the size of the coagulation zones. This result particularly motivates further research in this field, such as the investigation of a mathematical approach for the determination of a patient-individual, optimal control of the generator power.

A recent overview on the state-of-the-art and future trends in the simulation and planning of RF ablation is given by Berjano et al. [14]. He names several approaches for modeling RF ablation and numerous different groups that work on these models. In particular, he reviews the basic equations with different initial and boundary conditions for modeling the physical process of RF heating. He further describes common simplifications to the models such as dimensional reductions, and discusses different approaches to model the physical properties of the tissue (e.g. as temperature dependent quantities). In addition, he states current numerical

1 Introduction

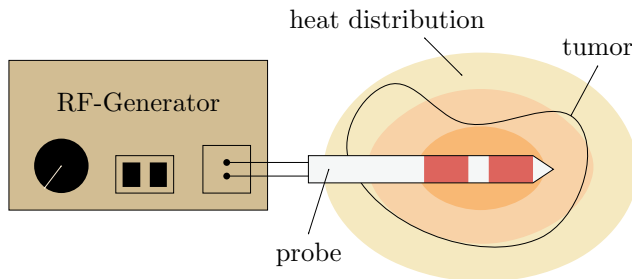
methods (such as finite difference and finite element methods) with appropriate solvers and grid generators to compute the mathematical models. After a discussion on different techniques for an experimental validation of the simulation models, he detects current limitations and suggests research objectives for the future. Among these are e.g. the development of a more realistic modeling of the cooling effect of large blood vessels and an investigation of the behavior of the tissue during saline-enhanced RF ablation. The planning of RF ablation by e.g. optimizing the probe placement unfortunately is missing in his report, which apart from that provides a clear and detailed overview.

The next chapters of this work are organized as follows: In Chapt. 2 the modeling and calculation of the forward problem of simulating RF ablation, as well as appropriate simplifications to the model for optimizing the probe placement will be discussed. Chapt. 3 then deals with the optimization of the location and orientation of an RF needle probe in two and three space dimensions. After an appropriate objective functional has been chosen, the optimization is performed via a gradient descent method and applied to an artificial tumor-vessel configuration, as well as to an example based on real patient data. Finally, the optimization is extended to work with a cluster of parallel, monopolar probes and to use a multi-grid approach which reduces the computational time. In Chapt. 4 a stochastic approach for modeling the patient- and state-dependent tissue properties is presented. Thereby, the electrical and thermal conductivity of the tissue are assumed to lie in given ranges of values and to be stochastically distributed within these intervals. Then, based on the resulting system of stochastic partial differential equations, a stochastic optimization and sensitivity analysis of the optimal probe placement with respect to changes in the electrical and thermal conductivity are performed by using a stochastic collocation approach [91]. In Chapt. 5 a method for a fast estimation of the cooling effects of large blood vessels to RF ablation is developed. The method is based on a change of perspective in considering the heat equation together with a dimensional reduction and a precalculation of all patient-independent data in advance. As result, for critical tumor regions close by large vessels, the maximum allowable distances an RF probe may have to these vessels are identified, such that the heating energy suffices to destroy the tumor regions under investigation. Finally, the results are visualized by a tumor-coloring and so-called vessel surrounding “criticality tubes” of vital tissue. Moreover, Chapt. 6 deals with further extensions to the basic algorithm of optimizing the probe placement developed in Chapt. 3 and Chapt. 7 discusses a first approach for the calculation of an optimal control of the generator power. Finally, a summary of this work and several ideas for future investigations are presented in Chapt. 8.

2 Simulation of Radiofrequency Ablation - Forward Modeling

2.1 Problem Formulation

As already motivated in the introduction, the success of a radiofrequency (RF) ablation carefully depends on the placement of the applied RF probe. Hence, one of the main objectives within this work is the optimization of the RF probe positioning. However, before we can make a first step towards this optimization we have to consider the forward problem of modeling RF ablation. To this end, let us shortly review the main principle of this minimally invasive therapy for cancer treatment:



At the beginning of an RF ablation, a probe which is connected to an electric high frequency generator, is placed inside the malignant tissue. When the generator is switched on, it produces an electric current in the range of radiofrequency waves. As a consequence

the tissue near the probe is heated up to temperatures at which the proteins of the heated tissue coagulate and thus the tissue cells die. If the treatment is successful, the volume of destroyed tissue completely contains the malignant lesion including a safety margin. The role of this safety margin is to reduce the risk of a recrudescence, since sometimes tissue cells on the boundary of the coagulation zone survive.

Altogether, simulation models for RF ablation mainly can be divided into three distinct parts:

- The first part is the calculation of the *electric energy* which is induced into the tissue by an RF probe connected to an electric RF generator. In more detail, from the generator voltage an electric potential arises, such that an electric current flows through the tissue and causes a heat source (also referred to as Joule heating).
- The second part of RF simulation models is to determine the *evolution of heat* throughout the tissue. Naturally, the evolution of heat depends on the heat source, as well as a heat sink due to vessel cooling. Moreover, the thermal

conductivity, the density and the heat capacity of the tissue are factors of influence.

- The third part is the determination of the *tissue damage* up to tissue destruction which is caused by high tissue temperatures and depends on the protein composition of the tissue.

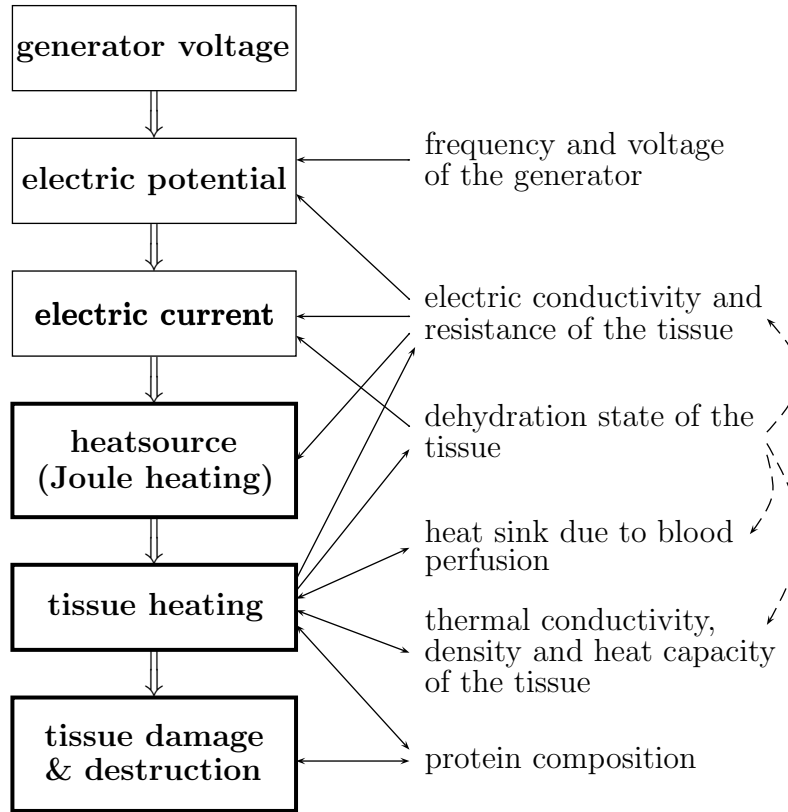


Figure 2.1: Dependencies in the modeling of RF ablation.

As can be seen in the diagram (Fig. 2.1), the physical coherences that play a role during an RF ablation are very complex. Many of the involved physical quantities (directly or indirectly) interact with each other: For example, the electric conductivity influences the electric current and thereby the tissue heating, while on the other hand the tissue heating changes the electric conductivity. Hence, the modeling and simulation of RF ablation trying to consider all dependencies of the physical process, is a very complex and challenging problem. In the next section (Sect. 2.2), a three-dimensional model for the simulation of RF ablation based on the model developed in the work of Stein [79], will be reviewed in order to familiarize the reader with the physical background of RF ablation. Since the simulation and in particular the optimization of RF ablation based on the fully complex model naturally would be too expensive and thus not really practicable, in Sect. 2.3 a simplified version of the model will be presented.

2.2 Mathematical Modeling

In this section a complex mathematical model for the simulation of an RF ablation, including partial differential equations for the electric potential and the temperature distribution together with appropriate boundary conditions, is presented. The description starts with an explanation of the considered configuration.

Geometrical Setting. We consider the computational domain to be a cuboid $D \subset \mathbb{R}^3$ with boundary $\Gamma_{\text{out}} = \partial D$ in which a tumor $D_t \subset D$ and vascular structures $D_v \subset D$ are located. Further, we assume that a mono- or bipolar RF probe is applied in D , whose position $p \in D$ (of the active zone's center) and direction $d \in S^2 = \{x \in \mathbb{R}^3 : |x| = 1\}$ are variables (which we would like to optimize later on). The subset of D that is covered by the probe is denoted by D_{pr} , the subsets covered by the electrodes are denoted by D_+ and/or D_- , and $D_{\pm} = D_+ \cup D_-$ (cf. Fig. 2.2). Note that these sets depend on the position p and the orientation d . In practical applications the sets D_t and D_v are determined from segmented image data in advance by the methods presented in [15].

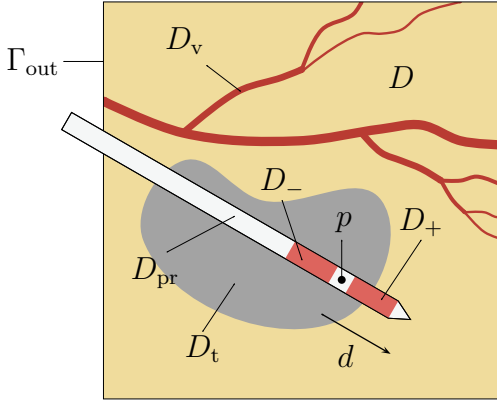


Figure 2.2: Schematic setting of the considered configuration. Note that $D_+ \cup D_- = D_{\pm} \subset D_{\text{pr}}$, where all these sets depend on p and d .

In the following, the time interval $[0, t_{\text{end}}]$ during which the RF ablation takes place will be denoted by I .

Electric Energy. Since for an RF ablation radiofrequencies of about 500 kHz are used, the electromagnetic field can be considered to be static. Hence, Maxwell's equations yield the following electrostatic equation for the potential $\phi : I \times D \rightarrow \mathbb{R}$

$$-\text{div}(\sigma(t, x)\nabla\phi(t, x)) = 0 \quad \text{in } I \times (D \setminus \overline{D_{\pm}}) , \quad (2.1a)$$

where the material parameter $\sigma(t, x) = \sigma(t, x; F_D, F_C, T)$ is the electric conductivity of the tissue and depends on the temporal and spatial position (t, x) , on the water content F_D , the coagulation state (i.e. the protein status) F_C and the temperature T of the tissue. Since on the electrodes the electric conductivity is near to infinity, the gradient of the potential $\nabla\phi$ must be zero there (see Eq. (2.1a)), so that the potential ϕ itself must be constant on the electrodes. Here the potential is set to

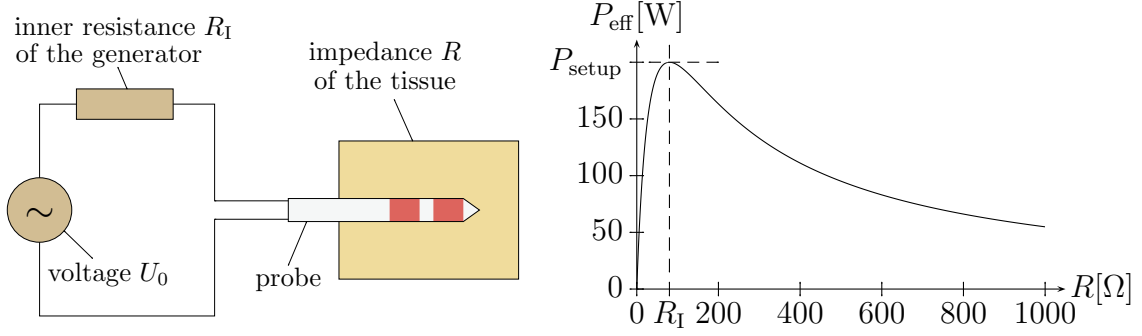


Figure 2.3: Left: Equivalent circuit diagram for the calculation of the scaling factor which is needed to convert the unscaled power P into the effective heat source Q_{rf} . Right: The characteristic curve of the generator shows the dependence of the effective power P_{eff} on the impedance R of the tissue, while R_{I} and P_{setup} are fixed (here: $R_{\text{I}} = 80 \Omega$, $P_{\text{setup}} = 200 \text{ W}$).

± 1 on the electrodes, i. e.

$$\phi(t, x) = \pm 1 \quad \text{on } I \times \overline{D_{\pm}} . \quad (2.1b)$$

Note that this is an arbitrarily chosen value, so that after having solved the potential equation, the potential has to be scaled. Moreover, a condition for the potential on the outer boundary of the tissue under consideration (the so-called *ROI = region of interest*), i. e. on the outer boundary Γ_{out} of the computational domain D , is needed. Such a boundary condition can be obtained by making the assumption that far away from the probe, the potential behaves approximately as induced by a point load at the barycenter p of the probe. Then, on the outer boundary Γ_{out} of the computational domain (i. e. far away from the probe) the following Robin boundary condition can be established

$$n \cdot \nabla \phi(t, x) = \frac{n \cdot (p - x)}{|p - x|^2} \phi(t, x) \quad \text{on } I \times \Gamma_{\text{out}} , \quad (2.1c)$$

where n denotes the outer normal on Γ_{out} .

Due to the electric resistance of the tissue, the potential ϕ induces a heat source Q_{rf} . This heat source depends on the power P_{setup} of the generator and the impedance (resistance) R of the tissue. To model this dependence on the characteristics of the generator we take the equivalent circuit diagram shown on the left of Fig. 2.3 into account [79]. This yields a characteristic curve of the type presented on the right of Fig. 2.3, which shows that, depending on the resistance of the tissue, the effective power P_{eff} applied to the tissue is in general smaller than the maximum power of the generator.

In more detail, the impedance R of the tissue is given by

$$R(t) = \frac{U^2}{P_{\text{total}}(t)} \quad \text{with} \quad P_{\text{total}}(t) = \int_D \sigma(t, x) |\nabla \phi(t, x)|^2 dx , \quad (2.2)$$

where U is the difference of the potential ϕ on the two electrodes ($U = 2\text{ V}$ for bipolar probes and $U = 1\text{ V}$ for monopolar probes) (cf. Eq. (2.1b)) and P_{total} is the space integral of the unscaled electric power density $P(t, x) := \sigma(t, x) |\nabla\phi(t, x)|^2$. According to the equivalent circuit diagram shown in Fig. 2.3, the effective power of the generator is now given by

$$P_{\text{eff}}(t) = \frac{4 P_{\text{setup}} R(t) R_{\text{I}}}{(R(t) + R_{\text{I}})^2} , \quad (2.3)$$

where R_{I} is the inner resistance of the generator and P_{setup} is the value set up at the generator's control unit. Finally, the heat source is given by

$$Q_{\text{rf}}(t, x) = \frac{P_{\text{eff}}(t)}{P_{\text{total}}(t)} \sigma(t, x) |\nabla\phi(t, x)|^2 . \quad (2.4)$$

Evolution of Heat. The temporal and spatial distribution of heat $T : I \times D \rightarrow \mathbb{R}$ is modeled by the so-called *Bioheat-Transfer-Equation*

$$\partial_t((\rho c)(t, x)T(t, x)) - \text{div}(\lambda(t, x)\nabla T(t, x)) = Q(t, x) \quad \text{in } I \times (D \setminus \overline{D_{\text{pr}}}) , \quad (2.5a)$$

$$T(t, x) = T_{\text{probe}} \quad \text{on } I \times \overline{D_{\text{pr}}} , \quad (2.5b)$$

$$T(t, x) = T_{\text{body}} \quad \text{on } I \times \Gamma_{\text{out}} , \quad (2.5c)$$

$$T(0, x) = T_{\text{body}} \quad \text{in } D . \quad (2.5d)$$

Here, $\rho(t, x) = \rho(t, x; F_{\text{D}}, F_{\text{C}}, T)$ is the density, $c(t, x) = c(t, x; F_{\text{D}}, F_{\text{C}}, T)$ the heat capacity, and $\lambda(t, x) = \lambda(t, x; F_{\text{D}}, F_{\text{C}}, T)$ the thermal conductivity of the tissue. Again it must be pointed out that these material properties depend on the temporal and spatial position (t, x) , on the dehydration state F_{D} , the coagulation state F_{C} and the temperature T of the tissue. The value $T_{\text{probe}} = 290\text{ K}$ in the inner boundary condition (2.5b) is the temperature of the internally cooled probe. In (2.5c), a Dirichlet boundary condition is presented, which is built on the assumption that there is no heating effect on the outer boundary of the region of interest (ROI), i. e. far away from the probe. For the sake of completeness it should be remarked that as an alternative to the Dirichlet condition (2.5c), also a Neumann (or natural) boundary condition of the form

$$n \cdot \nabla T(t, x) = 0 \quad \text{on } I \times \Gamma_{\text{out}} \quad (2.6)$$

can be used. This condition is due to the assumption that no heat flow across the outer boundary takes place. Finally, the initial condition (2.5d) is due to the fact that at the beginning of an RF ablation the tissue naturally has body temperature.

The right hand side $Q = Q(t, x)$ of the heat equation (2.5a) is composed as follows

$$Q = Q_{\text{rf}} + Q_{\text{perf}} + Q_{\text{PC}} , \quad (2.7)$$

2 Simulation of Radiofrequency Ablation - Forward Modeling

where $Q_{\text{rf}} = Q_{\text{rf}}(t, x)$ is the heat source due to the electric current as described above (see (2.4)), $Q_{\text{perf}} = Q_{\text{perf}}(t, x)$ is a heat sink due to the cooling influence of the vascular system, and $Q_{\text{PC}} = Q_{\text{PC}}(t, x)$ is a heat source or -sink dependent on the phase change of water.

For the modeling of the cooling effects Q_{perf} due to blood perfusion, one e. g. can use a weighted variant of the approach of Pennes [69], which is

$$Q_{\text{perf}}(t, x) = -\nu(x) (T(t, x) - T_{\text{body}}) , \quad (2.8a)$$

where

$$\nu(x) = \nu(x; F_C) = \begin{cases} \nu_{\text{vessel}} \rho_{\text{blood}} c_{\text{blood}} , & \text{for } x \in D_v, F_C < F_C^* , \\ \nu_{\text{cap}} \rho_{\text{blood}} c_{\text{blood}} , & \text{for } x \notin D_v, F_C < F_C^* , \\ 0 , & \text{for } F_C \geq F_C^* . \end{cases} \quad (2.8b)$$

Here, F_C again is the coagulation state of the tissue (see paragraph ‘‘Tissue Damage’’ and in particular Eqs. (2.9) and (2.10)) and $F_C^* = 1 - \exp(-1)$ is the value from which the tissue can be regarded as completely coagulated. Consequently, if the coagulation state F_C reaches this value, blood flow is no longer possible. Moreover, the coefficient ν depends on the relative blood circulation rate ν_{vessel} [s^{-1}] of vessels and ν_{cap} [s^{-1}] of capillaries respectively, as well as on the blood density ρ_{blood} [kg/m^3] and the heat capacity c_{blood} [$\text{J}/\text{kg K}$] of blood. Here, we assume that the whole tissue is pervaded by capillary vessels and thus is exposed to their cooling influence. Note that this is only one among several approaches to modeling the blood perfusion during RF ablation (see e. g. [47, 88, 72]) and that the modeling of blood perfusion, moreover, is a current field of research.

For modeling the energy balance $Q_{\text{PC}} = Q_{\text{PC}}(t, x)$ with respect to phase changes and the dehydration state $F_D = F_D(t, x)$ of the tissue, one e. g. can use a discrete correction step in the numerical algorithm as described in the work of Stein [79], and moreover in [56].¹ Although the phase change of water (and also nitrogen) play an important role in the energy balance during an RF ablation, they are rarely considered. An approach for modeling the vaporization of water at temperatures around 100°C , via a so-called Stefan boundary condition that models the jump of gradients at the border between fluid and gaseous material has been developed in [68]. Here, at least, it should be pointed out that the main influence of the vaporization on the energy balance is that if the water content of the tissue cells converges to zero, the electric conductivity σ and consequently the heat source Q_{rf} also converge to zero, so that no further heating occurs. Hence, the temperature is bounded by the boiling temperature of approximately 100°C . Note that before the temperature reaches the boiling temperature, the term Q_{PC} for modeling the phase changes in the heat equation (2.5a) can be omitted. Moreover, it should be mentioned that also

¹Note that in the model described in [56] instead of one function $F_D = F_D(t, x)$ for modeling the dehydration state, two functions $F_W = F_W(t, x)$ and $F_V = F_V(t, x)$ for modeling the content of fluid water and vapor are needed.

the coagulation of proteins is a phase change which is described in more detail below.

Tissue Damage. The denaturation of tissue proteins and the corresponding tissue damage (up to tissue destruction) can be calculated by a model which is based on the so-called ‘‘Arrhenius formalism’’ [9]. The damage $D_A : I \times D \rightarrow \mathbb{R}$ which describes the rate between coagulated and native tissue cells can be modeled by the so-called *damage integral*:

$$D_A(t, x) = A_A \int_0^t \exp\left(\frac{-E_A}{RT(\tau, x)}\right) d\tau . \quad (2.9)$$

Here, $R = 8.314 \text{ J/K mol}$ is the universal gas constant, T is the temperature, and the constants A_A and E_A are the so-called ‘‘Arrhenius parameters’’. More precisely, the parameter E_A [J/mol] can be compared with the activation energy of the reaction, while the parameter A_A [s^{-1}] (which on closer examination shows a dependence on the temperature itself) is a frequency factor which is related to the number of impulses between the reactants and significantly depends on the activation entropy. Regarding the interpretation of the damage integral, the value $D_A = 0$ represents a purely native protein concentration, whereas for $D_A \rightarrow \infty$ a complete coagulation of proteins will be reached. Hence, the tissue at location $x \in D$ can be considered destroyed at a time t if the damage $D_A(t, x)$ becomes greater than or equal to a critical value $D_{A, \text{crit}}$ with e. g. $D_{A, \text{crit}} = 1$ (cf. Stein, p.61). The coagulation state F_C of the tissue (i. e. the relative portion of coagulated proteins with respect to the total protein concentration) is then defined on the basis of the tissue damage $D_A(t, x)$ as

$$F_C(t, x) = 1 - \exp(-D_A(t, x)) , \quad (2.10)$$

where $F_C = 0$ stands for purely native tissue, and $F_C \geq F_C^* := 1 - \exp(-D_{A, \text{crit}})$ means that the tissue is completely destroyed.

One problem of this model is that typical values of the Arrhenius parameter A_A for native liver lie in the range $10^{40} - 10^{104} \text{ s}^{-1}$ (cf. [79], pp.71 and 155), whereas the integrand typically lies around $\exp(10^{-5})$ which makes the computation of the damage integral $D_A(t, x)$ quite ill-conditioned and unstable.

A second, much simpler approach considers the tissue being destroyed if a high critical temperature T_{crit} is reached for a time period of at least $\Delta t = 1 \text{ s}$. For human tissue this critical temperature lies at $T_{\text{crit}} \approx 333.15 \text{ K}$ ($= 60^\circ \text{C}$). But indeed the tissue is being damaged at lower temperatures as well, if they are applied for a longer time than 1 s . This effect can only be considered if the history of heating is taken into account, as in the Arrhenius formalism.

Material Parameters. In the above described model for an RF ablation the material parameters of the tissue under consideration, i. e. the electric and thermal conductivity σ and λ , as well as the density ρ and the heat capacity c of the tissue depend not only on time and space, but also on the dehydration state F_D , the coagulation state F_C and the temperature T of the tissue. Although these dependencies

are nonlinear (see [79]), one can use e. g. the following approximation which is linear in F_D , F_C and T to model the dependence of the material parameters on these quantities (see [79] and [56]):

$$\sigma(t, x) = \sigma_1 (1 + \sigma_2(T - T_{\text{body}})) (1 + \sigma_3 F_D) (1 + \sigma_4 F_C(t, x)) \quad (2.11)$$

and analog for λ , ρ and c . The constants for this equation and for the equivalent equations to calculate λ , ρ and c are

$$\begin{aligned} \sigma_1 &= 0.21 \text{ A/Vm} , & \sigma_2 &= 0.013 \text{ K}^{-1} , & \sigma_3 &= -1 , & \sigma_4 &= 1.143 , \\ \rho_1 &= 1080 \text{ kg/m}^3 , & \rho_2 &= -0.00056 \text{ K}^{-1} , & \rho_3 &= -0.657 , & \rho_4 &= 0 , \\ c_1 &= 3455 \text{ J/gK} , & c_2 &= 0 , & c_3 &= -0.596 , & c_4 &= 0 , \\ \lambda_1 &= 0.437 \text{ W/Km} , & \lambda_2 &= 0.0025 \text{ K}^{-1} , & \lambda_3 &= 0 , & \lambda_4 &= 0 \end{aligned}$$

(again taken from [79], [56]).

Another approach to model the material parameters is to approximate measured data by appropriate functions. For example Zurbuchen et al. [97] approximated a curve of measured values for the electric conductivity in dependence on the temperature T (given in centigrades), by a polynomial of degree four:

$$\sigma(T) \approx \sum_{k=0}^4 a_k T^k . \quad (2.12)$$

A linear regression with least squares minimization yielded the following coefficients a_k , $k = 0, \dots, 4$ for the polynomial approximation of the forward part of the curve of measured data

$$\begin{aligned} a_0 &= 4.6109 \cdot 10^{-2} , & a_1 &= 2.5699 \cdot 10^{-2} , & a_2 &= -8.5026 \cdot 10^{-4} , \\ a_3 &= 1.4467 \cdot 10^{-5} , & a_4 &= -8.0153 \cdot 10^{-8} . \end{aligned}$$

Moreover, for the approximation of the backward part² of this curve the following coefficients have been computed:

$$\begin{aligned} a_0 &= -5.8939 \cdot 10^{-1} , & a_1 &= 5.9956 \cdot 10^{-2} , & a_2 &= -1.3856 \cdot 10^{-3} , \\ a_3 &= 1.4601 \cdot 10^{-5} , & a_4 &= -5.5016 \cdot 10^{-8} . \end{aligned}$$

The two curves of the resulting polynomials are shown in Fig. 2.4 together with the measured values for the electric conductivity. Note that in order to obtain the coefficients a_k (and thus the curves of the resulting polynomials) in dependence on a temperature given in kelvin, the temperature T within the polynomial (2.12) has to be converted accordingly.

²The backward part of the curve of $\sigma(T)$ is a consequence of hysteresis effects, i. e. the values of σ decrease, if after a certain time period of tissue heating the energy supply decreases due to tissue coagulation.

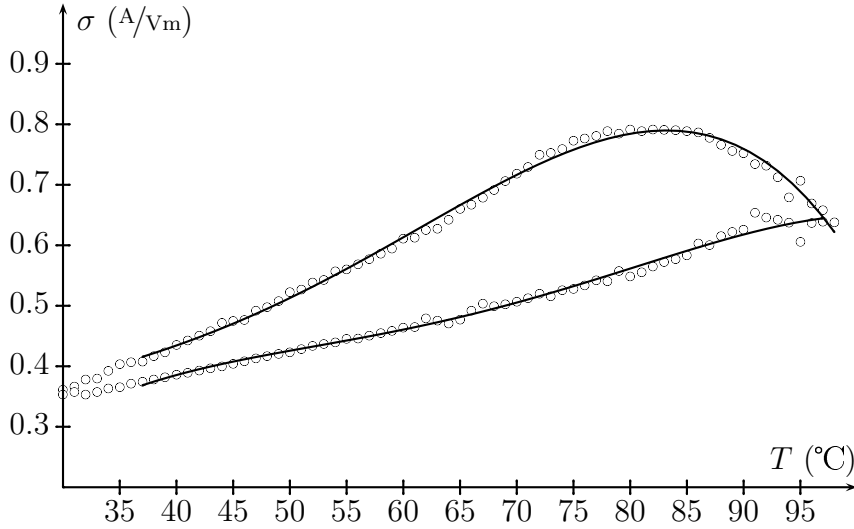


Figure 2.4: Dotted curve: Measured values for the electric conductivity. Solid curves: Curves of two fourth order polynomial functions the coefficients of which have been determined to approximate the measured data as good as possible.

2.3 A Simplified Model for the Optimization of the Probe Placement

For the optimization of the probe placement (i. e. the optimization of the probe's position and orientation) the forward simulation described in the previous section has to be computed several times (in each step of the optimization), so that an optimization with the fully complex forward model would be too time consuming. Hence, for the optimization of the probe placement the following simplifications are made here:

- *Steady State* The time dependence is omitted, so that the temperature distribution at the end of an RF ablation (after infinite long time) is studied. Here, it is admissible to neglect the time dependence in a first approach for optimizing the probe placement, because not the intensity of the heat source, but only the distribution of heat will be optimized by optimizing the probe placement. Note that the temperature will not be infinitely high with this approach, (i. e. after infinite time), because the vessel cooling works against an infinitely high temperature increase.
- *Constant Tissue Parameters* The electric and thermal conductivity σ and λ are assumed to be constant here, which further simplifies the model, and thus accelerates the computation. In later models (cf. Chapt. 4) the material parameters will be regarded as inhomogeneous, i. e. different on the native tissue, the tumor tissue and inside vessels. In addition, σ and λ will be assumed to lie in different ranges varying for the native tissue, the tumor tissue and vessels.

Then, on the basis of that, a stochastic optimization will be performed taking into account the uncertainty in the tissue parameters.

- *Uncooled Probe* The Dirichlet boundary condition for the temperature on the probe (2.5b), which models an inner cooling of the RF probe, is omitted here. The reason for this is that when incorporating the inner cooling of the RF probe, the temperature depends not only indirectly via the heat source on the probe location, but also directly via the inner boundary condition. In the optimization this would change the derivative of the objective functional with respect to the probe location and therewith the descent direction. More precisely, the calculation of the descent direction would become more complex, so that the numerical effort and the computational costs would increase significantly. (In a later model for calculating an optimal control of the generator power (see Sect. 7.1) the internal probe cooling will be reintroduced).
- *No Phase Changes and Coagulation* The term Q_{PC} on the right hand side of the heat equation, (cf. (2.5a)), which models the phase changes due to the vaporization of cell water, is omitted. Also the dependence of the tissue parameters on the dehydration state F_D , and all dependencies on the coagulation state F_C are neglected. The reason for this is that for the optimal probe placement the effects of phase changes and coagulation play a minor role, because here, not the intensity of the heat source, but only the positioning of the heat source shall be optimized. This means that the absolute value of input energy will be fixed and chosen, such that the temperature lies below boiling temperature, so that almost no coagulation will take place.

Altogether, these simplifications yield the following steady state model for the forward simulation of RF ablation:

Electrostatic Equation: The steady state potential equation with constant electric conductivity σ and Dirichlet boundary condition on the electrodes, as well as Robin boundary condition on the outer boundary Γ_{out} of the computational domain, is calculated by the following PDE system (cf. (2.1)):

$$-\sigma\Delta\phi(x) = 0 \quad \text{in } D \setminus \overline{D_{\pm}} \text{ ,} \quad (2.13a)$$

$$\phi(x) = \pm 1 \quad \text{on } \overline{D_+} \text{ and } \overline{D_-} \text{ ,} \quad (2.13b)$$

$$n \cdot \nabla\phi(x) = \frac{n \cdot (p - x)}{|p - x|^2} \phi(x) \quad \text{on } \Gamma_{\text{out}} \text{ .} \quad (2.13c)$$

Heat Source: After that the heat source Q_{rf} is calculated from the electric potential ϕ by the following formulas (cf. (2.2), (2.3), (2.4)):

$$Q_{\text{rf}}(x) = \frac{P_{\text{eff}}}{P_{\text{total}}} \sigma |\nabla\phi(x)|^2 \quad \text{in } D \text{ ,} \quad \text{with} \quad P_{\text{eff}} = \frac{4 P_{\text{setup}} R R_{\text{I}}}{(R + R_{\text{I}})^2} \text{ ,} \quad (2.14)$$

where

$$R = \frac{U^2}{P_{\text{total}}} \quad \text{and} \quad P_{\text{total}} = \int_D \sigma |\nabla \phi(x)|^2 dx . \quad (2.15)$$

As in Sect. 2.2, $U = 2\text{ V}$ for bipolar probes and $U = 1\text{ V}$ for monopolar probes.

Perfusion: Moreover, the heat sink due to the cooling influence of blood perfusion is taken into account by the weighted variant of Pennes [69] presented in Sect. 2.2, Eq. (2.8):

$$Q_{\text{perf}}(x) = -\nu(x) (T(x) - T_{\text{body}}) , \quad (2.16a)$$

where

$$\nu(x) = \begin{cases} \nu_{\text{vessel}} \rho_{\text{blood}} c_{\text{blood}} , & x \in D_v , \\ \nu_{\text{cap}} \rho_{\text{blood}} c_{\text{blood}} , & \text{else} . \end{cases} \quad (2.16b)$$

As well as in Sect. 2.2, ν_{vessel} and ν_{cap} are the relative blood circulation rates of vessels and capillaries, respectively, ρ_{blood} is the blood density, and c_{blood} is the heat capacity of blood. Here, again it is assumed that the whole tissue is pervaded by capillary vessels.

Heat Equation: Finally, the steady state heat equation with constant thermal conductivity λ and Dirichlet boundary condition on the outer boundary Γ_{out} of the computational domain can be calculated from the heat source Q_{rf} and -sink Q_{perf} by the following PDE system (cf. (2.5)):

$$-\lambda \Delta T = Q_{\text{rf}} + Q_{\text{perf}} \quad \text{in } D , \quad (2.17a)$$

$$T = T_{\text{body}} \quad \text{on } \Gamma_{\text{out}} . \quad (2.17b)$$

Note that these are first steps towards an optimization of the RF probe placement which partly will be extended later on. Moreover, it should be pointed out that, when taking into account the whole complexity of the model (as presented in Sect. 2.2), each step of the optimization and in particular each calculation of the potential and heat equation would need considerably more time.

2.4 Solution of the Potential- and Heat Equation

In this section possibilities for approximately solving the potential and heat equation (cf. (2.13) and (2.17)) will be presented. We start with an analytical way of solving the potential equation, in which the cylindric probe electrodes are approximated by a concatenation of overlapping charged balls. After that, a numerical approach will be presented for solving the potential as well as the heat equation with help of finite elements.

2.4.1 An Analytical Solution to the Potential Equation (Approximation by a Concatenation of Balls)

As a first step we study the optimization with only one PDE, namely the temperature equation, while calculating the potential by an analytical approximation. More precisely, we approximate the potential ϕ_{el} of a probe electrode (i. e. of a finite long charged rod) by the potential ϕ_{b} of a concatenation of overlapping, charged balls (see Fig. 2.5). The distance l of two neighboring balls of the concatenation is chosen

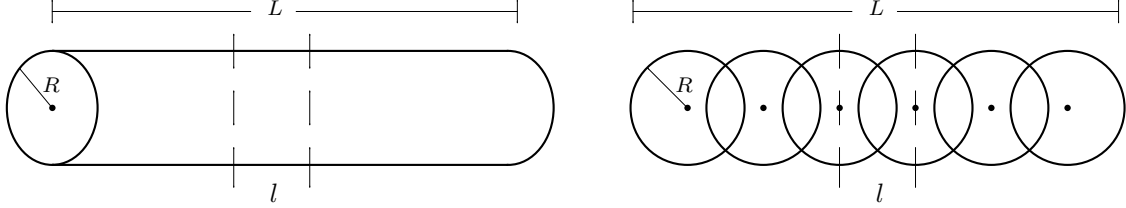


Figure 2.5: Approximation of an electrode of length L and radius R (left) by a concatenation of overlapping charged balls (right).

such that the volume between the corresponding two center points is the same as the volume of a part of the electrode of length l . Since the volume of the concatenation between two ball centers is exactly the volume of one ball (overlapping parts are counted twice), the distance l of two center points has to fulfill

$$V_{\text{ball}} = \frac{4}{3}\pi R^3 = \pi R^2 l = V_{\text{el},l} , \quad \text{i. e.} \quad l = \frac{4}{3}R .$$

Moreover, the number n of balls for the approximation has to fit to the length L of the corresponding electrode, so that the concatenation of balls has approximately the same length. Therefore, the number of balls is chosen as $n = \lfloor L/l \rfloor + 1$. Note that with this definition there will be a completely or at least partly redundant ball. This is compensated by weighting the potential of this ball with the factor $w := L/l - \lfloor L/l \rfloor \in [0, 1)$. Then the potential ϕ_{el} of an electrode is approximately the sum of the potentials ϕ_i , $i = 1, \dots, n$ of the balls:

$$\phi_{\text{el}} = \sum_{i=1}^n \phi_i . \quad (2.18)$$

The potential ϕ_i of the i -th ball can be calculated for all $x \in D$ by the following formula (see [26]):

$$\phi_i(x) = \begin{cases} \frac{Q}{4\pi\epsilon_0 r_i} , & r_i \geq R , \\ \frac{Q}{4\pi\epsilon_0 R} \left(\frac{3}{2} - \frac{r_i^2}{2R^2} \right) , & r_i < R , \end{cases} \quad (2.19)$$

where $\epsilon_0 \approx 8.8542 \cdot 10^{-12} \text{ As/V m}$ is the permittivity, Q is the charge of each ball, and r_i is the distance between point x and the center of the i -th ball (see Fig 2.6).

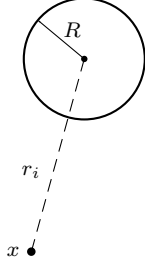


Figure 2.6: Schematic setting of the considered configuration. Here, r_i is the distance of a point $x \in D$ from the centerpoint of the i -th ball of radius R and charge Q .

For simplicity the charge Q of each ball is expressed by the charge density ϱ . Obviously, the charge density ϱ of each ball is the same as the charge density of the whole electrode, namely

$$\varrho = \frac{Q_{\text{ball}}}{V_{\text{ball}}} = \frac{Q_{\text{el}}}{V_{\text{el}}} = \frac{\pm 1}{\pi R^2 L} , \quad (2.20)$$

where the sign depends on whether the electrode is positively or negatively charged. Here, the absolute value 1 for the charge Q_{el} of the probe electrode is chosen arbitrarily, so that later on, the heat source Q_{rf} , which is calculated from the potential, has to be scaled in order to correct its dimension (see next page and in particular Eq. (2.21)). For optimizing the probe placement this is a legitimate setting, because not the intensity, but only the distribution of the heat which is induced into the tissue will be optimized via the probe positioning. Hence, the charge Q of each ball can be determined as

$$Q = Q_{\text{ball}} = \varrho \cdot V_{\text{ball}} = \varrho \cdot \frac{4}{3}\pi R^3 = \frac{\pm 1}{\pi R^2 L} \cdot \frac{4}{3}\pi R^3 = \pm \frac{4}{3} \cdot \frac{R}{L} .$$

The potential at a point $x \in D$ with respect to a bipolar probe is then the overlay of both electrode potentials, i. e.

$$\phi(x) = \phi_{\text{probe}}(x) = \phi_{\text{el1}}(x) + \phi_{\text{el2}}(x) = \sum_{i=1}^n \phi_{\text{el1}}^i(x) + \sum_{i=1}^n \phi_{\text{el2}}^i(x) \quad \forall x \in D$$

(see Fig. 2.7). For the calculation of the distance r_i of a point $x \in D$ from the center m_i of the i -th ball of electrode 1 (and the distance \tilde{r}_i of point x from the center \tilde{m}_i of the i -th ball of electrode 2, respectively), we have to consider the probe position p and direction d (again see Fig. 2.7). More precisely, that means for all balls $i = 1, \dots, n$ of an electrode

$$r_i = |x - m_i| \quad \text{with} \quad m_i = p \pm s_i \cdot \frac{d}{|d|} \quad \text{and} \quad s_i = \frac{L_{\text{iso}} - l}{2} + i \cdot l ,$$

where L_{iso} is the length of the probe's isolator, and the sign in the calculation of the center point m_i of the i -th ball depends on the location of the corresponding electrode in relation to the probe position p .

2 Simulation of Radiofrequency Ablation - Forward Modeling

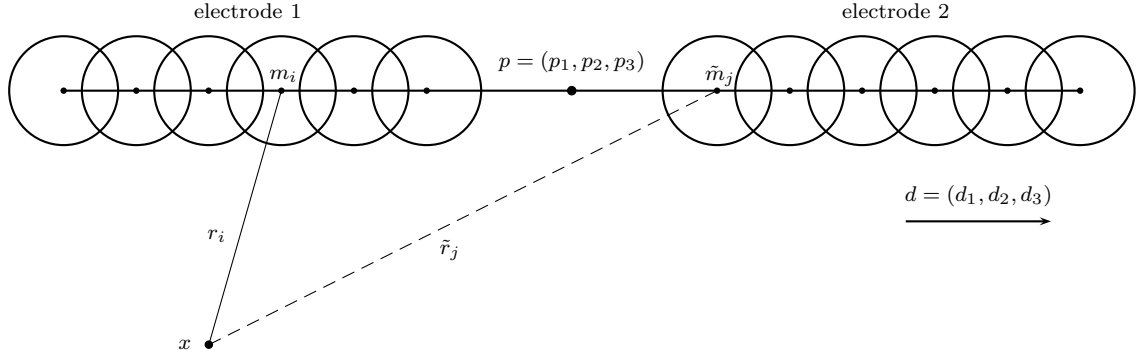


Figure 2.7: Approximation of a bipolar probe of position $p = (p_1, p_2, p_3)$ and direction $d = (d_1, d_2, d_3)$ by a concatenation of overlapping charged balls.

Now we have an analytic approximation of the potential ϕ of a mono- or bipolar probe and thus can calculate the heat source Q_{rf} from the potential as

$$Q_{\text{rf}}(x) = \frac{P_{\text{setup}}}{P_{\text{total}}} \cdot \sigma |\nabla \phi(x)|^2 \quad \forall x \in D \quad (2.21)$$

with help of e. g. central differences or analytically by using the formula

$$Q_{\text{rf}}(x) = \frac{P_{\text{setup}}}{P_{\text{total}}} \cdot \sigma \left(\sum_{i=1}^n \left(\frac{Q}{4\pi\epsilon_0} \frac{x - m_i}{|x - m_i|^3} + \frac{\tilde{Q}}{4\pi\epsilon_0} \frac{x - \tilde{m}_i}{|x - \tilde{m}_i|^3} \right) \right)^2$$

for all $x \in D \setminus D_{\pm}$, i. e. outside the electrodes. On the electrodes we obtain the slightly modified expression

$$Q_{\text{rf}}(x) = \frac{P_{\text{setup}}}{P_{\text{total}}} \cdot \sigma \left(\sum_{i=1}^n \left(\frac{Q}{4\pi\epsilon_0 R^3} (x - m_i) + \frac{\tilde{Q}}{4\pi\epsilon_0 R^3} (x - \tilde{m}_i) \right) \right)^2$$

due to the distinction of cases in (2.19). Note that here the heat source Q_{rf} is scaled by the setup power P_{setup} divided by the whole power P_{total} . This scaling is introduced because the charge Q for calculating the potential is arbitrarily set to ± 1 on the electrodes (cf. (2.20)), which leads to the fact that the overall intensity of the heat source Q_{rf} is not correct. The scaling of Q_{rf} in (2.21) does not completely correct this overall intensity, but it improves the magnitude of Q_{rf} and therewith the magnitude of the temperature T , which increases the numerical stability of the system (see also the footnote on p. 32). This is a legitimate first approach in calculating the potential and therewith the heat source for an optimization of the RF probe placement, because not the intensity of heat, but only its distribution is influenced by a movement of the probe.

After the calculation of the heat source Q_{rf} and -sink Q_{perf} as in (2.16), the temperature can be calculated by the heat equation (2.17) with help of finite elements which is topic of the next subsection.

2.4.2 Numerical Solution with Finite Elements

In this section a numerical solution of the potential equation (2.13) as well as the temperature equation (2.17) with help of finite elements will be presented. (Later on, the adjoint state which is needed to calculate a descent direction for the optimization will be determined in the same way.)

Before starting with the description of the applied finite element method (FEM), some remarks have to be made on the domains of the involved quantities:

Function Spaces

Here, the potential ϕ defined by the PDE system (2.13) and the temperature T given by (2.17) lie in the Sobolev space $H^1(D)$ which follows from the Lax-Milgram theorem (see e. g. [41]). In order to define the Sobolev space $H^1(D)$, we first need the definition of the Lebesgue space $L^2(D)$ which is the space of all measurable, square integrable functions $f : D \rightarrow \mathbb{R}$ with norm

$$\|f\|_{L^2(D)} = \left(\int_D |f(x)|^2 dx \right)^{1/2} < \infty .$$

Then $H^1(D)$ can be defined as the Sobolev space of all functions $f \in L^2(D)$ with weak derivative $\nabla f \in L^2(D)$ and with norm

$$\|f\|_{H^1(D)} = \left(\int_D (f^2 + |\nabla f|^2) dx \right)^{1/2} < \infty .$$

A special case is the Sobolev space $H_0^1(D) \subset H^1(D)$ which is the space of functions in $H^1(D)$ that vanish weakly on the boundary $\partial D = \Gamma_{\text{out}}$. More precisely, $H_0^1(D)$ is the closure of $C_0^\infty(D)$ in $H^1(D)$.

Further, the heat source Q_{rf} defined by equations (2.14) and (2.15) only lies in the Sobolev space $H^{-1}(D)$ (see [8]), where $H^{-1}(D) = H_0^1(D)^*$ is the dual space of $H_0^1(D)$ with elements $f : H_0^1(D) \rightarrow \mathbb{R}$ and norm

$$\|f\|_{H^{-1}(D)} = \|f\|_{H_0^1(D)^*} = \sup_{v \neq 0} \frac{|f(v)|}{\|v\|_{H_0^1(D)}} < \infty .$$

Hence, the complete right hand side $Q_{\text{rf}} + Q_{\text{perf}}$ of the heat equation (2.17a) also is an element of the Sobolev space $H^{-1}(D)$.³

Finite Element Method

For reasons of analogy the following description is restricted to the solution of the temperature equation, i. e. to the solution of the elliptic boundary value problem (2.17). After insertion of the formula modeling the heat sink Q_{perf} due to perfusion

³Note that Q_{perf} per definition (2.16) lies in the same space as T , i. e. in $H^1(D)$. Further we have $H^1(D) \subset H^{-1}(D)$, since by use of e. g. the L^2 scalar product $(v, w)_{L^2(D)} = \int_D v w dx$ we can define an embedding $\Psi : H^1(D) \rightarrow H^{-1}(D)$ via $\Psi(v)[w] := (v, w)_{L^2(D)}$.

into (2.17) and shifting the temperature dependent term to the left hand side, the temperature equation becomes:

$$\begin{aligned} -\lambda\Delta T + \nu T &= Q_{\text{rf}} + \nu T_{\text{body}} && \text{in } D \\ T &= T_{\text{body}} && \text{on } \Gamma_{\text{out}} . \end{aligned} \quad (2.22)$$

Let us assume the problem to be adjusted to homogeneous Dirichlet boundary conditions (see [17]) which here we obtain by setting e. g. $T := T - T_{\text{body}}$ and omitting the term νT_{body} on the right hand side of (2.22). Then the variational (or weak) form is obtained by multiplying the modified PDE (2.22) with a test function $v \in H_0^1(D)$. Integrating by parts over D leads to

$$(\lambda \nabla T, \nabla v)_{L^2(D)} + (\nu T, v)_{L^2(D)} = (Q_{\text{rf}}, v)_{L^2(D)} \quad (2.23)$$

for all $v \in H_0^1(D)$, where $(v, w)_{L^2(D)} := \int_D v w \, dx$ denotes the scalar product on the Lebesgue space $L^2(D)$. By abuse of notation we use the term $(v, w)_{L^2(D)}$ also in the case that v is only in $H^{-1}(D)$ and w is in $H^1(D)$ which becomes relevant for the evaluation of the right hand side of (2.23).

In a second step the variational problem (2.23) is discretized by covering the computational domain D with a three-dimensional uniform Cartesian grid \mathcal{G} . For that purpose (2.23) is restricted to a finite dimensional subspace $V^h \subset H_0^1(D)$ consisting of piecewise trilinear, globally continuous functions on \mathcal{G} . It is spanned by the so called hat-functions ψ_i , i. e.

$$V^h = \text{span}\{\psi_i \mid i = 1, \dots, n\} ,$$

where n is the number of grid nodes on \mathcal{G} , and ψ_i is given by the requirements that ψ_i is trilinear on each grid cell of \mathcal{G} and $\psi_i(x_j) = \delta_{ij}$ for all nodes x_j , $j = 1, \dots, n$ of \mathcal{G} . Here, δ_{ij} is the Kronecker symbol. Then every function $w \in V^h$ is determined by its nodal values w_i at the vertices x_i of \mathcal{G} :

$$w(x) = \sum_{i=1}^n w_i \psi_i(x) .$$

Since the weak form (2.23) is linear in the test function v , it suffices to test this equation with all the basis functions of V^h , i. e. $v = \psi_j$ for $j = 1, \dots, n$. This leads to a system of equations in the nodal values t_i of the temperature T . Denoting the vector of nodal values for the temperature with $\vec{t} = (t_i)_i$ and the vector of nodal values q_i for the right hand side Q_{rf} with $\vec{q} = (q_i)_i$ one has to solve

$$(\lambda L + M_\nu) \vec{t} = M_1 \vec{q} ,$$

where $L = (L_{ij})_{ij}$ is the so-called *stiffness matrix* and $M_\kappa = (M_{\kappa, ij})_{ij}$ with $\kappa = 1, \nu$ is the so-called (weighted) *mass matrix* defined by

$$L_{ij} = (\nabla \psi_i, \nabla \psi_j)_{L^2(D)} \quad \text{and} \quad M_{\kappa, ij} = (\kappa \psi_i, \psi_j)_{L^2(D)} , \quad \kappa \in L^\infty(D) .$$

For the integration of the (weighted) mass matrices M_κ a simple tensor product trapezoidal quadrature rule (cf. Sect. 3.3.1) can be used. The matrix $\lambda L + M_\nu$ is symmetric and positive definite and thus the system can be solved by a conjugate gradient (CG) method. Since L and M_κ are high-dimensional matrices (in dependence of the number of grid nodes), in order to save memory, for the implementation it is advisable not to store the matrices explicitly, but to implement the necessary matrix-vector multiplications of the CG method “on-the-fly”, i. e. by traversals of the grid and local operations on the elements of the grid [71].

The electric field $\nabla\phi$, which is needed to calculate the heat source Q_{rf} for (2.17), is determined with central differences after the solution ϕ of (2.13) has been obtained from the analog system of equations.

Now we are able to solve the forward simulation of RF ablation, so that on the basis of this we can optimize the placement of the RF probe for best possible tumor destruction. The optimization of the RF probe position and orientation will be subject of the next chapter.

3 Optimal Probe Placement for Radiofrequency Ablation

After having discussed the forward problem for the simulation of RF ablation, now the aim is to find a best positioning (i. e. a best position p and direction d) of the RF probe, such that the tumor is completely destroyed while as much native tissue as possible is saved. Hence, the result is an optimization problem with the forward simulation, or more precisely the potential and temperature equation as side conditions.

Before starting with the formal description of the model for optimizing the probe placement, in the next section two basic optimization procedures, which are referred to later on, will be shortly reviewed.

3.1 Introduction of Two Basic Optimization Methods

In this section we will consider a gradient descent and Lagrange-Newton (SQP) method for numerically solving optimization problems. For this purpose, let us assume to have the following optimization problem:

$$\begin{aligned} \min_{(y,u) \in Y \times U} \quad & f(y, u) \\ \text{s.t.} \quad & g(y, u) = 0 \quad , \end{aligned} \tag{3.1}$$

where Y and U are e. g. Banach spaces, $u \in U$ is a set of optimization parameters and $y \in Y$ is the state of the system. Moreover, the functions $f : Y \times U \rightarrow \mathbb{R}$ and $g : Y \times U \rightarrow V$ (with a Banach space V) are at least two times Fréchet differentiable.

A pair $(\bar{y}, \bar{u}) \in Y \times U$ with $g(\bar{y}, \bar{u}) = 0$ is called *optimal solution* to the optimization problem (3.1), if $f(\bar{y}, \bar{u}) \leq f(y, u)$ for all $(y, u) \in Y \times U$ that fulfill $g(y, u) = 0$.

Formal Lagrange Technique

Now in order to find an optimal solution (\bar{y}, \bar{u}) for (3.1) we introduce the so-called *Lagrange function* with a Lagrange multiplier $v \in V^*$, where V^* is the dual space of V . The Lagrange multiplier v is also called *adjoint state* and associated with the side condition $g(y, u) = 0$. The Lagrange function of the optimization problem (3.1) is then defined as $\mathcal{L} : Y \times U \times V^* \rightarrow \mathbb{R}$,

$$\mathcal{L}(y, u, v) := f(y, u) - (g(y, u), v)_{V, V^*} \tag{3.2}$$

(see e.g. [83, 40, 2, 57]). Here, $(\cdot, \cdot)_{V, V^*}$ is a pairing of functions in V and V^* .¹ According to the first order necessary optimality conditions, the so-called *Karush-Kuhn-Tucker (KKT) conditions* (see e.g. [83], pp. 244ff. and [64]), we expect that the gradient of the Lagrange function vanishes at a local optimal solution (\bar{y}, \bar{u}) of problem (3.1) with associated Lagrange multiplier \bar{v} . Hence, we obtain the optimality system:

$$D_y \mathcal{L}(\bar{y}, \bar{u}, \bar{v})[\delta y] = D_y f(\bar{y}, \bar{u})[\delta y] - (D_y g(\bar{y}, \bar{u})[\delta y], \bar{v})_{V, V^*} = 0 \quad \forall \delta y \in Y, \quad (3.3a)$$

$$D_u \mathcal{L}(\bar{y}, \bar{u}, \bar{v})[\delta u] = D_u f(\bar{y}, \bar{u})[\delta u] - (D_u g(\bar{y}, \bar{u})[\delta u], \bar{v})_{V, V^*} = 0 \quad \forall \delta u \in U, \quad (3.3b)$$

$$D_v \mathcal{L}(\bar{y}, \bar{u}, \bar{v})[\delta v] = (g(\bar{y}, \bar{u}), \delta v)_{V, V^*} = 0 \quad \forall \delta v \in V^* \quad (3.3c)$$

with test functions δy , δu and δv (also called directions).²

From condition (3.3a) we obtain the adjoint state which is the solution of the so-called *adjoint equation*

$$D_y g(\bar{y}, \bar{u})^* \bar{v} = D_y f(\bar{y}, \bar{u}), \quad (3.3a')$$

where $*$ is the adjoint operator. Moreover, from condition (3.3b) we obtain the *optimality condition*

$$D_u g(\bar{y}, \bar{u})^* \bar{v} = D_u f(\bar{y}, \bar{u}). \quad (3.3b')$$

Finally, condition (3.3c) yields our original side constraint

$$g(\bar{y}, \bar{u}) = 0. \quad (3.3c')$$

3.1.1 Gradient Descent Method

The gradient descent method (also called *method of steepest descent*) is a simple procedure (firstly investigated by Cauchy in 1847) for solving optimization problems as e.g. the one defined in (3.1) (see e.g. [83, 17, 46, 7]). The idea of a gradient descent method is to find a local minimum of a function f by following the slope of the function, i.e. by taking steps in direction of the negative gradient of f (which is the direction of the steepest descent). Starting from an arbitrarily chosen initial guess the method proceeds until no numerical improvement can be achieved any more (see Fig. 3.1).

The particular steps of the gradient descent method applied to the optimization problem (3.1) are the following:

¹Alternatively, we can assume that V is a Hilbert space and $v \in V$.

²Note that if we have restrictions on the optimization parameters $u \in U$ (e.g. box constraints $u \in U_{ad} := \{u \in U \mid a \leq u \leq b\}$), then condition (3.3b) changes to the *variational inequality*

$$D_u \mathcal{L}(\bar{y}, \bar{u}, \bar{v})[\delta u] = D_u f(\bar{y}, \bar{u})[\delta u] - (D_u g(\bar{y}, \bar{u})[\delta u], \bar{v})_{V, V^*} \geq 0 \quad \forall \delta u \in U_{ad} \quad (3.3b')$$

(see e.g. [83]). This condition expresses the observance that the Lagrange function \mathcal{L} , if coming from a minimum point (\bar{y}, \bar{u}) , cannot decrease in any direction.

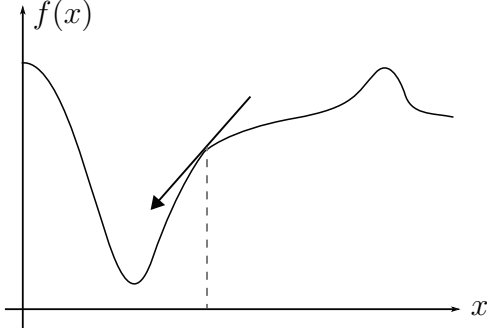


Figure 3.1: One-dimensional schematic showing the idea of the gradient descent method: A local minimum of an objective function f shall be found by taking steps in direction of the anti-gradient of f .

1. Initialize u_0, y_0, v_0 and $n := 0$.
2. Repeat
 - a) Calculate the adjoint state v_n from the adjoint equation³

$$D_y \mathcal{L}(y_n, u_n, v_n)[\delta y] = 0 \quad \forall \delta y \in Y .$$

- b) Calculate the descent direction $w_n \in U$ from the current iterates as

$$w_n = \underset{\delta u \in U}{\operatorname{argmin}} D_u \mathcal{L}(y_n, u_n, v_n)[\delta u] .$$

Since we search for a steepest descent this is $w_n = -D_u L(u_n, y_n, v_n)$.

- c) Determine the step size $s_n > 0$, such that the resulting new iterate $(y_{n+1}, u_{n+1}) \in Y \times U$ is admissible, i. e. fulfills $g(y_{n+1}, u_{n+1}) = 0$ and reduces the value of the objective function, i. e. $f(y_{n+1}, u_{n+1}) < f(y_n, u_n)$.
 - d) Update the set of optimization parameters $u_{n+1} = u_n + s_n w_n$, calculate the new state of the system y_{n+1} from u_{n+1} and update the counter $n := n + 1$.

Until $D_u L(u_n, y_n, v_n)[\delta u] < tol_1$ or $|u_n - u_{n-1}| < tol_2$.

Note that the gradient descent method dictates no special procedure for the determination of the step size. However, in order to obtain appropriate estimations for the convergence of the method, it is reasonable to choose efficient step sizes which e. g. can be determined by a bisection rule (see e. g. [83]), Armijo's rule ([35], pp. 23-27 and [36], pp. 35-37) or by the method of Wolfe-Powell (see e. g. [35], pp. 27-38 and [36], pp. 37-42).

A known drawback of the gradient descent method is that sometimes it converges only very slowly (i. e. it takes many iterations to converge towards a local minimum). This is the case if e. g. a zig-zag course is taken to the minimum (which is typical for functions with long, narrow valley structures), or if the absolute value of the gradient close by the minimum is very small which consequently results in small iteration steps (see Fig. 3.2). In such cases e. g. a conjugate gradient method (see

³The calculation of the adjoint state v is needed to be able to calculate the descent direction w_n which depends on v_n .

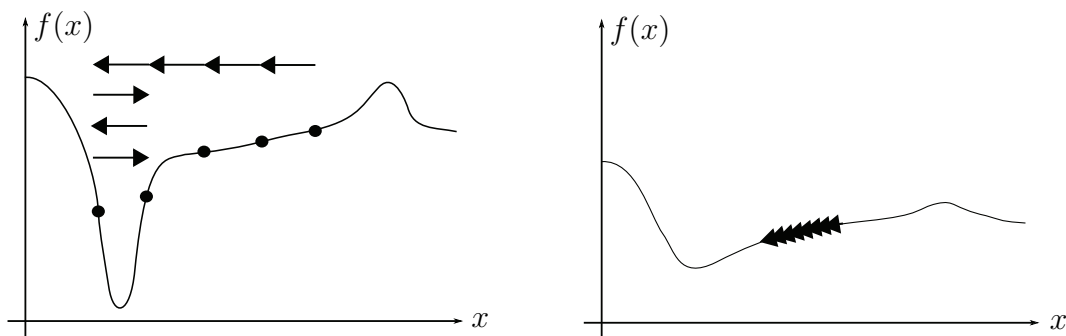


Figure 3.2: Two different schematics showing disadvantageous scenarios that lead to a slow convergence of the gradient descent method. Left: Zig-zag course to the minimum. Right: Only very small iteration steps.

[17, 46, 7]) may improve the convergence. The main idea of a conjugate gradient method is to ensure that sequent directions are not to almost parallel. Instead orthogonal directions are aimed for.

In general the gradient descent method shows a linear convergence [46, 7] that strongly depends on the rule which is used for the determination of the step size. Since the gradient descent method is based on linear approximations of the objective functional it is called a first-order optimization method. In the next paragraph a second-order method based on quadratic approximations of the objective functional (i. e. on linear approximations of the gradient of the objective functional) will be reviewed.

3.1.2 Lagrange-Newton (SQP) Method

The basic Newton method is a standard procedure for numerically solving optimization problems (see e. g. [46, 27, 35, 78, 7]). The idea of the Newton method is to search for a root of the gradient $F = \nabla f$ of a function f (i. e. to search for an optimum of f) by calculating the tangent on F at a carefully chosen starting point and taking the root of the tangent as approximation of the root of F . In a next step this approximation serves as new starting point, i. e. the root of the tangent on F at this new point yields the next, improved approximation to the root of F (see Fig. 3.3). The iteration proceeds until the gradient $F = \nabla f$ of the function f is small enough or the changes between the new and old iterates fall under a predefined threshold.

The Lagrange-Newton method employs Newton's method for the iterative solution of optimization problems (see e. g. [83, 40, 2, 3, 19, 57]). Applied to our optimization problem (3.1) the steps of the basic Lagrange-Newton method can be stated as follows:

1. Initialize y_0, u_0, v_0 and $n := 0$.

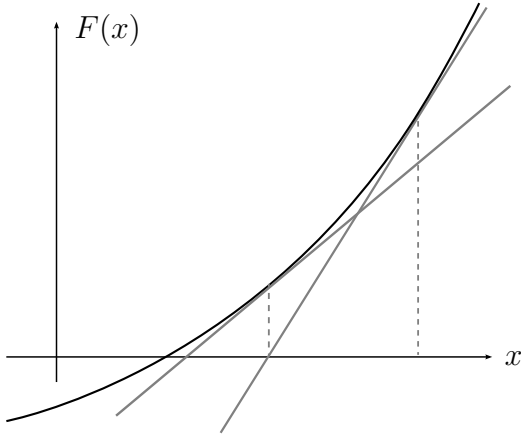


Figure 3.3: One-dimensional schematic showing the idea of the Newton method to find a root of a function $F = \nabla f$: An approximation to the root is successively improved by linearising F at this approximation and taking the root of the resulting tangent on F as new approximation to the root of F .

2. Determine the residual

$$r_0 := \begin{pmatrix} D_y \mathcal{L}(y_0, u_0, v_0) \\ D_u \mathcal{L}(y_0, u_0, v_0) \\ g(y_0, u_0) \end{pmatrix} .$$

3. Repeat

a) Solve the Newton system

$$\underbrace{\begin{pmatrix} D_{yy} \mathcal{L}(y_n, u_n, v_n) & D_{yu} \mathcal{L}(y_n, u_n, v_n) & D_y g^*(y_n, u_n) \\ D_{uy} \mathcal{L}(y_n, u_n, v_n) & D_{uu} \mathcal{L}(y_n, u_n, v_n) & D_u g^*(y_n, u_n) \\ D_y g(y_n, u_n) & D_u g(y_n, u_n) & 0 \end{pmatrix}}_{=: H_n} \begin{pmatrix} \delta y \\ \delta u \\ \delta v \end{pmatrix} = -r_n \quad (3.4)$$

b) Update the iterates

$$y_{n+1} = y_n + \delta y, \quad u_{n+1} = u_n + \delta u, \quad v_{n+1} = v_n + \delta v .$$

c) Calculate the new residual

$$r_{n+1} := \begin{pmatrix} D_y \mathcal{L}(y_{n+1}, u_{n+1}, v_{n+1}) \\ D_u \mathcal{L}(y_{n+1}, u_{n+1}, v_{n+1}) \\ g(y_{n+1}, u_{n+1}) \end{pmatrix}$$

and update the counter $n := n + 1$.

Until $\|r_n\| < tol$.

The coherency of the Lagrange-Newton method with an SQP (*sequential quadratic programming*) method can be seen as follows: To solve the Newton system (3.4) is

equivalent to find a solution $(\delta y, \delta u)$ of the quadratic problem⁴

$$\begin{aligned} \min_{(\delta y, \delta u) \in Y \times U} \quad & \frac{1}{2}(\delta y, \delta u) \begin{pmatrix} D_{yy}\mathcal{L} & D_{yu}\mathcal{L} \\ D_{uy}\mathcal{L} & D_{uu}\mathcal{L} \end{pmatrix} \begin{pmatrix} \delta y \\ \delta u \end{pmatrix} + (D_y\mathcal{L}, D_u\mathcal{L}) \begin{pmatrix} \delta y \\ \delta u \end{pmatrix} \\ \text{s.t.} \quad & (D_y g, D_u g) \begin{pmatrix} \delta y \\ \delta u \end{pmatrix} + g = 0 . \end{aligned} \quad (3.5)$$

The reason for this is that the Newton system (3.4) is equivalent to the first order necessary optimality (KKT) conditions of (3.5). Hence in each step of the main iteration, we have to approximately solve the quadratic problem (3.5). The solution of (3.5) then e.g. can be used as search direction of a *quasi-Newton method* which approximates the Hessian H_n of the Lagrange function (see (3.4)) in each step of the main iteration. One of the most common quasi-Newton algorithms is the so-called *BFGS method* developed by C. G. Broyden, R. Fletcher, D. Goldfarb and D. F. Shanno in 1970 (see e.g. [78, 7, 35]).

To ensure that the Newton system (3.4) is uniquely solvable in the vicinity of a local optimal solution (y, u) of (3.1) with associated adjoint state v and to guarantee that the quadratic problem (3.5) has a unique solution in the vicinity of (y, u) respectively, the second order sufficient optimality conditions which extend the necessary first order optimality conditions by the inequality

$$(\delta y, \delta u) \begin{pmatrix} D_{yy}\mathcal{L}(y, u, v) & D_{yu}\mathcal{L}(y, u, v) \\ D_{uy}\mathcal{L}(y, u, v) & D_{uu}\mathcal{L}(y, u, v) \end{pmatrix} \begin{pmatrix} \delta y \\ \delta u \end{pmatrix} \geq C \left\| \begin{pmatrix} \delta y \\ \delta u \end{pmatrix} \right\|_{Y,U}^2 \quad (3.6)$$

for all $(\delta y, \delta u)$ with $(D_y g(y, u), D_u g(y, u))(\delta y, \delta u)^T = 0$ and for $C > 0$ (see e.g. [83], p. 253 and [40, 64]) have to be fulfilled.

The stepwise approximative solution of the series of quadratic optimization problems (3.5) shows a locally quadratic convergence like the classical Newton method ([83], p. 196). If a reduced Newton method is used, which calculates the Hessian H_n of the Lagrange function not in each Newton step, but only in each k -th step of the Newton iteration, or if a quasi-Newton method is chosen, the costs for each single iteration step can be reduced significantly, whereas the convergence of the method decreases from a quadratic convergence to e.g. a superlinear convergence depending on the quality of the chosen approximation (see [2, 78]).

A known drawback of the Newton method is its local convergence. More precisely, the convergence of a Newton iteration is only guaranteed, if the initial guess is sufficiently close by the optimal solution. To find an appropriate initial guess one can incorporate Newton's method into a more robust method (see [46, 35]) as e.g. a gradient descent or a conjugate gradient method.

Finally it has to be remarked, that if we have additional constraints for our optimization parameters (as for example anatomical constraints for the placement of

⁴Note that as a matter of clarity, in (3.5) the arguments of the functions \mathcal{L} and g have been omitted.

the probe in radiofrequency ablation), so-called *active set strategies* or *interior point methods* (see [83, 40, 7]) are normally used for the optimization.

In the next section, as a first step the optimization of the RF probe placement is performed in only two dimensions by using a rather simple temperature based objective function. Thereby, the analytical calculation of the potential equation as described in Sect. 2.4.1 is used, while the temperature equation is solved numerically with help of finite elements (see Sect. 2.4.2). In the following, this two-dimensional optimization approach and some first results are presented. Note that this is only a preliminary step of a more sophisticated optimization in three dimensions, which will be presented in the subsequent sections (Sects. 3.3 - 3.8).

3.2 A First Approach in 2D

For the optimization of the RF probe placement, we first need a suitable objective function that measures the “quality” of an RF ablation. Here, the aim is the complete destruction of the tumor with minimum amount of affected native tissue. Moreover, the tissue is considered destroyed if it is heated above a critical high temperature T_{crit} (typically between 50°C and 60°C). Thus for an optimal outcome of the ablation, the temperature shall be high in the region of the tumor D_t and close to body temperature on the native tissue D_n . Formally, the following target temperature shall be reached

$$T_{\text{target}} = T_{\text{target}}(T)(x) = \begin{cases} T_{\text{high}} & , \text{ for } x \in D_t & , \\ T(x) & , \text{ for } x \in D_\varepsilon & , \\ T_{\text{body}} & , \text{ for } x \in D_n \setminus D_\varepsilon & , \end{cases}$$

where the region D_ε prescribes a margin between the tumor and the native tissue on which no requirements for the temperature are made, such that we have a continuous transition from the critical high temperature inside the tumor to a lower temperature (near body temperature) on the native tissue.⁵ To achieve this aim, in a first choice the following temperature based objective function, $f : L^2(D) \rightarrow \mathbb{R}$ defined by

$$f(T) = \frac{1}{2} \int_{D_t} (T - T_{\text{high}}) dx + \frac{1}{2} \int_{D_n \setminus D_\varepsilon} (T - T_{\text{body}}) dx \quad (3.7)$$

is used. Again, as in Sect. 2.4.2, $L^2(D)$ is the space of square integrable functions on D and $\|\cdot\|_{L^2(D)}^2$ is the norm on $L^2(D)$. Further, $T_{\text{high}} = T_{\text{crit}} \cdot w$ is the critical high temperature T_{crit} multiplied by a weight $w \in \mathbb{R}$ for the tumor destruction in contrast to the saving of the native tissue. For further choices of objective functionals for optimizing the RF probe placement see Sect. 3.3. Also note that here we have an

⁵Later, the integration of this explicit margin into the objective functional has been discarded (see Sect. 3.3), since it has been noticed that this margin is not needed to reach a continuous transition of the temperature from a critical high value to body temperature.

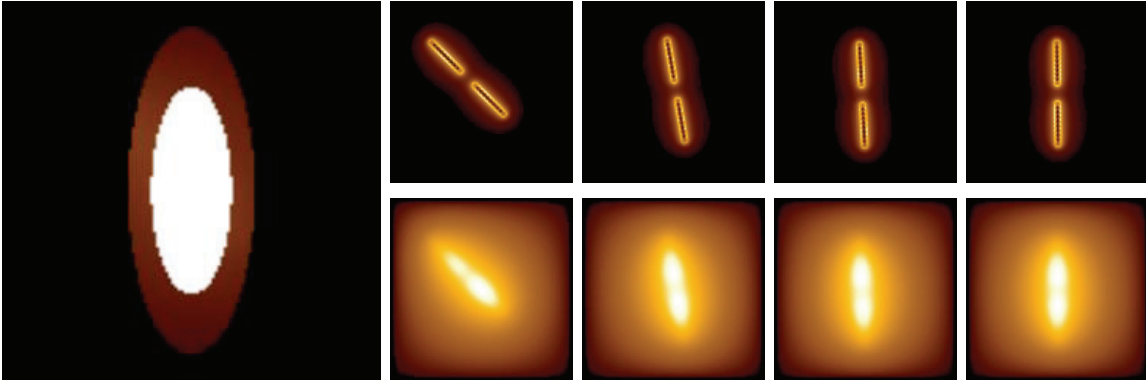


Figure 3.4: 2D-optimization of the positioning of a bipolar RF probe for an artificial example with elliptically shaped tumor. The left image shows the target temperature T_{target} , and the small images show from left to right steps 0 (start), 2, 3, and 8 (end) of the optimization. In the top row the energy source Q_{rf} from the probe is depicted, and in the bottom row the steady state of the heat distribution T is shown.

indirect dependence of the objective functional f on the optimization parameters, i. e. on the probe position p and direction d via the calculation of the electric potential ϕ , which is used to calculate the heat source Q_{rf} and thus the temperature T .

Implementation

The numerical integration which is needed to evaluate the objective functional (3.7), is performed by a simple tensor product trapezoidal quadrature rule which evaluates the integrand on the four vertices of each grid cell. For further explications of the numerical integration see Sect. 3.3.1, where this integration is implemented in three dimensions. Moreover, here the potential equation is solved analytically as described in Sect. 2.4.1, while the steady state of the temperature is calculated numerically with help of finite elements (see Sect. 2.4.2). Finally, for the optimization, here a gradient descent method (see Sect. 3.1.1) is used. A motivation for using this optimization method, as well as a detailed description of the corresponding optimization algorithm, including the calculation of the descent direction, the determination of the step size, and the choice of a suitable stopping criterion, are presented in Sect. 3.4.

3.2.1 First Results

In the following, some first results of a two-dimensional optimization of the RF probe placement, as described in the previous section, are presented. Figure 3.4 shows the optimization results for an artificial, elliptically shaped tumor without any vessel, and in Fig. 3.5, the results for an artificial, irregular shaped tumor with a linear vessel close-by are depicted. In both calculations, the computational domain D is of extent $64 \times 64 [\text{mm}^2]$ and discretized by a uniform Cartesian grid of 120^2 grid cells. Moreover, a bipolar RF probe of radius $R = 1.2 \text{ mm}$ with an

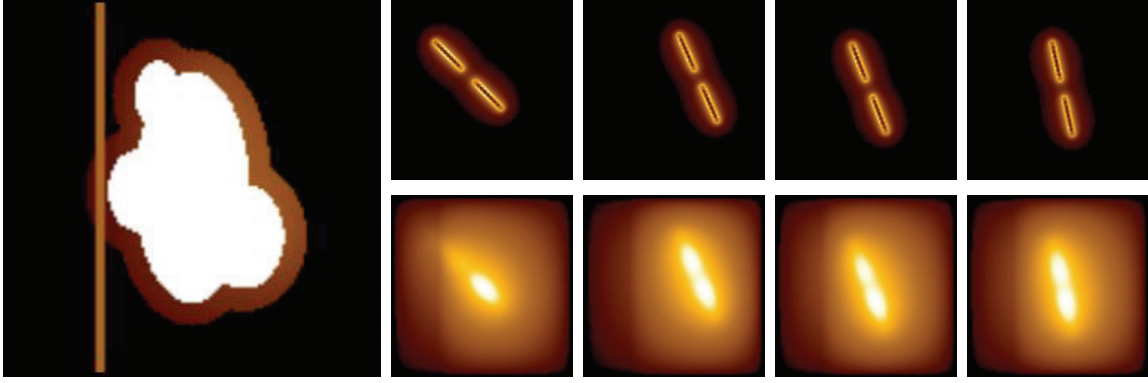


Figure 3.5: 2D-optimization of a bipolar RF probe's positioning for an artificial example with irregular shaped tumor and linear vessel. The left image again shows the target temperature T_{target} , and the small images show from left to right steps 0 (start), 1, 3, and 10 (end) of the optimization. As in Fig. 3.4, in the top row the heat source Q_{rf} is shown, and in the bottom row the steady state of the heat distribution T is presented.

electrode length of $L = 14.4$ mm and an electrode gap of $L_{\text{iso}} = 6.0$ mm is applied. Further, the generator is set up to a power of $P_{\text{setup}} = 100$ W, and the electric and thermal conductivity are set to $\sigma = 0.20757$ S/m and $\lambda = 0.5$ W/Km, respectively (cf. [79]). The perfusion in the second optimization is modeled by taking the values $\nu_{\text{cap}} = 0.0$ s $^{-1}$ (i. e. no perfusion outside vessels) and $\nu_{\text{vessel}} = 0.01765$ s $^{-1}$ (i. e. only capillary perfusion), where the value for the blood density is $\rho_{\text{blood}} = 1059.0$ kg/m 3 and the heat capacity of blood is set to $c_{\text{blood}} = 3850.0$ J/kg K (cf. Sect. 2.2/2.3 and [84, 79]). For both optimizations, the initial probe position is located at 5 mm distance in each direction from the center of D , and its orientation is $d = (1, 1)$. The left large figure in both cases shows the geometrical setting of the tumor with safety margin and vessel (if existing) – one can also interpret this as the target temperature, which is high inside the tumor and descends to body temperature on the native tissue. The small figures on the right show the energy source from the probe (top row) and the steady state of the temperature distribution (bottom row) for several steps of the optimization.

As one can see from the figures, in both cases the optimal probe position is located in the center of the tumor, and its optimal direction adapts to the shape of the tumor. Moreover, the impact of the vessel cooling can be explicitly seen on the temperature distribution depicted in the bottom row of Fig. 3.5.

In the next sections (Sects. 3.3 - 3.8) we will consider a three-dimensional optimization of the RF probe placement (together with a numerical calculation of both, the potential and heat equation (cf. Sect. 2.4.2)).⁶ Thereto, again we need a suit-

⁶The reason for now using the numerical approach for calculating the potential instead of the analytical one, is that within the analytical approach the *charge* has been set arbitrarily to ± 1 on the electrodes, while in the numerical approach the *potential* has been set to ± 1 on the electrodes. Thus, the resulting heat source has to be scaled by a factor which in the numerical case can be easily determined with help of the equivalent circuit diagram shown in Sect. 2.2 (see

able objective function which measures the “quality” of an RF ablation. Hence, as a first step towards a three-dimensional optimization, in the next section several temperature based objective functionals are presented and compared.

3.3 Formulation and Comparison of Different Objective Functionals for the Optimization in 3D

The aim of the RF therapy is the complete destruction of the lesion with minimum amount of affected native tissue. To reach this aim, now some temperature based objective functions that measure the “quality” of a given temperature distribution will be formulated and compared. Again, as in Sect. 3.2, the tissue is considered destroyed if it is heated above a critical high temperature T_{crit} between 50 °C and 60 °C. Hence, the temperature shall be high in the region of the tumor D_t and near body temperature on the native tissue D_n . To achieve this aim, there are several variants of objective functions possible:

- A first choice is the objective function (3.7) which has been used for an initial optimization approach in two dimensions (see Sect. 3.2).
- A similar first choice of an objective function, but with an explicit weighting of the tumor destruction in contrast to the saving of the native tissue, is the objective function $f : L^2(D) \rightarrow \mathbb{R}$ defined as

$$f(T) = \frac{w_{\text{in}}}{2} \|T - T_{\text{crit}}\|_{L^2(D_t)}^2 + \frac{w_{\text{out}}}{2} \|T - T_{\text{body}}\|_{L^2(D_n)}^2 \quad (3.8)$$

with w_{in} and w_{out} being suitable weights for the destruction of the tumor and the saving of the native tissue, respectively (cf. [4]). Since it is more important to destroy the tumor completely than to save the native tissue, obviously the weight w_{in} has to be much higher than the weight w_{out} . Further, within objective functional (3.8) the margin D_ε has been omitted, since computational experiments have shown that this margin is not needed to achieve a continuous transition of the temperature from critical high values to body temperature.⁷

Just as the previously defined objective function (3.7), this objective function serves as first approach. Unfortunately, both objective functions ((3.7) and

Fig. 2.3 and Eqs. (2.3), (2.4)). In the analytical case, this factor is not that easily calculable, so that a realistic scaling of the heat source has been neglected in Sects. 2.4.1 and 3.2. Note that for the optimization of the probe placement the exact overall intensity of heat is not needed, but only the correct distribution of heat. However, if later one would like to optimally control the generator power and consequently the intensity of heat which is induced into the tissue, a correct scaling of the heat source will become indispensable.

⁷Note, that the margin D_ε has not the same meaning as the tumor surrounding safety margin that should be included into the region of coagulated tissue in order to avoid recrudescences. Such a safety margin easily can be included into the model indirectly by enlarging the considered tumor region D_t .

(3.8)) penalize temperatures in the tumor region D_t which lie above the critical temperature T_{crit} , in a similar way as they penalize temperatures in D_t which are too small for tumor destruction.

- An advanced objective function $f : L^2(D) \rightarrow \mathbb{R}$ not penalizing high temperatures larger than T_{crit} inside the tumor can be obtained by the following considerations: Since by optimizing the probe placement, not an optimization of the generator power P_{setup} (i. e. of the intensity of heat induced into the tissue) is aimed, but only an optimization of the distribution of heat, it would be more reasonable to force the temperature to be *as high as possible* inside the tumor, than to consider deviations of the tumor temperature from a given critical temperature T_{crit} . Moreover, a uniform heat distribution inside the tumor should be aimed, such that there is not only one very hot region inside the tumor (cf. Fig. 3.6, left), but that the tumor is uniformly heated (cf. Fig. 3.6, right).



Figure 3.6: Left: Non-uniform tumor heating (only one hot region inside the tumor) Right: Uniform tumor heating.

These requirements are combined in the following objective function:

$$f(T) = \int_{D_t} \exp(-T(x)) dx . \quad (3.9)$$

By using the exponential function the lowest temperature inside the tumor is penalized most (see black curve in Fig. 3.7), so that configurations with only a small sufficiently hot volume inside the tumor lead to a higher value of the objective function than a uniform tumor heating. Moreover, the integral over the native tissue has been omitted, due to observations that the requirement of a high temperature inside the tumor is sufficient to force the probe to its optimal location.

A further variation of the objective function is the inclusion of a factor $\alpha > 0$ into the argument of the exponential function, i. e.

$$f(T) = \int_{D_t} \exp(-\alpha T(x)) dx . \quad (3.10)$$

This allows for a modification of the grade of penalization of a non-uniform temperature distribution inside the tumor (lower penalization for $\alpha < 1$; stronger penalization for $\alpha > 1$; cf. gray curves in Fig. 3.7).

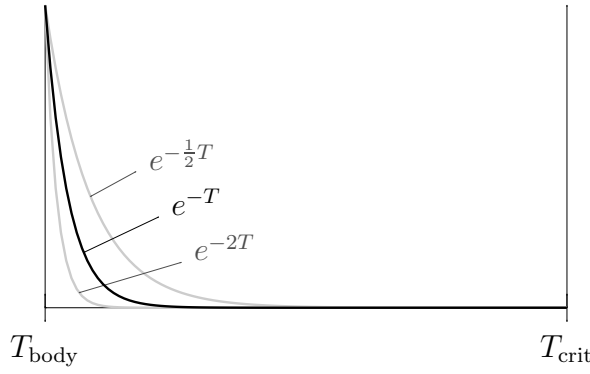


Figure 3.7: Different curves of exponential functions without additional weighting (black) or with a weighting factor in the argument (gray). The steep slope leads to a high penalty for low temperatures.

Note that the objective functions (3.9) and (3.10) are numerically unstable, i. e. they cannot be robustly evaluated, because the value of the exponential function will lead to a numerical underflow. Therefore, in the implementation of the optimization algorithm, one has to use a modification of (3.9) and (3.10), respectively, which retains the desired behavior and changes the numerical evaluation only. For that purpose, one can multiply e. g. the objective function (3.10) with the constant factor $\exp(\alpha T_{\min})$, where T_{\min} is the minimal temperature of the current iteration step and thus has to be recalculated in each step of the iteration

$$\Rightarrow f_{T_{\min}}(T) = \int_{D_t} \exp(\alpha(T_{\min} - T(x))) dx . \quad (3.11)$$

Such a modification guarantees that the argument of the exponential function does not become too small. Obviously, the analog modification for the objective function (3.9) is straightforward.

- A minor disadvantage of the approach presented above is, that for a comparison of the objective function values of e. g. different iteration steps, one has to account for the numerical modification described in (3.11). For that purpose one can e. g. calculate the logarithm and subtract the minimum temperature of the corresponding iteration step multiplied by the weighting factor α , i. e.

$$\begin{aligned} & f(T_1) < f(T_2) \\ \Leftrightarrow & f_{T_{\min,1}}(T_1) \cdot \exp(-\alpha T_{\min,1}) < f_{T_{\min,2}}(T_2) \cdot \exp(-\alpha T_{\min,2}) \\ \Leftrightarrow & \ln(f_{T_{\min,1}}(T_1) \cdot \exp(-\alpha T_{\min,1})) < \ln(f_{T_{\min,2}}(T_2) \cdot \exp(-\alpha T_{\min,2})) \\ \Leftrightarrow & \ln(f_{T_{\min,1}}(T_1)) - \alpha T_{\min,1} < \ln(f_{T_{\min,2}}(T_2)) - \alpha T_{\min,2} , \end{aligned} \quad (3.12)$$

where T_1 and T_2 are two different temperature distributions of two different iterations steps and $T_{\min,1}$ and $T_{\min,2}$ are the corresponding minimum temperatures. In short that means: For a comparison of different function values of $f(T)$ for different temperature distributions T one can e. g. calculate

3 Optimal Probe Placement for Radiofrequency Ablation

$\ln(f_{T_{\min}}(T)) - \alpha T_{\min}$ and compare the respective function values for the respective temperature distributions T and the corresponding minimum temperatures T_{\min} . Note that it is not the same to compare the function values of $f_{T_{\min}}(T)$ for different temperature distributions T , since $f_{T_{\min}}(T)$ depends on the minimum temperature T_{\min} of the corresponding iteration step.

These considerations give the idea for a further improvement of the objective function $f : L^2(D) \rightarrow \mathbb{R}$ defined in (3.10) by inserting the logarithm, i. e.

$$f(T) = \ln \left(\int_{D_t} \exp(-\alpha T(x)) dx \right). \quad (3.13)$$

As seen above, by using the logarithm a comparison of different objective function values can be performed without any conversions now, although the minimum temperature T_{\min} is still needed for the numerical evaluation as described below. More precisely, this means that the objective function f in (3.13) can be implemented as

$$f(T) = f_{T_{\min}}(T) = \ln \left(\int_{D_t} \exp(\alpha(T_{\min} - T(x))) dx \right) - \alpha T_{\min}, \quad (3.14)$$

(cf. (3.12)) which can be evaluated numerically robust, but also can be compared without any transformations.

On closer examination of the last defined objective function (3.13), one can see that this objective function shows exactly the desired behavior, because (apart from some multiplicative constants) for $\alpha \rightarrow \infty$ it converges to a function which maximizes the minimum temperature inside the tumor lesion.

More precisely, one can make the following considerations: The aim of the optimization of the RF probe placement is (as seen before) to find an optimal probe location such that the tumor is uniformly heated and the minimum temperature in the tumor region becomes as high as possible, such that all malignant cells are completely destroyed. That means the aim is to find an optimal probe location $(\bar{p}, \bar{d}) \in U := D \times S^2$, such that

$$(\bar{p}, \bar{d}) = \operatorname{argmax}_{(p,d) \in U} \min_{x \in D_t} T(x) = \operatorname{argmin}_{(p,d) \in U} \left(- \min_{x \in D_t} T(x) \right) \quad (3.15)$$

(cf. with the minmax-function in [52], where the probe placement and generator power of a steady state model are optimized, such that the temperature on the tumor tissue converges to an upper given temperature distribution, and the temperature on the native tissue converges to a lower given temperature distribution, respectively.) Since the min-function is not differentiable, (3.15) has to be approximated by a differentiable function of the same behavior. More precisely, it can be approximated by the following objective function

$$F(T) = \frac{1}{\alpha} \ln \left(\frac{1}{|D_t|} \int_{D_t} \exp(-\alpha T(x)) dx \right) \quad (3.16)$$

for some $\alpha > 0$. Note that for $\alpha \rightarrow \infty$, the integrand $\exp(-\alpha T(x))$ converges to zero slowest for the smallest value of $T(x)$. Thus, for large α the integration of $\exp(-\alpha T(x))$ can be approximated by an integration of the constant value $\exp(-\alpha \min_{x \in D_t} T(x))$. Consequently the integral $\int_{D_t} \exp(-\alpha T(x)) dx$ reduces to $|D_t| \exp(-\alpha \min_{x \in D_t} T(x))$, and $F(T)$ simplifies to $-\min_{x \in D_t} T(x)$. A formal proof for this convergence will be presented in [54].

Obviously, $F(T)$ can be simplified to $F(T) = K + \alpha^{-1} f(T)$ with $K = \alpha^{-1} \ln(|D_t|^{-1})$ and

$$f(T) = \ln \left(\int_{D_t} \exp(-\alpha T(x)) dx \right) ,$$

which is the objective function from above (3.13). Consequently the optimization problem becomes

$$(p, d) = \underset{(p,d) \in U}{\operatorname{argmin}} f(T) = \underset{(p,d) \in U}{\operatorname{argmin}} \ln \left(\int_{D_t} \exp(-\alpha T(x)) dx \right) \quad (3.17)$$

since K is a constant that can be omitted for the minimization and the factor α^{-1} is a scaling of the objective function only.

3.3.1 Numerical Integration

The evaluation of the objective function f involves the integration over the domain D_t (of the tumor). In applications, the segmented image data which specifies the domains D_t and D_v (of the tumor and vessel system, respectively) is defined on a three-dimensional grid \mathcal{G} as defined in Sect. 2.4.2. Let $\mathcal{N} = \{x_i \mid i = 1, \dots, n\}$ denote the set of vertices of \mathcal{G} , and $E \in \mathcal{G}$ denoting a grid cell. Further, assume that we have characteristic Ansatz-functions χ_t and χ_v which lie in the finite dimensional subspace $V^h \subset H_0^1(D)$ defined in Sect. 2.4.2, and which are supported on the discretized domains D_t and D_v . More precisely, χ_t and χ_v are hat-functions on \mathcal{G} which have values 0 and 1 on the grid nodes (depending on whether a grid node belongs to the tumor and vessel, respectively, or to the remaining tissue) and are trilinear between the grid nodes (cf. Sect. 2.4.2). Integrations are then performed with a simple tensor product trapezoidal quadrature rule which evaluates the integrand on the eight vertices of each grid cell (i. e. of each element E of the grid), only. Formally that means for e. g. the objective function (3.13):

$$\begin{aligned} \int_{D_t} \exp(-\alpha T(x)) dx &= \sum_{E \in \mathcal{G}} \int_E \chi_t(x) \exp(-\alpha T(x)) dx \\ &\approx \sum_{E \in \mathcal{G}} \frac{|E|}{8} \sum_{x_i \in E \cap \mathcal{N}} (\chi_t \exp(-\alpha T))(x_i) . \end{aligned}$$

For the evaluation of the mass matrices $M_\kappa = (M_{\kappa, ij})_{ij}$ with components $M_{\kappa, ij} = \int_D \kappa(x) \psi_i(x) \psi_j(x) dx$ (as defined in Sect. 2.4.2), *lumped masses* [81] are used, which corresponds to a trapezoidal quadrature rule as described above.

3.4 An Algorithm for the Optimization

In this section, an algorithm for the optimization of the RF probe placement will be presented. In particular, a detailed description of the calculation of the descent direction, the determination of a suitable step size and the choice of an appropriate stopping criterion for the optimization (cf. Sect. 3.1 and in particular 3.1.1) will be given.

Formally the objective function f can be considered as a function of the temperature distribution T , where T is a function of the heat source Q_{rf} , and Q_{rf} is a function of the optimization parameter $(p, d) =: u \in U := D \times S^2$. Hence, one can write

$$\begin{aligned} Q_{\text{rf}} &= \mathcal{Q}(u) \quad , \quad \mathcal{Q} : U \rightarrow H^{-1}(D) \quad , \\ T &= \mathcal{T}(Q_{\text{rf}}) \quad , \quad \mathcal{T} : H^{-1}(D) \rightarrow H^1(D) \quad . \end{aligned} \tag{3.18}$$

To optimize the probe location, we are looking for $u \in U$ such that $F : U \rightarrow \mathbb{R}$, $u \mapsto F(u) := f \circ \mathcal{T} \circ \mathcal{Q}(u)$ becomes minimal.

Before starting with the description of the optimization method, it has to be remarked that in certain situations the uniqueness of a minimizing configuration is not guaranteed, e. g. for spherical tumors. This situation may also occur in practice for hepatic tumors which often have a spherical-like shape. However, such a symmetry is broken by the consideration of surrounding blood vessels and their cooling effects. Moreover, for practical reasons the uniqueness of a solution is not needed and even local minima give important information about good probe and generator configurations. In addition, an incorporation of constraints for the optimization parameters given by anatomical structures as e. g. bones, colon, or diaphragm that must not be punctured during the ablation, will break any existing symmetry even further.

For the optimization, i. e. the minimization of the objective function f , here, a gradient descent method (see Sect. 3.1.1) is applied. This choice is due to the fact that the experiments (cf. Sects. 3.5 and 3.8) have shown that the optimization needs only very few iteration steps. Thus, here it is not needed to use higher order methods like Lagrange-Newton (SQP) approaches (cf. Sect. 3.1.2). Moreover, for the RF ablation model described in the previous sections, the corresponding Hessian turns out to be very ill-conditioned (cf. (3.20) and Fig. 3.8). In more detail, we have to consider the following case: Classically, to derive the optimality system, one would define a Lagrange function by subtracting all constraints (with appropriate multipliers) from the objective function. But since in our case the connection between the electric potential ϕ (as the solution of (2.13)) and the heat source Q_{rf} is rather complicated through equations (2.14) and (2.15), we do not insert this constraint into a Lagrange function. Instead, as described above (see (3.18)), we consider the source term Q_{rf} to depend directly on the probe parameters u (i. e. $Q_{\text{rf}} = \mathcal{Q}(u)$).

Hence, we have the following reduced Lagrange function:

$$\begin{aligned} \mathcal{L}(T, u, v) := & f(T) - \int_D \lambda \nabla T(x) \nabla v(x) dx - \int_D \nu(x) T(x) v(x) dx \\ & + \int_D Q_{\text{rf}}(x) v(x) dx \end{aligned} \quad (3.19)$$

with the Lagrange multiplier $v \in H_0^1(D)$.⁸ Twice differentiation of the reduced Lagrange function (3.19) yields the following Hessian (cf. Sect. 3.1.2):

$$H(T, u, v) = \begin{pmatrix} D_{TT}\mathcal{L} & D_{Tu}\mathcal{L} & D_{Tv}\mathcal{L} \\ D_{uT}\mathcal{L} & D_{uu}\mathcal{L} & D_{uv}\mathcal{L} \\ D_{vT}\mathcal{L} & D_{vu}\mathcal{L} & D_{vv}\mathcal{L} \end{pmatrix} = \begin{pmatrix} \frac{\partial^2}{\partial T^2} f & 0 & \lambda\Delta - \nu \\ 0 & v \frac{\partial^2}{\partial u^2} Q_{\text{rf}} & \frac{\partial}{\partial u} Q_{\text{rf}} \\ \lambda\Delta - \nu & \frac{\partial}{\partial u} Q_{\text{rf}} & 0 \end{pmatrix}, \quad (3.20)$$

where the derivatives of the heat source Q_{rf} with respect to u are evaluated numerically with help of central differences. Unfortunately, we have a steep slope of the heat source Q_{rf} next to the boundary of the probe, so that the components of the derivative

$$\frac{\partial}{\partial u} Q_{\text{rf}} = \left(\frac{\partial}{\partial p_1} Q_{\text{rf}}, \frac{\partial}{\partial p_2} Q_{\text{rf}}, \frac{\partial}{\partial p_3} Q_{\text{rf}}, \frac{\partial}{\partial a_1} Q_{\text{rf}}, \frac{\partial}{\partial a_2} Q_{\text{rf}}, \frac{\partial}{\partial a_3} Q_{\text{rf}} \right) \quad (3.21)$$

with

$$\frac{\partial}{\partial p_1} Q_{\text{rf}} = \frac{Q_{\text{rf}, p_1 + \varepsilon} - Q_{\text{rf}, p_1 - \varepsilon}}{2\varepsilon} = \frac{Q_{\text{rf}}(x - \varepsilon) - Q_{\text{rf}}(x + \varepsilon)}{2\varepsilon}, \quad \dots \quad (3.22)$$

have very large amplitudes and even converge to $\pm\infty$ next to the probe's boundary (see Fig. 3.8).

Consequently, the entries $\frac{\partial}{\partial u} Q_{\text{rf}}$ within the Hessian contain very large absolute values, so that values which are approximately (but not exactly) zero, and which are multiplied with these entries of the Hessian H , become very large (compared to zero). More precisely, in case of using a Lagrange-Newton method (see Sect.3.1.2), in each step of the optimization one would have to solve the Newton system:

$$H(T, u, v) \begin{pmatrix} \delta T \\ \delta u \\ \delta v \end{pmatrix} = -r_n, \quad (3.23)$$

where $r_n = (\mathcal{L}_T, \mathcal{L}_u, \mathcal{L}_v)^t$ is the residuum of the n -th iteration step, and δT , δu , δv are the current changes in T , u and v , respectively, which have to be calculated here. (Note that the zero-block on the diagonal of the Hessian H (cf. (3.20)) easily

⁸Note that within the definition of the Lagrange function (3.19), where we use the weak form of the heat equation adjusted to homogeneous boundary conditions by setting $T := T - T_{\text{body}}$ (see Sect. 2.4.2), the objective functional $f(T)$ formally changes to $f(T + T_{\text{body}})$.

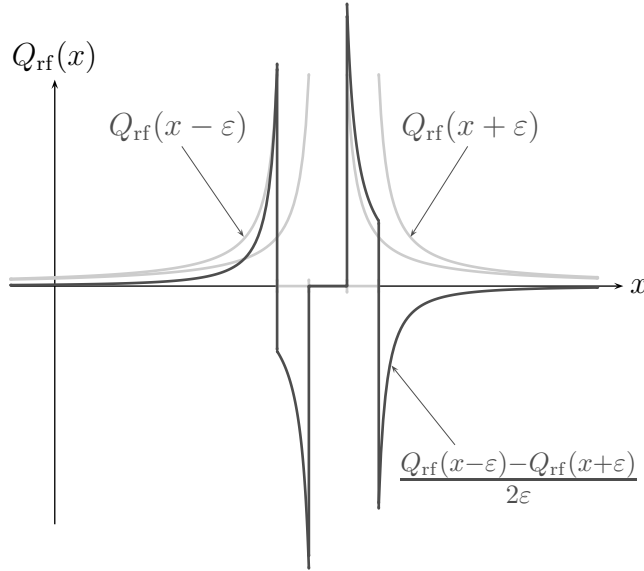


Figure 3.8: Light Gray: Slope of the heat source next to the boundary of the probe for $p = (p_1 + \varepsilon, p_2, p_3)$ and $p = (p_1 - \varepsilon, p_2, p_3)$, respectively. Dark Gray: Central difference quotient for approximating the derivative of Q_{rf} with respect to the x -component p_1 of the probe's position.

can be eliminated by a permutation of rows or by a multiplication of the Newton system (3.23) with the Hessian H , such that on the left hand side H turns into H^2 which is positive definite.) Now, when T , u , and v are nearly optimal (i. e. $(\delta T, \delta u, \delta v) \approx 0$ and $r_n \approx 0$), the large absolute values of $\frac{\partial}{\partial u} Q_{\text{rf}}$ within the Hessian H will cause the product on the right hand side of the Newton system (3.23) to be far away from zero which will lead to numerical problems in solving the Newton system. For example, a Jacobi method for solving the Newton system unfortunately will not converge (which also can be seen by the fact that obviously the Hessian is not diagonally dominant). Also the usage of a relaxation method would not yield better results, since the relaxation parameter would have to be chosen such small for convergence, that the optimization never would be finished. Therefore, a Lagrange-Newton (SQP) method would not be a good choice for solving our optimality system. Instead, as already mentioned above, we use a gradient descent method which is less sensitive with respect to the large absolute values of $\frac{\partial}{\partial u} Q_{\text{rf}}$. (Here, no system like the Lagrange-Newton system (3.23) has to be solved, and the large values of $\frac{\partial}{\partial u} Q_{\text{rf}}$ within the descent direction are compensated by the composition with the adjoint v and by the choice of the step size s ; see the following explanation).

Before starting with a detailed description of the applied gradient descent method, some remarks on the domain of the probe's positioning (p, d) have to be made: Since the orientation d of the probe lies on the sphere S^2 one would have to compute a gradient of the objective function on the sphere. This would involve some difficulties, in particular because there is no basis of the tangent space of S^2 at d that depends continuously on d . For this reason, the domain $U = D \times S^2$ for the probe's position p and orientation d is replaced by the open set

$$\tilde{U} = D \times (\mathbb{R}^3 \setminus \{0\}) \supset U . \quad (3.24)$$

Moreover, let the projection $P : \tilde{U} \rightarrow U$ be defined by

$$P : (p, d) \mapsto (p, d/|d|) . \quad (3.25)$$

Then one can set

$$\mathcal{Q}(u) = \mathcal{Q}(p, d) := (\mathcal{Q} \circ P)(p, d) = \mathcal{Q}(p, d/|d|) , \quad (3.26)$$

i. e. \mathcal{Q} does not depend on the length of d .

Now the particular ingredients of the gradient descent method which is used here for solving the optimality system, are the following, which will be discussed in more detail below:

- **Initial value.** First an arbitrary probe positioning $u^0 \in U$ is chosen as an initial guess for the optimization.
- **Descent direction.** Then, in each iteration step $n \geq 0$, the descent direction $w^n \in \mathbb{R}^6$ is calculated from the current iterate u^n as an approximation of $-\nabla_u f(u^n)$.
- **Step size.** Next, the step size $s^n > 0$ is determined, such that the resulting new iterate $u^{n+1} = P(u^n + s^n w^n)$ is admissible, i. e. fulfills $u^{n+1} \in U$ and reduces the value of the objective function $f(u^{n+1}) < f(u^n)$. By using the projection P , it is ensured that the new orientation lies on the sphere.
- **Stopping criterion.** The iteration continues until the difference $|u^{n+1} - u^n|$ falls below a given threshold θ .

3.4.1 Descent Direction

For the calculation of the descent direction w we have to consider the reduced Lagrange function $\mathcal{L}(T, u, v)$ in (3.19). Then minimizing the objective function f is equivalent to finding solutions of $D_T \mathcal{L}(T, u, v)[\gamma] = 0$ and $D_u \mathcal{L}(T, u, v)[\gamma] = 0$ for all test functions γ .

In the following, we exemplarily consider the objective function f of (3.13). The analog calculations for the other objective functions (3.7)-(3.10) are straightforward. Then the variation $D_T \mathcal{L}(T, u, v)[\gamma]$ is given by

$$\begin{aligned} D_T \mathcal{L}(T, u, v)[\gamma] = & -\alpha \left(\int_{D_t} \exp(-\alpha T(y)) dy \right)^{-1} \int_{D_t} \exp(-\alpha T(x)) \gamma(x) dx \\ & - \int_D \lambda \nabla v(x) \nabla \gamma(x) dx - \int_D \nu(x) v(x) \gamma(x) dx \end{aligned} \quad (3.27)$$

for all test functions $\gamma \in H^1(D)$. This variation leads us to the so-called *adjoint equation*. More precisely, now one can calculate the Lagrange multiplier v (the so-called *adjoint state*) as the solution to the equation $D_T \mathcal{L}(T, u, v) = 0$ in D which

3 Optimal Probe Placement for Radiofrequency Ablation

is

$$-\lambda\Delta v(x) + \nu v(x) = -\alpha \left(\int_{D_t} \exp(-\alpha T(y)) dy \right)^{-1} \chi_{D_t}(x) \exp(-\alpha T(x)) \quad (3.28)$$

for all $x \in D$, with the boundary condition $v = 0$ on ∂D . Here, $\chi_{D_t}(x)$ is an indicator function which is 1 for $x \in D_t$ and 0 elsewhere. Furthermore, the variation $D_u \mathcal{L}(T, u, v)[\gamma]$ is given by

$$D_u \mathcal{L}(T, u, v)[\gamma] = \int_D \frac{\partial}{\partial u} Q_{\text{rf}}(u)(x) \cdot \gamma v(x) dx \quad (3.29)$$

for all $\gamma \in D \times S^2$. Now, one can calculate the gradient $D_u \mathcal{L}(T, u, v)[w]$ in direction of w . Since we search for a steepest descent, this direction is

$$w(x) := -\frac{\partial}{\partial u} Q_{\text{rf}}(u)(x) v(x) , \quad (3.30)$$

where v is given by the adjoint equation from above (3.28). Obviously, for this direction the variation (3.29) attains its minimal value

$$D_u \mathcal{L}(T, u, v)[w] = -\|w\|_{L^2(D)}^2 . \quad (3.31)$$

Here, the calculation of the adjoint v is performed by a conjugated gradient (CG) method on a finite element grid, analog to the calculation of the temperature T (cf. Sect. 2.4.2). Further, (as already described before; cf. (3.22)) the derivative $\frac{\partial}{\partial u} Q_{\text{rf}}(u)$ of the heat source with respect to the probe location is calculated with help of central differences. Note that in (3.22) the variable ε must be at least as large as the corresponding size of one grid cell, i.e. for the derivative of Q_{rf} with respect to the probe position $p = (p_1, p_2, p_3)$ the variable ε has to be at least as large as the voxel size of the grid in the corresponding direction, and for the derivative of Q_{rf} with respect to the probe direction $d = (d_1, d_2, d_3)$ the variable ε has to be at least as large as the voxel size of the grid in the corresponding direction multiplied by $2/L_{\text{active}}$ where L_{active} is the length of the probe's active zone. Moreover, in the implementation the descent direction for the probe's orientation additionally is multiplied by a weighting factor, which is needed to adjust the weight on the optimization of the probe's orientation to the weight on the optimization of the probe's position (which is due to the fact that typically, changes in the probe's orientation have a lower effect on the optimization than changes in the probe's position).⁹

⁹The scaling of the descent direction for the probe's orientation corresponds to an adaption between the units of the probe's position (which is given in meter) and the probe's orientation (which is dimensionless).

3.4.2 Step Size

To determine the optimal step size s in each step of the iteration, the equation

$$s = \underset{s > 0}{\operatorname{argmin}} f(P(u + s w)) \quad (3.32)$$

has to be evaluated, where the projection P defined in (3.25) ensures that the orientation lies on the sphere. For the identification of the optimal step size a bisection rule similar to Armijo's rule (cf. [34]) can be applied:

First an initial guess is chosen which is adapted to the magnitude of the descent direction. Then, if necessary, the step size is decreased until the new iterate is admissible and reduces the objective function value. The choice of the initial guess for the step size is different for the first iteration step and the following ones. For the first iteration step $n = 0$ s^0 is chosen such that

$$s^0 |w^0| = \frac{1}{2} \operatorname{diam}(D) \quad , \quad \text{i. e.} \quad s^0 = \frac{\operatorname{diam}(D)}{2 |w^0|} \quad ,$$

where $\operatorname{diam}(D)$ is the diameter of the computational domain D , and $|\cdot|$ is the ordinary 2-norm. In the following iteration steps $n > 0$ we start with a step size that fulfills

$$|w^n| s^n = 2 |w^{n-1}| s^{n-1} \quad , \quad \text{i. e.} \quad s^n = \frac{2 |w^{n-1}|}{|w^n|} s^{n-1} \quad .$$

After having chosen an initial value for the step size s^n , this value is bisected until the new iterate $u^{n+1} = P(u^n + s^n w^n)$ fulfills $u^{n+1} \in U$ and $f(u^{n+1}) < f(u^n)$. If these conditions are not matched after a certain number of bisections, the step size s^n is set to zero and the algorithm stops.

Note that the search for the optimal step size can be accelerated by using a scheme which not only uses bisections, i. e. the step size s^n can also be divided by e. g. 2^i ($i = 2, \dots, 9$) after a fixed number of bisections. Moreover, after having found a suitable step size, it should be tested, if a larger step size for only the position or only the orientation is admissible and still leads to a better value of the objective function.

3.4.3 Stopping Criterion

It is popular to stop the iteration when the norm of the gradient of the objective function f falls below a given threshold, i. e. when the shape of the objective function becomes flat. Unfortunately, this criterion cannot be used with the type of discretization presented here (cf. Sect. 2.4.2 and 3.3.1).

In Sect. 2.3 we have seen that the position p and orientation d of the probe enter into the system of PDEs as Dirichlet boundary (2.13)-(2.17). Since, as described in Sect. 2.4.2, the probe is resolved on a Cartesian grid, we obtain a piecewise constant

discretization of the probe's position and orientation. This induces a piecewise constant approximation of the objective function f , so that the gradient of f actually should be zero almost everywhere, but in fact does not vanish, since it is evaluated numerically with help of central differences including a variable $\varepsilon > 0$ depending on the grid size (cf. Eq. (3.22) and p. 42, bottom). Hence, the evaluation of the norm of the gradient of f is not a robust stopping criterion any more. In fact the descent direction will not converge to zero, but only decrease up to a certain positive value which depends on the voxel size of the underlying grid and is not easily predictable.

Therefore, the iteration is repeated until the norm of the difference $|u^{n+1} - u^n|$ between the new and old iterate falls below a suitably chosen threshold θ . In the experiments shown in Sects. 3.5 and 3.8 the stopping criterion θ is split into different components $\theta = (\theta_i)_i$. This allows to prescribe different accuracies for the probe's position p , and the orientation d . The algorithm stops if both criteria are met, i. e.

$$|p^{n+1} - p^n| < \theta_1 \quad \text{and} \quad |d^{n+1} - d^n| < \theta_2 . \quad (3.33)$$

Another reason for the fact that the norm of the gradient of the objective function f would not be a good choice for a stopping criterion might be the large absolute values of the derivative of the heat source Q_{rf} with respect to the probe location u . More precisely, the large absolute values of $\frac{\partial}{\partial u} Q_{\text{rf}}$ possibly lead to an effect, where on some grid nodes the corresponding values of the gradient of f are very large, but only sometimes perchance become very small.

3.4.4 Optimization Algorithm

To summarize the last sections, now the basic algorithm that is used for the optimization of the probe placement will be presented in pseudo-code (see Alg. 3.1).

Consider that the computation of the descent direction in line 4 includes the calculation of the adjoint v (3.28) with help of finite elements, as well as the application of central differences for the calculation of the derivative $\frac{\partial}{\partial u} Q_{\text{rf}}$, which involves multiple evaluations of the electrostatic equation (2.13).

Furthermore, for each test in the while-condition (see Alg. 3.1, line 12), an evaluation of the complete system of PDEs (2.13)-(2.17) and the objective function f are needed.

Finally, note that the determination of the step size s (lines 10-19) in practical applications is accelerated by dividing s by e. g. powers of two after a fixed number of bisections (cf. Sect. 3.4.2), and that the stopping criterion (line 20) in practice is split in a condition for the probe position and a separate condition for the probe orientation (cf. Sect. 3.4.3).

Algorithm 3.1 Basic algorithm for the optimization of the probe placement

```

1: Choose  $u^0$  ▷ Initialize start positioning
2:  $n \leftarrow 0$ 
3: repeat
4:    $w^n \leftarrow -\nabla_u f(u^n)$  ▷ Initialize step size
5:   if  $n = 0$  then
6:      $s^0 = (2|w^0|)^{-1} \text{diam}(D)$ 
7:   else
8:      $s^n = 2|w^{n-1}|(|w^n|)^{-1}s^{n-1}$ 
9:   end if ▷ Determine step size
10:   $m \leftarrow 0$  ▷ Reset counter
11:   $u^{n+1} \leftarrow P(u^n + s^n w^n)$ 
12:  while  $f(u^{n+1}) > f(u^n)$  or  $u^{n+1} \notin U$  do
13:     $m \leftarrow m + 1$  ▷ Increase counter
14:    if  $m = m_{\max}$  then
15:      STOP.
16:    end if
17:     $s^n \leftarrow s^n/2$  ▷ Bisect step size
18:     $u^{n+1} \leftarrow P(u^n + s^n w^n)$ 
19:  end while ▷ Check stopping criterion
20: until  $|u^{n+1} - u^n| \leq \theta$ 
21:  $\bar{u} \leftarrow u^{n+1}$  ▷ Save optimal probe positioning

```

3.5 Results Obtained with a Monopolar Probe

In this section the application of the above described optimization to artificial settings as well as to geometries obtained from real CT scans is presented (see also [4])¹⁰. For the optimization, here the objective function (3.8) (cf. Sect. 3.3) is used together with the weights $w_{\text{in}} = 100$ and $w_{\text{out}} = 1$ for the destruction of the tumor and the protection of the native tissue, respectively.¹¹ Note that the critical temperature T_{crit} within (3.8) only formally is a temperature value, but in fact serves as additional weighting for the tumor destruction. The reason for this is that via the probe location only the distribution of heat is optimized, whereas the overall energy which is induced into the tissue, is not optimized or even changed here. In the presented optimization (cf. Figs. 3.9 and 3.10), T_{crit} is set to the high value of 1000 K, which is

¹⁰Compared with [4], for better visibility, in Figs. 3.9 and 3.10 a silhouette around the temperature's iso-surface is drawn. Moreover, in Figs. 3.9-3.11 the perspective and the smoothing factor for the tumor and vessel system are slightly changed.

¹¹As we have seen in Sect. 3.3, the objective function (3.8) is not the best possible choice, but since this work also describes the successive development and improvement of the application, here also preliminary approaches will be shown.

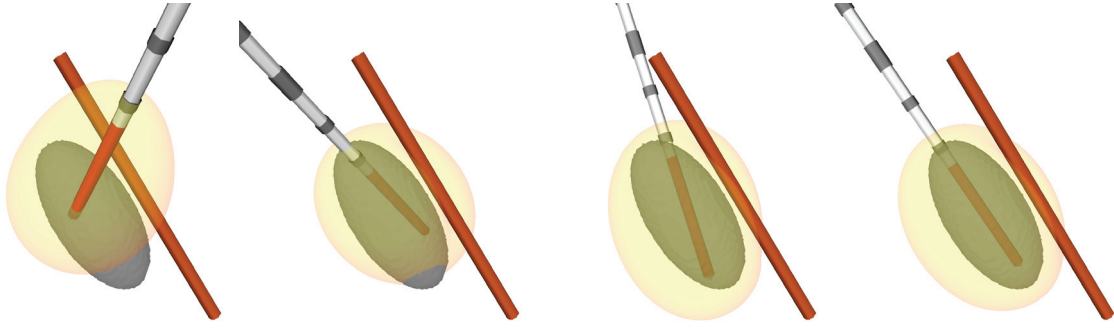


Figure 3.9: Optimization of the probe’s placement for an artificial example with an ellipsoid-shaped tumor (dark gray) and a linear vessel (black). The pictures show from left to right steps 0 (start), 4, 6, and 9 of the optimization and display the probe (white-gray) and a corresponding iso-surface of the temperature (transparent) as well.

necessary because of several reasons: One reason is that (as will be described below) the perfusion is modeled still too weak here. Another reason is that we consider the steady state model which corresponds to an infinite ablation time. Finally, with the objective function (3.8), high temperatures above T_{crit} in the tumor region are penalized, which is an unwanted effect that can be avoided by increasing the critical temperature T_{crit} .

Now, in a first step, the performance of the algorithm is verified in a case where the correct solution is qualitatively obvious. To this end, D is a domain of extent $60 \times 60 \times 60$ [mm³] with an overlaid grid consisting of 121 grid points in each direction.¹² As a tumor an ellipsoid is considered, which lies in the center of D , together with a straight vessel in the vicinity of the tumor (cf. Fig. 3.9). Moreover, a monopolar probe with a radius of 1.2 mm and an electrode length of 25 mm is used. The initial probe position for the optimization is located at 10 mm distance in each direction from the center of D and its orientation is $d = (5, 2, 3)$ normalized to length 1. Further, the heat conductivity is set to $\lambda = 0.5$ W/K m and the electric conductivity is set to $\sigma = 0.21$ S/m. The perfusion (cf. Sect. 2.3, Eq. (2.16)) is modeled by taking the values $\nu_{\text{vessel}} = 0.01765$ 1/s and $\nu_{\text{cap}} = 0$ 1/s together with $\rho_{\text{blood}} = 1059.0$ kg/m³ and $c_{\text{blood}} = 3850.0$ J/kgK (cf. [84, 79]). (Here it has to be remarked that with this values for ν_{vessel} and ν_{cap} the perfusion in this first approach is still modeled too weak, which however is not really a drawback for the optimization, since as already mentioned above, not the overall intensity of heat, but only the distribution of heat is optimized.) Finally, the generator has an inner resistance of 80 Ω and is set up to a power of 80 W. The results of this experiment are shown in Fig. 3.9. It is clearly visible that the probe placement adapts to the ellipsoidal shape of the tumor and thus corresponds to the expected positioning along the long principal axis of the ellipsoid. Note that only the shape of the shown temperature’s iso-surface is important here, whereas its absolute value is irrelevant for the same reasons that

¹²Note that in a later example (see Sect.4.7.1) it is demonstrated that this size of D is large enough not to influence the result of the optimizer.

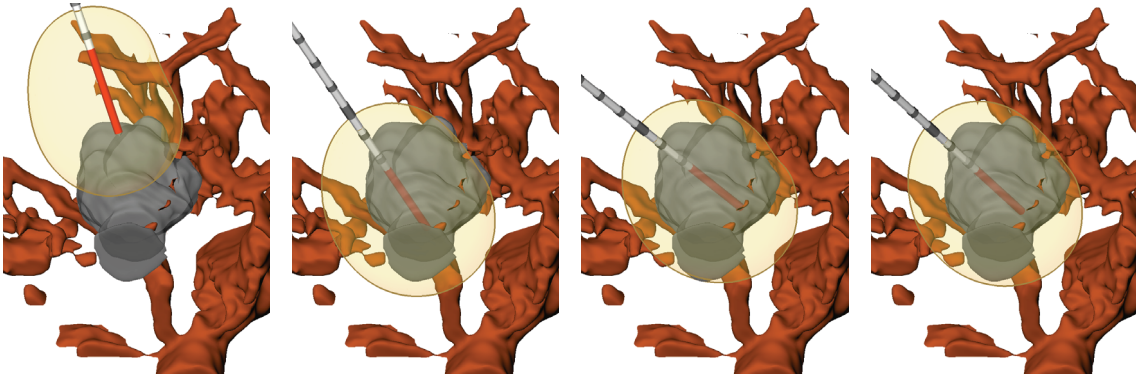


Figure 3.10: Optimization for an example based on patient data with segmented tumor and surrounding vessels. The pictures show from left to right steps 0, 5, 10 and 15 of the optimization process and display the tumor together with the vascular system, the probe position and a corresponding isosurface of the temperature (cf. Fig. 3.9).

are responsible for T_{crit} in (3.8) only being a weighting factor.

The second example is performed with a real segmented tumor and a set of surrounding vessels. The tumor and the vascular system have been segmented using the methods described in [15]. The computational domain D has a dimension of $120.6 \times 79.9 \times 79.9$ [mm³], which is a typical size for the region of interest (ROI) for RF ablation (cf. e.g. [84]). Moreover, the domain D is discretized with a Cartesian grid consisting of $155 \times 103 \times 103$ grid points. The tumor located in this domain has main axes of approximate length 45.9 mm, 41.9 mm, and 36.2 mm, and its volumetric centroid is located at $(0.5, -0.8, -1.4)$ mm apart from the center of D . The probe data, the values for modeling the perfusion, the heat conductivity and the electric conductivity are the same as in the first example. The initial position of the probe is $(30.3, 10.0, 10.0)$ mm distant from the center of D and the probe's initial direction is $d = (5, 2, 3)$ normalized to 1. Further, for this second example the generator settings are $R_{\text{I}} = 80 \Omega$ and $P_{\text{setup}} = 30 \text{ W}$.

As the pictures in Fig. 3.10 show, the optimal probe position lies in the center of the tumor, and its optimal direction adapts to the shape of the tumor as well as to the influence of the vessels. In particular in the left configuration (step 0) of Fig. 3.10, the cooling effect of the blood perfusion can be seen explicitly on the steady state of the temperature (i.e. a lower temperature near the vessels, visible by a dent in the temperature's iso-surface).

Finally, the result of the second optimization is compared to the positioning chosen by the responsible physician. Instead of one probe of radius 1.2 mm, the physician had taken a fixed cluster of three parallel probes of radius 0.75 mm. For the time-being let us assume that these act like a single probe of larger radius. Although this is only a rough approximation, the result depicted in Fig. 3.11 shows that the probe placement suggested by the optimization algorithm and the one chosen by the physician nearly coincide in their position (i.e. in the barycenter of the probes' active zones). In fact, the probe positions only vary by a norm of about 5.5 mm,

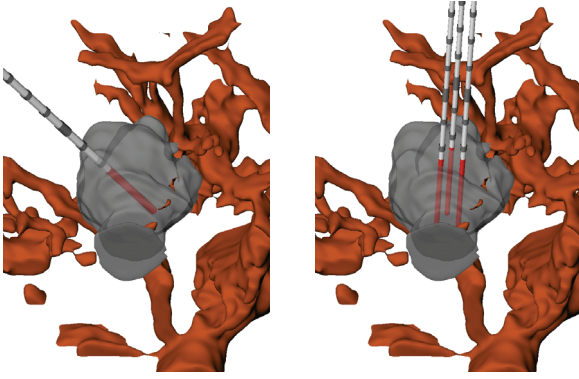


Figure 3.11: Comparison of the computed optimal probe placement (left) with the probe placement chosen by the responsible physician (right).

whereas the orientation differs by an angle of about 36.9° . One reason for this could be the spherical-like shape of the tumor – an intrinsic property of the problem (cf. Sect. 3.4, p. 38). Also, anatomical structures (e. g. bones or internal organs), which are not respected in the model yet, could have excluded the orientation found by the algorithm from the physician’s choice.

3.6 Application of Multiple Coupled Probes

To have a better approximation for an RF ablation of large tumors, which are usually ablated with several probes, in the following the optimization method presented in the previous sections is extended to the case of ablating with a cluster of multiple probes in a fixed geometrical arrangement where all the probes have the same orientation d . The point p now models the barycenter of all the active zones (cf. Fig. 3.6). Further, the whole cluster can be rotated. Thus, the set u of optimization parameters is enlarged by a rotation vector $r \in S^2$ with $r \perp d$. Hence, we have

$$U = \{(p, d, r) \in D \times S^2 \times S^2 : r \perp d\} .$$

Again, for easier handling of the gradient with respect to the optimization variable, we replace U by the open set

$$\tilde{U} = \{(p, d, r) \in D \times \mathbb{R}^3 \times \mathbb{R}^3 : r \not\parallel d\}$$

and use the projection

$$P : \tilde{U} \rightarrow U , \quad (p, d, r) \mapsto \left(p, \frac{d}{|d|}, \frac{|d|^2 r - (r, d)d}{\| |d|^2 r - (r, d)d \|} \right) ,$$

which guarantees that the orientation d and the rotation vector r of the probe cluster lie on the sphere S^2 and are orthogonal to each other. Otherwise, the optimality system from the last sections remains unchanged. However, the numerical evaluation of the gradient $\frac{\partial}{\partial u} Q_{\text{rf}}$ with help of central differences (cf. 3.4) needs more effort, since $u = (p, d, r)$ has more components now.

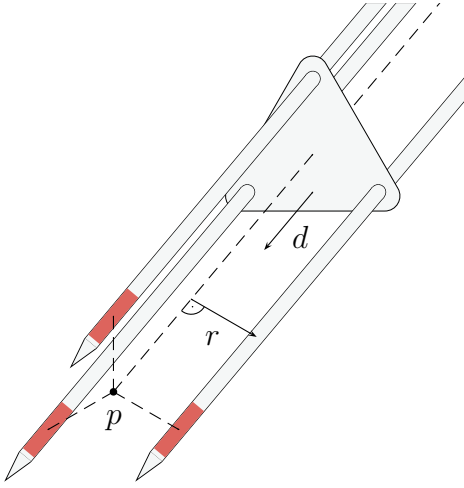


Figure 3.12: Cluster of three monopolar probes together with the optimization parameters: the position p (i. e. the barycenter of the probes' active zones), the direction d and the rotation vector r .

Note that the placement of umbrella probes, another type of probes that is frequently used by radiologists, can be treated by this extension as well. However, in this case, the use of a locally refined grid would be advisable in order to resolve the fine tines of the umbrella probe.

3.7 Multi-Level Optimization on Coarse Grids

The minimization of the objective function can be accelerated significantly by performing pre-optimization runs on coarse grids and taking the optimal probe location of each pre-optimization as the start positioning for the optimization on the next finer grid.

In more detail, to be able to provide such pre-optimizations, we first have to assume that we work on an octree grid, i. e. a hexahedral grid with $2^L \times 2^L \times 2^L$ cells for some $L \in \mathbb{N}$. Note that this is in fact no restriction, since every Cartesian grid can be embedded into an octree grid. Because the number of grid cells in each coordinate direction is a power of two, we implicitly have a hierarchy of grids $\mathcal{G}_L \subset \dots \subset \mathcal{G}_0$ such that for $0 \leq l \leq L$ each grid \mathcal{G}_l has $2^l \times 2^l \times 2^l$ cells. Thus, the coarsest grid \mathcal{G}_0 contains only one hexahedron and consequently has only 8 vertices. A hexahedral grid cell $E_l \in \mathcal{G}_l$ is split into 8 child elements in the next grid of finer resolution \mathcal{G}_{l+1} . In the following, the number $l \in \{0, \dots, L\}$ is referred to as the *level* of the grid \mathcal{G}_l . Moreover, the vertices of the grids are ordered lexicographically, and the set of vertices of \mathcal{G}_l is denoted by $\mathcal{N}_l = \{x_i \mid i = 1, \dots, n_l\}$, where $n_l = (2^l + 1)^3$. Finally, the minimal edge length of the cells on grid level l is denoted by h_l .

Now, in order to perform a multi-level optimization, one starts on a coarse grid of level $l_0 \in \{0, \dots, L - 1\}$ and optimizes the probe location on \mathcal{G}_{l_0} yielding a set of parameters \bar{u}_{l_0} . Then, this parameter-set is used as the initial guess for an optimization on the following finer grid \mathcal{G}_{l_0+1} . This has to be continued until the finest grid \mathcal{G}_L is reached and an optimal set \bar{u}_L has been obtained.

This approach provides the possibility to descent much faster in the energy profile

of the objective function. Moreover, one can expect that with decreasing level l in the grid hierarchy the energy profile is regularized and existing local minima are smoothed. Thus, already on coarse levels the probe location and orientation are led to a dominant minimum and the algorithm is not likely to end up in a suboptimal local minimum. Finally, as already mentioned above, the multi-scale approach reduces the computational time by minimizing the number of iteration steps on the finest grid.

Obviously the multi-scale method requires the definition of the geometrical shape of the tumor and the vascular system on coarser grids. To be more precise, we need a restriction

$$R_{l+1}^l : V_{l+1}^h \rightarrow V_l^h \quad \text{for } l = 0, \dots, L-1 ,$$

where V_l^h is the finite element space of globally continuous, piecewise trilinear functions on the grid \mathcal{G}_l (cf. Sect. 2.4.2). This means we need a restriction that transports the characteristic finite element functions $\chi_t^{l+1}, \chi_v^{l+1} \in V_{l+1}^h$ (cf. Sect. 3.3.1), on the next coarser level. A straightforward approach would use the trivial restriction which directly multiplies the nodal values of a fine-grid function with the coarse-grid basis function. However, this leads to unsatisfactory results, since on coarse grids it does not preserve details of the tumor that have important influence on the choice of the optimal probe positioning. Therefore, it is much more advisable to use the classical restriction of multigrid approaches for the solution of PDEs [42]. Let us set $R_{l+1}^l = (P_{l+1}^l)^T$ where P_{l+1}^l is the trilinear interpolation from grid \mathcal{G}_l to grid \mathcal{G}_{l+1} involving the weights $\{1/8, 1/4, 1/2, 1\}$. Then one can apply the restriction R_{l+1}^l to the characteristic finite element functions χ_t^{l+1} and χ_v^{l+1} :

$$\chi_t^l = R_{l+1}^l \chi_t^{l+1} , \quad \chi_v^l = R_{l+1}^l \chi_v^{l+1} . \quad (3.34)$$

This restriction accumulates the nodal values of fine-grid points into the coarse-grid nodes such that important details cannot be lost. In fact, it is mass conserving and leads to fuzzy boundaries of the tumor and vessel. So on coarse grids we encounter grid cells whose nodal values lie in the interval $[0, 1]$. We can interpret the nodal values as the proportions of the coarse grid cells which lie inside the tumor or vessel. Still the quadrature presented in Sect. 3.3.1 can be applied on coarse levels using χ_t^l and χ_v^l .

Depending on the elements' size on coarse levels, it can happen that the probe radius is too small to be resolved on a coarse grid. Therefore, a special construction of the approximation of the probe D_{pr} on coarse grids is needed. If the probe is not resolved on \mathcal{G}_l , its radius has to be adapted to the resolution h_l . More precisely, the probe radius has to be greater than or equal to $h_l\sqrt{2}/2$. This adaptation of the radius guarantees that each slice of the probe contains at least one grid node (see Fig. 3.13).

In the left graph of Fig. 3.14, the progression of the value of the objective function (3.10) during the optimization for a configuration shown in Sect. 3.8 (cf. Fig. 3.16) is depicted.¹³ The transitions between different grid levels are marked by vertical

¹³Remember, that using the objective function (3.10) in fact means to use the numerical modifica-

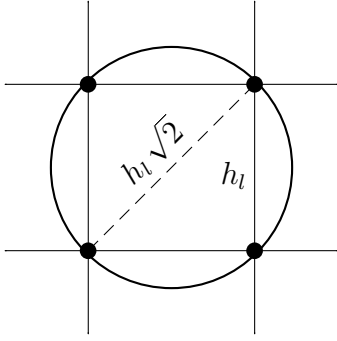


Figure 3.13: Intersection of the probe with a slice of the grid orthogonal to the probe. Here, h_l is the minimal voxel size of the grid \mathcal{G}_l , so the diameter of the probe must be at least $h_l\sqrt{2}$.

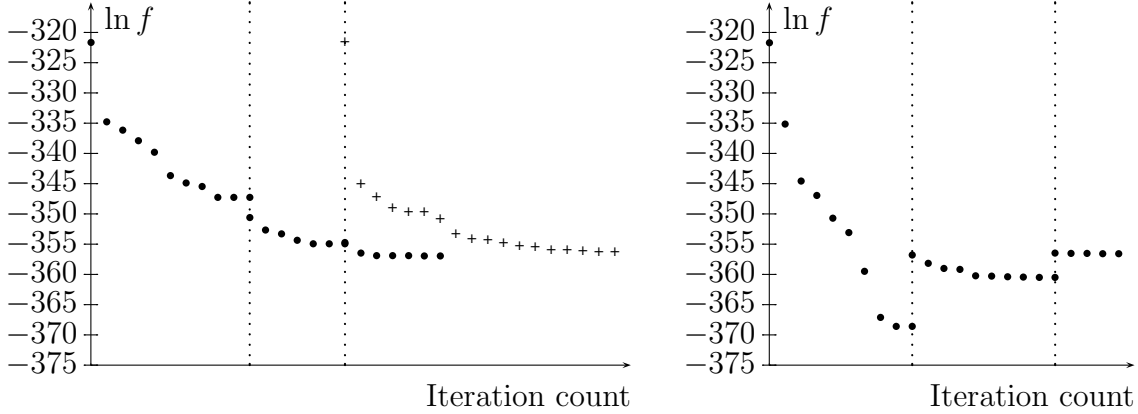


Figure 3.14: Left: The progression of the objective function value is shown for the multi-scale optimization algorithm (\bullet) and the standard algorithm ($+$). In contrast to the standard algorithm, the multi-scale optimization finds a slightly better minimum with a considerably smaller number of iterations on the finest-grid. Right: The progression of the objective function value is shown for the definition of a coarse-grid tumor and vascular domains which involve a thresholding.

dotted lines in the energy plot. At these stages of the algorithm, the probe placement $u \in U$ has been found on a coarse level is re-interpreted on the finer grid. Consequently, the energy jumps at the transition points in the graph. The progression of the energy during the iterations of the standard algorithm is shown in the left graph of Fig. 3.14 as well. The minimum found by the multi-scale algorithm is slightly better ($\ln f \approx -356.9$) than the one found by the standard algorithm ($\ln f \approx -356.3$). Moreover, the multi-scale optimization needs significantly less fine-grid steps than the standard algorithm.

In the numerical examples presented in Sect. 3.8, a further speedup of the multi-level algorithm is obtained by thresholding the restricted values of χ_t^l and χ_v^l .

tion (3.11), which for a comparison of different objective function values has to be transformed as described in (3.12). Therefore, in Fig. 3.14 the logarithm $\ln f$ of the objective function f is shown.

Thereby, it is set

$$\chi_t^l(x_j) = \begin{cases} 1 & \text{if } (R_{l+1}^l \chi^{l+1})(x_j) \geq 0.5 \text{ ,} \\ 0 & \text{else ,} \end{cases} \quad (3.35)$$

and analog for χ_v^l . Here, the speedup of the algorithm can be explained by the following considerations: Without a thresholding, for all voxels that belong to the tumor, too low temperatures would be penalized approximately equal (due to the deep slope of the exponential function), even if the respective voxels belong to the tumor only by a minor portion. Hence, for a pre-optimization on a coarse grid, the active tumor region that influences the objective function value would be significantly larger than the real tumor region which influences the objective function value in the main optimization. Thus, the result of a pre-optimization without thresholding the tumor would yield a worse initial value for the main optimization than the result of a pre-optimization that uses a thresholding. The progression of the corresponding objective function value is shown in the right graph of Fig. 3.14. Since here the masses of the tumor and the vessels are not conserved on the coarse levels, the values of the objective function increase at the transition stages.

The accelerated algorithm stops already after four fine-grid iterations and from the graphs we see that the minimal value of the objective function is only slightly larger ($\ln f \approx -356.6$) than the one obtained by the non-thresholded restriction variant. For the configuration shown in Fig. 3.16, the optimal probe positions p of both multi-scale variants differ by at most 0.5 mm and the orientations differ by at most 5° . Since this lies below the accuracy that can be achieved in practice, here the faster algorithm is preferable.

3.7.1 The Multi-Level Optimization Algorithm

In Alg. 3.2 the extension of the basic Alg. 3.1 (see Sect. 3.4.4) for the optimization of the RF probe placement to a multi-level approach as described above is depicted. For each level l (see lines 3–10 of Alg. 3.2), the optimization is performed as seen in Sect. 3.4.4, but with the difference that the initial start positioning u^0 is set to the optimal solution \bar{u} of the previous optimization. Thus, it can be expected that the algorithm needs only very few iteration steps on the finest grid, since therefore the initial start positioning can be expected to be already very close to the optimal solution.

3.8 Results Obtained with the Multi-Level Optimization

In the following, the application of the multi-level optimization to the examples shown in Sect. 3.5 (i. e. to an artificial configuration and to a geometry obtained from

Algorithm 3.2 Multi-scale algorithm for the optimization of the probe placement

- 1: $l \leftarrow l_0$ ▷ Start with level l_0
 - 2: Choose \bar{u} . ▷ Initialize start positioning
 - 3: **while** $l \leq L$ **do**
 - 4: $u^0 \leftarrow \bar{u}$ ▷ Initialization on current grid
 - 5: $n \leftarrow 0$
 - 6: **repeat**
 - 7: \vdots ▷ Lines 4-19 of Alg. 1
 - 7: **until** $|u^{n+1} - u^n| \leq \theta$
 - 8: $\bar{u} \leftarrow u^{n+1}$
 - 9: $l \leftarrow l + 1$ ▷ Proceed to next level
 - 10: **end while**
-

real patient data) will be presented (see also [5])¹⁴. In contrast to the optimization shown in Sect. 3.5, in case of the real example, here a fixed cluster of three parallel monopolar probes is used. Moreover, the two multi-scale optimizations presented here are performed with the objective function (3.10) with factor $\alpha = 1$. Like in Sect. 3.5, first the performance of the multi-scale algorithm is proved in a case where the correct solution is qualitatively known. To this end, we first consider the artificial example of Sect. 3.5, i.e. D is a domain of extent $60 \times 60 \times 60$ [mm³] which is discretized as described in Sect. 3.7 with a fine-grid of 120^3 grid cells that is embedded into an octree grid of level $L = 7$. Hence, here we have two coarser grids of 60^3 , respectively 30^3 grid cells. Further, a tumor domain D_t having ellipsoidal shape is assumed to lie in the center of D with a straight vessel D_v in the vicinity of the tumor (cf. Fig. 3.15). The values for the thermal and electric conductivity are the same as in Sect. 3.5. In addition, the probe and generator settings are identical. The differences of the optimization considered here, compared to the corresponding optimization in Sect. 3.5, are the objective function, the multi-scale character of the algorithm, and the modeling of the perfusion, which here is modeled by taking the values $\nu_{\text{cap}} \approx 0.01765 \text{ s}^{-1}$ and $\nu_{\text{vessel}} \approx 0.05 \text{ s}^{-1}$ (cf. [84, 79] and Sect. 2.3). The values for the blood density ρ_{blood} and heat capacity of blood c_{blood} remain unchanged. Finally, in this experiment the stopping criterion is set to a very small value $\theta = 10^{-10}$.

The result and some intermediate steps of the optimization algorithm for this configuration are shown in Fig. 3.15. Obviously the algorithm finds the optimal probe location, which is positioned in the center of the tumor and oriented along the main principal axis of the ellipsoidal tumor shape. Moreover, it is clearly visible that already on coarse levels the algorithm gives good predictions of the optimal

¹⁴Compared with [5], here the results have been recalculated with a slightly higher accuracy for solving the potential and heat equation, as well as with another initial probe location for the optimization performed on real CT data.

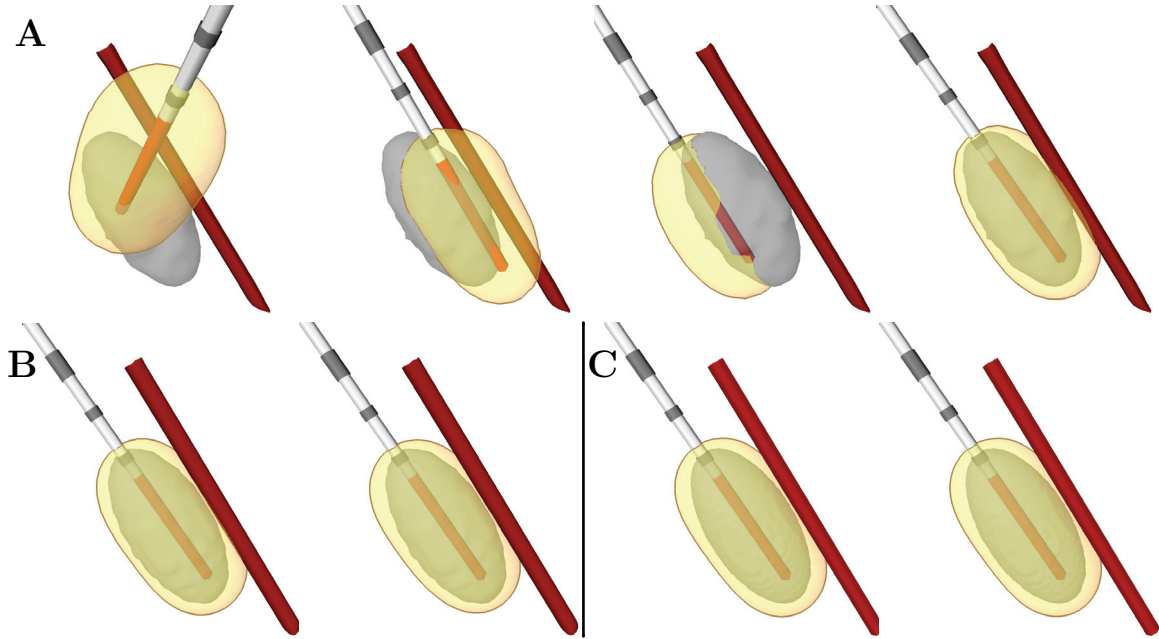


Figure 3.15: Optimization of the probe’s placement for an artificial example with an ellipsoid-shaped tumor (dark gray), a linear vessel (black), and a monopolar probe (white-gray). The transparent layer is the corresponding 60° -isosurface of the temperature. **A:** Steps 0 (start), 1, 2 and 20 of the 1st pre-optimization (coarsest grid). **B:** Steps 0 and 15 of the 2nd pre-optimization. **C:** Steps 0 and 11 (end) of the main optimization.

positioning.

If the standard optimization algorithm Alg. 3.1, which operates on the finest grid only, is utilized with the same accuracy, convergence is achieved after 16 iteration steps (17 hours and 4 minutes). By performing pre-optimizations on two coarser levels, the number of fine-grid iteration steps is reduced to 11 (11 hours and 41 minutes in total). Thus, altogether about 32% of the computational time could be saved by using a multi-scale approach. Note that an optimization step on grid-level $l < L$ needs roughly only about 8^{l-L} times the effort compared to a fine-grid optimization step. In the above-described example optimization was performed on two coarser levels first. Thus, one coarse-grid iteration step took only $8^{-2} = 1/64$ and $8^{-1} = 1/8$, respectively, of the time a fine-grid step would need.

To conclude the examination of this artificial test-example, finally it has to be remarked that the extended algorithm for the handling of probe-clusters also yields the correct probe location in this test-scenario. The results of the extended algorithm are not shown here, instead we now consider the following more interesting real configuration together with the multi-scale optimization of a probe-cluster.

The second example is performed with a real segmented tumor and vessel system (see Fig. 3.16). The computational domain D , the heat conductivity λ , and the electric conductivity σ are the same as in Sect. 3.5. For the discretization we con-

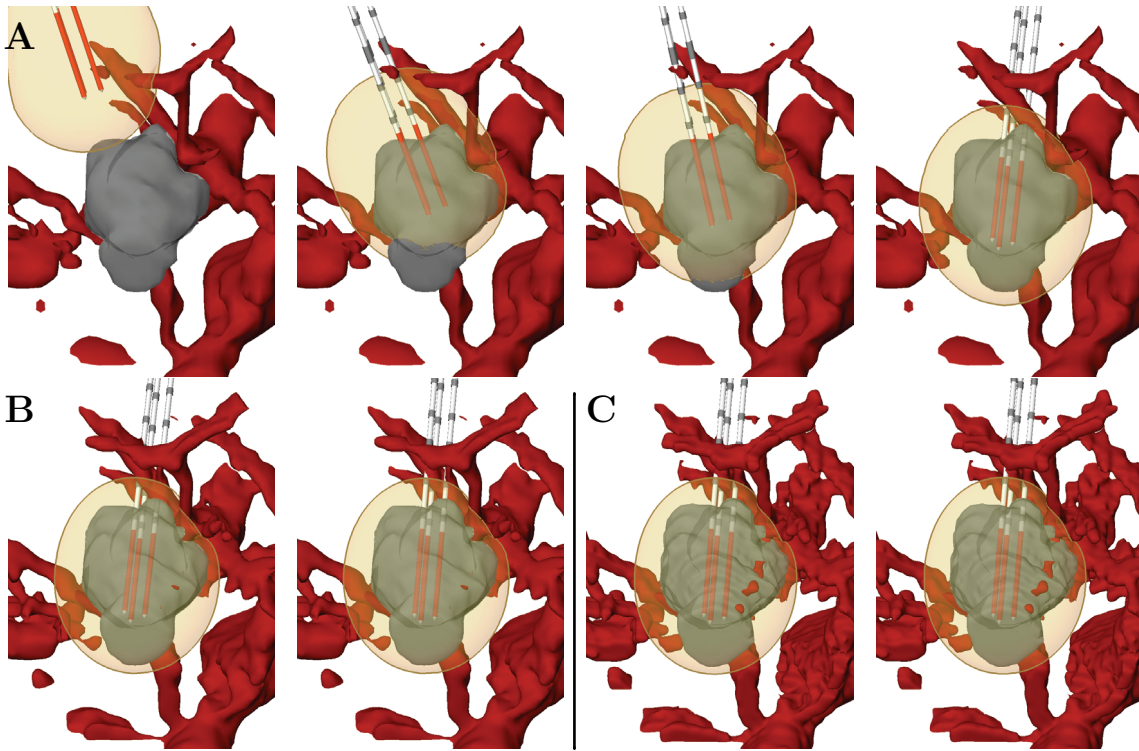


Figure 3.16: Optimization for an example based on patient data with segmented tumor and surrounding vascular system. Here, we have a fixed cluster of three monopolar probes with the corresponding 60° -isosurface of the temperature. **A:** Steps 0 (start), 1, 2 and 9 of the 1st pre-optimization (coarsest grid). **B:** Steps 0 and 9 of the 2nd pre-optimization. **C:** Steps 0 and 4 (end) of the main optimization.

sider a fine-grid of $154 \times 102 \times 102$ grid cells (cf. Sect. 3.5) which (as in the artificial case) is embedded into an octree grid of level $L = 7$ (i. e. we have two coarser grids of $77 \times 51 \times 51$, respectively $38 \times 25 \times 25$ grid cells). The generator settings are $R_{\text{I}} = 80 \Omega$ and $P_{\text{setup}} = 200 \text{ W}$. For modeling the perfusion, $\nu_{\text{cap}} = 0.006067 \text{ s}^{-1}$ and $\nu_{\text{vessel}} = 0.05 \text{ s}^{-1}$ are used together with ρ_{blood} and c_{blood} as before. Note that this is a weaker modeling of the perfusion than in the test-example where a weighted variant of Pennes (cf. [84, 79] and (2.16)) has been used. This weaker modeling of the perfusion is due to the fact that here, infinite many time steps are performed without modeling the coagulation. The coagulation, however, causes that the capillary vessels become closed after a certain ablation time, which implies $\nu_{\text{cap}} = 0$. Hence, without modeling the coagulation, this effect has to be adjusted by using a weaker overall perfusion. In the artificial example, this compensation (i. e. a weaker modeling of the perfusion) is not needed because there the tumor is sufficiently small. For the optimization of this second realistic configuration, a fixed cluster of three parallel monopolar probes is applied. The cluster is of radius 3.3 mm (i. e. the probe distance is $3.3 \cdot \sqrt{3} \text{ mm} \approx 5.72 \text{ mm}$), where each probe of the cluster is of

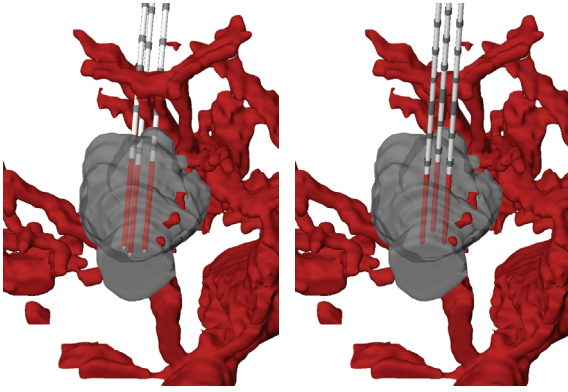


Figure 3.17: Comparison of the optimal probe placement found by the optimization algorithm (left) with the probe placement chosen by the responsible physician (right).

1.0 mm radius and has an electrode length of 30.0 mm. The initial position of the probe cluster is at $(40.3, 20.0, 20.0)$ mm distance from the center of D , and the initial direction is $d = (5, 2, 3)$ again normalized to length 1. Moreover, here a weaker stopping criterion of 10^{-4} , 10^{-3} and 10^{-2} for the position, orientation and rotation, respectively, is used. This stopping criterion is adapted to the accuracy of probe placement which can be achieved in practice.

As in the first example, the optimization runs are started on a grid that is two levels coarser. Thereby, the number of iteration steps for the main optimization is reduced from 17 steps (19 hours and 34 minutes) (in the case of no multi-scale optimization) to 4 steps (5 hours and 30 minutes in total) (with multi-scale optimization). Thus, about 72% of the computational time can be saved. For a discussion of the corresponding energy graphs see Sect. 3.7, Fig. 3.14.

When considering the last picture (bottom right) of Fig. 3.16, one can see that the optimal probe position lies in the center of the tumor, and its optimal direction adapts to the shape of the tumor. Moreover it has to be remarked, that here the orientation seems to fit even better to the tumor shape than the optimal orientation found by the optimization presented in Sect. 3.5. This might be due to several reasons: First, as can be seen in Figs. 3.10 and 3.16, the considered tumor has a rather spherical-like shape, such that the uniqueness of a minimizing configuration cannot be guaranteed, and it is reasonable that different optimization methods lead to different optimal probe directions (cf. Sect. 3.4, p. 38). In the here considered particular case, the following differences in the optimization methods could be responsible for the deviation in the optimal probe directions: As described above, here a more sophisticated objective function (see (3.10)) than in Sect. 3.5 (see objective function (3.8)) is used for the optimization. Further, the application of a probe cluster instead of one single probe together with a stronger weighting of the orientation (and rotation) than in the optimization presented in Sect. 3.5, could have lead to a different optimal probe direction. Moreover, here two pre-optimizations on coarser grids are performed, such that a very good initial guess for the main optimization on the fine-grid is given, whereas for the optimization in Sect. 3.5 an arbitrarily chosen start positioning is used as initial guess for the (fine-grid) optimization.

Finally (as in Sect. 3.5), the result of this second optimization is compared to the

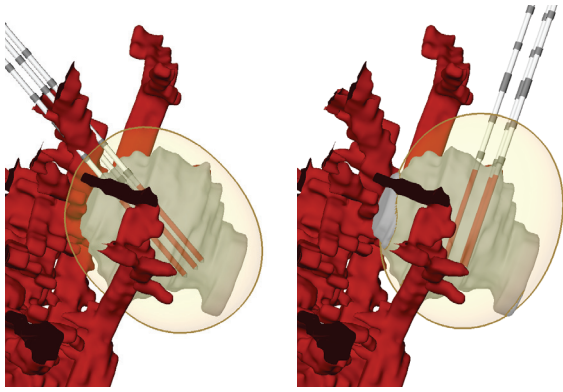


Figure 3.18: Comparison of the 60° C - temperature profiles yield by the different probe placements suggested by the algorithm (left) and applied by the physician (right).

positioning chosen by the responsible physician (see Figs. 3.17 and 3.18). The two probe positions only vary by a norm of about 5.9 mm, whereas the probe orientations differ by an angle of about 59.2°. Moreover, the value of the objective functional for the probe placement suggested by the multi-level algorithm ($\ln f \approx -356.6$) turns out to be considerably smaller than the value of the same objective functional applied to the probe placement chosen by the physician ($\ln f \approx -338.5$). As can be seen in Fig. 3.18 for the optimal probe placement suggested by the algorithm, the 60° C - isosurface of the temperature completely encloses the tumor lesion, while for the probe placement chosen by the physician, the tumor region nearest to the vessels is not completely enclosed. One reason for the difference in the probe orientations chosen by the optimization algorithm and the physician, respectively, could be the location of anatomical structures that must not be punctured (e. g. bones, internal organs, or large vessels). The consideration of such constraints is computationally expensive and has not been included in the mathematical model, yet, but is a current field of research studied by my colleague S. Haase¹⁵ at the CeVis institute of the university of Bremen.

3.9 Conclusions and Discussion

A basic fine-grid model and a more sophisticated multi-scale approach for the optimization of one single probe and a fixed cluster of multiple coupled probes, respectively, have been presented (cf. Algs. 3.1, 3.2, and Sects. 3.5, 3.8). Both algorithms first have been evaluated on an artificial example for which the optimal probe positioning is qualitatively obvious. Furthermore, results of the optimization with a CT-segmented tumor surrounded by a vascular system have been presented and compared to the probe location the responsible physician had chosen for the RF ablation. While in both examples the probe position nearly coincides with the one chosen by the physician (i. e. they only vary by a norm of about 5.5 mm and 5.9 mm, respectively), the probe orientations differ by angles of about 36.9° and 59.2°. Mea-

¹⁵sabrina.haase@ewetel.net; CeVis (Center for Complex Systems and Visualization) - University of Bremen

sured in terms of the objective function (3.10), the positioning proposed by the multi-scale optimization algorithm is indeed better than the positioning chosen by the physician. This impression is also confirmed by considering the corresponding 60°C -temperature profiles in Fig. 3.18. However, there are further aspects of the probe placement (e. g. anatomical structures) which are not considered in the current model yet, but can be the reason for a different positioning.

Formally, the multi-scale optimization scheme applied to the examples shown in Sect. 3.8 uses the results of pre-optimizations on coarser grids as initial guess for the fine-grid optimization. In the second of these examples (based on real patient data), the multi-scale optimization approach yields a computational time that is only 28 % of the effort of a standard approach.

Altogether, the optimization of the probe placement is a helpful tool for the planning of RF ablations, as well as for educational purposes. On the one hand a correct placement of the probe increases the chance of a total tumor destruction and therefore reduces the risk of a recurrence, and on the other hand the optimization results help understanding how experienced physicians choose their RF ablation parameters.

For ongoing and future investigations, several extensions and improvements of the presented optimization approaches are suggestive: For instance, the incorporation of constraints for the optimization parameters respecting anatomical structures that must not be punctured would be a reasonable extension. Further, the consideration of the corresponding time-dependent PDE models and an optimal control of the overall energy dose during an RF ablation would be a promising enhancement (see Sect. 7.1). Moreover, note that the tissue parameters like e. g. the thermal and electrical conductivity are not known exactly, since they depend on the physical constitution of the patient and thus vary from patient to patient and even from day to day. In the following chapter (Chapt. 4) several questions resulting from this uncertainty are investigated, e. g. the sensitivity of the model with respect to the tissue parameters, or the optimal probe positioning of the stochastic model taking the parameter uncertainty into account. Additionally it has to be remarked, that in practice it will be hard for the interventionist to achieve the computed optimal positions exactly. Inevitably there will be deviations from the optimal configuration. Therefore, a sensitivity analysis with respect to the optimization parameters (i. e. the optimal probe positioning), which provides an estimation of the risk of failure of the therapy, would be a further benefit for an RF ablation planning. Finally, a more comprehensive evaluation on artificial and real configurations with different tumor shapes and vascular systems has to be performed.

4 Analysis of Material Parameter Uncertainty

4.1 Problem Formulation

As seen in the previous sections, mathematical/bio-physical models for simulating RF ablation depend on the physical properties of the tissue, i. e. its electrical and thermal properties such as electrical and thermal conductivity, heat capacity, density, and water content. The modeling of these tissue properties poses a particular challenge, because they depend on the current state of the tissue; e. g. the electrical conductivity depends on the temperature, the water content, and also on the grade of destruction of the tissue [79, 45, 16]. Moreover, the tissue properties vary inter-individually (i. e. from patient to patient) and in fact they also vary from day to day depending on the patients physical constitution. Hence, these quantities are not exactly known. Values used in simulations are e. g. based on *ex-vivo* experiments of animal tissue [79]. In addition, experimental measurements are always accompanied with a certain range of errors. Consequently, truly patient-individual models for RF ablation are not currently feasible, and the question arises whether results obtained through simulations can be used efficaciously in the clinical setting. The issue of patient individual models is probably the most challenging task for mathematical modeling and simulation in medicine.

In the following sections the optimization of the probe placement under consideration of the uncertainty that is associated with material parameters, i. e. the electric and thermal conductivity, will be investigated. Taking this uncertainty into account leads to the following questions whose answers are relevant to the practical (clinical) application of the numerical support for RF ablation:

- **Sensitivity of optimal probe placement:** How sensitive is the optimal probe placement found by a certain optimization algorithm (as e. g. Alg. 3.1/3.2) to variations (either due to uncertainty or errors) in the material parameters?
- **Optimal probe placement for expected tumor destruction:** From which probe position and orientation can we expect a maximum volume of destroyed tumor tissue (in the sense of (3.13); see also (4.13))? ¹

¹In other words this means, we search for a probe placement that yields an optimal expected temperature distribution, for which the objective functional becomes minimal. Within this work, the terms “expected maximal tumor destruction” and “expected optimal temperature distribution” are always used in this sense.

- **Optimal probe placement for result with maximum confidence:** For which probe placement can we be most confident about the success of the therapy?

Discussing these points does not improve the accuracy of the simulation or the optimization (as numerical verification is a matter divorced from the answer to these questions); rather, it enables us to quantify how the uncertainty of the electric and thermal conductivities affects (or propagates through) the numerical results. Also note, that answering the second question does not yield information about the optimal probe placement for the individual patient, since in general the expected value is not characteristic for a specific sample (i. e. a certain patient). Hence, the investigations related to the second question in fact should be seen as preliminary step towards the optimization of confidence (which belongs to ongoing work; see Sects. 4.8 and 7.2).

To be able to study the questions from above, the electric and thermal conductivity are not considered to have fixed values, but to be probabilistically distributed. The ranges for these parameters can be taken from experiments which are documented in the literature, or estimations of the measurement error can be taken into account. Substituting the probabilistically distributed values into the PDE model for the simulation of RF ablation (see Sect. 2.3) yields a system of stochastic partial differential equations (SPDE).

Classically one would use a (slowly converging) Monte-Carlo method to analyze this system. Under the assumption of having a smoothly-varying random process, more rapid convergence to the true stochastic process that steers the dependence of the temperature distribution on the electric and thermal conductivity can be obtained by employing the stochastic collocation method [91]. By evaluating the SPDE system for certain realizations of the material parameters (i. e. at collocation points in the stochastic space) the sensitivity of the system can be analyzed with respect to variations in the coefficients of the PDE system, i. e. with respect to variations in the material parameters. Moreover, the optimization of the probe placement for stochastically distributed conductivity values can be investigated by minimizing an objective function which involves the expectance of deterministic objective functions (see Sect. 3.3). Again one can use a stochastic collocation method, now to solve the stochastic optimality system.

Stochastic Collocation: The general procedure which is advocated here, applies to many other models in medical simulation. In particular for nonlinear models like the one which is investigated in this work, it is often difficult to analyze the sensitivity with respect to parameter perturbations. The stochastic collocation approach is a convenient technique that is easily implemented, since it allows to reuse existing deterministic code. In Sect. 4.6 this simplicity is emphasized by showing the extensions that are needed to augment the existing deterministic optimization code (Alg. 3.2) to the more general stochastic setting (Alg. 4.1).

The main stochastic theoretical underpinning of the next sections is generally referred to as *generalized Polynomial Chaos* (gPC). Based upon the Wiener-Hermite

polynomial chaos expansion [90], generalized polynomial chaos seeks to approximate second-order random processes by a finite linear combination of stochastic basis functions. Once one has chosen an approximation space of the random process of interest, a solution within that space can be found by solving the stochastic partial differential system of interest in the weak form. Because of its analogy with the classic Galerkin method as employed in finite elements, this methodology is often referred to as the generalized Polynomial Chaos - Stochastic Galerkin method (gPC-SG). It has been applied as a method for uncertainty quantification in the field of computational mechanics for a number of years and has recently seen a revival of interest [65, 20, 21, 63, 25, 62, 92, 94]. Also within the biological modeling world and for conducting sensitivity analysis this approach has been applied successfully: In [38], Geneser *et al.* demonstrated that the gPC-SG methodology is a valid and useful tool for the assessment of current noise in Markovian ion channel models with stochastic rate constants. Further, in [37] they employed the gPC-SG approach to evaluate the effects of variations and uncertainty in the conductivity values assigned to organs in a two-dimensional electrocardiograph simulation of the human thorax.

Although the stochastic Galerkin method provides a solid mathematical framework from which one can do analysis and can derive algorithms, it is not always the most computationally efficient instrument of solving large problems. Nor is it the case that one always has the freedom to re-architect their currently available deterministic solver to employ gPC-SG. To address these issues, the Stochastic Collocation (SC) method was developed [91], combining the advantages of the Monte Carlo approach (as a sampling methodology) with the idea of there being an underlying approximation representation of the stochastic process (gPC). The gPC-SC method evaluates solutions of a stochastic system at carefully chosen points within the random space to compute accurate statistics with significantly fewer solutions than Monte Carlo methods. In the following sections, the gPC-SC approach will be employed for specifically these reasons.

The aim in the next sections is to extend the PDE model for the simulation and optimization of RF ablation presented in Sect. 2.3, such that it incorporates the uncertainty in the material properties, i. e. in the electrical and thermal conductivity of the tissue. Then with help of the extended model, in an initial approach the first two of the above described questions arising from material parameter uncertainty will be discussed: In Sect. 4.2 the notion of random fields is introduced as a model for the uncertainty associated with material parameters. Moreover, the extension of the deterministic PDE model to an SPDE system is presented. After that, in Sect. 4.3 the stochastic collocation method is reviewed. Different approaches for an analysis of the sensitivity of the optimal probe placement with respect to variations in the material parameters are discussed in Sect. 4.4. Sects. 4.5 and 4.6 then deal with the stochastic optimization of the probe placement. Here, a suitable objective function and the derivation of the optimality system are discussed. Since this system is solved with help of a stochastic collocation method, further the corresponding modifications of the deterministic optimization algorithm are presented. Finally, applications are

presented in Sect. 4.7 and conclusions are drawn in Sect. 4.8, including a discussion about the next steps of ongoing and future work.

4.2 A Stochastic Model for RF Ablation

Let $(\Omega, \mathcal{A}, \mu)$ be a probability space expressing the behavior of the thermal and electrical conductivity where Ω is the event space, $\mathcal{A} \subset 2^\Omega$ the σ -algebra, and μ the probability measure. We now consider the case that the tissue parameters σ and λ are not fixed to particular (deterministic) values, but rather lie within a range of possible values. An event ω in our probability space consists of a particular choice of the material properties (σ, λ) . The physical parameters can be considered as random fields expressible in terms of random variables and characterizable by their probability density functions (PDFs). For the problem of interest, let us assume that we have three main types of tissue present in our computational domain: tumor tissue (t), native liver tissue (n), and blood vessels (v). For each of these tissue types let us further assume that the distribution of σ and λ are controlled by uniform independent random variables, each of which is defined over the interval $[-1, 1]$.²

Following [49], we know that we can represent any general second-order *random process* $g(\omega)$, $\omega \in \Omega$ in terms of a collection of random variables $\boldsymbol{\xi} = (\xi_1, \dots, \xi_N)$ with independent components. Here, the stochastic process under investigation is the optimal probe placement \bar{u} as it is obtained by algorithm Alg. 3.1 and 3.2, respectively, described in Sects. 3.4.4 and 3.7.1. Since the optimal probe placement depends on the material parameters σ and λ , any uncertainty associated with those parameters will induce uncertainty in the optimal probe placement. Note that in the following, *random fields* will also be referred to as *stochastic processes*.

To describe the electric field emerging from the RF probe regarded as a random field, let us consider the vector of random variables $\boldsymbol{\xi}^\sigma = (\xi_t^\sigma, \xi_n^\sigma, \xi_v^\sigma) \in \Gamma_\sigma := [-1, 1]^3$ (i.e. $N = 3$) which describes the uncertainty in the electric conductivity of the tumor, the native tissue, and the vessels. Therewith, the stochastic field $\sigma(x, \boldsymbol{\xi}^\sigma)$ can be modeled by

$$\sigma(x, \boldsymbol{\xi}^\sigma) = \begin{cases} \sigma_t(\xi_t^\sigma) & \text{if } x \in D_t \text{ ,} \\ \sigma_n(\xi_n^\sigma) & \text{if } x \in D_n \text{ ,} \\ \sigma_v(\xi_v^\sigma) & \text{if } x \in D_v \text{ .} \end{cases} \quad (4.1)$$

To model the uncertain distribution of heat one can proceed similarly by considering $\boldsymbol{\xi}^\lambda = (\xi_t^\lambda, \xi_n^\lambda, \xi_v^\lambda) \in \Gamma_\lambda := [-1, 1]^3$. The three components of $\boldsymbol{\xi}^\lambda$ represent the

²Note that from the mathematical viewpoint it is very convenient to assume the independence of random variables since it allows to construct tensor-product Hilbert spaces on the stochastic domain. Though, the independence may not be justified from the anatomical viewpoint, since e. g. the different conductivities are correlated through the water content of the tissue. However, there exists a mathematically rigorous (nonlinear) mapping which transforms a set of random variables into a set of independent random variables. This research falls into the area of numerical representation of non-Gaussian processes, which remains an active research field [91].

heat conductivity in the malignant and the native tissue as well as in the vascular structures. The overall heat conductivity $\lambda(x, \boldsymbol{\xi}^\lambda)$ is defined like in (4.1). We will henceforth consider our input parameters to be of the form $\sigma(x, \boldsymbol{\xi}^\sigma)$ and $\lambda(x, \boldsymbol{\xi}^\lambda)$ given by $\boldsymbol{\xi} = (\boldsymbol{\xi}^\sigma, \boldsymbol{\xi}^\lambda) \in \Gamma := \Gamma_\sigma \times \Gamma_\lambda = [-1, 1]^3 \times [-1, 1]^3$ distributed over ranges of values for σ and λ , which are given in the literature: From e.g. [79, 28, 84, 16] we learn that for native liver tissue ³

$$\sigma = 0.17 \text{ S/m} - 0.60 \text{ S/m} \quad \text{and} \quad \lambda = 0.47 \text{ W/Km} - 0.64 \text{ W/Km} . \quad (4.2)$$

The specific single values have mostly been obtained from in vitro experiments on cadaveric human tissue or animals, and they are certainly furthermore associated with realistic measurement errors of 10% or more. The broad range of values for σ and λ in (4.2) underlines the uncertainty associated with these tissue properties and hence emphasizes the need of a further examination of the dependencies on these parameters.

Now, after having introduced the uncertain electric conductivity in (4.1), we can formulate a *stochastic electrostatic equation* similar to (2.13) (see Sect. 2.3, p. 16) by: Find a stochastic field $\phi(x, \boldsymbol{\xi}^\sigma)$ such that

$$\begin{aligned} -\operatorname{div}(\sigma(x, \boldsymbol{\xi}^\sigma) \nabla \phi(x, \boldsymbol{\xi}^\sigma)) &= 0 && \text{a.e. in } D \setminus \overline{D_\pm} \times \Gamma_\sigma , \\ \phi(x, \boldsymbol{\xi}^\sigma) &= 1 && \text{a.e. on } \overline{D_\pm} \times \Gamma_\sigma , \\ n \cdot \nabla \phi(x, \boldsymbol{\xi}^\sigma) &= \frac{n \cdot (p - x)}{|p - x|^2} \phi(x, \boldsymbol{\xi}^\sigma) && \text{a.e. on } \partial D \times \Gamma_\sigma . \end{aligned} \quad (4.3)$$

Straightforwardly, one can proceed to incorporate the uncertainty into the remaining components of the model that has been presented in Sect. 2.3. This yields a stochastic field for the heat source and stochastic processes for the total and the effective power. Formally that means

$$Q_{\text{rf}}(x, \boldsymbol{\xi}^\sigma) = \frac{P_{\text{eff}}(\boldsymbol{\xi}^\sigma)}{P_{\text{total}}(\boldsymbol{\xi}^\sigma)} \sigma(x, \boldsymbol{\xi}^\sigma) |\nabla \phi(x, \boldsymbol{\xi}^\sigma)|^2 , \quad (4.4)$$

where

$$P_{\text{eff}}(\boldsymbol{\xi}^\sigma) = \frac{4P_{\text{setup}} R(\boldsymbol{\xi}^\sigma) R_{\text{I}}}{(R(\boldsymbol{\xi}^\sigma) + R_{\text{I}})^2} \quad \text{with} \quad R(\boldsymbol{\xi}^\sigma) = \frac{U^2}{P_{\text{total}}(\boldsymbol{\xi}^\sigma)} , \quad (4.5)$$

$$P_{\text{total}}(\boldsymbol{\xi}^\sigma) = \int_D \sigma(x, \boldsymbol{\xi}^\sigma) |\nabla \phi(x, \boldsymbol{\xi}^\sigma)|^2 dx .$$

We may also define the *stochastic heat equation* in analogy to (2.17) (again see Sect. 2.3, p. 17). Since the source term on the right hand side depends on the solution of the stochastic electrostatic equation, the temperature distribution is going to be a random field that depends on both $\boldsymbol{\xi}^\sigma$ and $\boldsymbol{\xi}^\lambda$, i. e.

$$\begin{aligned} -\operatorname{div}(\lambda(x, \boldsymbol{\xi}^\lambda) \nabla T(x, \boldsymbol{\xi})) &= Q_{\text{rf}}(x, \boldsymbol{\xi}^\sigma) + Q_{\text{perf}}(x, \boldsymbol{\xi}) && \text{a.e. in } D \times \Gamma , \\ T(x, \boldsymbol{\xi}) &= T_{\text{body}} && \text{a.e. on } \partial D \times \Gamma , \end{aligned} \quad (4.6)$$

³The ranges of values for σ and λ in tumor tissue and vessels are presented in Sect. 4.7, p. 72.

where $\boldsymbol{\xi} = (\boldsymbol{\xi}^\sigma, \boldsymbol{\xi}^\lambda)$. The sink term Q_{perf} in (4.6) is modeled like in (2.16) of Sect. 2.3:

$$Q_{\text{perf}}(x, \boldsymbol{\xi}) = -\nu(x) (T(x, \boldsymbol{\xi}) - T_{\text{body}}) , \quad \text{where} \\ \nu(x) = \begin{cases} \nu_{\text{vessel}} \rho_{\text{blood}} c_{\text{blood}} & \text{for } x \in D_{\text{v}} , \\ \nu_{\text{cap}} \rho_{\text{blood}} c_{\text{blood}} & \text{else .} \end{cases} \quad (4.7)$$

4.3 Generalized Polynomial Chaos and Stochastic Collocation

The generalized Polynomial Chaos (gPC) approach represents any second-order stochastic process $g(\boldsymbol{\xi})$ written in terms of random variables, by a weighted (infinite) sum of orthogonal polynomials [39, 92, 93, 94], which are functions of the vector of random variables $\boldsymbol{\xi}$ of known probability density function (PDF). In the case of this study, the random input fields of interest are the (stochastic) input parameters σ and λ , and the random process of interest is the optimal probe placement \bar{u} , for which the optimality system (2.13) - (2.17) and (3.13) is solved in Sect. 3.4. An approximation of a stochastic process can be expressed by truncating the infinite summation to $P + 1$ terms for some $P \in \mathbb{N}$. Denoting the stochastic orthogonal polynomial set as $L_i(\boldsymbol{\xi})$ and the polynomial weights as \hat{g}_i , the approximation of the stochastic process can be written as

$$\tilde{g}(\boldsymbol{\xi}) = \sum_{i=0}^P \hat{g}_i L_i(\boldsymbol{\xi}) , \quad \text{with} \quad \hat{g}_i = \left(\int_{\Gamma} L_i^2 d\mu(\boldsymbol{\xi}) \right)^{-1} \int_{\Gamma} g(\boldsymbol{\xi}) L_i(\boldsymbol{\xi}) d\mu(\boldsymbol{\xi}) . \quad (4.8)$$

In the case of random processes g that depend on a scalar random variable ξ (e. g. $\sigma_k(\xi_k^\sigma)$, $k \in \{t, n, v\}$, cf. (4.1)) and which have uniform distribution, the Legendre polynomials are the optimal orthogonal polynomials to employ [93]; this allows us to express $g(\xi)$ exactly in terms of two coefficients such that $g(\xi) = \hat{g}_0 L_0(\xi) + \hat{g}_1 L_1(\xi) = \hat{g}_0 + \hat{g}_1 \xi$, where the first coefficient is the midpoint of the uniform interval and the second coefficient is the half-length of the uniform interval.

Now, let the uniform random process $g(\boldsymbol{\xi})$ denote the input parameter of interest (i. e. the electric conductivity $\sigma(x, \boldsymbol{\xi}^\sigma)$ or the thermal conductivity $\lambda(x, \boldsymbol{\xi}^\lambda)$) and let $f(\boldsymbol{\xi})$ denote the random field which is a consequence of the solution of the optimality system from Sect. 2.3 with 3.3 (i. e. $f(\boldsymbol{\xi})$ denotes the optimal probe placement $\bar{u}(\boldsymbol{\xi}) = (\bar{p}(\boldsymbol{\xi}), \bar{d}(\boldsymbol{\xi}))$)⁴. If g is distributed uniformly, there is no guarantee that f will be of uniform distribution as well; all that is guaranteed is that a finite sum of Legendre polynomials is a good representation of the process (with the approximation quality increasing as a function of the number of terms which are used).

⁴For a better understanding, again it should be emphasized, that in this section and also in the following section (Sect. 4.4) $f(\boldsymbol{\xi})$ does not denote the objective function as it did before, but instead denotes the optimal probe placement $\bar{u}(\boldsymbol{\xi})$.

In the stochastic collocation (gPC-SC) approach [91] quadrature rules are employed which collocate the stochastic process of interest for accomplishing the integration over the stochastic domain in order to compute the coefficients \hat{g}_i of the expansion (4.8). It is popular to use a set of quadrature points $\{\boldsymbol{\xi}_j\}_{j=1}^q$ which lie on a sparse grid in the stochastic space and which are generated by Smolyak's algorithm [91].⁵

In this work a different aspect of the collocation approach is turned to account by not using the points $\boldsymbol{\xi}_j$ for an integration of the coefficients in the expansion (4.8), but instead considering an approximation of the stochastic process $f(\boldsymbol{\xi})$ on the incomplete polynomial space resulting from Smolyak's algorithm. Thus, the interpolation approximation of $f(\boldsymbol{\xi})$ is defined by

$$\tilde{f}(\boldsymbol{\xi}) = \sum_{j=1}^q f(\boldsymbol{\xi}_j)h_j(\boldsymbol{\xi}) = \sum_{j=1}^q \mathcal{F}(g(\boldsymbol{\xi}_j))h_j(\boldsymbol{\xi}) \quad (4.9)$$

with a set of Lagrange interpolating basis functions $h_i(\boldsymbol{\xi}_j) = \delta_{ij}$. Here, \mathcal{F} denotes the solution operator for the deterministic optimality system from Sect. 2.3 with 3.3, i.e. $f(\boldsymbol{\xi}) = \mathcal{F}(g(\boldsymbol{\xi}))$. Solving the deterministic system at the collection of samples $\{\boldsymbol{\xi}_j\}_{j=1}^q$ allows us to construct an approximation such that the residual $R(f(\boldsymbol{\xi}) - \tilde{f}(\boldsymbol{\xi}))$ between the interpolated system $\tilde{f}(\boldsymbol{\xi})$ and the true process $f(\boldsymbol{\xi})$ is zero at these points.

An approximation of the mean of the process $f(\boldsymbol{\xi})$ is given by

$$\bar{f} = \mathbb{E}[(f)(\boldsymbol{\xi})] = \int_{\Gamma} f(\boldsymbol{\xi})d\mu(\boldsymbol{\xi}) \approx \sum_{j=1}^q w_j f(\boldsymbol{\xi}_j) = \sum_{j=1}^q w_j \mathcal{F}(g(\boldsymbol{\xi}_j)) \quad , \quad (4.10)$$

where w_j are the collocation weights derived by integration of the interpolation functions $w_j = \int_{\Gamma} h_j(\boldsymbol{\xi})d\mu(\boldsymbol{\xi})$. Similarly, an approximation of the variance can be calculated as follows:

$$\text{Var}[f(\boldsymbol{\xi})] = \mathbb{E}[(f(\boldsymbol{\xi}) - \bar{f})^2] \approx \sum_{j=1}^q w_j (f(\boldsymbol{\xi}_j) - \bar{f})^2 \quad . \quad (4.11)$$

The accuracy of the collocation approach in multi-dimensions is often discussed in terms of the so-called *level k* of integration (a term which is related to the space of functions which is integrated exactly). In Sect. 4.7, the level k and number q of quadrature points are reported in accordance with [91].

Note, that the collocation approach discussed above is one of multiple possible collocation methods used in the solution of SPDE [49, 50]. With increasing rate of convergence (and increasing assumptions on smoothness) one can use approaches

⁵Here, the sparse grid of quadrature points is generated by Clenshaw-Curtis (CC) formulas which are based on a Tshebyshev interpolation of the integrand. The advantage of using CC formulas compared to e.g. Gauss type formulas which have higher order, is that the nodes of the CC formulas are nested, here.

based e. g. on the classical Monte-Carlo method, the Newton-Cotes formulas, Gaussian or Clenshaw-Curtis quadrature, or the sparse-grid spectral collocation method discussed here.

4.4 Sensitivity Analysis

From the approximation of the stochastic process describing the optimal probe placement one can analyze the sensitivity of the system to perturbations in the parameters. In the following, three different variants for the parametric sensitivity analysis through the stochastic collocation approach will be discussed. Later, in Sect. 4.7, examples for all variants considered in the following will be presented.

4.4.1 Local Sensitivity Analysis

The local behavior of the stochastic process yields information about the robustness of the probe placement with respect to very small perturbations in the material parameters. To investigate this local behavior, let us consider derivatives of the stochastic process with respect to the input data, i. e. $df(\boldsymbol{\xi})/dg(\boldsymbol{\xi}) = d\mathcal{F}(g(\boldsymbol{\xi}))/dg(\boldsymbol{\xi})$, which can be evaluated at any point $\boldsymbol{\xi} \in \Gamma$. For example, we can assume that $\boldsymbol{\xi} = 0$, i. e. we can consider the local sensitivity of the process around the mean of the input parameter (i. e. around the midpoint of the uniform distribution of the input parameter). This can easily be accomplished within the current framework: Combining the representation (4.9) of $f(\boldsymbol{\xi})$ in the incomplete polynomial space resulting from Smolyak's algorithm yields

$$\left. \frac{d\tilde{f}}{dg}(\boldsymbol{\xi}) \right|_{\boldsymbol{\xi}=0} = \left. \frac{d\tilde{f}}{d\boldsymbol{\xi}} \frac{d\boldsymbol{\xi}}{dg}(\boldsymbol{\xi}) \right|_{\boldsymbol{\xi}=0} = \frac{d\boldsymbol{\xi}}{dg}(0) \sum_{j=1}^q f(\boldsymbol{\xi}_j) \frac{dh_j}{d\boldsymbol{\xi}}(0) . \quad (4.12)$$

For example, for the sensitivity of the optimal probe position $\bar{p} = (\bar{p}_1(\boldsymbol{\xi}), \bar{p}_2(\boldsymbol{\xi}), \bar{p}_3(\boldsymbol{\xi})) \in D$ with respect to σ , this formula yields a 3×3 matrix S having entries

$$S_{ik} = \frac{d\bar{p}_i}{d\sigma_k} = (\hat{\sigma}_1^k)^{-1} \sum_{j=1}^q \bar{p}_i(\boldsymbol{\xi}_j) \frac{dh_j}{d\xi_k^\sigma}(0) \quad \text{for } i \in \{1, 2, 3\} , k \in \{t, n, v\} ,$$

where $\hat{\sigma}_1^k$ is the coefficient \hat{g}_1 , i. e. the half-length of the uniform interval of the input parameter σ_k . Analog expressions hold for the sensitivities of the other quantities (such as the probe's orientation) involved in our system.

4.4.2 Probability Density of Joint Distribution

Another approach that reveals the robustness of the optimal probe placement with respect to variations in the material parameters is yield by a direct analysis of the probability density function (PDF) of the probe placement. In contrast to the

local sensitivity analysis presented above, an analysis of the PDF does not disclose the local behavior of the process. Instead, it yields information about the global behavior of the optimal probe placement with respect to variations in the material parameters. In general, the PDF is not calculable analytically; one has to evaluate the stochastic process, i. e. the representation (4.9) of the random field f , at a large number of sampling points to get an appropriate approximation of the PDF. For more details see [49, 50] and in particular [55], where for the case of considering only one-dimensional quantities an improved algorithm for approximating the PDF (getting a comparable accuracy with a less number of evaluation points) is presented.

4.4.3 Covariance of Joint Distribution

Instead of the calculation of the PDF, one can investigate the covariance matrix of the joint distribution of the components of the optimal probe placement. The covariance matrix of the approximation \tilde{f} of the random field f (cf. (4.9)) can be calculated analytically and it can be computed much faster than the PDF. Moreover, as will be seen in Sect. 4.7, its results are easier to interpret. Formally, the covariance matrix of the joint distribution of the coordinates of e. g. the optimal probe position $\bar{p}(\boldsymbol{\xi}) = (\bar{p}_1(\boldsymbol{\xi}), \bar{p}_2(\boldsymbol{\xi}), \bar{p}_3(\boldsymbol{\xi}))$ can be written as

$$\text{Cov}[\bar{p}] = (\text{Cov}[\bar{p}_i, \bar{p}_j])_{i,j \in \{1,2,3\}} \quad , \quad \text{where} \quad \text{Cov}[\bar{p}_i, \bar{p}_j] = \mathbb{E}[(\bar{p}_i - \mathbb{E}[\bar{p}_i])(\bar{p}_j - \mathbb{E}[\bar{p}_j])]$$

for all pairs of coordinates $i, j \in \{1, 2, 3\}$. The covariance matrix is a symmetric (in this case 3×3) matrix that quantifies how the coordinates of e. g. the optimal probe position are coupled through the random variable $\boldsymbol{\xi}$. If this matrix were diagonal, the coordinates would be independent.

Difficulties in Interpreting the PDF and its Covariance Matrix

For some cases an interpretation of the PDF and its covariance matrix is delicate. In those cases a large elongation of the PDF and a large variance of the PDF do not necessarily result from a strong dependence on the input parameters. In fact, a large sensitivity of the optimal probe placement can be the result of either of two essentially different situations:

- Either, the whole energy graph of the objective function varies strongly in dependence of the uncertain parameters. This is the kind of sensitivity which is aimed to be detected and analyzed, here.
- Or, the energy graph of the objective function is in some area flat, so that small changes (e. g. in the settings of the optimizer) can influence the optimal probe placement strongly. This local insensitivity of the objective function to changes in the probe positioning leads to a false sensitivity. More precisely that means, even if the optimal probe position varies strongly with respect to changes in the material parameters, the objective function values might show

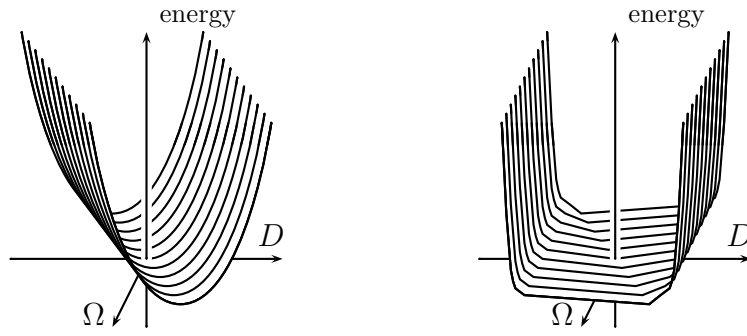


Figure 4.1: Two essentially different situations for the energy graph of the objective function that lead to similar distributions of the optimal probe placement in dependence of the uncertain tissue parameters. Left: Desired situation of a strong variation of the energy graph in dependence of the optimal probe position and tissue parameters, respectively. Right: Disadvantageous situation of a local insensitivity of the objective function to changes in the optimal probe position.

only minor changes, due to the local insensitivity of the objective function to changes in the probe position.

Hence, to sensibly interpret the PDF and the covariance matrix, more information about the graph of the objective function is needed. In Fig. 4.1, a schematic of the two described situations is shown. Both plots represent the objective function in dependence of the probe placement $u \in D$ and in dependence of the event $\omega \in \Omega$ that leads to a certain realization of the material properties $(\sigma(\boldsymbol{\xi}(\omega)), \lambda(\boldsymbol{\xi}(\omega)))$. For an easier presentation both spaces D and Ω are represented one-dimensional. In order to differentiate between these two cases, and to detect false sensitivities, it is strongly advisable to analyze the values of the objective function.

Finally, it has to be emphasized that special care must be taken concerning the accuracy of the numerical solvers involved. In [48] Kaipio and Somersalo discuss that limited numerical accuracies (i. e. discretization errors) can sometimes (effectively or ineffectively) be interpreted as the behavior of a random process. Consequently, in the numerical experiments shown in Sect. 4.7 the stopping criteria of the iterative solvers as well as for the optimization loops have been set appropriately.

4.5 Optimizing the Probe Location in the Presence of Uncertain Material Parameters

Let us now proceed to an optimization of the probe location under the constraint of the system of stochastic partial differential equations (4.3) and (4.6). The aim is to find a position and direction of the probe such that one can expect a maximum of destroyed tumor tissue. Therefore, an objective function is needed which maps the stochastic temperature distribution to a real number. Such an energy can be obtained by considering the expectance of the objective function $f(T(x, \boldsymbol{\xi}))$ which

has been defined in (3.13) of Sect. 3.3 (p. 36). This yields the stochasticity-aware objective function \bar{f} defined as

$$\begin{aligned} \bar{f}(T) &:= \mathbb{E}[f(T(x, \boldsymbol{\xi}))] = \mathbb{E} \left[\log \left(\int_{D_t} \exp(-\alpha T(x, \boldsymbol{\xi})) dx \right) \right] \\ &= \int_{\Gamma} \log \left(\int_{D_t} \exp(-\alpha T(x, \boldsymbol{\xi})) dx \right) d\mu(\boldsymbol{\xi}) , \end{aligned} \quad (4.13)$$

and allows the search for optimal probe locations

$$(\bar{p}, \bar{d}) = \underset{(p,d) \in U}{\operatorname{argmin}} \bar{f}(T) .$$

In the following section the optimality system for this objective function under the constraint of the SPDE system (4.3) and (4.6) will be derived, and the extensions of the deterministic optimization algorithm (Alg. 3.2) that are necessary for the stochastic variant (see Alg. 4.1), will be presented.

4.6 Optimality System and Stochastic Gradient Descent

To derive the optimality system, the corresponding stochastic Lagrange function has to be defined as e. g. an extension of the reduced Lagrange function introduced in (3.19) (see Sect. 3.4, p. 39)⁶, i. e.

$$\begin{aligned} \mathcal{L}(T, u, v) &:= \bar{f}(T) - \int_{\Gamma} \int_D \lambda(x, \boldsymbol{\xi}^\lambda) \nabla T(x, \boldsymbol{\xi}) \nabla v(x, \boldsymbol{\xi}) dx d\mu(\boldsymbol{\xi}) \\ &\quad - \int_{\Gamma} \int_D \nu(x) T(x, \boldsymbol{\xi}) v(x, \boldsymbol{\xi}) dx d\mu(\boldsymbol{\xi}) \\ &\quad + \int_{\Gamma} \int_D Q_{\text{rf}}(x, \boldsymbol{\xi}^\sigma) v(x, \boldsymbol{\xi}) dx d\mu(\boldsymbol{\xi}) \end{aligned} \quad (4.14)$$

with the Lagrange multiplier v , which is a random field. In this definition of the Lagrange function the constraint imposed by the stochastic heat equation (4.6) is subtracted from the objective function (4.13). Like in the deterministic case (cf. Sect. 3.4.1), minimizing the objective function under the constraint of the SPDE system is equivalent to finding solutions of $D_T \mathcal{L}(T, u, v)[z] = 0$ and $D_u \mathcal{L}(T, u, v)[w] = 0$ for all temperature random fields z and for all probe placements w . Analog to (3.27)

⁶Remind that the reduction in this context, is to consider the source term Q_{rf} to depend directly on the probe parameters u , such that the rather complicated connection between the electric potential ϕ and the heat source Q_{rf} through equations (4.4) and (4.5) is evaded.

of Sect. 3.4.1, here the variation $D_T \mathcal{L}(T, u, v)[z]$ is given by

$$\begin{aligned} D_T \mathcal{L}(T, u, v)[z] &= -\alpha \int_{\Gamma} \left[\left(\int_{D_t} \exp(-\alpha T(y, \boldsymbol{\xi})) dy \right)^{-1} \int_{D_t} \exp(-\alpha T(x, \boldsymbol{\xi})) z(x, \boldsymbol{\xi}) dx \right] d\mu(\boldsymbol{\xi}) \\ &\quad - \int_{\Gamma} \int_D \lambda(x, \boldsymbol{\xi}^\lambda) \nabla v(x, \boldsymbol{\xi}) \nabla z(x, \boldsymbol{\xi}) dx d\mu(\boldsymbol{\xi}) \\ &\quad - \int_{\Gamma} \int_D \nu(x) v(x, \boldsymbol{\xi}) z(x, \boldsymbol{\xi}) dx d\mu(\boldsymbol{\xi}) \end{aligned} \quad (4.15)$$

for all temperature random fields $z \in H^1(D) \times \Gamma$. Moreover, for the variation $D_u \mathcal{L}(T, u, v)[w]$ we have

$$D_u \mathcal{L}(T, u, v)[w] = \int_{\Gamma} \int_D \frac{\partial}{\partial u} Q_{\text{rf}}(u)(x, \boldsymbol{\xi}^\sigma) \cdot w v(x, \boldsymbol{\xi}) dx d\mu(\boldsymbol{\xi}) \quad (4.16)$$

for all probe placements $w \in D \times S^2$ (cf. (3.29) of Sect. 3.4.1).

Now, the optimization process is very similar to the deterministic setting described in Sect. 3.4 together with the extension to a multi-level optimization explained in Sect. 3.7. Starting from an initial probe location u^0 on a coarse grid, one can perform a gradient descent to yield an optimal probe placement, which then is the initial guess for an optimization on the next finer grid. The optimization, i. e. the gradient descent on each grid involves the following steps (as in Sects. 3.4 and 3.7.1, the superscript $n \in \mathbb{N}$ again denotes the iteration count):

1. Calculate $v^n(x, \boldsymbol{\xi})$ as the solution to the adjoint equation $D_T \mathcal{L}(T^n, u^n, v^n) = 0$ in $D \times \Gamma$, i. e.

$$\begin{aligned} &-\operatorname{div}(\lambda(x, \boldsymbol{\xi}^\lambda) \nabla v^n(x, \boldsymbol{\xi})) + \nu(x) v^n(x, \boldsymbol{\xi}) \\ &= -\alpha \left(\int_{D_t} \exp(-\alpha T^n(y, \boldsymbol{\xi})) dy \right)^{-1} \chi_{D_t}(x) \exp(-\alpha T^n(x, \boldsymbol{\xi})) \end{aligned} \quad (4.17)$$

for a.e. $(x, \boldsymbol{\xi}) \in D \times \Gamma$, with boundary condition $v^n(x, \boldsymbol{\xi}) = 0$ a.e. on $\partial D \times \Gamma$. As in Sect. 3.4.1, here again $\chi_{D_t}(x)$ is an indicator function which is 1 for $x \in D_t$ and 0 elsewhere. The weak form of the adjoint SPDE is given by (4.15).

2. The gradient in direction of w is given by the variation $D_u \mathcal{L}$, whose weak form has been derived in (4.16). Since we search for a steepest descent, we take

$$\begin{aligned} w^n(x) &:= - \int_{\Gamma} \int_D \frac{\partial}{\partial u} Q_{\text{rf}}(u^n)(x, \boldsymbol{\xi}^\sigma) v^n(x, \boldsymbol{\xi}) dx d\mu(\boldsymbol{\xi}) \\ &= -\mathbb{E} \left[\int_D \frac{\partial}{\partial u} Q_{\text{rf}}(u^n)(x, \boldsymbol{\xi}^\sigma) v^n(x, \boldsymbol{\xi}) dx \right], \end{aligned} \quad (4.18)$$

because for this direction (4.16) reaches its minimal value which is

$$D_u \mathcal{L}(T^n, u^n, v^n)[w^n] = -\|w^n\|_{L^2(D)}^2. \quad (4.19)$$

3. To determine the optimal step size s^n one can evaluate

$$s^n = \operatorname{argmin}_{s>0} \bar{f}(P_{D \times S^2}(u^n + sw^n)) , \quad (4.20)$$

where the constraint $u \in U = D \times S^2$ is ensured by using a projection P as before in the deterministic approach (see (3.25) of Sect. 3.4). For the identification of the optimal step size e. g. a bisection rule similar to Armijo's rule as described in Sect. 3.4.2 can be used.

4. Finally, the new iterate is $u^{n+1} = u^n + s^n w^n$.

In fact this stochastic optimization is very similar to the deterministic one (cf. Alg. 3.1 and 3.2). The main differences result in the computation of the gradient descent (4.18) in step 2 and in the evaluation of the objective function (4.13) for the determination of the optimal step size (4.20) in step 3. To compute the expectation in the steepest descent direction and the expected objective function value, respectively, the collocation method as described in Sect. 4.3 is used. As before for the deterministic optimization, the derivative $\frac{\partial}{\partial u} Q_{\text{rf}}(u^n)$ can be calculated by central differences (see (3.22) and Sect. 3.4.1), and for the spatial integration a simple tensor-product trapezoidal quadrature rule (cf. Sect. 3.3.1) can be used.

4.6.1 The Stochastic Multi-Level Optimization Algorithm

In Alg. 4.1 the modifications that transform Alg. 3.1 and 3.2, respectively, into a stochastic optimization algorithm are presented. The calculation of the descent direction (line 4 of Alg. 3.1) and the determination of the step size (lines 10-19 of Alg. 3.1) which involves several evaluations of the objective function, are expanded in Alg. 4.1: now we have a loop over all collocation points ξ_j and the temperature iterate T_j^n and the adjoint state v_j^n are computed for the realizations $\lambda(\cdot, \xi_j^\lambda)$ and $\sigma(\cdot, \xi_j^\sigma)$. Next, the descent direction and the objective function value for the respective realizations are computed. After that, all descent directions for the different realizations are combined according to (4.10) of Sect. 4.3, to yield the expectation described in (4.18). In the same way, all objective function values for the different realizations are composed yielding the expectation of the objective function (cf. (4.13)) which is used for calculating the step size in (4.20). Finally, the step size s^n is determined as described in lines 10-19 of Alg. 3.1, but with repeated computations of T_j^{n+1} and \bar{f}_j^{n+1} for the different realizations of λ and σ to calculate the new objective function value \bar{f}^{n+1} and compare it with the old one after each bisection of s^n . Note, that the pseudo-code presented here is not optimized but rather is guided by pedagogical considerations. In practice, algorithmic optimizations such as writing the linear combination for w in accumulator form within the loop and re-use of storage for temporary values of T and v are employed.

Algorithm 4.1 Stochastic multi-scale algorithm for probe placement optimization

```

1:  $l \leftarrow l_0$  ▷ Start with level  $l_0$ 
2: Choose  $\bar{u}$ . ▷ Initialize start positioning
3: while  $l \leq L$  do
    $\vdots$  ▷ Lines 4, 5 of Alg. 3.2
4:   repeat
     

---


5:     for  $j = 1, \dots, q$  do ▷ For all collocation points  $\xi_j$ 
6:        $T_j^n \leftarrow T^n(u^n)(x, \xi_j)$  ▷ Compute states for realization  $\xi_j$ 
7:        $v_j^n \leftarrow v^n(T^n)(x, \xi_j)$ 
8:        $w_j^n \leftarrow -\frac{\partial}{\partial u} Q_{\text{rf}}(u^n)(x, \xi_j^\sigma) v_j^n$  ▷ Compute descent for realization  $\xi_j$ 
9:        $\bar{f}_j^n \leftarrow \log \left( \int_{D_t} \exp(-\alpha T_j^n) dx \right)$  ▷ Compute obj.  $\bar{f}$  for realization  $\xi_j$ 
10:    end for
11:     $w^n \leftarrow \sum_{j=1}^q \alpha_j w_j^n$  ▷ Compute descent direction
12:     $\bar{f}^n \leftarrow \sum_{j=1}^q \alpha_j \bar{f}_j^n$  ▷ Compute objective function
     $\vdots$  ▷ Determine step size  $s^n$  :
     $\vdots$  ▷ Lines 10 - 19 of Alg. 3.1 with repeated
    computation of  $T_j^{n+1}$ ,  $\bar{f}_j^{n+1}$  and  $\bar{f}^{n+1}$ 
     

---


13:   until  $|u^{n+1} - u^n| \leq \theta$ 
     $\vdots$  ▷ Lines 8, 9 of Alg. 3.2
14: end while

```

4.7 Results

In the following the methodology derived in the previous sections will be applied to the artificial test scenario as well as to the real RF ablation case which both are known from the calculation of the optimal probe placement in Sects. 3.5 and 3.8. Again, as in Sects. 3.5 and 3.8, the artificial scenario is considered for benchmark purposes only, since it allows for an easy (mathematical) interpretation of the results. For the case of the real RF ablation scenario the focus will also be on the value the presented framework may yield to the attending physicians. In both settings the material parameters are considered to be uniformly distributed. The electric conductivity $\sigma = (\sigma_t, \sigma_v, \sigma_n)$ ranges in $[0.64, 0.96] \times [0.67, 0.86] \times [0.17, 0.60]$ [S/m], while the thermal conductivity $\lambda = (\lambda_t, \lambda_v, \lambda_n)$ ranges in $[0.51, 0.77] \times [0.51, 0.54] \times [0.47, 0.64]$ [W/km]. The respective intervals have been chosen based upon values found in the literature [79, 28, 84, 16] (cf. also (4.2)).

Here, the penalty-factor $\alpha = 1$ is used within the objective function \bar{f} in (4.13) (see also Sect. 3.3, p. 34). Moreover, the stopping criterion for the optimization

Table 4.1: Number of collocation points for the stochastic dimensions dim and the levels k of approximation used in this study.

		Level k			
		1	2	3	4
Dimension	$dim = 3$	7	25	69	177
	$dim = 6$	13	85	389	1457

algorithm has been set to $\theta = 10^{-5}$ for the probe position and direction. This stopping criterion is reasonable as it corresponds to an accuracy of 0.01 mm which, is smaller than what can be achieved in clinical practice. For the iterative solvers used in the computation of the forward problem an accuracy of 10^{-13} is required for the decrease of the residual. With these settings the optimization of the probe location for one collocation point typically takes about 10 h on a standard desktop PC with an Intel® Xeon™ 2.4 GHz processor and 2 GB RAM.

For the experiments shown in this section we either have the stochastic dimension $dim = 3$ (when uncertainty in thermal or electrical conductivity is considered separately) or $dim = 6$ (when uncertainty is considered in both conductivities simultaneously). Following [91], in Table 4.1 the stochastic dimension dim , approximation level k , and number q of collocation points employed in this work, are reported. If not mentioned otherwise the numerical results presented in the following paragraphs are obtained on the collocation level $k = 2$.

In general, to find the appropriate level k one can use the same procedure as for the determination of an appropriate spatial grid resolution: The respective computation is performed for a hierarchy of increasing k values and the results are tested for Cauchy convergence. In Sect. 4.7.2 the results of such a hierarchy of computations for the sensitivity of the probe placement w.r.t. variations in the electric conductivity σ are shown.

4.7.1 Artificial Scenario

In the artificial test scenario the size of the computational domain D and the spatial discretization are the same as in Sects. 3.5 and 3.8, i.e. D is of extent $60 \times 60 \times 60 \text{ mm}^3$, discretized with a fine grid of 120^3 cells. As in Sect. 3.8, for the multi-scale optimization, the fine grid is embedded into an octree grid of grid-level $L = 7$ (cf. Sect. 3.7), i.e. we consider two coarser grids of 60^3 and 30^3 grid cells, respectively. Further, a lesion D_t , which has ellipsoidal shape, is assumed to be located in the center of D with a linear vessel D_v in the vicinity of the lesion. For the perfusion, here, the same values as in Sect. 3.8 are taken (i.e. $\nu_{\text{cap}} = 0.01765 \text{ s}^{-1}$, $\nu_{\text{vessel}} = 0.05 \text{ s}^{-1}$, $\rho_{\text{blood}} = 1059.0 \text{ kg/m}^3$ and $c_{\text{blood}} = 3850.0 \text{ J/kgK}$). Also the probe and generator settings are the same as in Sects. 3.5 and 3.8, i.e. a monopolar probe of radius 1.2 mm and 25 mm electrode length is applied, and the electric generator has an inner resistance of 80Ω , and is set to a maximum power of 80 W. For the opti-

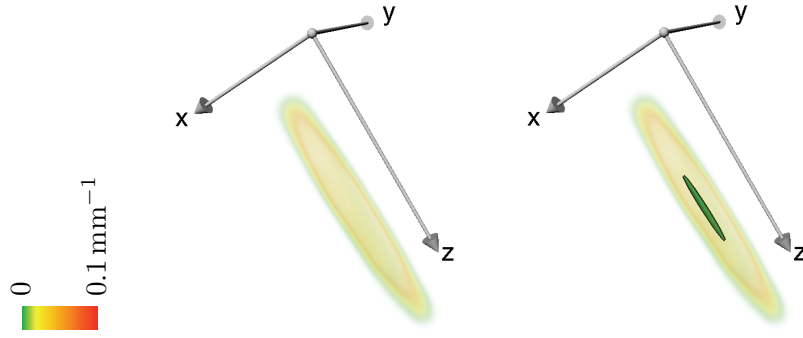


Figure 4.2: The sensitivity of the optimal probe location is investigated for the artificial scenario with an ellipsoidal lesion and a linear vessel. Left: The PDF of the optimal probe location with distributed σ is shown with a volume rendering. The transfer function uses the color ramp shown on the left such that likely locations appear orange/red whereas unlikely locations appear green. Right: The ellipsoid shown inside the volume rendering cloud reveals a simpler visualization. It is centered at the mean of the distribution and it is oriented and scaled with the eigenvectors and eigenvalues of the distribution's covariance matrix. Moreover, for better visibility, it is magnified by a factor of 10.

mization, the initial probe position is always located at a distance of 10 mm in each coordinate direction from the center of D and its initial orientation is $d = (5, 2, 3)$, projected on the sphere (i. e. normalized to length 1).

To guarantee that the size of D does not influence the result of the optimizer, a comparison between forward simulations using Dirichlet or Neumann boundary conditions at ∂D , respectively, has been performed. Both temperature profiles differ by less than 0.5 K in the interior of D , i. e. at locations which are more than 10 grid cells (≈ 5 mm) apart from ∂D . Closer to the boundary the temperatures differ slightly more. Hence, it can be concluded that in the vicinity of the lesion the particular choice of boundary condition does not influence the result significantly.

Sensitivity of the Optimal Probe Location

In Sect. 4.4 different variants for the analysis of the sensitivity with respect to variations in the material parameters have been described. Note, that since the space of admissible probe placements U is a multi-dimensional space, a visualization and an analysis of the PDFs of the corresponding distributions is not straightforward (cf. also [55]), because the PDFs are functions $U \rightarrow \mathbb{R}$. In fact, when taking uncertainty in λ and σ into account, we get a six-dimensional stochastic space Γ . On this space a stochastic process has been approximated through collocation that reveals the dependence of the optimal probe placement \bar{u} w.r.t. variations in the parameters λ and/or σ . The optimal probe placement \bar{u} lies in again a six-dimensional space U (three dimensional probe location p and three-dimensional orientation vector d).

Now, first a visualization that reduces the complexity of the data and allows for an easy perception of the distribution of the optimal probe location \bar{p} will be

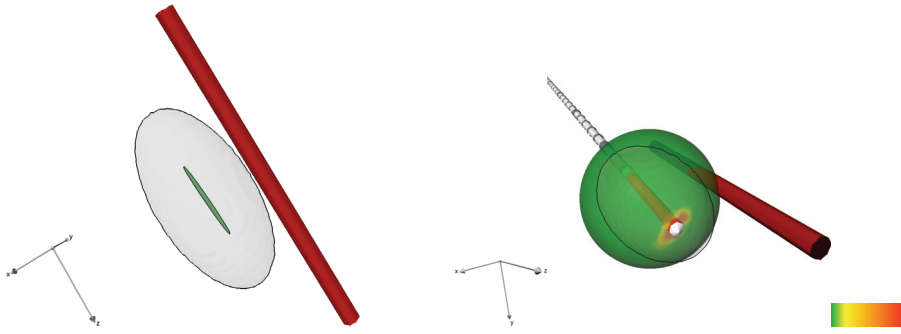


Figure 4.3: For the artificial scenario the sensitivity of the optimal probe position and orientation w.r.t. variations in the electric conductivity σ is shown. Left: Sensitivity of the optimal probe position visualized through an ellipsoidal representation of the covariance matrix (magnified by a factor of 10). Right: PDF of the optimal probe orientation visualized through a coloring of the sphere. As shown by the color ramp on the right, green colors indicate unlikely orientations, whereas red colors show likely orientations. In both images the RF probe is drawn at the mean of the placement’s distribution, the linear vessel D_v is displayed in red and the ellipsoidal shaped tumor lesion D_t is displayed in a transparent gray color.

discussed. The PDF of the optimal probe location is a mapping $\mathbb{R}^3 \rightarrow \mathbb{R}$ which can be visualized through a volume rendering as shown in Fig. 4.2 (left). There, the PDF of the optimal probe location depending on the three-dimensional vector of random variables ξ^σ is shown. In terms of a Monte Carlo experiment, this visualization can be explained in the following way: For any realization of the electrical conductivity σ an optimal probe location \bar{p} is computed (cf. Sect. 4.4.2). In Fig. 4.2 the color codes “how often” a certain probe location is obtained as the optimum.

A deep understanding and analysis of the three-dimensional PDF can be achieved only by an interactive three-dimensional display of the data. Therefore, the approach described in Sect. 4.4.3 can be used to provide a simpler and better perceptible visualization. From the probability distribution of the optimal probe location the first and the second moment, corresponding to the mean and the covariance, are computed. Then, an eigenanalysis allows to draw an ellipsoid centered at the mean, oriented with the eigenvectors, and scaled with the square root of the eigenvalues of the covariance matrix. Indeed, as shown in Fig. 4.2 (right) the ellipsoid (magnified by a factor of 10 for reasons of better visibility) is aligned with the PDF. It can be interpreted as a principal component analysis of the PDF: large eigenvalues imply that the distribution is wide (has a high variance) in the corresponding direction.

Moreover, in Fig. 4.3 (left) the ellipsoid is embedded in the surrounding artificial anatomy. There, the sensitivity of the optimal probe placement with respect to variations in σ (left) is visualized. We see that the cigar-shaped ellipsoid is aligned with the linear vessel.

However, as mentioned earlier, an interpretation of this results must be done with care since a high sensitivity of the optimal probe position (as seen here) can also be

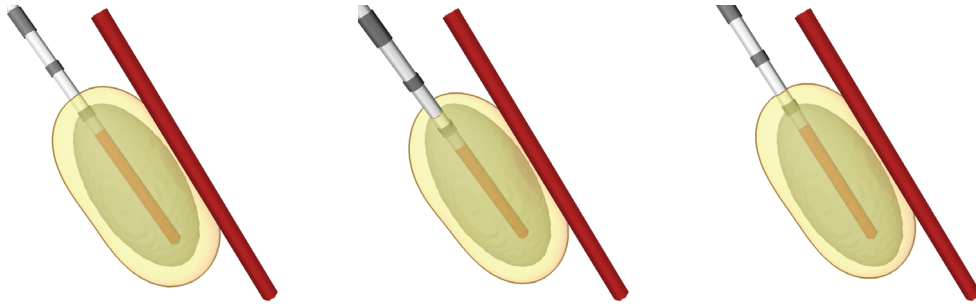


Figure 4.4: The 60°C iso-surface of the temperature is shown for the optimal probe placement obtained in collocation point 5 (left), collocation point 16 (middle) and collocation point 23 (right) of the sensitivity analysis of the probe placement w.r.t. uncertainties in σ . In all three cases the lesion is ablated completely.

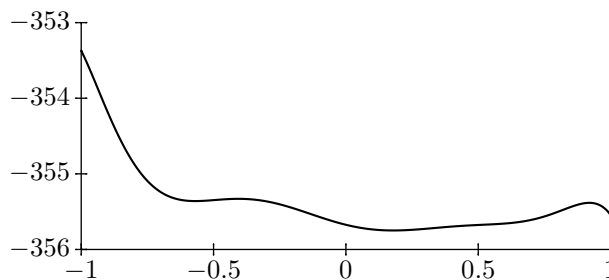


Figure 4.5: Approximation of the graph of the objective function $f(x)$ where the position x varies along the eigenvector corresponding to the largest eigenvalue of the covariance matrix (longest principal axis of the ellipsoid).

the result of a flat energy graph of the objective function f (cf. Sect. 4.4, p. 67). In such a case, not only variations in the tissue parameters, but also small changes in e.g. the numerical settings can influence the optimal probe location strongly. In fact, the situation of the artificial scenario induces such a false sensitivity. The reason is that the same fraction of the lesion can be ablated for many different placements of the probe. Thus, for many different probe locations, the value of the objective function is very similar. The energy graph of the objective function is flat and the minima found by the optimizer for different realizations of the material parameters can be far apart from each other. Indeed, as shown in Fig. 4.4 there are different placements which allow for a complete ablation of the ellipsoidal shaped lesion in the artificial example.

In order to differentiate between these two cases, and to detect false sensitivities, one can e.g. analyze the values of the objective function f . In Fig. 4.5 (left) a one-dimensional interpolation of the energy in direction of the largest eigenvalue of the covariance-matrix (i. e. in direction of the largest principal axis of the ellipsoid) is depicted. This interpolation is obtained by the same means as the approximation of the stochastic processes: Here, a one-dimensional collocation table with approximation order $k = 3$ containing 9 collocation points has been used. At these points

the energy f was evaluated for a probe location and material parameters which lie central in the PDF. Indeed, Fig. 4.5 (left) shows a relatively flat graph and just relatively small variations of the objective function's value. Thus the strong sensitivity shown by the PDF and the ellipsoidal representation of the covariance matrix in Figs. 4.2 and 4.3 (left) may be due to an insensitivity of the objective function w.r.t. the probe location. Hence, as seen here for the artificial scenario, the local graph of the objective function is a useful tool for evaluating sensitivity distributions.

Sensitivity of the Optimal Probe Orientation

The visualization of the PDFs of the optimal probe orientation is much easier, since the orientation lies on the two dimensional sphere S^2 . In Fig. 4.3 (right) a PDF of the optimal probe orientation is shown by a color coding of the sphere. Also for the probe orientation, a false sensitivity can be caused by an insensitivity of the objective function w.r.t. rotations of the probe (e. g. spherical lesion with no vascular structures). Again, an analysis of the local behavior of the energy graph can help to rule those cases out.

4.7.2 Real RF Scenario

In the second part of the evaluation we consider the real RF ablation case which we already know from Sects. 3.5 and 3.8. Here, the computational domain D has the same size and is discretized by the same grids as in Sect. 3.8 (i. e. $120.6 \times 79.9 \times 79.9$ [mm³] ROI-size, $154 \times 102 \times 102$ fine-grid cells and $77 \times 51 \times 51$, respectively $38 \times 25 \times 25$ cells of coarser grids). Also the modeling of the perfusion and the generator settings are the same as in Sect. 3.8 (i. e. $\nu_{\text{cap}} = 0.006067 \text{ s}^{-1}$, $\nu_{\text{vessel}} = 0.05 \text{ s}^{-1}$, $\rho_{\text{blood}} = 1059.0 \text{ kg/m}^3$ and $c_{\text{blood}} = 3850.0 \text{ J/kgK}$, as well as $R_{\text{I}} = 80 \Omega$ and $P_{\text{setup}} = 200 \text{ W}$). As in the artificial scenario, we consider a monopolar probe of radius 1.2 mm and an electrode length of 25 mm. The initial probe position is located at (40.3, 20.0, 20.0) mm distance from the center of D and its orientation is $d = (5, 2, 3)$, normalized to length 1.

Sensitivity of the Optimal Probe Location

In Fig. 4.6 the sensitivity of the optimal probe location w.r.t. variations in the material parameters is shown. As before the visualization of the ellipsoidal representations of the covariance matrix is embedded in the surrounding anatomy of the patient. Again, the ellipsoids are magnified by a factor of 10 for reasons of better visibility.

From left to right the images of Fig. 4.6 display this approximation of the PDF of the optimal probe location (cf. Sect. 4.4.3) w.r.t. variations in λ (i. e. σ is fixed at the midpoints of the intervals given on p. 72), w.r.t. variations in σ (i. e. λ is fixed at the interval midpoints) and w.r.t. variations in both parameters simultaneously.

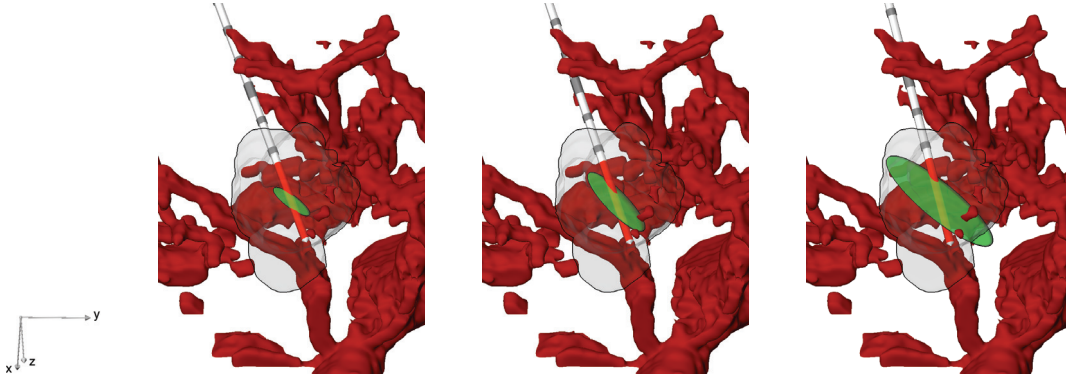


Figure 4.6: Visualization of the sensitivity of the optimal probe position through an ellipsoidal representation of the covariance matrix. The sensitivity with respect to the thermal conductivity λ (left), the electric conductivity σ (middle), and both parameters (right), yield by a collocation on level $k = 2$ and scaled by a factor of 10, is shown. The RF probe is drawn at the mean of the placement's distribution. The segmented vascular system D_v is shown in red and the segmented lesion D_t is shown in transparent gray.

Table 4.2: Eigenvalues of covariance matrices for the PDF of the probe location for the real RF scenario (values given in millimeters).

all	$3.866 \cdot 10^{-3}$	$3.669 \cdot 10^{-4}$	$1.084 \cdot 10^{-4}$
λ	$4.131 \cdot 10^{-4}$	$6.008 \cdot 10^{-5}$	$2.481 \cdot 10^{-5}$
σ	$1.373 \cdot 10^{-3}$	$2.402 \cdot 10^{-4}$	$2.861 \cdot 10^{-5}$
λ_n	$1.062 \cdot 10^{-4}$	$3.586 \cdot 10^{-6}$	$6.005 \cdot 10^{-7}$
λ_v ($4.178 \cdot 10^{-4}$)	$1.446 \cdot 10^{-5}$	$7.469 \cdot 10^{-9}$	
λ_t ($8.372 \cdot 10^{-5}$)	$1.468 \cdot 10^{-5}$	$9.784 \cdot 10^{-7}$	
σ_n	$1.898 \cdot 10^{-4}$	$1.560 \cdot 10^{-5}$	$6.210 \cdot 10^{-8}$
σ_v	$2.017 \cdot 10^{-4}$	$2.016 \cdot 10^{-5}$	$2.194 \cdot 10^{-6}$
σ_t ($5.916 \cdot 10^{-4}$)	$1.270 \cdot 10^{-5}$	$6.832 \cdot 10^{-7}$	

All ellipsoids are cigar-shaped. Moreover, with this configuration we see a stronger dependence on the electrical conductivity σ than on the thermal conductivity λ . This observation corresponds to the intuition since σ influences the system much more in terms of the energy source and the effective generator power (cf. Sect. 4.2, Eq. (4.4) and (4.5)). Indeed this is not a proof for the stronger dependence on σ , yet (because in theory the results might change, if the constant parameter λ is fixed at a point of the interval different from the midpoint), but the results in Fig. 4.6 at least show a tendency in this direction.

The eigenvalues of the covariance matrices w.r.t. all material parameters, w.r.t. solely λ and σ as well as w.r.t. variations in their single components $\sigma_{n,v,t}$, $\lambda_{n,v,t}$ are shown in Table 4.2. From the table we see that the largest dependences are w.r.t. the

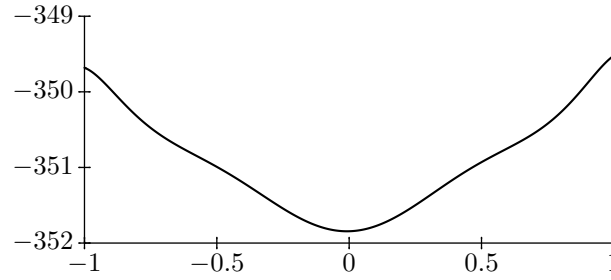


Figure 4.7: Approximation of the energy graph of the objective function $f(x)$ where the position x varies along the eigenvector corresponding to the largest eigenvalue of the covariance matrix (longest principal axis of the ellipsoid).

thermal conductivity of the vascular system λ_v and w.r.t. the electric conductivity of the lesion σ_t . These observations again coincide with the intuition: Firstly, the electric conductivity σ_t of the lesion influences the heat source and the application of energy. Secondly, the thermal conductivity λ_v influences the heat sinks. As we see from the table and from Fig. 4.6 the sum of the eigenvalues of the covariance matrices for all σ components leads to a higher variation than we obtain in the sum for all λ components. Note that although these observations match our intuition, they may change for a model which takes into account the nonlinear dependence of the material parameters on the temperature and the water content of the tissue.

The cigar-shaped ellipsoids shown in Fig. 4.6 mean that the optimal location varies mainly in the direction of the large principal axis of the ellipsoid. Again, as for the artificial scenario, one must test for a false sensitivity by a local analysis of the energy. From Fig. 4.7 we see that for the real RF ablation case, the graph is not flat and that the range of the values attained is much wider. Thus, it can be concluded that a real strong dependence of the probe location w.r.t. the material parameters is present.

The shape and the orientation of the ellipsoids shown in Fig. 4.6 can be explained by the local vascular structure. In fact, the ellipsoids are aligned with the prominent direction of the vessels (in the images from bottom right to top left) in the vicinity of the lesion. Further note, that the ellipsoid related to variations in the thermal conductivity λ is aligned better with the nearby vessel than the ellipsoid related to variations in the electrical conductivity σ . In Fig. 4.8, two zoomed views of the vessels next to the tumor lesion are depicted. Here, the prominent direction of these vessels can be seen very clearly.

From Fig. 4.9 we see that indeed there exist material parameter settings for which a complete ablation of the tumor is not achieved. This further motivates the consideration of the material parameter uncertainty for the planning of RF ablation.

Finally, from the histograms in Fig. 4.10 showing the one-dimensional PDFs of the probe locations evaluated along the three principal axes of the corresponding ellipsoids, we find that the combined uncertainty in both material parameters can result in probe locations which are about 6 mm apart – a deviation which indeed is

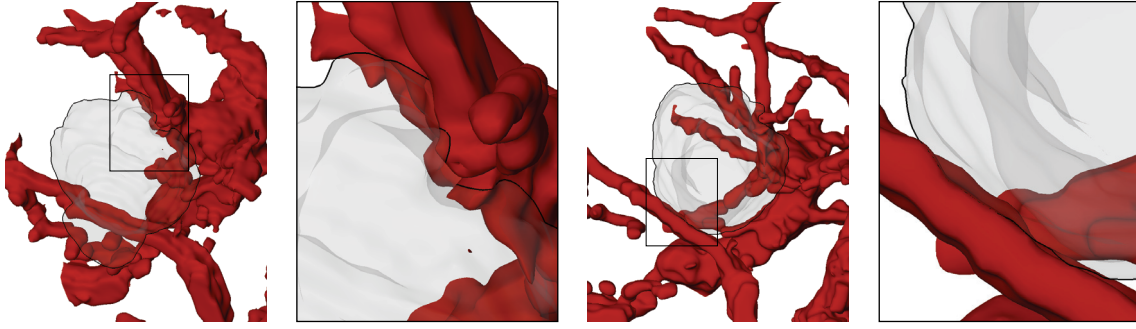


Figure 4.8: Two different views of the tumor’s surface close to the vessels, together with a zoomed view of the framed area, where tumor and vessel are directly neighboring. Note, that for better visibility in all these figures, the front vessel has been pruned.

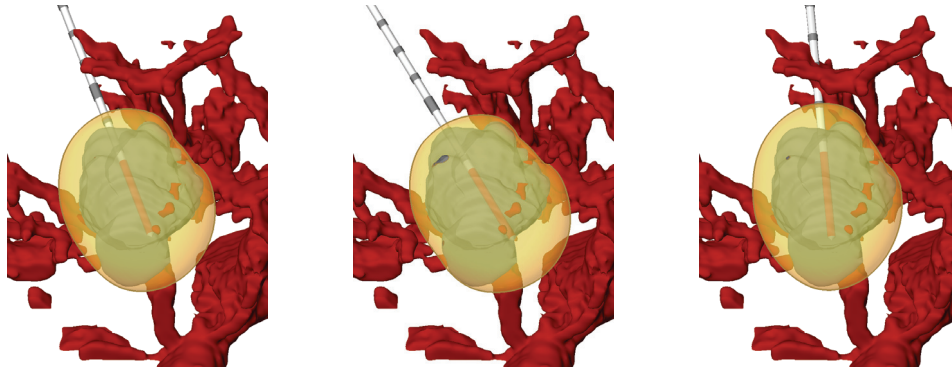


Figure 4.9: The 60°C iso-surface of the temperature is shown for the optimal probe placement obtained in node 60 (left), node 38 (middle) and node 14 (right) of the sensitivity analysis of the probe location w.r.t. uncertainties in λ and σ , performed with collocation on level $k = 2$. As can be seen in the figure, the shown temperature iso-surfaces for these parameter settings do not always destroy the lesion completely.

relevant in praxis.

As described in Sect. 4.4.1 we can evaluate the local sensitivity of the probe placement with derivatives of the polynomial approximations of the stochastic process. In Table 4.3 the values of the derivatives of the process describing the optimal probe location w.r.t. the stochastic quantities are shown. These values show the local strength of the dependence of the probe location on the material parameters. However, these data are of theoretical interest only, since for a specific patient the actual material parameters are unknown.

In Fig. 4.11 the sensitivity of the model with respect to σ is depicted, and the results for the collocation levels $k = 1, \dots, 4$ are compared. The ellipsoidal representations of the covariances of the distribution increase up to the finest level of approximation $k = 4$. This lack of convergence can be attributed to two different observations:

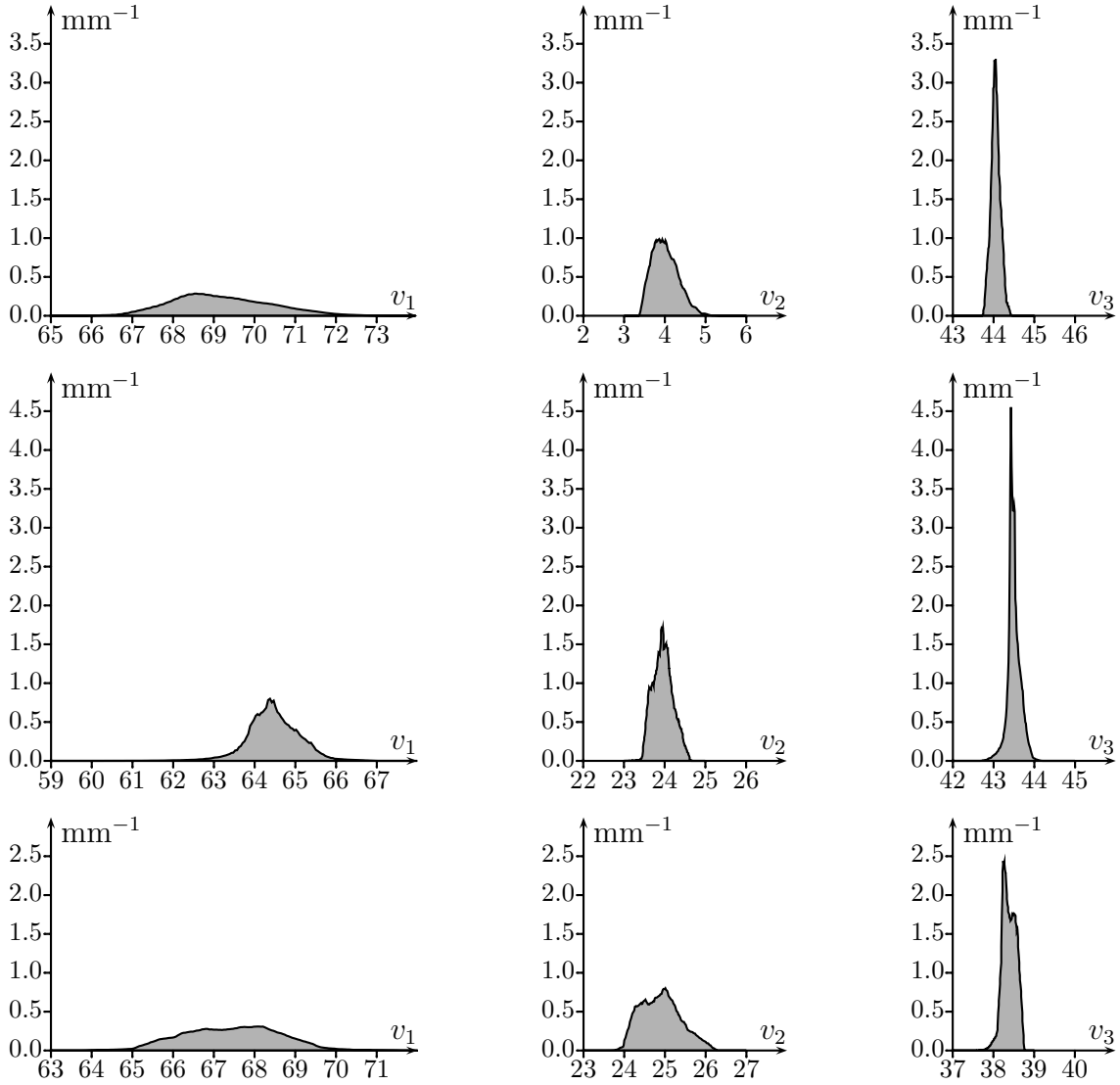


Figure 4.10: One-dimensional PDFs of the optimal probe locations along the three principal axes v_1 , v_2 , and v_3 [mm] of the covariances. PDFs are shown for variations w.r.t. all material parameters (top row), w.r.t. λ (middle row) and w.r.t. σ (bottom row).

- The stochastic process under consideration or the underlying numerics (for solving the optimization problem) may have a lower order of smoothness than supposed by the corresponding polynomial approximation for the respective level k . Indeed, increasing k also tacitly implies assuming a higher level of smoothness of the process.
- Bifurcations of the stochastic process may exist which lead to outliers in the stochastic collocation samples used. This issue is also related to the fact that for certain configurations of lesion, vascular system, probe, and generator the energy graph may be flat as discussed for the artificial scenario. Moreover, in

Table 4.3: Sensitivities of the probe position with respect to the six stochastic quantities. The derivatives are evaluated at the midpoint of the hyper-cuboid in the stochastic space. The values are given in the respective SI units.

	$\frac{\partial}{\partial \lambda_n}$	$\frac{\partial}{\partial \lambda_v}$	$\frac{\partial}{\partial \lambda_t}$	$\frac{\partial}{\partial \sigma_n}$	$\frac{\partial}{\partial \sigma_v}$	$\frac{\partial}{\partial \sigma_t}$
p_x	$1.180 \cdot 10^{-3}$	$1.620 \cdot 10^{-2}$	$1.168 \cdot 10^{-3}$	$-2.442 \cdot 10^{-3}$	$-7.087 \cdot 10^{-3}$	$-2.564 \cdot 10^{-3}$
p_y	$9.109 \cdot 10^{-3}$	$2.133 \cdot 10^{-2}$	$5.685 \cdot 10^{-3}$	$-4.160 \cdot 10^{-3}$	$-3.062 \cdot 10^{-3}$	$-8.196 \cdot 10^{-3}$
p_z	$4.181 \cdot 10^{-3}$	$-2.932 \cdot 10^{-3}$	$3.414 \cdot 10^{-3}$	$8.519 \cdot 10^{-5}$	$-1.512 \cdot 10^{-3}$	$-1.651 \cdot 10^{-2}$

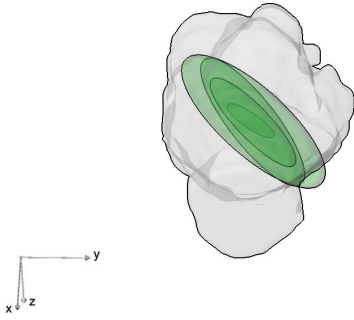


Figure 4.11: The sensitivities of the optimal probe position with respect to the electric conductivity σ yield by a collocation on level $k = 1$ (inner ellipsoid), $k = 2$, $k = 3$ and $k = 4$ (outer ellipsoid) are compared. Here as in Fig. 4.6 the tumor is shown in a transparent gray color.

the experiments an extreme sensitivity of the results to the stopping criteria of the numerical solvers is noticed (i. e. discretization errors can be mimicked as stochasticity). This situation is also considered by Kaipio and Somersalo in [48] (cf. Sect. 4.4; last comment).

To obtain a better approximation of the stochastic process, in an ongoing work a different collocation approach using piecewise multilinear functions instead of polynomials for the stochastic interpolation, is investigated (see also Sect. 4.8). Again (as typical for the stochastic collocation) one obtains a sparse grid in the stochastic domain which additionally is adaptively refined in critical stochastic regions.

From the current results it can be concluded that using the collocation level $k = 2$ apparently leads to an underestimation of the true variance. Further, having in mind that realistic measurement errors of 10% or more are not considered for the ranges of material parameters used here, it can be expected that the real variance will be even larger.

Sensitivity of the Optimal Probe Orientation

As for the artificial scenario (cf. Sect. 4.7.1, Fig. 4.3, right), in Fig. 4.12 the sensitivity of the optimal probe orientation \bar{d} is analyzed through a color coding of the sphere. These images confirm our observation from the analysis of the optimal probe location: The dependence on σ seems to be stronger than the dependence on λ since

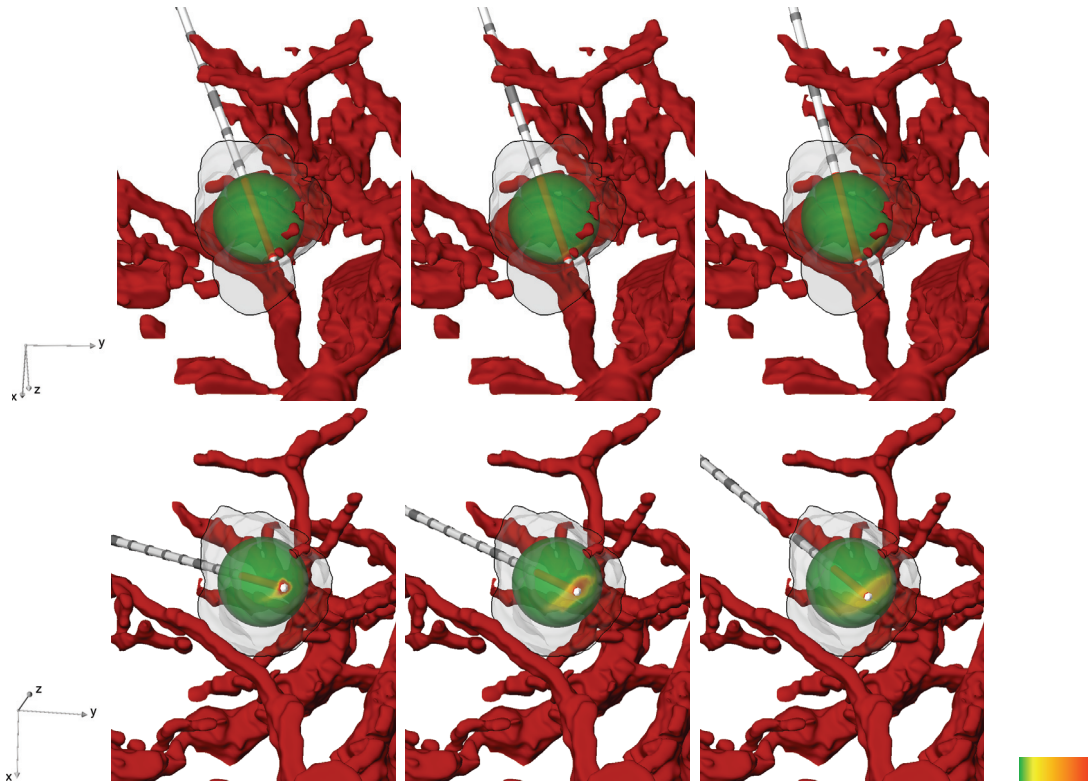


Figure 4.12: The sensitivity of the optimal probe orientation with respect to variations in the heat conductivity λ (left), the electric conductivity σ (middle), and both material parameters (right) is shown. As in the artificial example (see Fig. 4.3), the PDFs of the corresponding distributions of the optimal probe orientation are visualized by a coloring of the sphere. Again, green colors indicate unlikely orientations, whereas red colors show likely orientations (see color ramp on the right). The top row and the bottom row show two different viewpoints on the scene. The RF probe is drawn at the mean of the placement's distribution.

the PDF for σ is more elongated. Again, this is likely due to the nonlinear influence of the electric conductivity through the resistance of the tissue and its effect on the generator. Moreover, for varying thermal and electric conductivity the PDF shows that a rotation of the RF probe of up to 30 degrees is possible.

4.7.3 Probe Placement for Expected Maximal Volume of Destroyed Tumor Tissue

In the following considerations the focus is on the optimization of the probe placement, such that from the result a maximum volume of destroyed tumor tissue can be expected. In Fig. 4.13 the results of the multi-scale optimization are shown together with the achieved temperature profile. The optimal probe position lies in the center of the tumor, and its optimal orientation adapts to the shape of the tumor.

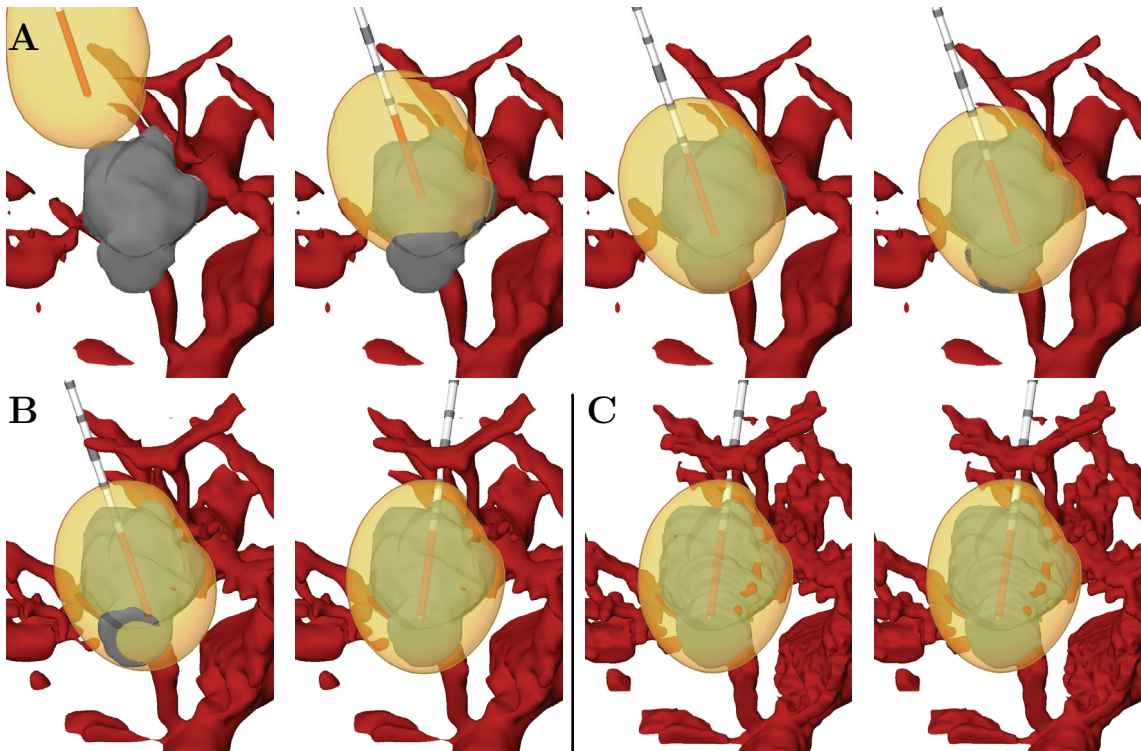


Figure 4.13: The optimization of the position and direction of a mono-polar probe is shown. The 60°C iso-surface of the expectation of the temperature distribution is depicted in a transparent yellow color. The vascular structure D_v is shown in red and the tumor domain D_t is shown in gray. **A:** Steps 0 (start), 1, 2 and 13 of the 1st pre-optimization (coarsest grid). **B:** Steps 0 and 12 of the 2nd pre-optimization. **C:** Steps 0 and 11 (end) of the main optimization.

Moreover, the 60°C iso-surface of the expected temperature distribution completely encloses the segmented lesion.

In addition, we see that the multi-scale character of the optimization algorithm finds a good probe placement already on a coarse level. In our example the optimal positioning found after the pre-optimization (see Fig. 4.13 (B)) does not differ much from the final optimal probe positioning found on the finest grid.

The progression of the energy defined by the objective function (4.13) is displayed in Fig. 4.14. The transitions between different grid levels are marked in the energy plot. At these stages of the algorithm the probe placement $u \in U$ which has been found on a coarse level is re-interpreted on the finer grid. Since the volume of the lesion is not exactly conserved on coarse grid levels, the energy jumps at the transition points in the graph (cf. Fig. 3.14 in Sect. 3.7). Note that as discussed above, in this example the solution of the pre-optimization already yields good probe parameters. This is also visible from the energy plot, since there is almost no decay of the energy during the last fine grid iterations.

For reasons of comparison, the optimization of the probe placement for the deter-

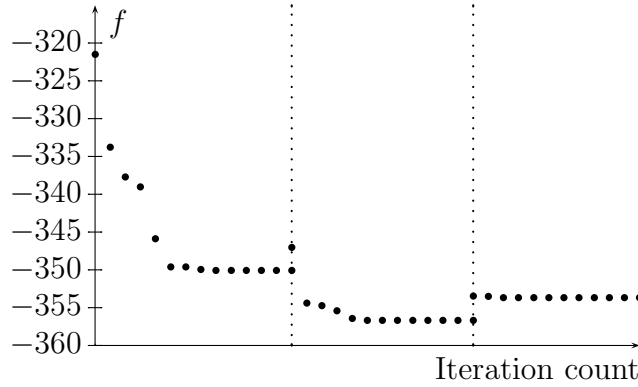


Figure 4.14: For the optimization of the probe placement with the stochastic multi-scale algorithm shown in Fig. 4.13 the decay of the energy is displayed. The transitions between different grids are marked with vertical dotted lines.

ministic model with parameters set at the mean of their distributions has also been performed. As we can see from the left images of Fig. 4.15 (compared to Fig. 4.13) the optimal probe placement for the deterministic model differs considerably from the optimal probe placement for the stochastic model, i.e. from the probe placement yielding a maximal expected tumor destruction (about 30.4° difference in the probes' orientations). This is an indication for the strength of the nonlinearity of our PDE model for the simulation of RF ablation. In the right image of Fig. 4.15 we see the expected optimal probe positioning, derived from the optimal probe placements for each stochastic collocation point of level $k = 1$. Although this probe positioning appears similar to the one obtained for the deterministic model, the orientations differ by an angle of about 12.6° .

4.8 Conclusions and Discussion

A model for the optimization of the placement of monopolar probes taking into account the uncertainty associated with electric and thermal conductivities of the tissue has been derived. In this model the material parameters are considered to be probabilistically distributed. Together with a stochastic collocation method the approach allows to evaluate the sensitivity of the results with respect to variations in the material parameters. Moreover, a stochastic objective function which involves the expectation of a deterministic objective function has been considered. Minimizing the stochastic objective function yields a probe placement for which a maximum volume of destroyed tissue can be expected. It has been shown that when taking the stochastic collocation approach into account very few modifications to an existing deterministic optimization code must be made to generalize it to the stochastic setting. In each step of the stochastic optimization the forward problem as well as the adjoint problem must be solved for every collocation point. Then, in an intermedi-

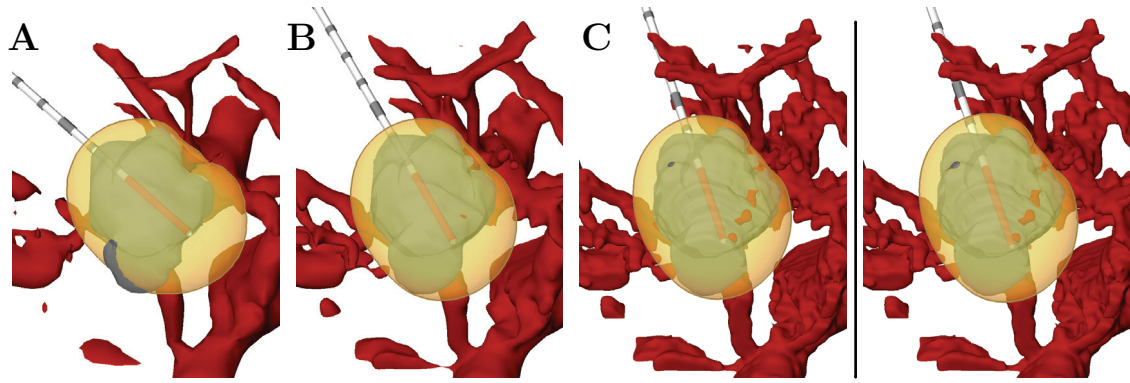


Figure 4.15: Left: The optimization of the probe placement for the deterministic model is shown. Again the 60°C iso-surface of the temperature distribution is depicted in a transparent yellow color. The vessel system D_v and tumor D_t are the same as in Fig.4.13. **A:** Step 11 (end) of the 1st pre-optimization. **B:** Step 10 (end) of the 2nd pre-optimization. **C:** Step 16 (end) of the main optimization. Right: Expected optimal probe placement, yield by a collocation on level $k = 1$, with corresponding 60°C iso-surface of the temperature.

ate step, all descent directions are combined to yield the expected descent direction. A step size control in the fashion of Armijo's algorithm leads to the update of the current iterate. Since the state and the adjoint state must be computed for every collocation point, the numerical effort can be estimated by the effort of the deterministic algorithm times the number of collocation points. An acceleration through a parallelization of the code is straightforward, since it requires only a very small amount of inter-process communication.

The numerical results which have been presented, are based on an artificial scenario as well as on a segmented lesion and vascular structures from a real CT scan (cf. Sects. 3.5 and 3.8). Because vector-valued data is optimized (probe location and probe orientation) a visualization of the resulting distributions is not straightforward. For the visualization of the distribution of the optimal probe location different approaches have been presented (see also [55]). Since a three-dimensional volume rendering of the histograms is difficult to interpret, an ellipsoidal representation is used, which easily reveals the mean and the covariance of the distribution. Also the one-dimensional PDFs of the distribution along the principal axes of its covariance ellipsoid have been shown. A visualization of the distribution of the optimal probe orientation is much simpler. Here a color coding of the sphere according to the one-dimensional PDF is used.

An interpretation of the resulting distributions must be done with care, since the anatomical configuration in combination with the involved objective function can induce a false sensitivity. In the artificial scenario with an ellipsoidal lesion and a linear vessel such a false sensitivity is produced because there exist many probe locations which allow for a complete destruction of the lesion. To detect these misleading results, a local analysis of the energy graph of the objective function has

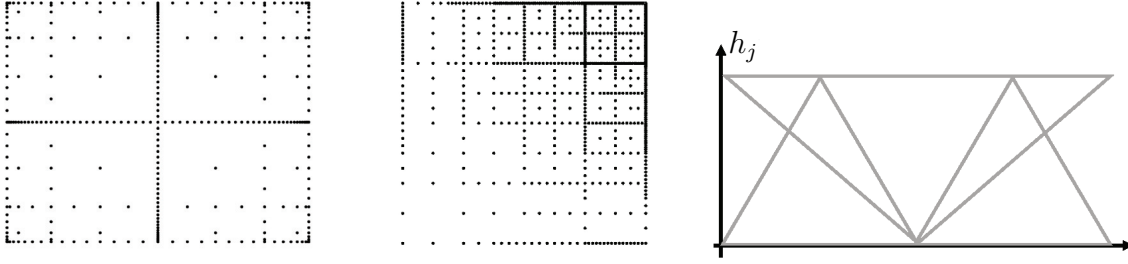


Figure 4.16: Left: Distribution of nodes obtained with the Smolyak algorithm (i. e. at the extreme values of the Chebychev polynomials which are well suited for polynomial interpolation). Middle: Uniform, adaptive distribution of nodes for the stochastic interpolation with piecewise multilinear, hierarchical basis functions Right: First five piecewise linear basis functions h_j for the interpolation approximation of the random field $f(\boldsymbol{\xi}) \approx \sum_{j=1}^q f(\boldsymbol{\xi}_j)h_j(\boldsymbol{\xi})$ (cf. Sect.4.3).

been performed.

The numerical experiments for the real RF ablation scenario show that both the sensitivity with respect to variations in the thermal conductivity λ and the sensitivity with respect to variations in the electrical conductivity σ , are aligned with the structure of the local vascular system. However, this alignment is stronger for the thermal conductivity than for the electrical conductivity. For the model a stronger sensitivity w.r.t. variations in the electric conductivity than w.r.t. variations in the thermal conductivity has been noticed: Under variations of the electric conductivity the results show changes in the optimal probe location up to 6 mm. In contrast to that, under variations of the thermal conductivity the largest variation is up to 3 mm. Further, the optimal probe orientation shows a stronger variation of up to 30° under uncertainties in the electric conductivity than it exhibits under variations in the thermal conductivity ($\ll 30^\circ$). Although this is not a final proof for a stronger dependence on σ , yet (since theoretically the results might change if the nonlinear dependence of the material parameters on the temperature and the water content of the tissue are modeled), but nevertheless it shows a considerable and clear tendency.

In the case of the real RF ablation scenario, the investigations show that the resulting stochastic process steering the optimal probe location and/or the underlying numerics for solving the optimization problem have a low level of smoothness. To obtain a better approximation of the stochastic process, in an ongoing work the application of piecewise multilinear Ansatz-functions for the interpolation in the stochastic space is considered. Again (as characteristic of stochastic collocation approaches) we have a sparse grid in the stochastic domain which additionally is adaptively refined in critical stochastic regions (see Fig. 4.16).

Besides of the sensitivity analysis, for the real RF ablation scenario, the optimization of the probe placement for which an optimal destruction of the lesion is expected, has been shown. The multi-scale character of the approach allows for a fast pre-optimization of the probe placement on coarse grid levels (cf. Sect. 3.8).

From the example considered here we see that the pre-optimization already gives good placements which could be improved marginally only on the finest grid level. A comparison of the expected optimal probe placement with the result found by the deterministic optimization algorithm applied to the expected material parameters shows a significant difference of about 30° in the probe's orientation.

Note, that the optimization of the placement of one monopolar probe presented here, easily generalizes to an optimization of the placement of a cluster of probes (again cf. Sect.3.8). Also the study of treatment by bi-polar probes, multi-polar probes, or umbrella-type probes is possible with this framework. In addition, the approach presented here can be used for many other models in medical simulation including cryosurgery or irreversible electroporation as well. In particular for complicated nonlinear models for which a theoretical sensitivity analysis is cumbersome or even infeasible, this approach is attractive.

With the numerical experiments considered here, it has been demonstrated that this approach allows to quantify the robustness of simulation results with respect to the uncertainty involved in the model parameters. In this sense these investigations can sensitize the user (i. e. a radiologist, surgeon, medical doctor) to use simulation results which are based on uncertain parameters with care. In the real RF ablation case shown in the last section, the attending physician can consider the uncertainty for the planning of the therapy. To guarantee a therapeutic success he may e. g. decide to use two probes to limit the influence of the large sensitivity of the optimal probe placement w.r.t. the unknown material parameters of the specific patient.

With these investigations a step towards patient-specific modeling in the field of medical simulation has been performed – here applied to the optimization of RF ablation. The problem of patient-specific parameters by trying to obtain more accurate material parameters, is not tackled here. Instead uncertainty is considered to be an intrinsic attribute of the modeling process. Moreover, the considered algorithms have been adjusted such that the best result possible is expected. Clearly, the expected best result is not characteristic for a specific patient, i. e. the investigations in this area must be seen as preliminary steps towards an optimization of the confidence for the success of the therapy which belongs to the ongoing work. Moreover, in practice one cannot expect the material parameters to be uniformly distributed. Thus, the following modifications are thinkable for future investigations:

- A first possibility is to analyze experimental results to obtain a first idea of the stochastic probability distribution of the tissue parameters. Additionally, a parameter identification by solving the inverse problem (see [82]) can help to get an impression of how the material parameters are stochastically distributed within the respective intervals. After having detected an appropriate stochastic distribution of the tissue parameters, then the current modeling of a uniform distribution easily can be replaced within the optimization model.
- A different approach is to model the tissue properties as fuzzy parameters for which the stochastic distribution is unknown (see [66]). Moreover, after

having determined the nodes in the stochastic space and having solved the forward problem for many different probe placements and realisations of tissue parameters, one can generate a “response surface approximation” (RSA), i. e. an approximation of the objective functional as function of the design parameters (which are the probe position and orientation) and the fuzzy parameters (which are the tissue properties). Such an approximation can be obtained by using e. g. piecewise multilinear Ansatz-functions as explained above. Then a “fuzzy reliability based design optimization” (FRBDO), i. e. an optimization of the design parameters that minimize e. g. the fuzzy probability of failure (FPF) can be performed on the RSA quite fast. In addition to one single optimal probe positioning, a final cluster analysis would yield optimal design subspaces which might compensate a slight deviation from the optimal needle insertion (due to the fact that in practice an accuracy up to millimeters hardly can be achieved).

Future investigations moreover might deal with the optimization of RF ablation under a refined time-dependent model for the simulation, such that the nonlinear dependence of the material parameters on the state of the system can be taken into account as well. Also, the consideration of the perfusion coefficients as sources of uncertainty is a promising further direction of research.

5 Fast Estimation of the Heat Sink Effect of Large Blood Vessels

5.1 Problem Formulation

A known difficulty in radio-frequency ablation is the cooling influence of large blood vessels. More precisely, close to large vessels the desired temperature increase is limited due to the relatively low temperature of the blood. Therefore, a consideration of the local vascular structures close to the tumor lesion is indispensable to assert a successful treatment.

Currently, radiologists and surgeons rely on their experience to judge how close they have to place the RF probe to large vessels to be able to destroy a certain region of a nearby lying tumor. Hence, inexperienced radiologists might try to insert the RF probe into the center of the tumor, so that tumor regions near large blood vessels might not be destroyed. Moreover, when taking only a fast look through the single layers of a CT-scan, even for experienced radiologists it is hard to identify just the distances between the tumors and the vessels. This in particular motivates the need for a computerized support for the planning of RF ablations. Hence, in this chapter a method that enables for a fast calculation of the cooling effect of large blood vessels and its impact on RF ablation is developed. More precisely, the aim is to compute for each point of a tumor lying near to large vessels, maximal distances an RF probe may have to these vessels in order to enable the emerging heat to destroy the tumor point under consideration.

The main idea of the approach considered here, is to efficiently estimate the heat sink effect of large blood vessels by means of repeated precalculations of the forward simulation and tabulation of the results. In more detail, the approach is based on a precomputation of various so-called “criticality tubes” of vital tissue, which for a certain vessel radius and distance of the applied RF probe to the vessel, describe the largest region around the vessel inside of which the tissue cannot be heated up to a fixed critical temperature which is needed for tumor destruction. Starting from the Bioheat-Transfer-Equation (cf. e.g. (2.5a)), mainly two steps of dimensional reduction are performed to calculate the temperature distribution of the tissue (which is needed to compute the criticality tubes) as fast as possible and, at the same time, as accurate as necessary. With help of the precalculation results (i. e. with help of the criticality tubes) then the maximal distances between the RF probe and large vessels can be determined very fast by a function inversion (see Sect. 5.2, Fig. 5.7).

The calculation results, i. e. the maximum allowable distances between the RF probe and large vessels, are visualized through a color coding of the tumors. Moreover, the corresponding criticality tubes of vital tissue are visualized by transparent tubes around the respective vessels. Such a visualization shall help the radiologist to estimate how close he has to place the RF probe to large blood vessels in order to destroy a nearby lying tumor, or (if the required probe-vessel distance cannot be achieved in practice) to decide, if additional steps that yield a more advantageous situation (as e. g. a pringle manoeuvre or a chemoembolization), should be performed.

The cooling influence of large blood vessels to RF ablation has been investigated by several authors [23, 95, 22, 44, 77, 30, 6]. These approaches range from complex models considering thermal equilibration effects (e. g. [23]) up to simple distance measurements between tumors and vessels (e. g. [95]). The main advantage of the approach considered here, is that after having calculated all patient-independent data in advance, the heat sink effects for the individual patient, i. e. for a certain tumor-vessel configuration can be estimated very fast. Moreover, compared to a simple distance measurement this approach additionally interprets the distances between tumors and vessels in terms of achievable coagulation zones depending on the distance of the applied RF probe to the vessel of interest.

In the following, details of the numerical implementation and the application to a real ablation scenario are presented. More precisely, the next sections are organized as follows: In Sect. 5.2 the dimensional reduction of the Bioheat-Transfer-Equation and all steps of the precalculation yielding the criticality tubes of vital tissue around large vessels, as well as the determination of the maximal probe-vessel distances are described. In Sect. 5.3 the model firstly developed for a sample configuration of an infinitely long linear vessel (or more precisely a vessel segment), is combined to a model for full vascular trees. Finally in Sect. 5.4, results for the application of the model to real patient data are shown, followed by conclusions and several ideas for future work presented in Sect. 5.5.

5.2 Mathematical Modeling

The main idea of the following explanation is the consideration of the heat equation from a different point of view: Instead of the heat originating from the probe, now the cooling effects originating from large blood vessels (of diameter $d > 3$ mm), are in the focus of our investigations (see Fig. 5.1). Vessels of diameter $d \leq 3$ mm are likely to coagulate during the RF ablation and thus are assumed to have no significant thermal impact.

As already mentioned in the previous section, here the aim is to efficiently calculate and visualize the cooling effect of large blood vessels and its influence on RF ablation. More precisely, for arbitrary tumor regions the aim is to compute the maximal distance d_{\max} an RF probe may have to large vessels in order to enable the emerging heat to destroy the particular tumor region under consideration.

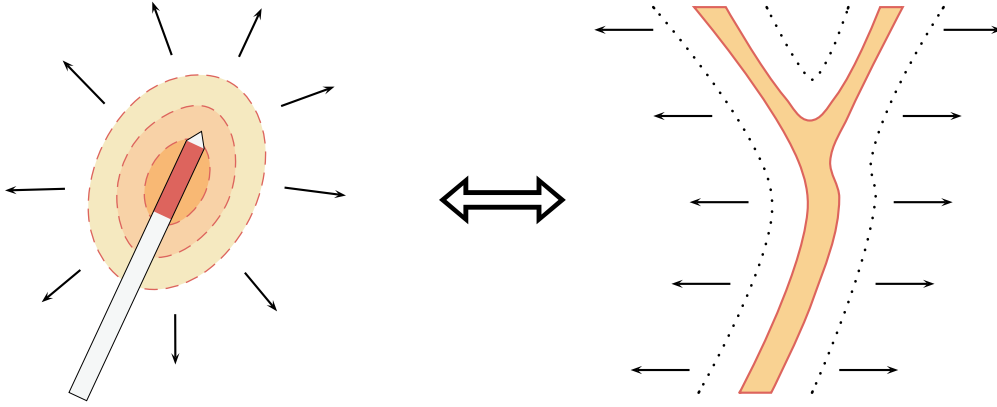


Figure 5.1: Change of the perspective in considering the heat equation. Left: Previous perspective, i. e. propagation of heat from the probe into the surrounding tissue. Right: New perspective, i. e. propagation of the cooling effects from a blood vessel into the tissue.

Unfortunately, the calculation of such a value for the maximal distance d_{\max} between the RF probe and large vessels (which has to be determined for each point of the tumor) cannot be performed analytically. Hence, as initial step, the temperature profile around each vessel, or more precisely, the thickness d_{vt} of a vessel surrounding tube of vital tissue, is calculated in advance depending on the corresponding vessel radius R_{bv} and distance d between the RF probe and the respective vessel. Thereby, the tissue is considered to be vital, if the tissue temperature stays below a certain critical temperature T_{crit} which here is assumed to be fixed at 50°C . An idea for future work is to model the critical temperature as additional parameter.

To be able to calculate the thicknesses d_{vt} of the vessel surrounding tubes of vital tissue as fast as possible, the complexity of the model, i. e. of the temperature equation, can be reduced by the following steps:

Steady state of the temperature equation: Since here, the dynamics of the temperature propagation are only of minor interest, like in the previous sections, the time dependence of the temperature equation is neglected. Instead it is assumed that the RF ablation is performed until the steady state of the heat distribution is reached. Moreover, for the time being let us consider only one single vessel $V = V(R_{\text{bv}}) \subset D$ of vessel radius R_{bv} (here, as in the previous chapters, $D \subset \mathbb{R}^3$ is a three-dimensional cuboid modeling the computational domain). Later (in Sect. 5.3) the results for this single-vessel-model are applied to the branches of a complex vascular tree.¹ Hence, the following calculations are performed with the steady state heat function $T : \mathbb{R}^+ \times \mathbb{R}^+ \rightarrow H^1(D)$, $(R_{\text{bv}}, d) \mapsto T(R_{\text{bv}}, d)$, such that $T(R_{\text{bv}}, d)$ solves the partial differential equation

$$-\lambda \Delta u(R_{\text{bv}}, d)(\vec{x}) = Q_{\text{rf}}(d)(\vec{x}) + Q_{\text{perf}}(\vec{x}) \quad \text{in } D \setminus V(R_{\text{bv}})$$

¹In Sect. 5.3, also a formal definition of a single vessel V , or more precisely a vessel segment V_i can be found.

(cf. (2.17)), with Dirichlet boundary condition

$$u(R_{\text{bv}}, d)(\vec{x}) = T_{\text{body}} \quad \text{on } \partial V(R_{\text{bv}}) ,$$

i. e. on the boundary of the vessel, and Neumann boundary condition

$$n \cdot \nabla u(R_{\text{bv}}, d)(\vec{x}) = 0 \quad \text{on } \Gamma_{\text{out}} ,$$

i. e. on the outer boundary of the computational domain D . As in Sect. 2.2, p. 10, here n denotes the outer normal of Γ_{out} . Note, that the heat source density $Q_{\text{rf}} = Q_{\text{rf}}(d)$ induced by the applied RF probe, depends on the probe-vessel distance d through the potential $\phi = \phi(d)$ of the probe. In more detail, we consider the potential equation:

$$\begin{aligned} -\sigma \Delta \phi(d)(\vec{x}) &= 0 && \text{in } D \setminus \overline{D_{\text{el}}}(d) , \\ \phi(d)(\vec{x}) &= \pm 1 && \text{on } \overline{D_{\text{el}}}(d) , \\ n \cdot \nabla \phi(d)(\vec{x}) &= \frac{n(p(d) - \vec{x})}{|p(d) - \vec{x}|^2} \phi(\vec{x}) && \text{on } \Gamma_{\text{out}} . \end{aligned}$$

Here, p is the probe position (i. e. the center of the probe's active zone; cf. e. g. Sect. 2.2, Fig. 2.2) which obviously depends on the probe-vessel distance d , and D_{el} denotes the set of the probe's electrodes the location of which also depends on d . After having calculated the whole power P_{total} and the effective power P_{eff} as described in Sect. 2.3, Eqs. (2.14) and (2.15), the heat source density $Q_{\text{rf}} = Q_{\text{rf}}(d)$ is calculated as

$$Q_{\text{rf}}(d)(\vec{x}) = \frac{P_{\text{eff}}}{P_{\text{total}}} \sigma |\nabla \phi(d)(\vec{x})|^2 \quad \text{in } D .$$

Note, that the calculation of the heat source density Q_{rf} and thereby also the calculation of the temperature T , depends on the type of the considered RF probe and (through P_{eff}) on the power P_{setup} set up at the generator's control unit. If another type of RF probe or another generator power is used, the calculation has to be rerun for this setting.

Reduction to a two-dimensional differential equation: In a next step, let us assume the considered vessel V to be infinitely long and oriented along the z -axis of the \mathbb{R}^3 . Further, let us assume the applied RF probe to lie parallel to the vessel, and the temperature to be homogeneous along the whole z -axis.² Then consequently the derivatives in direction of z vanish, so that the z -direction can be omitted and we obtain a heat equation of only two dimensions (depending just on the x - and y -coordinate of the computational domain D). In the following, let $D' \subset \mathbb{R}^2$ be the

²Later, in Sect. 5.4, we will also consider configurations where the probe lies orthogonal to the vessel.

two-dimensional computational domain extracted from the cuboid D by omitting the z -direction. Moreover, let Γ'_{out} be the corresponding outer boundary of D' , and let $V' = V'(R_{\text{bv}}) \subset D'$ be a two-dimensional vessel (obtained from a vessel $V \subset D$ again by neglecting the z -direction). Then the two-dimensional heat function can be written as $T : \mathbb{R}^+ \times \mathbb{R}^+ \rightarrow H^1(D')$, $(R_{\text{bv}}, d) \mapsto T(R_{\text{bv}}, d)$, such that $T(R_{\text{bv}}, d)$ solves the two-dimensional heat equation

$$-\lambda \Delta u(R_{\text{bv}}, d)(x, y) = Q_{\text{rf}}(d)(x, y) + Q_{\text{perf}}(x, y) \quad \text{in } D' \setminus V'(R_{\text{bv}}) , \quad (5.1a)$$

$$u(R_{\text{bv}}, d)(x, y) = T_{\text{body}} \quad \text{on } \partial V'(R_{\text{bv}}) , \quad (5.1b)$$

$$n \cdot \nabla u(R_{\text{bv}}, d)(x, y) = 0 \quad \text{on } \Gamma'_{\text{out}} . \quad (5.1c)$$

Here, the heat source density $Q_{\text{rf}}(d) = Q_{\text{rf}}^{3D}(d)$ can be reduced to two dimensions with help of e. g. the following transformation:

$$f_{\text{Trans}} : H^{-1}(D) \rightarrow H^{-1}(D') ,$$

$$f_{\text{Trans}}(Q)(x, y, z) = \int_a^b \varphi(z) Q(x, y, z) dz , \quad (5.2)$$

where $a = p_z - 0.5L_{\text{active}}$ and $b = p_z + 0.5L_{\text{active}}$ are the beginning and end of the probe's active zone in z -dimension, respectively (see Fig. 5.2, left). Moreover, φ is a smoothing function which ensures the reduced heat source density $Q_{\text{rf}}^{2D}(x, y) = f_{\text{Trans}}(Q_{\text{rf}}^{3D})(x, y, z)$ to lie in the Hilbert space $H^{-1}(D')$. More precisely, φ is a C^∞ -function with compact support in $[a, b]$, such that $\varphi(z) = 1 \forall z \in (a + \varepsilon, b - \varepsilon)$ with $\varepsilon > 0$. This can be seen by the following consideration: In order that Q_{rf}^{2D} lies in $H^{-1}(D')$, i. e. in order that the definition of f_{Trans} in (5.2) is well defined, the following inequality has to be fulfilled

$$\left| \int_{D'} Q_{\text{rf}}^{2D}(x, y) w(x, y) dx dy \right| \leq C \|w\|_{H^1(D')} \quad \forall w \in C_0^\infty(D') , \quad (5.3)$$

with C independent of w .³ For the verification of (5.3) we consider the following relation (which is valid for $Q_{\text{rf}}^{3D} \in H^{-1}(D)$):

$$\begin{aligned} \left| \int_{D'} Q_{\text{rf}}^{2D}(x, y) w(x, y) dx dy \right| &= \left| \int_{D'} \int_a^b \varphi(z) Q_{\text{rf}}^{3D}(x, y, z) dz w(x, y) dx dy \right| \\ &= \left| \int_D Q_{\text{rf}}^{3D}(x, y, z) \underbrace{\varphi(z) w(x, y)}_{=: \tilde{w} \in C_0^\infty(D)} dx dy dz \right| \\ &\leq C \|\tilde{w}\|_{H^1(D)} \quad \forall w \in C_0^\infty(D'), \tilde{w} \in C_0^\infty(D) . \end{aligned}$$

³Note, that if (5.3) is valid for all $w \in C_0^\infty(D')$, it also holds for all $w \in H^1(D')$, since $C_0^\infty(D')$ is dense in $H^1(D')$ (according to the theorem of Meyers and Serrin; see [41], p. 134, and [1]).

Now, in order to obtain the desired inequality (5.3), we further estimate the $H^1(D)$ -norm of \tilde{w} by

$$\|\tilde{w}\|_{H^1(D)}^2 = \|\nabla\tilde{w}\|_{L^2(D)}^2 + \|\tilde{w}\|_{L^2(D)}^2 \leq C \left(\|\nabla w\|_{L^2(D')}^2 + \|w\|_{L^2(D')}^2 \right) = C \|w\|_{H^1(D')}^2 ,$$

where this estimation can be seen by the following considerations:

Firstly, we transform the L^2 -norm of \tilde{w} :

$$\begin{aligned} \|\tilde{w}\|_{L^2(D)}^2 &= \int_D |\tilde{w}|^2 dx dy dz = \int_D |\varphi(z)w(x, y)|^2 dx dy dz = \int_{D'} \int_a^b |\varphi(z)|^2 |w(x, y)|^2 dz dx dy \\ &= \int_{D'} \int_a^b |\varphi(z)|^2 dz |w(x, y)|^2 dx dy = \underbrace{\int_a^b |\varphi(z)|^2 dz}_{=:\tilde{C}} \underbrace{\int_{D'} |w(x, y)|^2 dx dy}_{=\|w\|_{L^2(D')}^2} . \end{aligned}$$

Secondly, a similar transformation holds for the L^2 -norm of the gradient $\nabla\tilde{w}$:

$$\begin{aligned} \|\nabla\tilde{w}\|_{L^2(D)}^2 &= \int_D |\nabla\tilde{w}|^2 dx dy dz = \int_D |\nabla(\varphi(z)w(x, y))|^2 dx dy dz \\ &= \int_D \left| \left(\varphi(z) \frac{\partial}{\partial x} w(x, y), \varphi(z) \frac{\partial}{\partial y} w(x, y), \frac{\partial}{\partial z} \varphi(z) w(x, y) \right) \right|^2 dx dy dz \\ &= \int_D \varphi(z)^2 \left(\frac{\partial}{\partial x} w(x, y) \right)^2 + \varphi(z)^2 \left(\frac{\partial}{\partial y} w(x, y) \right)^2 + \left(\frac{\partial}{\partial z} \varphi(z) \right)^2 w(x, y)^2 dx dy dz \\ &= \int_D \varphi(z)^2 |\nabla w(x, y)|^2 dx dy dz + \int_D \left(\frac{\partial}{\partial z} \varphi(z) \right)^2 w(x, y)^2 dx dy dz \\ &= \int_{D'} \int_a^b \varphi(z)^2 |\nabla w(x, y)|^2 dz dx dy + \int_{D'} \int_a^b \left(\frac{\partial}{\partial z} \varphi(z) \right)^2 w(x, y)^2 dz dx dy \\ &= \underbrace{\int_a^b \varphi(z)^2 dz}_{=:\tilde{C}} \underbrace{\int_{D'} |\nabla w(x, y)|^2 dx dy}_{=\|\nabla w\|_{L^2(D')}^2} + \underbrace{\int_a^b \left(\frac{\partial}{\partial z} \varphi(z) \right)^2 dz}_{=:\hat{C}} \underbrace{\int_{D'} w(x, y)^2 dx dy}_{=\|w\|_{L^2(D')}^2} . \end{aligned}$$

Altogether, we finally obtain the required estimation:

$$\begin{aligned} \|\nabla\tilde{w}\|_{L^2(D)}^2 + \|\tilde{w}\|_{L^2(D)}^2 &= \tilde{C} \|w\|_{L^2(D')}^2 + \tilde{C} \|\nabla w\|_{L^2(D')}^2 + \hat{C} \|w\|_{L^2(D')}^2 \\ &= \tilde{C} \|\nabla w\|_{L^2(D')}^2 + (\tilde{C} + \hat{C}) \|w\|_{L^2(D')}^2 \\ &\leq \underbrace{\tilde{C} + \hat{C}}_{=:C} \left(\|\nabla w\|_{L^2(D')}^2 + \|w\|_{L^2(D')}^2 \right) . \quad \square \end{aligned}$$

Unfortunately, for $\varepsilon \rightarrow 0$ within the definition of the smoothing function φ , at the moment, it only can be shown that the constant \tilde{C} stays bounded, whereas for the constant \hat{C} this cannot be seen, yet (i. e. with the basic instruments). Hence, this remains to show in a future work.

Note, that in (5.2) the integral cannot be replaced by taking simply the cross section through the center $p = (p_x, p_y, p_z)$ of the probe's active zone, because for bipolar probes this cross section would pass the isolator and thus the corresponding heating profile would be too low (see Fig. 5.2, right schematic). However, the

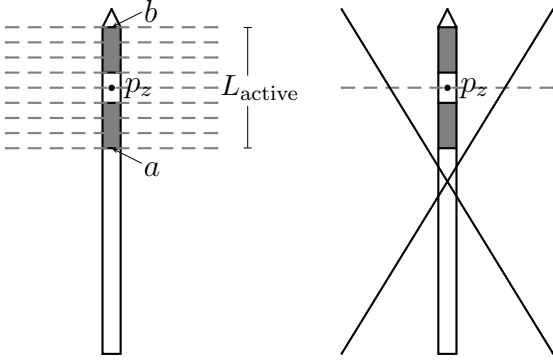


Figure 5.2: Left: Determination of the integral over all orthogonal cross sections through the probe's active zone. Right: Orthogonal cross section through the center of the probe's active zone. (If the probe is bipolar, this cross section passes the isolator and thus the corresponding heating profile along this cross section is unrepresentatively low.)

transformation f_{Trans} obviously can be extended to

$$f_{\text{Trans}}(Q)(x, y, z) = \text{mean}_{a \leq z \leq b} (\varphi(z) Q(x, y, z)) = \frac{1}{b-a} \int_a^b \varphi(z) Q(x, y, z) dz.$$

Also note, that calculating the probe's heating profile directly in 2D is impossible here, because the physical units within equation (2.15) for calculating the whole power P_{total} do not fit for 2D. More precisely, when integrating the unscaled power $P = \sigma |\nabla \phi|^2$ (of unit $\text{V}^2/\Omega \text{m}^3$) over only two dimensions, one would obtain the whole power P_{total} in $\text{V}^2/\Omega \text{m}$ (instead of $\text{V}^2/\Omega = \text{W}$) which obviously is unfeasible.

For the results shown in Sect. 5.4, as a first approach here instead of the integral, the pointwise maximum of all cross sections of heat source density profiles through the probe's active zone has been taken. Formally, that means the transformation

$$f_{\text{Trans}}(Q)(x, y, z) = \max_{a \leq z \leq b} Q(x, y, z)$$

has been used. Unfortunately, with this definition $Q_{\text{rf}}^{2D}(x, y) = f_{\text{Trans}}(Q_{\text{rf}}^{3D})(x, y, z)$ does not lie in $H^{-1}(D')$, such that in later calculations the transformation defined in (5.2) should be preferred.

Finally it should be remarked, that a first idea had been to model the heat source density Q_{rf} uniformly to be able to reduce the heat equation to only one-dimension,

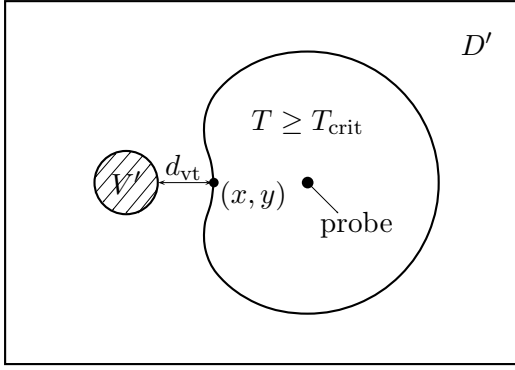


Figure 5.3: Thickness d_{vt} of a tube of vital tissue around a vessel V in dependence of the temperature $T = T(R_{bv}, d)$.

i. e. to an ordinary differential equation that only depends on the distance r of the currently considered point $\vec{x} \in D$ to the nearest vessel V . This additional reduction had been performed via a transformation of the heat equation to cylindrical coordinates and the assumption of rotational symmetry. However, the assumption of a uniform heat source density Q_{rf} had been too strong, since directly around the probe the heat source density is very high and then rapidly decreases with increasing distance from the probe. A comparison with the result of a three-dimensional forward simulation has confirmed this insight. Hence, it has been decided to compute the temperature distribution $T = T(R_{bv}, d)$ in two space-dimensions.

After having calculated the two-dimensional temperature distribution $T = T(R_{bv}, d)$ for numerous different vessel radii R_{bv} and probe-vessel distances d , one now can determine the so-called criticality tubes C of vital tissue around large vessels with help of the following considerations:

Calculation of Vessel Surrounding Tubes of Vital Tissue: First, the thickness d_{vt} of a criticality tube C of vital tissue has to be defined in dependence of the tissue temperature $T = T(R_{bv}, d)$. This can be done with help of the following function definition:

$$\begin{aligned} d_{vt} : H^1(D') &\rightarrow \mathbb{R}^+ , \\ \mathcal{T} &\mapsto d_{vt}(\mathcal{T}) , \end{aligned} \quad (5.4)$$

$$d_{vt}(\mathcal{T}) = \min \{ \text{dist}(\partial V'(R_{bv}), (x, y)) \mid \mathcal{T}(x, y) \geq T_{\text{crit}}, (x, y) \in D' \} .$$

Here, $\text{dist}(\partial V'(R_{bv}), (x, y))$ is the distance between the boundary $\partial V'(R_{bv})$ of the vessel V' and a point (x, y) of the computational domain D' (see Fig. 5.3). With this definition, $d_{vt}(T(R_{bv}, d))$ is the thickness of the criticality tube C for the tissue temperature $T(R_{bv}, d)$, i. e. for the vessel of radius R_{bv} and the probe-vessel distance d . Note, that the existence of the minimum within equation (5.4) is a result of Sobolev's embedding theorem (see e. g. [41], p. 136, and [1]).

Now, with help of the thickness $d_{vt} = d_{vt}(T(R_{bv}, d))$ the vessel surrounding criticality tube C of vital tissue can be calculated. Thereto, the following function

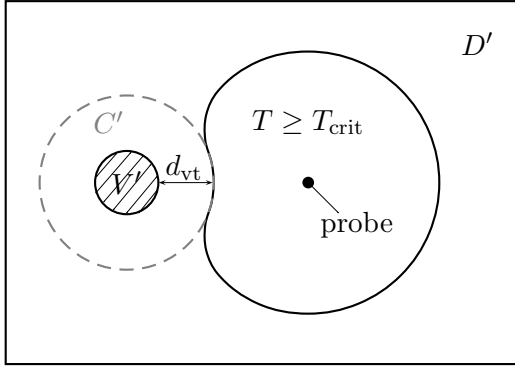


Figure 5.4: Two-dimensional view of the criticality tube C (which in two dimensions is denoted as C') of thickness d_{vt} around a vessel V . (Note, that even if depicted in only two dimensions, the criticality tube C of course is three-dimensional.)

definition is used:

$$\begin{aligned}
 C : \mathbb{R}^+ \times \mathbb{R}^+ &\rightarrow \mathcal{P}(D) , \\
 (\rho, R_{bv}) &\mapsto C(\rho, R_{bv}) , \\
 C(\rho, R_{bv}) &= V(R_{bv}) \oplus B_\rho(0) = \bigcup_{v \in V(R_{bv})} B_\rho(v) .
 \end{aligned} \tag{5.5}$$

Here, $\mathcal{P}(D)$ is the power set of D , and $B_\rho(v)$ is the open ball of radius ρ centered at v :

$$B_\rho(v) = \{ \vec{x} \in \mathbb{R}^3 \mid |\vec{x} - v| < \rho \} ,$$

where $|\cdot|$ denotes the Euklclidean norm. Moreover, the symbol ' \oplus ' within formula (5.5) denotes the dilation, i.e. for two elements A and B of an arbitrary vector space the dilation $A \oplus B$ is defined as $A \oplus B := \{ a + b \mid a \in A, b \in B \}$. With this definition, $C(d_{vt}, R_{bv}) = C(d_{vt}(T(R_{bv}, d)), R_{bv}) \subset \mathcal{P}(D)$ is the three-dimensional criticality tube of thickness d_{vt} for the tissue temperature $T(R_{bv}, d)$, i.e. for the vessel of radius R_{bv} and the probe-vessel distance d (cf. Fig. 5.4).

After having calculated the vessel surrounding criticality tubes C of vital tissue and in particular the thicknesses $d_{vt} = d_{vt}(T(R_{bv}, d))$ of these tubes for numerous different vessel radii R_{bv} and probe-vessel distances d , we now are able to quickly determine the maximum allowable distances d_{\max} between the RF probe and the vessels for different vessel radii R_{bv} and points \vec{x} of the computational domain, such that the considered point \vec{x} lies on the outer boundary of C , where the temperature starts to be high enough for cell destruction.

Calculation of Maximal Probe-Vessel Distances: As already indicated above, the maximal probe vessel distances $d_{\max} = d_{\max}(R_{bv}, \vec{x})$ for a vessel V of radius R_{bv} and a point \vec{x} of the computational domain D , can be defined with help of the concatenation of the functions T (see (5.1)) and d_{vt} (see (5.4)), i.e. with help of the concatenation

$$\begin{aligned}
 d_{vt} \circ T : \mathbb{R}^+ \times \mathbb{R}^+ &\rightarrow \mathbb{R}^+ , \\
 (R_{bv}, d) &\mapsto (d_{vt} \circ T)(R_{bv}, d) .
 \end{aligned}$$

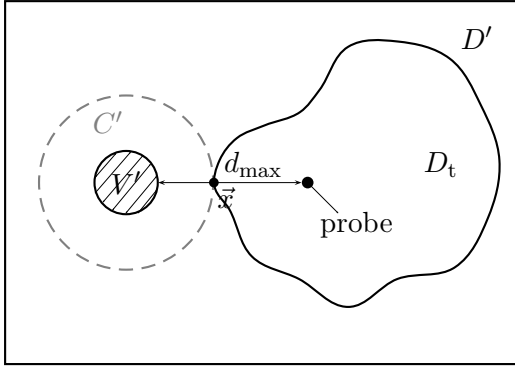


Figure 5.5: Maximal distance d_{\max} between the RF probe and the vessel V , such that the point \vec{x} of the tumor D_t lies on the outer boundary of the criticality tube C . Thus, d_{\max} is the maximal distance the probe may have to the vessel V , in order to destroy the point \vec{x} of the tumor.

More precisely, for the definition of d_{\max} the inversion of the concatenation $d_{\text{vt}} \circ T$ with respect to the second argument is used:

$$d_{\max} : \mathbb{R}^+ \times D \rightarrow \mathbb{R}^+ , \quad (5.6)$$

$$d_{\max}(R_{\text{bv}}, \vec{x}) = (d_{\text{vt}} \circ T)(R_{\text{bv}}, \cdot)^{-1}(\text{dist}(\partial V(R_{\text{bv}}), \vec{x})) .$$

That means, the determination of d_{\max} simply can be performed by considering the calculation results from an inverse point of view: By evaluating the function $(d_{\text{vt}} \circ T)(R_{\text{bv}}, \cdot)^{-1}$ for a certain radius R_{bv} of the vessel of interest and the distance $\text{dist}(\partial V(R_{\text{bv}}), \vec{x})$ of the considered point \vec{x} from the vessel, one obtains the corresponding value of maximal distance d_{\max} between the probe and the vessel, such that the tube C of vital tissue has the thickness $d_{\text{vt}} = \text{dist}(\partial V(R_{\text{bv}}), \vec{x})$ and the considered point \vec{x} (which appropriately should be a point of the tumor) lies on the outer boundary of C , where the temperature starts to reach the critical temperature T_{crit} (cf. Figs. 5.5 and 5.6).

To conclude the explanations on the single-vessel-model presented in this section, in Fig. 5.7 the main functional relations in calculating the criticality tubes C and maximal probe-vessel distances d_{\max} are schematically summarized.

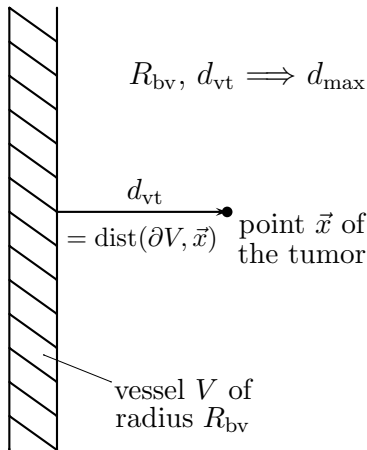


Figure 5.6: With help of the 2D calculation results of $(d_{\text{vt}} \circ T)(R_{\text{bv}}, d)$ for different vessel radii R_{bv} and probe-vessel distances d , now one quickly can determine how the maximal distance d_{\max} between the probe and a vessel V of radius R_{bv} has to be chosen, such that a considered point \vec{x} of the tumor lies on the outer boundary of the criticality tube C of vital tissue around the vessel V .

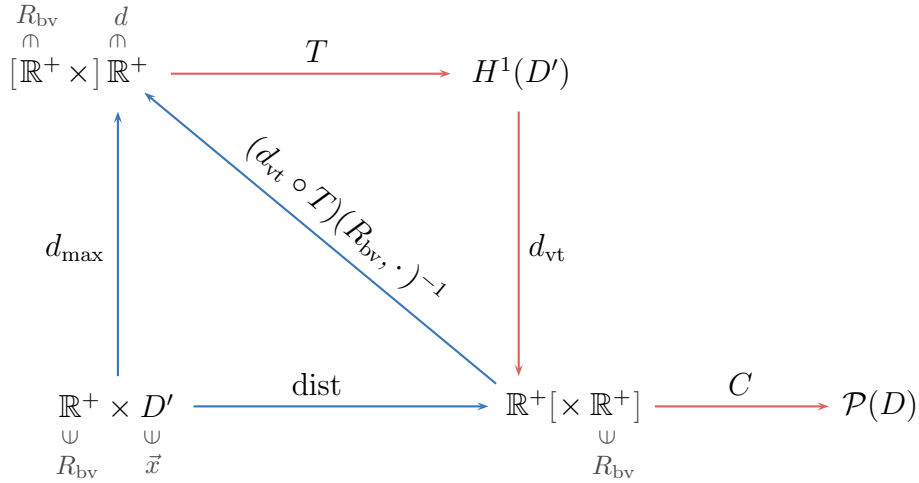


Figure 5.7: Commutative diagram showing all compositions of functions for calculating the criticality tubes C and maximum allowable probe vessel distances d_{max} . Red: Functions which are precalculated. Blue: Functions which are evaluated ad hoc for the individual patient.

5.3 Completion of the Single-Vessel-Model to a Model for a Complex Vascular Tree

In the previous section, a method has been presented which for each point \vec{x} of the computational domain D and in particular of the tumor D_t , enables us to calculate the maximum allowable distance d_{max} between a nearby lying vessel V of radius R_{bv} and a given kind of RF probe, such that the corresponding point \vec{x} of the tissue is heated up to a critical temperature T_{crit} at which tissue cells die. Now this single-vessel-model has to be combined to the branches of a whole vascular system yielding the set of maximal distances d_{max} for the color coding of the tumors and the set of criticality tubes for a whole organ (see Fig. 5.8).

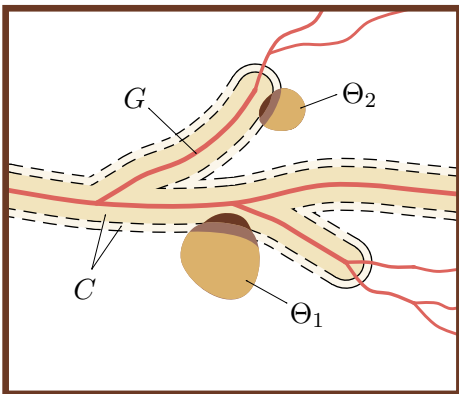


Figure 5.8: Considered configuration of a whole vascular tree G with two nearby lying tumors Θ_1 and Θ_2 provided with a color coding, where different colors represent different maximum allowable distances d_{max} between the given RF probe and the respective vessel. The dashed tubes around the large vessels are the criticality tubes corresponding to the coding colors of the tumors.

5.3 Completion of the Single-Vessel-Model to a Model for a Complex Vascular Tree

Let us consider the segmented vascular tree of an organ (e. g. the liver) as a set

$$G := \{V_i := (S_i, E_i, R_{\text{bv}}^i) \mid i = 1, \dots, N\}, \quad (5.7)$$

with $S_i, E_i \in \mathbb{R}^3, R_{\text{bv}}^i > 0$ which can be obtained from e. g. a CT-dataset by the methods presented in [15, 76]. Each V_i represents a linear vessel segment, starting at S_i , ending at E_i , and having a radius R_{bv}^i . Consequently, for each i there exists an affine orthogonal transformation $O_i : \mathbb{R}^3 \rightarrow \mathbb{R}^3$ such that $O_i(S_i) = 0$ and $O_i(E_i) = (0, 0, e_i)^T$ lies on the z -axis. Now one can apply the single-vessel-method to a given vessel V_i of radius R_{bv}^i and thus obtains for each point of the tumor a maximum allowable distance d_{max}^i of the RF probe to this vessel, as well as a corresponding thickness d_{vt}^i of vital tissue around this vessel. The color coding of the tumor, as well as the criticality tube C_i corresponding to one of the coding colors and containing all points of the tumor for which the RF probe must have at most a certain distance d_{max}^i , are then defined as the color coding and criticality tube, respectively, belonging to the vessel segment V_i . In particular we have

$$C_i := O_i^{-1} (V_i(R_{\text{bv}}^i) \oplus B_{\rho_i}(0)) \quad \text{and} \quad (5.8)$$

$$d_{\text{max}}^i := (d_{\text{vt}}^i \circ T_i)(R_{\text{bv}}^i, \cdot)^{-1}(\text{dist}(\partial V_i(R_{\text{bv}}^i), \vec{x})) . \quad (5.9)$$

Then the whole criticality tube C simply can be defined by the combination of all criticality tube segments C_i :

$$C = \bigcup_{i=1}^N C_i . \quad (5.10)$$

Since the segmentation of the blood vessels by the methods presented in [15, 76] unfortunately is afflicted with a segmentation error of about 1-2 voxel diagonals of underestimation, here the length of one voxel diagonal v_d of the underlying grid (cf. Sect. 5.4) has been added to each vessel radius R_{bv}^i ($i = 1, \dots, N$). Note, that this will become unnecessary once the vessel segmentation algorithm has been improved, which is a different area of research.

Like in the previous sections, the 2D calculation of the steady state temperature equation (see Sect. 5.2, Eq. (5.1)) is performed numerically with help of finite elements (cf. Sect. 2.4.2) on a uniform Cartesian grid. After having solved the temperature equation (5.1) for numerous different vessel radii R_{bv} and probe-vessel distances d , the respective thicknesses $d_{\text{vt}} = d_{\text{vt}}(T(R_{\text{bv}}, d))$ of vessel surrounding criticality tubes C of vital tissue are determined with help of the function (5.4) and stored within a look-up-table, where the vessel radii R_{bv} and distances d between the RF probe and the vessels are the input parameters (see Sect. 5.4, Fig. 5.9). Since here, one dimension of the computational domain D is neglected, the look-up-table can be filled with numerous entries and the underlying grid for the calculation of the temperature equation can be refined for a best possible outcome. After having filled the look-up-table, the results are interpolated by using piecewise bilinear functions

on an adaptively refined, hierarchical grid (see Sect. 5.4), such that finally for each vessel radius R_{bv} and point \vec{x} of the tumor D_t with distance $d_{\text{vt}} = \text{dist}(\partial V, \vec{x})$ from the vessel V , the maximum allowable distance d_{max} between the applied RF probe and the vessel quickly can be determined with help of the function (5.6).

In the following, some first results in visualizing the cooling influence of large blood vessels on an RF ablation, computed with the method described above, are presented and discussed.

5.4 Results

In this section, the algorithm described before, is applied to real CT data, i. e. to a segmented vessel tree with nearby lying tumors. The segmentation of all vessel trees and tumors, as well as the transformation into a three-dimensional graph, have been performed by the methods presented in [15, 76].

As already mentioned in Sect. 5.3, first a look-up-table is calculated with help of the concatenation $(d_{\text{vt}} \circ T)(R_{\text{bv}}, d)$ of the functions T (see (5.1)) and d_{vt} (see (5.4)) for numerous different vessel radii R_{bv} and probe-vessel distances d . In more detail, let f be the concatenation of functions $f := d_{\text{vt}} \circ T$, and let h_{ij} ($i, j = 1, \dots, n$) be some suitable Ansatz functions. Then an approximation $\bar{f} \in \text{Span}\{h_{ij}\}$ of the function f is given by:

$$\bar{f}(R_{\text{bv}}, d) = \sum_{i,j=1}^n f_{ij} h_{ij}(R_{\text{bv}}, d) \ , \quad f_{ij} = f(R_{\text{bv}}^i, d^j) \ . \quad (5.11)$$

In the easiest case, the Ansatz functions h_{ij} can be modeled by e. g. piecewise bilinear functions at a uniform grid. Then the corresponding look-up-table inside of which the results $f_{ij} = (d_{\text{vt}} \circ T)(R_{\text{bv}}^i, d^j)$ are stored, can be represented as shown in Fig. 5.9. Note, that in the actual implementation an adaptively refined, hierarchical grid is used.

For the calculation of the look-up-table, we consider an RF probe cluster of three parallel monopolar probes (cf. Sect. 3.8). Here, the probe cluster is of radius 3.5 mm (i. e. the probe distance is $3.5 \cdot \sqrt{3}$ mm ≈ 6.06 mm), where each probe of the cluster is of 1.0 mm radius and has an electrode length of 30.0 mm. Moreover, the connected RF generator has an inner resistance of 80 Ω and is set up to a power of 100 W.

Now, first the heat source density Q_{rf} induced into the tissue by the applied RF probe cluster has to be determined with help of e. g. a three-dimensional forward simulation. Then the three-dimensional heat source density has to be reduced to a two-dimensional heat source density as described in Sect. 5.2, i. e. with help of the transformation function f_{Trans} . Here, the 3D-calculation of Q_{rf} is performed at a computational domain D of extent $40 \times 20 \times 50$ [mm³] and discretized by a grid of $400 \times 200 \times 50$ grid cells (see Fig. 5.10).

After the dimensional reduction of D by omitting the z -direction, the resulting two-dimensional computational domain D' is of extent 40 mm (horizontal) \times 20 mm

$R_{bv} \backslash d$		d^j	\dots
R_{bv}^i		f_{ij}	
\vdots			

$R_{bv} \backslash d$	2.0	\dots	8.4	\dots	14.8
1.0	0.152	\dots	0.868	\dots	5.160
\dots	\dots	\dots	\dots	\dots	\dots
4.2	0.189	\dots	1.023	\dots	5.179
\dots	\dots	\dots	\dots	\dots	\dots
7.4	0.197	\dots	1.064	\dots	5.187

Figure 5.9: Left: Schematic of the two-dimensional look-up-table, containing the different thicknesses $f_{ij} = (d_{vt} \circ T)(R_{bv}^i, d^j)$ of tubes of vital tissue in dependence of the vessel radii R_{bv}^i and the probe-vessel distances d^j . Right: Part of the filled look-up-table. Here, all values are given in millimeters [mm].

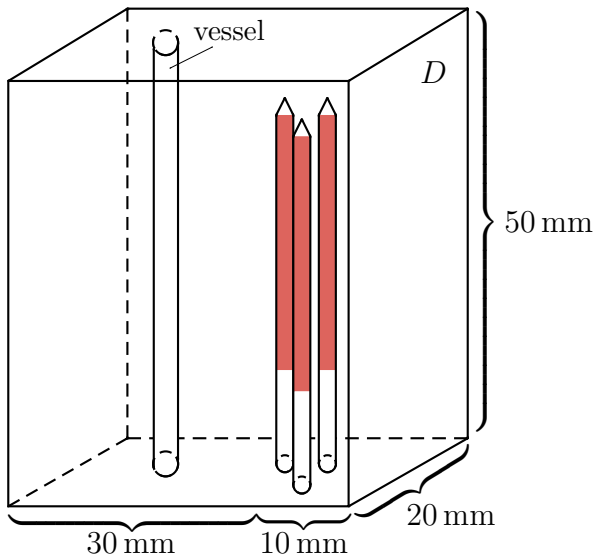


Figure 5.10: Extent of the three-dimensional computational domain D for the calculation of the heat source density Q_{rf} induced into the tissue by the applied RF probe cluster.

(vertical) and discretized by a grid of 400×200 grid cells. Further, the probe cluster is placed 10 mm right from the center of D' and parallel to the considered vessel which always is located left to the probe (see Fig. 5.11).

With help of the calculated two-dimensional heat source density Q_{rf} , then the two-dimensional temperature equation (5.1) can be solved for numerous vessel radii R_{bv} and probe-vessel distances d . As already can be seen from the partly filled look-up-table shown in Fig. 5.9 (right picture), here the values of vessel radii R_{bv} range from 1.0 mm to 7.4 mm and the distances d between the RF probe cluster and the vessels

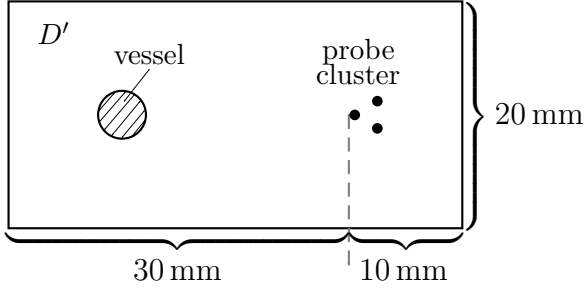


Figure 5.11: Extent of the two-dimensional computational domain D' obtained from D by omitting the z -direction, and used for the calculation of the temperature $T(R_{bv}, d)$ which is needed to calculate the entries of the look-up-table shown in Fig. 5.9.

vary from 2.0 mm up to 14.8 mm distance.⁴ Moreover, the heat conductivity is set to $\lambda = 0.437 \text{ W/K m}$ and the electric conductivity is set to $\sigma = 0.485 \text{ S/m}$. The capillary perfusion is modeled by taking the values $\nu_{\text{cap}} = 0.01765 \text{ 1/s}$, $\rho_{\text{blood}} = 1059.0 \text{ kg/m}^3$ and $c_{\text{blood}} = 3850.0 \text{ J/kg K}$ for the relative blood circulation rate, the blood density and the heat capacity of blood, respectively (cf. Sect. 3.8). The tissue is considered destroyed if it is heated above a critical temperature of $T_{\text{crit}} = 323.15 \text{ K}$ ($\hat{=} 50 \text{ }^\circ\text{C}$). (At this temperature, tissue cells coagulate after 10 minutes of RF ablation which is considered as steady state, here (cf. (2.9) and [87]).)

After having calculated the temperature $T(R_{bv}, d)$ for numerous vessel radii R_{bv} and probe-vessel distances d , the corresponding thicknesses $d_{\text{vt}}(T(R_{bv}, d))$ of vessel surrounding tubes C of vital tissue can be calculated with help of definition (5.4) and stored in the look-up-table shown in Fig. 5.9.

As mentioned before, for the interpolation between the values of the look-up-table, here piecewise bilinear Ansatz functions h_{ij} ($i, j = 1, \dots, n$) are used at an adaptively refined, hierarchical grid. The resulting look-up-table consists of 304 entries for the output parameter $f_{ij} = (d_{\text{vt}} \circ T)(R_{bv}^i, d^j)$, i. e. for the different thicknesses of vital tissue around the considered vessels. This rather small number of supporting points is due to the fact that here a fine grid is used only in regions where a coarse grid is not suitable to approximate f_{ij} as a function of R_{bv} and d sufficiently well (see [61] and the references therein, in particular [18]). In Fig. 5.12 some of the resulting curves are depicted for different vessel radii R_{bv} . In the case of no blood vessel (dotted line), the thickness $d_{\text{vt}} = d_{\text{vt}}(T(R_{bv}, d))$ of vital tissue around an imaginary vessel wall, is only a coding of the distance between this imaginary wall and the coagulated region of tissue around the probe cluster. If a point of this wall lies in the region of coagulated tissue, the distance (which actually is negative then) is set to zero. Hence, the bend of the curve at about 9.5 mm shows the radius of the coagulated tissue region around the probe cluster for the case that there is no large vessel close by. Behind the bend at about 9.5 mm, the curve shows a linear slope which corresponds to the linear increase of the distance d between the probe cluster and the imaginary vessel wall. Note, that above about 14.0 mm distance d between the probe cluster and the considered vessels, also the other two curves become approximately linear, which is due to the fact that far away from the vessel,

⁴Here, the distance between the RF probe cluster and the vessel is detected for the probe lying nearest to the vessel.

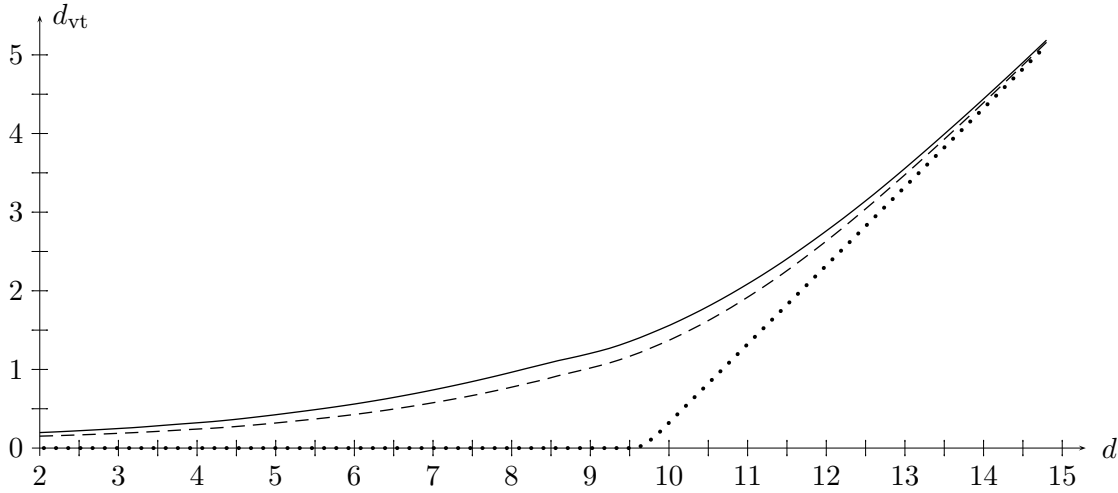


Figure 5.12: The curves show the thickness $d_{vt} = d_{vt}(T(R_{bv}, d))$ of the vessel surrounding region of vital tissue, in dependence of the distance d of the applied RF probe cluster from the vessel for different vessel radii. *Dotted Line:* No blood vessel, i. e. only a coding of the distance between an imaginary vessel wall and the coagulated region of tissue around the probe cluster. *Dashed Line:* Curve for a blood vessel of radius 1.0 mm. *Solid Line:* Curve for a blood vessel of radius 7.4 mm.

its cooling effect has no significant impact on the coagulated tissue region around the probe cluster any more. Thus, from this distance on, the curves become essentially independent of the vessel radius R_{bv} . Also note, that the curves for all other vessels of radii $R_{bv} \in (1.0 \text{ mm}, 7.4 \text{ mm})$ lie between the dashed and solid curve.

Finally, with help of the calculated look-up-table and the curves shown in Fig. 5.12, as well as the definition (5.6), one now can determine the maximum allowable distances $d_{\max} = d_{\max}(R_{bv}, \vec{x})$ between the RF probe cluster and each vessel $V = V(R_{bv})$ of a whole vascular tree to be able to destroy each single point \vec{x} of the tumors lying near to the vessels.

In Fig. 5.13 two different views of the resulting color coding of three hepatic tumors located close by the vessels of the hepatic vein, are shown for an example based on real patient data. Here, for each vessel of radius $R_{bv} > 1.5 \text{ mm}$, all tumor regions which cannot be destroyed (i. e. heated up to a critical temperature of $T_{\text{crit}} = 50 \text{ }^\circ\text{C}$) if the RF probe cluster is more than $d_{\max} = 5.0 \text{ mm}$ distant from the corresponding vessels, are colored in dark blue. The tumor regions which cannot be destroyed if the distance between the RF probe cluster and the respective vessels is larger than $d_{\max} = 10.0 \text{ mm}$, are colored in light blue, and the remaining tumor regions are colored in yellow. Moreover, in Fig. 5.14 different views of the single tumors and their coloring next to the vessels are shown together with the corresponding criticality tubes C (depicted in a transparent blue color) for $d_{\max} = 5.0 \text{ mm}$ (left column) and $d_{\max} = 10.0 \text{ mm}$ (middle right column). The other two columns present

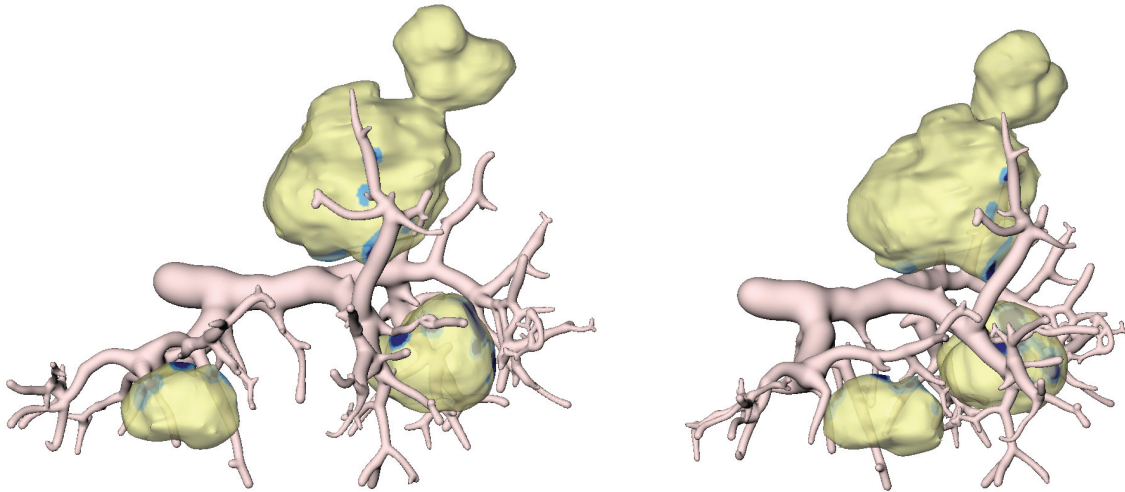


Figure 5.13: Example based on real patient data, showing the portal vein of the liver (light red) and three hepatic tumors near to the vessels. Tumor regions which cannot be destroyed if the distance between the applied RF probe cluster and the respective vessels (of radius $R_{bv} > 1.5$ mm) is more than $d_{\max} = 5.0$ mm, are colored in dark blue, those regions which cannot be destroyed if the distance is larger than $d_{\max} = 10.0$ mm, are colored in light blue, and all remaining tumor regions are colored in yellow.

zoomed views of the relevant regions.⁵

Note, that this visualization is only an indication of critical areas to which the radiologist should pay particular attention, and which might be hard to ablate without changing the general conditions. Since a requirement of only 5.0 mm distance from large vessels in some situations might be critical (especially for e.g. the hepatic artery which must not be punctured), the conclusion from such a visualization not necessarily must be to try to insert the RF probe up to 5.0 mm near to the respective vessel, but also could be an advise to perform additional steps (as e.g. a pringle manoeuvre, or a chemoembolization) to improve the general conditions, or even (as worst case) an indication for an exclusion from RF ablation.

Of particular interest in Fig. 5.14 is the jump between the dark blue and light blue colored tumor regions: By placing the probe cluster (only) 5.0 mm closer to the respective vessels, the amount of destroyed tumor region can be increased significantly. Since such a situation is only hardly (if at all) predictable by just looking at the segmented tumor and vessel data, this (in particular) motivates the need for the presented support by a color coding of the tumors and display of criticality tubes of vital tissue around large vessels, respectively, due to the maximum allowable distance of the applied RF probe to the vessels in order to destroy certain tumor regions.

Further it has to be remarked that after having calculated the two-dimensional

⁵Recall, that as already mentioned in Sect. 5.3, p. 101, here the length of one voxel diagonal v_d (which for the considered example is $v_d = 1.62$ mm) has been added to the vessel radii R_{bv} .

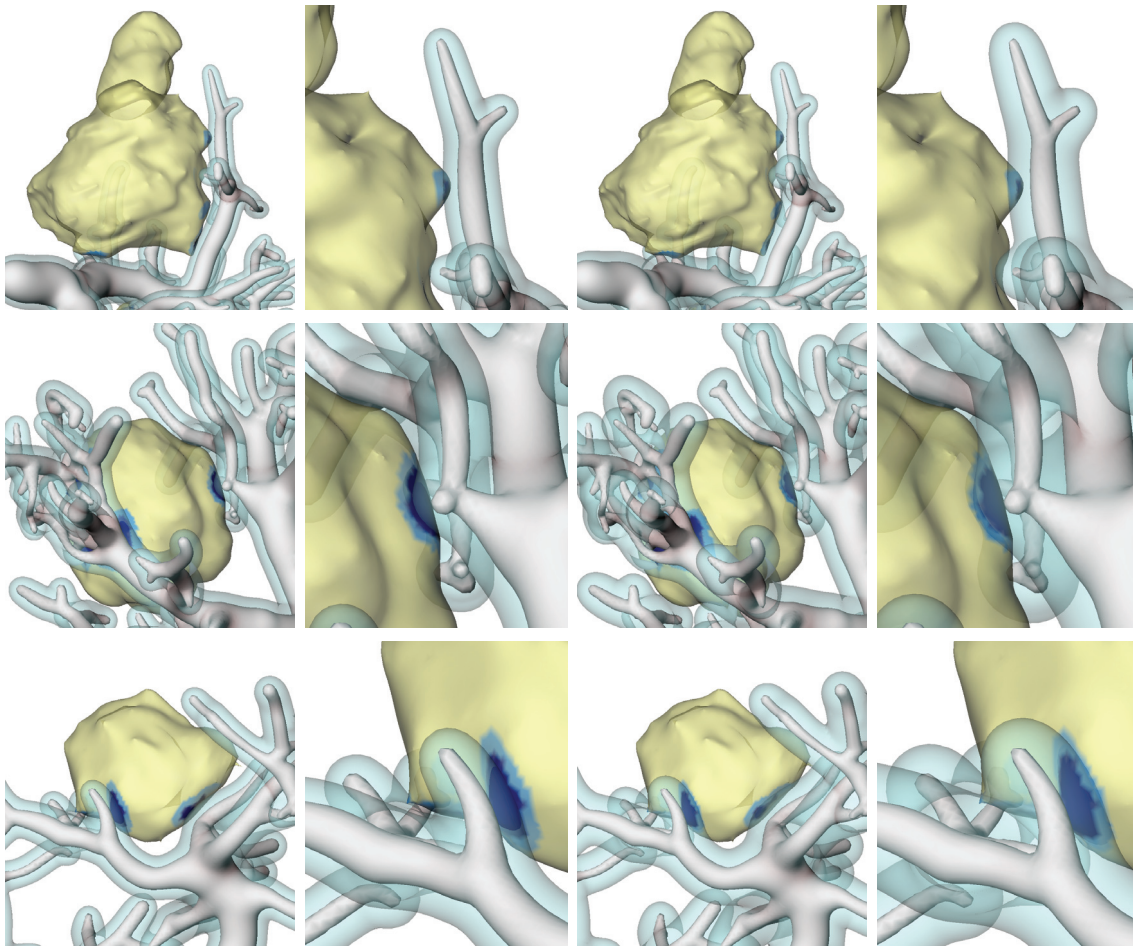


Figure 5.14: Different views of the single tumors from Fig. 5.13 next to the vessels of the portal vein, together with the corresponding color coding of the tumors (cf. Fig. 5.13), and criticality tubes (depicted in a transparent blue color) around the vessels, for $d_{\max} = 5.0$ mm (left two columns) and $d_{\max} = 10.0$ mm (right two columns). The figures in column 2 and 4 are zoomed views of the configurations shown in column 1 and 3. (Note, that slightly deviations of the criticality tubes from the color coding of the tumors are due to visualization artifacts.)

look-up-table which takes about 28 min and 19.13 s on a standard PC, but only has to be performed once in the beginning, the determination of the maximum allowable distances between the considered RF probe and the respective vessels, i. e. the determination of the color coding of the tumors and criticality tubes around the vessels takes only about 1 min and 33.20 s.⁶

In addition to the above described calculations for a probe cluster lying parallel to the vessel of interest, a three-dimensional forward simulation has been performed also for two different positionings of the RF probe cluster orthogonal to the consid-

⁶Note, that the visualization of the criticality tubes also needs some time.

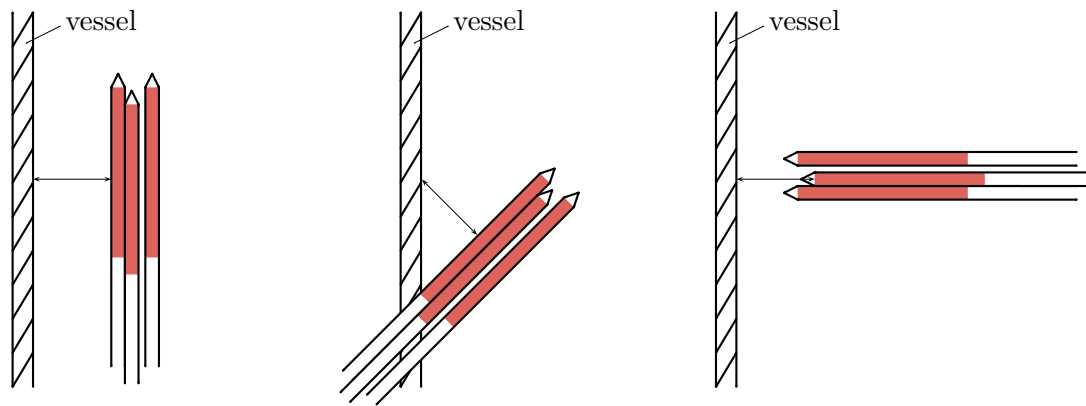


Figure 5.15: Three different positionings of the RF probe cluster with respect to the considered vessel. Left: Parallel setting. Middle: Skew-orthogonal setting. Right: Direct-orthogonal setting.

ered vessel (see Fig. 5.15). Here, in all three cases the RF probe cluster has been placed at a distance of 12.0 mm to the vessel and the generator has been set to a power of 100 W. Finally, the results of the forward simulations, have been compared after a simulated ablation time of 10 min and 20 min, respectively. The results have shown, that in the first two cases (Fig. 5.15, left and middle) the distance of the region of coagulated tissue to the considered vessel is the same, namely 2 voxels (i. e. 2.0 mm) after 10 min ablation time and 1 voxel (i. e. 1.0 mm) after 20 min ablation time. In the third case (Fig. 5.15, right), the distance of the region of coagulated tissue to the considered vessel is 2 voxels after 10 min and 20 min ablation time, respectively, i. e. such a probe positioning seems to be rather unfavorable, since it yields a slightly lower tumor destruction close to large vessels, than the other two probe placements. Consequently, the more favorable positionings (see Fig. 5.15, left and middle) are more interesting for the calculation of the maximal probe-vessel distances and criticality tubes. However, the respective calculations for the positioning shown in the right schematic of Fig. 5.15, still may be computed in a future work.

5.5 Discussion and Outlook

A model that allows for a fast calculation and visualization of the maximum allowable distances between an applied RF probe and large blood vessels near to tumors which are to be destroyed by RF ablation, has been presented. The model is based on a two-dimensional calculation of a look-up-table containing the thicknesses of vital tissue around large vessels in dependence of the vessel radius and the distance of the considered RF probe to the respective vessel. Moreover, the algorithm has been applied to a CT-segmented set of real patient data. The results of the respective color coding of the tumors and display of the corresponding criticality tubes, respectively, show that for a movement of the considered RF probe cluster by (only)

5.0 mm nearer to the vessels (from 10.0 mm to 5.0 mm distance to the vessels), the range of destroyable tumor region can be increased considerably. This result particularly confirms the benefit of a computerized support, as presented here, i. e. which analyzes the cooling influence of large blood vessels and in particular determines the corresponding maximum allowable distances of the applied RF probe to the respective vessels to be able to destroy certain tumor regions lying near to these vessels.

Note that as mentioned before, when considering the results of such a calculation, it has to be kept in mind that the approach considered here, indicates tumor regions which should be treated with care and yields quantitative information about the best probe positioning, whereas the conclusions drawn from this calculation are still up to the attending radiologist and may vary individually.

Finally, there are several ideas for future extensions to the presented algorithm:

- First the dependencies between the maximal probe-vessel distance d_{\max} , the vessel radius R_{bv} and the thickness d_{vt} of the criticality tube C can be extended by further quantities such as the critical temperature T_{crit} at which the tissue is considered destroyed, the blood flow rate in large vessels, as well as variable tissue properties.
- Moreover, since all involved material parameters are unknown for the specific patient, the corresponding PDEs might be modeled to consider stochastically distributed material parameters. Consequently, this would yield distributions of criticality tubes C and distances d_{\max} whose statistics could be visualized.
- Further, the visualization might be extended towards an interactive visualization, where the user can scroll through the different layers of criticality tubes C around the vascular tree, for varying probe-vessel distances d . Such a kind of visualization in particular would show the behavior of the criticality tubes with respect to changes in the probe-vessel distances and thus demonstrate the significance of the results. Fig. 5.16 shows a configuration where all layers of criticality tubes are shown simultaneously for $d_{\max} = 5.0$ mm, $d_{\max} = 10.0$ mm and $d_{\max} = 12.0$ mm. This gives a first impression of the described interactive view, where the user can scroll through these layers.

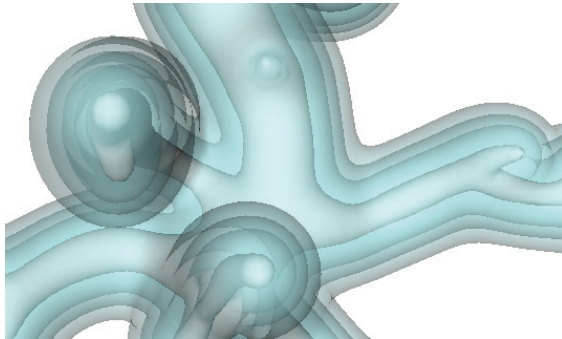


Figure 5.16: Configuration showing a cutout of the hepatic vein and all layers of criticality tubes simultaneously, for a probe-vessel distance of 5.0 mm, 10.0 mm and 12.0 mm.

Also the addition of a movable RF probe within the visualization is thinkable, such that the user himself can move the probe to see the resulting changes in the criticality tubes. Furthermore, the tubes of vital tissue alternatively could be visualized through a tumor coloring with only two colors marking destroyed and vital tumor regions, respectively and changing automatically according to the probe movements.

- A more basic step would be the improvement of the results of the underlying vessel segmentation, or more precisely the development of a correction model for the segmented vessel radii (based on mathematically and physically founded heuristics).
- Furthermore, some first steps towards an experimental validation and error quantification of the presented algorithm (i. e. of the forward modeling, as well as the reduction to the single-vessel-model) are planned in collaboration with the Charité Berlin.⁷
- Finally, of additional interest might be the transfer of the presented 2D calculation of the heat equation to the problem of optimizing the probe placement as described in Chapt. 3. Since the optimization of the probe placement is time consuming, because it requires the repeated solution of the potential and heat equation in each step of the optimization, the respective algorithms might be considerably accelerated (with hopefully not too much loss of accuracy which of course would have to be tested) by using such a two-dimensional approximation of the steady state heat equation as presented here (see Sect. 5.2, p. 94).

⁷Charité, Campus Benjamin Franklin, Hindenburgdamm 30, 12203 Berlin, Germany; <http://www.charite.de>.

6 Further Extensions and Improvements

6.1 Coupled Optimization of Bipolar Probe Placement and Setup Power

In the following an optimization of the location and direction of a bipolar probe together with a constant value for the setup power as additional optimization parameter will be considered. Thereby, mainly two challenges arise:

- Firstly, when optimizing the placement of bipolar (instead of monopolar) probes, the 60 °C–isosurface of the temperature and thus the region of coagulated tissue is no longer convex, but rather “peanut-shaped” (see Fig. 6.1 and 6.7 B). This, in some situations (especially for low setup power values where this “peanut-shape” is particularly distinctive), intensifies the problem of local optima for the probe’s positioning significantly, such that an adequate optimization has to be considered and implemented.
- Secondly, when incorporating a constant value for the setup power as additional optimization parameter, no longer only the distribution of heat is optimized, but also the intensity of heat which is induced into the tissue. Hence, we need a new objective functional that considers the saving of the native tissue.

To get the problem of local optima under control, as a first step a (geometric) pre-optimization with a convex, ellipsoidal-shaped region of coagulated tissue is implemented. Thereby, the region of coagulated tissue is not recomputed in each step of the pre-optimization, but only is moved according to changes in the probe positioning (cf. [85]). Moreover (since here, not only the probe placement but also the setup power is optimized) the size of the region of coagulated tissue must be changed in each step of the iteration according to changes in the size of the setup power. These changes in the size can be computed analytically with help of the following considerations:

To calculate the heat source Q_{rf} , the following formula (cf. (2.14)) is used:

$$P(x) = \sigma |\nabla \phi(x)|^2 \ ,$$
$$Q_{\text{rf}}(x) = P(x) \frac{P_{\text{eff}}(P_{\text{setup}})}{P_{\text{total}}} =: P(x) F(P_{\text{setup}}) \ ,$$

6 Further Extensions and Improvements

where the function $F : \mathbb{R} \rightarrow \mathbb{R}$ is defined by

$$F(P_{\text{setup}}) = \frac{P_{\text{eff}}(P_{\text{setup}})}{P_{\text{total}}} = \frac{4P_{\text{setup}}RR_{\text{I}}}{(R + R_{\text{I}})^2 \int_D P(x) dx} .$$

Here, P_{setup} is the value set up at the generator's control unit (see Sect. 2.2). This is one of the parameters which are to be optimized. Further, R_{I} is the inner resistance of the generator and $R = \frac{U^2}{P_{\text{total}}} = \frac{(2V)^2}{P_{\text{total}}}$ is the impedance for bipolar probes. Moreover, $\phi(x)$ is the electric potential of the tissue (see (2.13)), $P(x)$ is the unscaled, fixed power which is independent of P_{setup} , and $Q_{\text{rf}}(x)$ is the heat source, or more precisely the scaled power that depends on P_{setup} via the power P_{eff} that effectively acts on the tissue (cf. Sect. 2.2, Eq. (2.3)). Therewith, we can write the steady state heat equation as:

$$\begin{aligned} -\lambda\Delta T(x) + \nu(x)T(x) &= \nu(x)T_{\text{body}} + P(x)F(P_{\text{setup}}) && \text{in } D , \\ T(x) &= T_{\text{body}} && \text{on } \Gamma_{\text{out}} . \end{aligned} \tag{6.1}$$

Now assume $T_{P_{\text{setup}}}(x)$ to be the solution of (6.1) for given P_{setup} . Then the change in the size of the coagulated tissue for two different solutions $T_{P_{\text{setup},1}}$, $T_{P_{\text{setup},2}}$ is dependent on the difference $d_T := T_{P_{\text{setup},1}} - T_{P_{\text{setup},2}}$ between these solutions, where this difference d_T can be calculated by

$$\begin{aligned} -\lambda\Delta d_T(x) + \nu(x)d_T(x) &= P(x) (F(P_{\text{setup},1}) - F(P_{\text{setup},2})) && \text{in } D , \\ d_T(x) &= 0 && \text{on } \Gamma_{\text{out}} . \end{aligned} \tag{6.2}$$

Let $w(x) \in H^1(D)$ be the solution of

$$\begin{aligned} -\lambda\Delta w(x) + \nu(x)w(x) &= P(x) && \text{in } D , \\ w(x) &= 0 && \text{on } \Gamma_{\text{out}} , \end{aligned} \tag{6.3}$$

i. e. w is the solution of that part of the temperature equation (6.1) which is independent of P_{setup} . Then the solution $T_{P_{\text{setup}}}$ of (6.1) for a certain value of P_{setup} efficiently can be determined by using the solution of w , i. e. by

$$T_{P_{\text{setup}}}(x) = T_{\text{body}} + F(P_{\text{setup}})w(x) \quad \forall x \in \overline{D} , \tag{6.4}$$

which can be seen by inserting Eq. (6.4) into Eq. (6.1). Consequently, the difference $d_T(x)$ can be modeled by

$$d_T(x) = w(x) (F(P_{\text{setup},1}) - F(P_{\text{setup},2})) \quad \forall x \in \overline{D} .$$

Hence, for the pre-optimization, we only need to calculate the integral $P_{\text{total}} = \int_D P(x) dx$ (for the calculation of $F(P_{\text{setup}})$) and the function w numerically once

in the beginning.¹ Here, the integral $P_{\text{total}} = \int_D P(x) dx$ is determined by an RF-forward simulation with help of finite elements. For the calculation of the function w we need some further considerations:

With (6.4), the region of coagulated tissue for a particular setup power value P_{setup} is given by

$$\begin{aligned} I_{P_{\text{setup}}} &:= \{x \mid T_{P_{\text{setup}}}(x) \geq T_{\text{crit}}\} = \{x \mid T_{\text{body}} + F(P_{\text{setup}}) w(x) \geq T_{\text{crit}}\} \\ &= \left\{ x \mid w(x) \geq \frac{T_{\text{crit}} - T_{\text{body}}}{F(P_{\text{setup}})} \right\}, \end{aligned} \quad (6.5)$$

where all tissue cells that are heated above a critical temperature T_{crit} of e. g. $T_{\text{crit}} = 60^\circ\text{C}$, are assumed to be coagulated. Now $w(x) = \frac{T_{P_{\text{setup}}}(x) - T_{\text{body}}}{F(P_{\text{setup}})}$ (see (6.4)) can be calculated for e.g. $P_{\text{setup}} = 80\text{ W}$. Thereto, $T_{P_{\text{setup}}}(x)$ and P_{total} (which is needed to determine $F(P_{\text{setup}})$) are calculated previously by an RF-forward simulation. Then with the values of $w(x)$ for $P_{\text{setup}} = 80\text{ W}$ and with a suitable minimal and maximal value for the function $w(x)$ with $x \in I_{P_{\text{setup}}}$, the region of coagulated tissue $I_{P_{\text{setup}}}$ for different values of w (and thus indirect for different values of the setup power P_{setup}) can be determined via the definition presented in (6.5).²

In a next step the radii $r_i(I_{P_{\text{setup}}}(w)) = r_i(w)$, $i = 1, 2$ of a region $I_{P_{\text{setup}}}$ of coagulated tissue are determined by the following maximum-functions:

$$\begin{aligned} r_1(w) &= \max_{x \in I_{P_{\text{setup}}}} \text{dist}(x, g), & g &:= \{p + \alpha d \mid \alpha \in \mathbb{R}\}, \\ r_2(w) &= \max_{x \in I_{P_{\text{setup}}}} \text{dist}(x, E), & E &:= \{p + \alpha n_1 + \beta n_2 \mid \alpha, \beta \in \mathbb{R}\}, \end{aligned}$$

where (as in the previous chapters) p , d are the probe's position (i. e. the center of the probe's active zone) and the probe's orientation, respectively, and n_1 , n_2 are two different vectors orthogonal to the probe. Thus, g is the probe axis and E is the plane orthogonal to the probe and running through the center p of the probe's active zone. Note that for this first pre-optimization, the region of coagulated tissue is assumed to be rotationally symmetric around the probe axis, such that we have only two different radii. Moreover, since we use a bipolar probe, naturally the shapes of the isosurfaces of w and thus the shapes of the regions of coagulated tissue $I_{P_{\text{setup}}}$ are "peanut-shaped", which intensifies the problem of local optima. Thus, here the radii $r_1(w)$ and $r_2(w)$ are used to construct an ellipsoidal-shaped approximation D_{coag} of the region $I_{P_{\text{setup}}}$ of coagulated tissue (see Fig. 6.1), which then is used for the pre-optimization.

¹Note that for a new probe with new dimensions and/or a new grid with another voxel size, the integral $P_{\text{total}} = \int_D P(x) dx$ and the function w have to be recalculated, since they depend on the unscaled power P and thereby on the potential ϕ that itself depends on the length of the probe's isolator and the size of the probe's electrodes, as well as their resolution on the grid.

²Within the implementation, this determination is performed by a traversal of the voxels belonging to the computational domain D and by checking the value of w in each voxel.

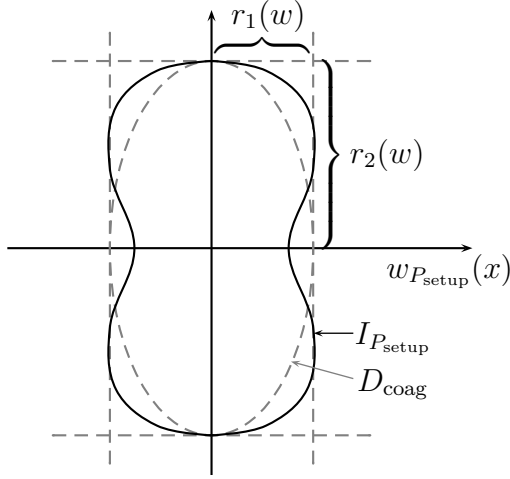


Figure 6.1: Two-dimensional schematic, showing the determination of the two radii $r_1(w)$ and $r_2(w)$ of the ellipsoid D_{coag} that approximates the rather “peanut-shaped” region $I_{P_{\text{setup}}}$ of coagulated tissue.

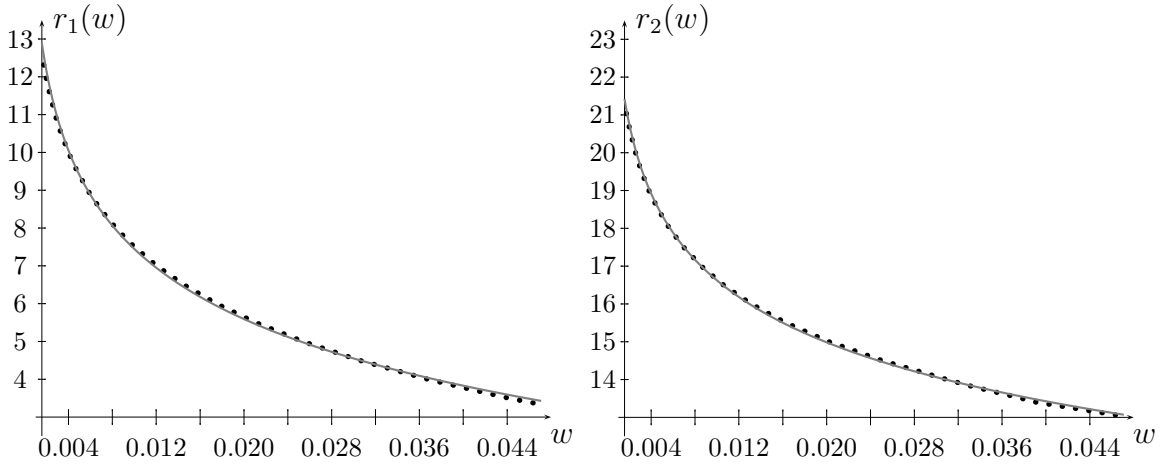


Figure 6.2: Radii of an ellipsoidal-shaped approximation of the region of coagulated tissue for a bipolar probe used for the artificial example with a grid of 120^3 grid cells and a voxel size of 0.5 mm^3 . Left: Radius of the latitude. Right: Radius of the longitude.

To approximate the radii detected for different iso-levels of w (see Fig. 6.2; black, dotted lines) by a smooth function (see Fig. 6.2; gray, solid lines), an analytical approximation with help of the following ansatz-functions is used:

$$y_i = a x_i^c + b , \quad i = 1, \dots, N , \quad (6.6)$$

where $x_i = \frac{T_{\text{crit}} - T_{\text{body}}}{F(P_{\text{setup}})}$ for N different values of P_{setup} . The values of the unknown parameters a , b and c are approximated numerically by a least squares optimization via a gradient descent method.

Now we have a smooth approximation of the radii r_1 and r_2 of the ellipsoidal-shaped, approximative region of coagulated tissue D_{coag} in dependence on the iso-levels of w (and thus on the setup power values P_{setup}). Next, we have to check

6.1 Coupled Optimization of Bipolar Probe Placement and Setup Power

whether a point x of the computational domain D lies within this ellipsoid of coagulated tissue or not. Thereto, we consider the schematic in Fig. 6.3. Let p , which is the center of the probe's active zone and thus the center of D_{coag} , be the reference point. Then $\lambda = (x-p, d)/(d, d)$ is the displacement of point x in direction of the longitudinal axis of the ellipsoid D_{coag} , and $\mu = |\vec{b}|$ with $\vec{b} = x - (p + \lambda d)$, is the displacement of x in direction of the latitudinal axis of D_{coag} . Hence, the point x

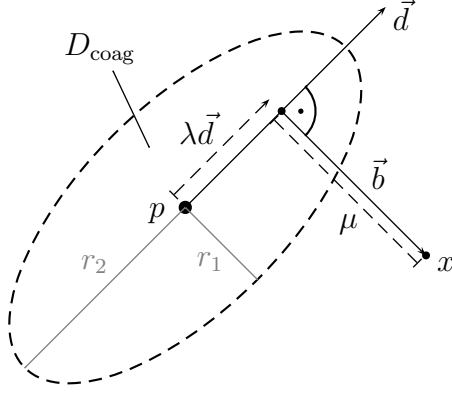


Figure 6.3: Schematic configuration of the ellipsoidal-shaped, approximative region of coagulated tissue D_{coag} with radii r_1 and r_2 , located in the center $p = (p_1, p_2, p_3)$ of the probe's active zone, and aligned with the probe's direction \vec{d} . For each point $x = (x_1, x_2, x_3)$ of the computational domain D , it has to be tested, if x lies in D_{coag} , or not.

belongs to D_{coag} if the inequality $\frac{\lambda^2}{r_1^2} + \frac{\mu^2}{r_2^2} \leq 1$ is fulfilled.

The next step in modeling a geometric pre-optimization with an ellipsoidal-shaped region of coagulated tissue (depending on the placement of the probe and size of the setup power) is the definition of a suitable objective functional. Since, besides the placement of the probe, i. e. the distribution of heat, also the intensity of heat shall be optimized here, the objective functional has to consist of at least two parts: One part modeling the destruction of the tumor, and another part modeling the saving of the native tissue. A first approach for an objective functional $f : \mathbb{R}^3 \rightarrow \mathbb{R}$ is defined by:

$$f(D_{\text{coag}}) = w_{\text{in}} \mathcal{L}(D_t \setminus D_{\text{coag}}) + w_{\text{out}} \mathcal{L}(D_{\text{coag}} \setminus D_t) , \quad (6.7a)$$

where \mathcal{L} is the Lebesgue measure, i. e.

$$f(D_{\text{coag}}) = w_{\text{in}} \int_{D_t} (1 - 1_{D_{\text{coag}}}(x)) dx + w_{\text{out}} \int_{D \setminus D_t} 1_{D_{\text{coag}}}(x) dx , \quad (6.7b)$$

where

$$1_{D_{\text{coag}}}(x) = \begin{cases} 1 , & \text{for } x \in D_{\text{coag}} , \\ 0 , & \text{for } x \in D \setminus D_{\text{coag}} . \end{cases} \quad (6.8)$$

By setting $s := \frac{\lambda^2}{r_1^2} + \frac{\mu^2}{r_2^2}$ (cf. Fig. 6.3) one can also write (6.8) as

$$1_{D_{\text{coag}}}(s) = \begin{cases} 1 , & \text{for } s = \frac{\lambda^2}{r_1^2} + \frac{\mu^2}{r_2^2} \leq 1 , \\ 0 , & \text{else} . \end{cases} \quad (6.9)$$

Unfortunately, (because of the jump in $1_{D_{\text{coag}}}(x)$ between coagulated and native tissue) the objective functional (6.7) is not totally differentiable (not even continuous), but only partially differentiable with respect to the components of the probe's position and direction, as well as with respect to the setup power. This is not sufficient for our optimization problem. To realize this, we consider the situation presented in Fig. 6.4: Obviously, in Fig. 6.4 an appropriate next step within an optimization

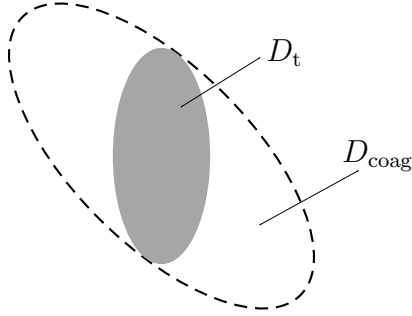


Figure 6.4: Schematic of a critical configuration for the location and size of the coagulated tissue region D_{coag} compared to the location and size of the tumor region D_t . Here, the objective functional (6.7) would be an unfavorable choice for an optimization.

of the probe placement (p, d) and setup power P_{setup} , i. e. within an optimization of the placement and size of the region of coagulated tissue D_{coag} , would be a rotation and reduction of the size of D_{coag} , such that the direction and size of D_{coag} better fits to the shape of the tumor. When using the objective functional (6.7), which is only partially differentiable, a rotation and reduction of the size of D_{coag} can only be considered separately. However, for the situation shown in Fig. 6.4, a rotation without a reduction of the size does not decrease the objective function value, since the tumor D_t already is completely covered by the region of coagulated tissue D_{coag} . In addition, a reduction of the size without a rotation does not decrease (but rather increase) the objective function value, since the tumor D_t ranges to the border of D_{coag} .

To obtain an objective functional that is totally differentiable, we have to consider a small range $D_{\pm\epsilon}$ between coagulated and native tissue (see Fig. 6.5) on which there is a smooth transition between the states of coagulation (modeled by the voxel value 1) and vitality (modeled by the voxel value 0).

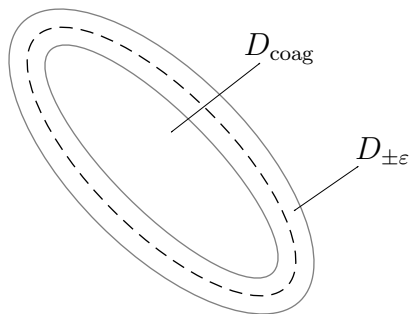


Figure 6.5: Region of coagulated tissue D_{coag} , where voxel values are set to 1, together with a small range $D_{\pm\epsilon}$, where the state of coagulation passes into the state of vitality, i. e. where the voxel value 1 from inside the region of coagulated tissue D_{coag} smoothly decreases to the voxel value 0 outside D_{coag} , i. e. on the native tissue $D \setminus D_{\text{coag}}$.

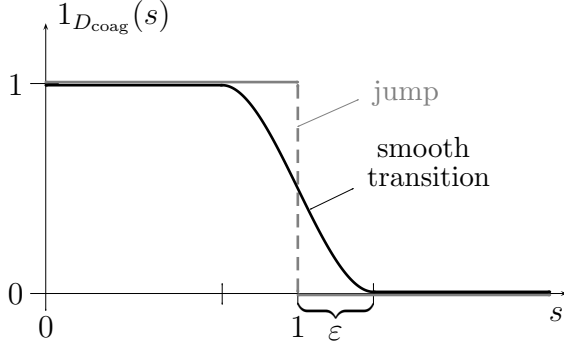


Figure 6.6: Function $1_{D_{\text{coag}}}(s)$, which is 1 for the state of coagulation and 0 for the state of vitality. *Gray Curve:* Jump between coagulated and native tissue (see formula (6.9)). *Black Curve:* ε -range of smooth transition between coagulated and native tissue (see formula (6.11)).

In Fig. 6.6, the black curve shows such a smooth transition between the states 1 of coagulation and the state 0 of vitality. This smooth transition can be modeled by e. g. the complementary error function $\text{erfc}(x) = 1 - \text{erf}(x) = \frac{2}{\sqrt{\pi}} \int_x^\infty e^{-t^2} dt$, or e. g. a polynomial of degree 3. Here, the polynomial

$$h_\varepsilon(s) = \frac{(s-1)^3}{4\varepsilon^3} - \frac{3(s-1)}{4\varepsilon} + \frac{1}{2}, \quad \text{for } s \in (1-\varepsilon, 1+\varepsilon) \quad (6.10)$$

has been used. Hence, the function $1_{D_{\text{coag}}}(s)$ (see (6.9)) within the objective functional (6.7) now subdivides into 3 different cases:

$$1_{D_{\text{coag}}}(s) = \begin{cases} 1, & \text{for } s \leq 1 - \varepsilon, \\ h_\varepsilon(s), & \text{for } s \in (1 - \varepsilon, 1 + \varepsilon), \\ 0, & \text{for } s \geq 1 + \varepsilon. \end{cases} \quad (6.11)$$

With this definition of $1_{D_{\text{coag}}}(s)$ we obtain a suitable objective functional for the pre-optimization.

For the main optimization the objective functional

$$f(T) = w_{\text{in}} \int_{D_t} \exp(\alpha(T_{\text{crit}} - T(x))) dx + w_{\text{out}} \int_{D \setminus D_t} (T(x) - T_{\text{body}})^2 dx \quad (6.12)$$

with $\alpha = 1$ and $T_{\text{crit}} = 60^\circ\text{C}$ is used. The pre-optimization and also the main optimization can be performed by e. g. a gradient descent method as described in the previous chapters. Note that for the gradient descent, the descent direction for the setup power value has to be additionally weighted, so that the impact of the probe placement and the setup power have the same magnitude and thus interact within the optimization. This is due to the requirement that the influence of one of the optimization parameters must not be completely covered by the other optimization parameters. Therefore, the units of the parameters belonging to the probe placement have to be adapted to the unit of the setup power. (cf. Sect. 3.4.1, p.43). Further, within the step size determination it is additionally tested if the step size can be re-increased for only the setup power, or for only the probe placement. All other parts of the implementation of the gradient descent method (i. e. all other details of

the calculation of the descent direction, determination of the step size and choice of an appropriate stopping criterion) are analog to the computation of the gradient descent method described in Sect. 3.4.

In the following, some first results are presented for a simultaneous optimization of a bipolar probe's placement and its setup power value by applying an additional geometric pre-optimization as described above.

6.1.1 Results and Conclusion

The optimization results shown in this section have been obtained by the optimization presented above and applied to the example with the artificial setting, as well as to the example based on real patient data, which both are known from Sects. 3.5, 3.8 and 4.7. Hence, as described in these sections, again the dimensions of the computational domain D are $60 \times 60 \times 60$ [mm³] and $120.6 \times 79.9 \times 79.9$ [mm³] for the artificial and real example, respectively. Moreover, D is discretized by a grid of 120^3 grid cells for the artificial setting, and $154 \times 102 \times 102$ grid cells for the configuration obtained from real CT data. The bipolar RF probe has a radius of 1.2 mm, an electrode length of 9.6 mm, and a gap of 6.0 mm between the two electrodes. The tissue parameters have the same values as in Sect. 3.8, i. e. the heat conductivity is set to $\lambda = 0.5$ W/Km, the electric conductivity is set to $\sigma = 0.21$ S/m, and the perfusion is modeled by taking the values $\nu_{\text{cap}} = 0.01765$ s⁻¹ and $\nu_{\text{vessel}} = 0.05$ s⁻¹ for the artificial example, and $\nu_{\text{cap}} = 0.006067$ s⁻¹ and $\nu_{\text{vessel}} = 0.05$ s⁻¹ for the real example, respectively, together with $\rho_{\text{blood}} = 1059.0$ kg/m³ and $c_{\text{blood}} = 3850.0$ J/kgK. Further, the weights within the objective functionals (6.7) with (6.11), and (6.12) (for the pre- and main optimization) are set to $w_{\text{in}} = 10000$ for the destruction of the tumor and $w_{\text{out}} = 1$ for the saving of the native tissue. The parameter ε in (6.11), i. e. the half thickness of the ε -ring which is needed within the pre-optimization for a smooth transition between the coagulated and native tissue (see Figs. 6.5 and 6.6), is set to $\varepsilon = 0.25$ mm. The constant factor α within the objective functional (6.12) for the main optimization is $\alpha = 1$. Moreover, the tissue is considered destroyed if it is heated above a critical temperature of $T_{\text{crit}} = 333.15$ K ($\hat{=} 60$ °C).

For the artificial example, the initial probe position is located at a distance of 10 mm in each coordinate direction from the center of D , and its initial orientation is $d = (5, 2, 3)$, normalized to length 1. In addition, the initial setup power value is set to 80 W, while the generator has an inner resistance of 80 Ω . During the optimization the setup power value can vary within a range of $P_{\text{min}} = 0$ W and $P_{\text{max}} = 300$ W. The pre-optimization stops if the (Euclidean) norm of the difference between the new and old iterate falls under the rather strict threshold of $\theta = 10^{-10}$ for the probe's position, the probe's direction, and the setup power value, respectively, while for the main optimization this threshold is set to $\theta = 10^{-4}$ which corresponds to the accuracy that can be achieved in practice (cf. Sect. 3.8).

The result and some intermediate steps of the optimization performed on the artificial setting are shown in Fig. 6.7. Obviously, already the pre-optimization (which here, takes 48 iteration steps due to the strict stopping criterion, but does not need

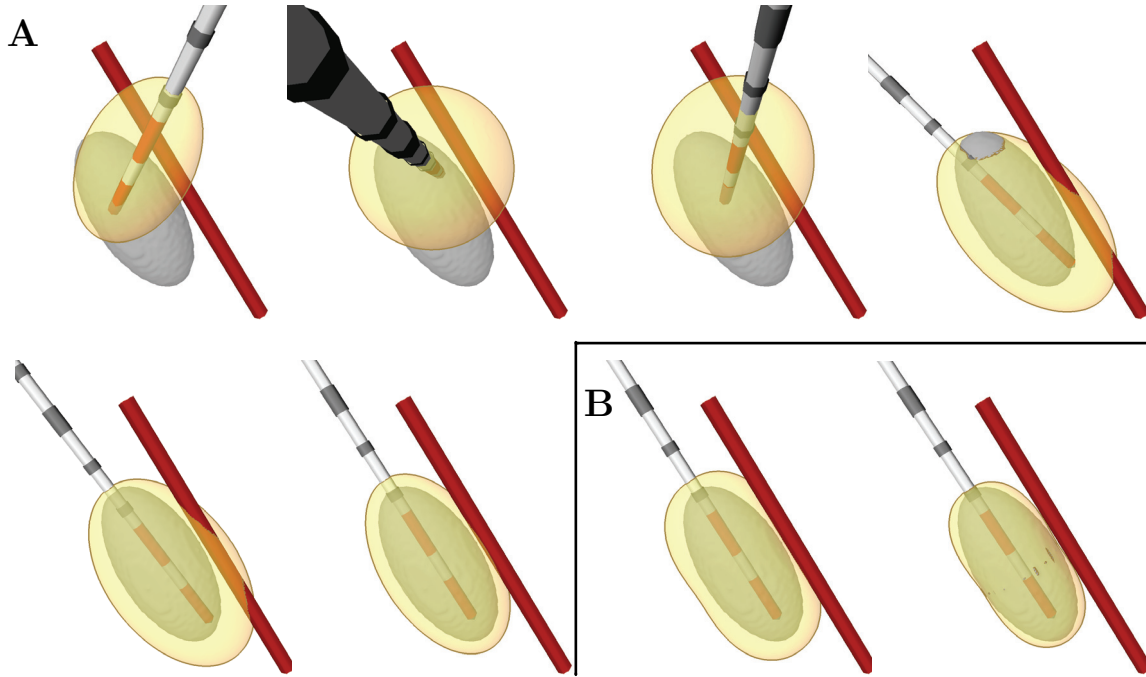


Figure 6.7: Optimization of the probe’s placement for an artificial example with an ellipsoid-shaped tumor (dark gray), a linear vessel (black), and a bipolar probe (white-gray). The transparent layer is the corresponding region of coagulated tissue and 60° -isosurface of the temperature, respectively. **A:** Steps 0 (start), 1, 2, 3, 4 and 48 of the (geometrical) pre-optimization with an ellipsoidal-shaped approximation of the region of coagulated tissue. **B:** Steps 0 and 9 of the main optimization with the 60° -isosurface of the temperature.

much computational time, because of its simple character) finds an optimal probe positioning (located in the center of the tumor and oriented along the main principal axis of the ellipsoidal tumor shape) (see Fig. 6.7 A, bottom right), while the setup power still can be decreased as notable at the result of the main optimization (see Fig. 6.7 B, right). Further, it can be observed that, compared to the 60°C -temperature profile within the pre-optimization, the corresponding temperature profile within the main optimization shows a slight “peanut shape”.

For the second example, based on real patient data, the initial probe position is located $(30.3, 10.0, 10.0)\text{mm}$ distant from the center of D and the probe’s initial direction again is set to $d = (5, 2, 3)$, normalized to length 1. Here, the initial setup power value is $P_{\text{setup}} = 200\text{ W}$ which, as for the artificial example, can vary between $P_{\text{min}} = 0\text{ W}$ and $P_{\text{max}} = 300\text{ W}$ during the optimization. Further, the inner resistance of the generator again is $R_{\text{I}} = 80\ \Omega$, and also the settings for the stopping criterion are the same as in the artificial case.

As the pictures in Fig. 6.8 show, again already the pre-optimization finds a good probe positioning which only slightly can be improved during the main optimization,

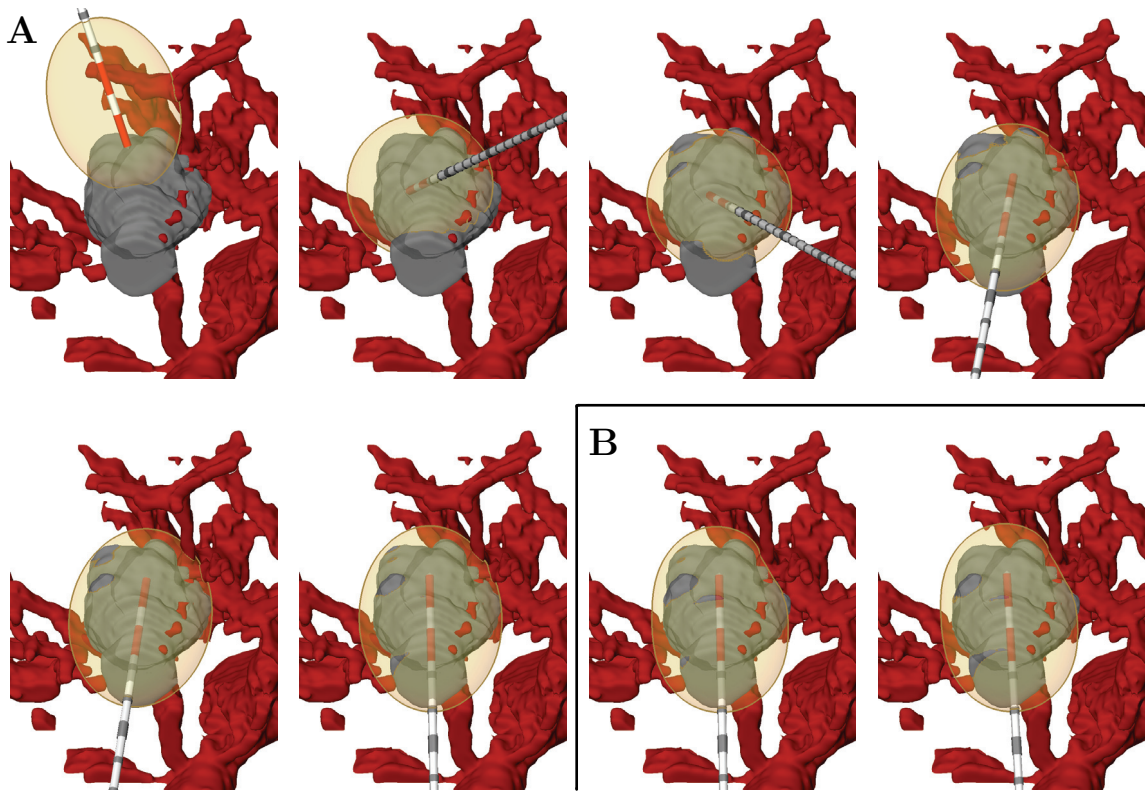


Figure 6.8: Optimization for an example based on patient data with a segmented tumor and surrounding vascular system. Here, we have a bipolar probe with the corresponding region of coagulated tissue and 60° -isosurface of the temperature, respectively. **A:** Steps 0 (start), 1, 2, 3, 4 and 15 of the (geometrical) pre-optimization with an ellipsoidal-shaped, approximative region of coagulated tissue. **B:** Steps 0 (start) and 10 of the main optimization with the 60° -isosurface of the temperature.

where the influence of the vessel cooling forces the probe to move a little bit closer to the vessels by performing a slight rotation (cf. Fig. 6.8 A, bottom right and Fig. 6.8 B, right). The optimal setup power value for the pre- and main optimization is the maximum value of $P_{\max} = 300$ W which is not really surprising, since the tumor is relatively large (length of main axes: 45.9 mm, 41.9 mm and 36.2 mm; see Sect. 3.5), so that in practice, the attending radiologist decided to use a cluster of three parallel monopolar probes (cf. Sects. 3.5 and 3.8).³ Here, the high setup power

³Here, the size of the 60° -temperature profile is even smaller than the one obtained in Sect. 3.5 (see Fig. 3.10) with a setup power of only 200 W (instead of 300 W as applied here). The reason for this, is that in Sect. 3.5, the perfusion is modeled still too weak (which however, for an optimization of only the probe placement without changing the overall intensity of heat, plays no major role, i. e. has no major impact on the optimal probe's positioning). Moreover, also the 60° -temperature profiles presented in Sect. 4.7.2, Figs. 4.9, 4.13 and 4.15, again obtained for a setup power value of (only) 200 W, are larger than the one depicted in Fig. 6.8, which in this case is caused by the different modeling of the tissue parameters.

value is responsible for the 60° –temperature profile not to look particularly “peanut-shaped” for this real example. However, an interesting detail of the optimization result presented in Fig. 6.8 is that the optimal probe direction found by the algorithm applied here, shows approximately the opposite orientation than the optimal probe directions found by all previously presented optimization algorithms. For example, compared to the optimal probe placement found by the algorithm presented in Sect. 3.7.1 (see Alg. 3.2 and Sect. 3.8, Fig. 3.16), the optimal probe position shown in Fig. 6.8 differs from the one shown in Fig. 3.16 only by a norm of about 0.7 mm, whereas the optimal probe orientations differ by an angle of about 169.8° . This is due to the fact that without considering constraints for the probe’s infeed channel due to anatomical structures that must not be punctured (as e.g. larger vessels, bones, or inner organs), obviously the infeed of the RF probe from a certain direction yields the same optimization result than the infeed from the opposite direction.

A further improvement of the presented algorithm for example might be the combination with a multi-grid approach as described in Sect. 3.7. Moreover, a coupling with a “simulated annealing” like scheme, as will be introduced in the next section, might be an additional enhancement of the algorithm.

6.2 Optimization of the Number and Placement of Uncoupled Probes

In this section we consider an optimization of the position and direction of several uncoupled RF probes. More precisely, if after an optimization with a fixed number of probes, the minimal temperature inside the tumor is not high enough, a new RF probe is added and the optimization starts anew. Unfortunately, when optimizing the placement of several uncoupled probes, the 60°C –isosurface of the temperature and therewith the region of coagulated tissue is no longer convex which intensifies the problem of local optima considerably (cf. Sect. 6.1).

To handle this problem, here a “simulated annealing” like scheme (see e.g. [53], [73]) is applied to the first pre-optimization of the multi-scale algorithm known from Sect. 3.7.⁴ More precisely, the following two extensions are added to the first pre-optimization of the existing algorithm for optimizing the probe placement:

- At the end of each iteration step the current solution, i.e. the new iterate is replaced by a random “nearby” solution before the iteration starts again. Thereby, the changes in the current solution are gradually decreased. As in Sect. 3.7, the iteration continues until the (Euclidean) norm of the differences between the new and old iterate passes a given threshold θ .
- Moreover, at the end of the first pre-optimization on the coarsest grid, the optimal solution is replaced by a random “nearby” solution and the complete

⁴A difference to the algorithm presented in Sect. 3.7 is, that here we do not have to optimize a rotation vector, since here the probes are uncoupled, instead of being arranged in a fixed cluster.

optimization starts anew. Just as the changes in the current iterate decrease gradually, the changes in the optimal solution grow smaller. The replacement of the optimal solution and restart of the optimization is repeated 18 times⁵. After that, the best optimal solution of these 18 optimizations is taken as initial configuration for the second pre-optimization (which remains unchanged).

A further enhancement to the existing algorithm is the modeling of a restriction for the probe's orientation. More precisely, the angle between each RF probe and a predefined axis \vec{a} must not exceed a given degree δ . This is a first step towards a consideration of anatomical structures that must not be punctured.

Implementation The implementation of the random changes in the probe position and direction after each iteration step, and coarse-grid optimization respectively is performed using the following equations:

$$p_i += \varepsilon \cdot |D_i| \cdot RV_i, \quad \text{for } i = 1, 2, 3, \quad (6.13a)$$

$$d_i += \varepsilon \cdot RV_{i+3}, \quad \text{for } i = 1, 2, 3. \quad (6.13b)$$

Here, p_i and d_i are the i -th component of the probe position and direction at the end of an iteration step, and at the end of the current or previous optimization respectively. In the second case, the optimal probe placement of the previous optimization is used if this yields a lower objective function value than the optimal probe placement of the current optimization. The other quantities of equations (6.13a) and (6.13b) are the extent $|D_i|$ of the computational domain D in direction i , a random number $RV_i \in [-1, 1] \subset \mathbb{R}$ which varies for each iteration step and optimization respectively, and a variable ε which is different for changes after each step of an iteration and changes after a complete optimization. In both cases, at the beginning (i. e. for each first iteration step, and for the first optimization respectively) the variable ε is set to the initial value of $\varepsilon = 1.0$ and then gradually decreases. More precisely, the gradual decrease of the variable ε (i. e. of the random changes of the probe placement) is modeled via the following heuristic approach:

- For decreasing the random changes of the current solution within an iteration, the variable ε is bisected after each iteration step.
- Further, for decreasing the random changes of the optimal solution after a complete optimization, the respective variable ε is multiplied by 0.8 after the first 10 optimizations, and is then multiplied by 0.7, 0.6, ... and 0.1, after the 11th, 12th, ... and 17th optimization, respectively.

After each replacement of the probe's position and direction by a random "nearby" solution (either during an iteration or after a complete optimization), tests need to be performed to verify that the new quantities are still feasible, i. e. that the

⁵Here, this number of restarts is heuristically chosen (see explanation on the next page).

probe's position p still lies within the computational domain D , and that the probe's direction d did not leave the predefined admissible range. If one of these constraints is violated, the respective component has to be projected onto the corresponding feasible domain.

The first pre-optimization on the coarsest grid is finished as soon as the 18th optimization of the method described above has been performed. Then, the best solution of these 18 optimizations is taken as initial guess for the second pre-optimization on the next finer grid. Note that the second pre-optimization and the main optimization remain unchanged, since applying to them the method explained above would take too much time. Moreover, a relatively good result can be expected even on the coarsest grid, so that the next optimizations on the finer grids start with a relatively good initial guess.

Finally, if at the end of the main optimization the tumor is not completely destroyed, i. e. if the minimal temperature $T_{\min,t} := \min_{x \in D_t} T(x)$ inside the tumor D_t is lower than a certain critical temperature T_{crit} at which the tissue is considered destroyed, an additional RF probe is added and the complete optimization procedure repeated. Thereby, each new RF probe is placed parallel to the last added probe, while to each component of the probe's position, the value of 1 cm is added. The optimization with n different probes is performed in the same way as the optimization with one single probe. However, for n different probes, we have $3n$ optimization parameters for the probes' positions and $3n$ optimization parameters for the probes' orientations to be optimized simultaneously. Moreover, for n different probes, the generator power P_{setup} is shared among these probes, so that the induced overall intensity of heat is still the same as for one single probe, but the local induction of heat via the electrodes becomes more distributed.

In the following some first results for the optimization of the number and placement of several uncoupled probes using the method described above are presented and discussed.

6.2.1 Results and Discussion

The optimization results shown in this section have been obtained by optimizing the number and placement of several uncoupled probes. To this end, the method presented in the previous section has been applied to the example based on real CT data which is already known from e. g. Sect. 3.8. Hence, the computational domain D is of extent $120.6 \times 79.9 \times 79.9$ [mm³] and, as in Sect. 3.8, the discretization of D is performed by using a fine grid of $154 \times 102 \times 102$ grid cells, which is embedded into an octree grid of level $L = 7$ (cf. Sect. 3.7). More precisely, this implies the computation of pre-optimizations on two coarser grids of $77 \times 51 \times 51$ and $38 \times 25 \times 25$ grid cells. Further, all used RF probes are monopolar and have a radius of 0.75 mm, as well as an electrode length of 25.0 mm. The tissue properties are modeled by taking the values $\sigma = 0.21$ S/m and $\lambda = 0.5$ W/Km for the electrical and thermal conductivity, respectively, as well as $\nu_{\text{cap}} = 0.006067$ s⁻¹, $\nu_{\text{vessel}} = 0.05$ s⁻¹, $\rho_{\text{blood}} = 1059.0$ kg/m³ and $c_{\text{blood}} = 3850.0$ J/kgK for the modeling of the perfusion (again, see Sect. 3.8).

For this optimization, the objective functional (3.13) has been used with the factor $\alpha = 1$. Moreover, the tissue is considered destroyed if it has been heated above a critical temperature of $T_{\text{crit}} = 333.15 \text{ K}$ ($\hat{=} 60^\circ\text{C}$). The optimization starts with only one probe, located at a distance of $(30.3, 10.0, 10.0)$ mm from the center of D . The probe's initial direction is $d = (5, 2, 3)$, normalized to length 1. During optimization, the probe's direction is restricted by a maximum angular deflection of $\delta = 10^\circ$ from the z -axis. Further, the setup power is set to 200 W and the generator has an inner resistance of 80Ω . For each pre-optimization on a grid coarser than the finest, the threshold for stopping the optimization is set to $\theta = 10^{-6}$ (i. e. the change between the new and old iterates has to fall below this threshold). Within the main optimization on the finest grid, this threshold has a lower value of $\theta = 10^{-4}$ which corresponds to the accuracy that can be achieved in practice.

In Fig. 6.9 some results of this optimization are presented. Specifically, the following steps of the different optimization runs are depicted:

- The top row (denoted by \mathbf{A}_1) shows the starting and ending configuration of the 1st, 9th and 16th optimization on the coarsest grid and with only a single probe. Altogether, 18 different optimization runs are performed on this grid. The best result is then used as initial guess for the optimization on the next finer grid. Here, the best result has been achieved by the 16th optimization.
- The second row (denoted by \mathbf{B}_1 and \mathbf{C}_1) presents the starting and ending configuration of the pre-optimization on the next finer grid and the main optimization on the finest grid, respectively. Here, again we have only a single probe, which in the end cannot heat the complete tumor tissue sufficiently to achieve cell destruction. This can be observed in the right-most figure within this row, where small parts of the tumor jut out of the 60°C -temperature profile.
- In the third row (denoted by \mathbf{A}_2), a second probe has been added to the configuration and steps of the restarted optimization process are shown. More precisely, we see the start and end of the 1st, 9th and 17th optimization on the coarsest grid. The 17th of the 18 optimizations yielded the best possible result on this grid. This was used as initial guess for the optimization on the next finer grid.
- Finally, the last row (denoted with \mathbf{B}_2 and \mathbf{C}_2) shows the start and end of the pre-optimization on the next finer grid and the main optimization. In the final configuration, depicted in the right-most figure, the tumor is completely covered by the 60°C -isosurface of the temperature. Hence, no additional probe is needed, and the optimization algorithm stops.

Although it is impossible to observe from the views in Fig. 6.9, a slightly rotated view (see Fig. 6.10, right-most picture) reveals that the two probes of the resulting configuration are relatively far away from each other. More precisely, one of the

6.2 Optimization of the Number and Placement of Uncoupled Probes

probes is located close to the vessels, while the other probe has moved in the opposite direction. This allows the probes to heat the entire tumor tissue to the critical temperature of $T_{\text{crit}} = 60^\circ\text{C}$ at which it is considered destroyed.

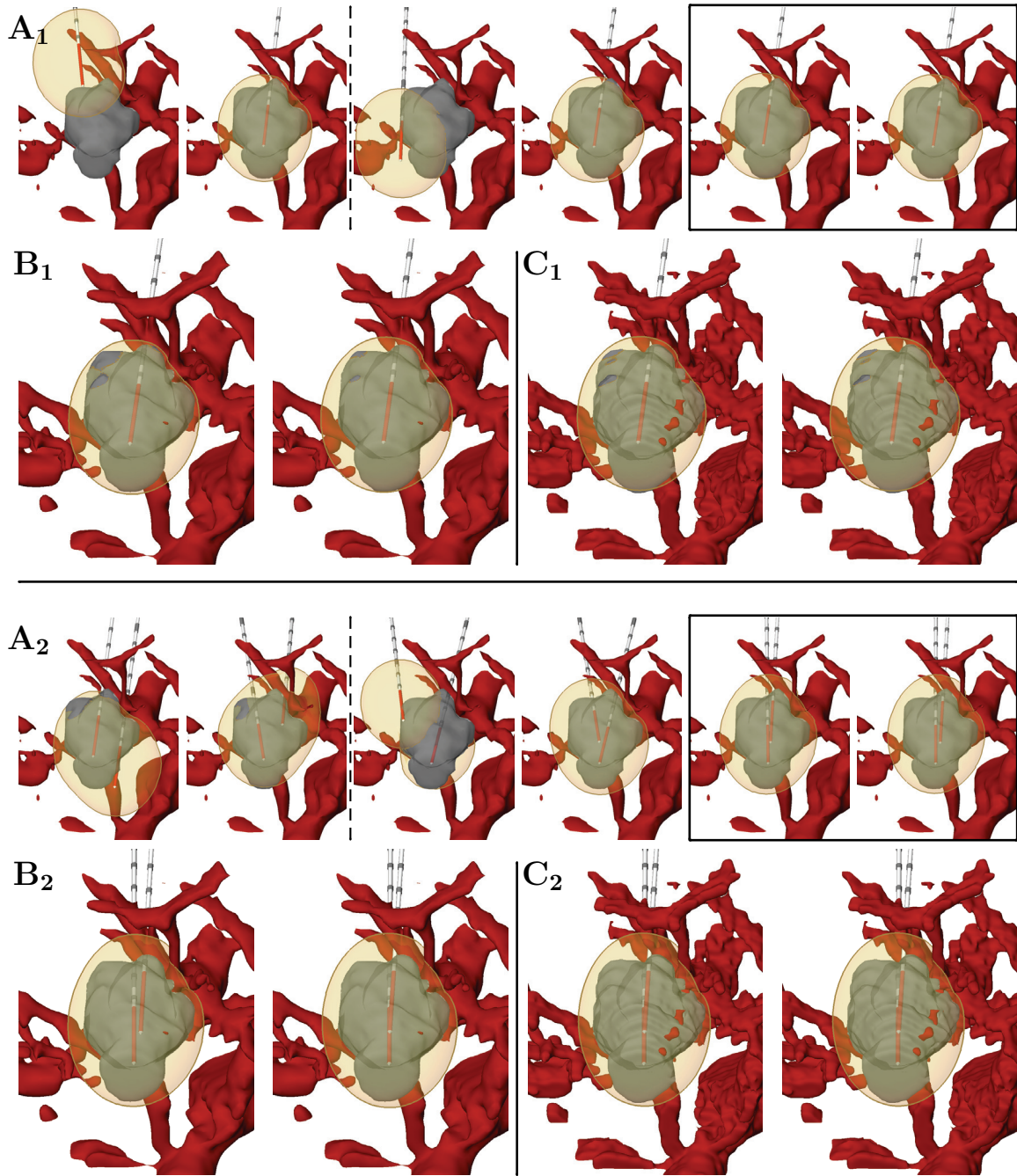


Figure 6.9: Optimization of the placement and number of monopolar probes for the example known from the previous sections (e. g. Sect. 6.1.1, Fig. 6.8). The optimization starts with a single probe (**A₁**, **B₁**, **C₁**) and ends with two probes (**A₂**, **B₂**, **C₂**). **A₁**: Steps 0 (start) and 25 of optimization (OP) 1, steps 0 and 6 of OP 9 and steps 0 and 7 of OP 16 on the coarsest grid. **B₁**: Steps 0 and 5 of the optimization on the next finer grid. **C₁**: Steps 0 and 2 (end) of the optimization on the finest grid. **A₂**: Steps 0 (start) and 25 of OP 1, steps 0 and 11 of OP 9 and steps 0 and 7 of OP 17 on the coarsest grid. **B₂**: Steps 0 and 9 of the optimization on the next finer grid. **C₂**: Steps 0 and 2 (end) of the optimization on the finest grid.

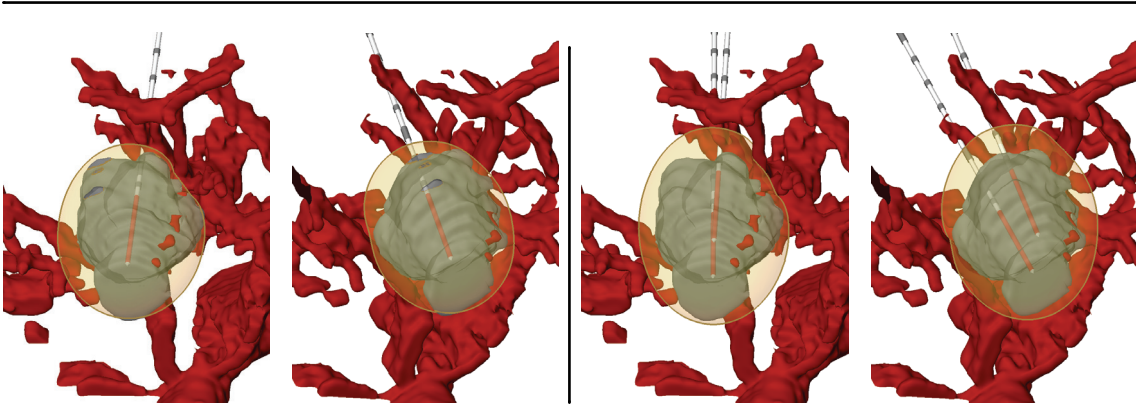


Figure 6.10: Two different views of the optimal probe placement for a single probe and for two uncoupled probes (cf. Fig. 6.9). In the case of a single probe, the tumor region is not completely covered by the 60°C -temperature profile, so that the algorithm decides to use an additional probe. In the case of two probes, one probe moves nearer to the vessels, while the other moves in the opposite direction, resulting in the entire tumor being covered by the 60°C -temperature profile.

7 Ongoing Work

7.1 Optimal Control of the Generator Power

As already addressed in Sect. 6.1, besides an optimal probe placement, also an optimization or optimal control of the generator power induced into the tissue during a radiofrequency (RF) ablation is desirable. Hence, in this section, some first considerations that aim at calculating an optimal control of the generator power are presented and discussed.

7.1.1 Problem Formulation

The temperature increase inside the tissue during an RF ablation depends considerably upon the power induced into the tissue by the electric generator. However, the calculation of an optimal control for the RF generator is challenging: On the one hand, a too high power value will dry out the tissue, making the electric conductivity of the tissue around the probe converge to zero and thus interrupting the heat supply. On the other hand, a too low power value results in a tissue temperature not high enough for tumor destruction. For these reasons, some instrument manufacturers already have equipped their generators with an automatic power management based on a temperature measurement and regulation (e. g. RITA Medical Systems), or an impedance control (e. g. Valleylab and Radionics). For example, if the tissue impedance exceeds a certain limit, the power supply is temporarily reduced or completely disabled. D. Schmidt et al. [74] have compared the efficacy of an impedance controlled power supply with a manually controlled power delivery during an RF ablation. Their results show that an impedance controlled power supply, i. e. a so-called pulsed RF ablation, significantly increases the size of the coagulation zones, because it allows for considerably longer ablation times without a significant increase of the impedance.

This in particular motivates the demand for further investigations in this direction and already indicates the benefit a more sophisticated mathematical approach for the determination of a patient-specific, *optimal* control of the generator power would yield.¹

¹Note that the automatic control of the generator power, provided by several instrument manufacturers, is based mainly on heuristics that describe the behavior of the tissue parameters under changes of the tissue impedance or temperature. In contrast to that, a mathematical approach for the calculation of an *optimal* control of the generator power would have the advantage that it is patient- and case-specific, and that it yields the best possible outcome.

In the following, an approach based on a time-dependent forward simulation of an RF ablation will be presented. After having discussed the modeling and solution of the potential and time-dependent temperature equation in Sect. 7.1.2, some first objective functionals will be derived in Sect. 7.1.3. In a next step, an algorithm for the calculation of an optimal control of the generator power, based on a gradient descent method, will be developed (see Sect. 7.1.4). Finally, the different approaches and preliminary results are discussed in Sect. 7.1.5.

7.1.2 Modeling of the Time-Dependent Problem and Numerical Solution with Finite Elements

In the following, the tissue temperature T is modeled to depend on time and space (t, x) . Moreover, as in the previous chapters, the computational domain $D \subset \mathbb{R}^3$ is modeled to be a cuboid, while the time t lies in the interval $I = [0, t_f] \subset \mathbb{R}_0^+$. Here, t_f is the time at the end of the RF ablation, i. e. the time when the generator is switched off.

Further, the electric potential with constant electric conductivity σ is calculated as in Sect. 2.3, i. e. via Eqs. (2.13).

Heat Source: After the potential ϕ has been calculated, the time-dependent heat source density Q_{rf} can be determined from ϕ by the following equations:

$$Q_{\text{rf}}(t, x) = \frac{P_{\text{eff}}(t)}{P_{\text{total}}} \sigma |\nabla \phi(x)|^2 \quad \text{in } I \times D, \quad \text{with} \quad (7.1a)$$

$$P_{\text{eff}}(t) = \frac{4 P_{\text{setup}}(t) R R_1}{(R + R_1)^2} \quad \forall t \in I, \quad (7.1b)$$

where the tissue impedance R and the whole power P_{total} are calculated as in Sect. 2.3, Eqs. (2.15). Moreover, R_1 is the inner resistance of the generator and P_{setup} is the power set up at the generator's control unit. Here, the setup power is supposed to be restricted by the following box constraint

$$P_{\text{setup}}(t) \in [P_{\text{min}}, P_{\text{max}}] \quad \forall t \in I, \quad (7.2)$$

where P_{min} is the minimal power value and P_{max} is the maximal power value which can be set up at the generator. Note that P_{setup} is the parameter for which we want to find an optimal control later on.

Perfusion: The time-dependent heat sink due to the cooling influence of blood perfusion (cf. Eqs. (2.8) and (2.16) of Sects. 2.2 and 2.3) is modeled by a weighted variant of the approach of Pennes [69]:

$$Q_{\text{perf}}(t, x) = -\nu(x) (T(t, x) - T_{\text{body}}), \quad \text{where} \quad (7.3a)$$

$$\nu(x) = \begin{cases} \nu_{\text{vessel}} \rho_{\text{blood}} c_{\text{blood}}, & x \in D_{\text{v}}, \\ \nu_{\text{cap}} \rho_{\text{blood}} c_{\text{blood}}, & \text{else.} \end{cases} \quad (7.3b)$$

As well as in Sects. 2.2 and 2.3, ν_{vessel} and ν_{cap} are the relative blood circulation rates of vessels and capillaries, respectively, ρ_{blood} is the blood density, and c_{blood} is the heat capacity of blood. Moreover, D_{v} denotes the region of the segmented vascular structures. As can be seen from Eq. (7.3b), it is assumed that the whole tissue is pervaded by capillary vessels and thus is exposed to their cooling influence.

Heat Equation: Finally, the temporal and spatial distribution of heat can be calculated from the heat source Q_{rf} and -sink Q_{perf} by the following equations:

$$\rho c \partial_t T(t, x) - \lambda \Delta T(t, x) = Q_{\text{rf}}(t, x) + Q_{\text{perf}}(t, x) \quad \text{in } I \times (D \setminus \overline{D_{\text{pr}}}) , \quad (7.4a)$$

$$T(t, x) = T_{\text{probe}} \quad \text{on } I \times \overline{D_{\text{pr}}} , \quad (7.4b)$$

$$T(t, x) = T_{\text{body}} \quad \text{on } I \times \Gamma_{\text{out}} , \quad (7.4c)$$

$$T(0, x) = T_{\text{body}} \quad \text{in } D \quad (7.4d)$$

(cf. Eqs. (2.5) and (2.17) of Sects. 2.2 and 2.3). Here, ρ , c and λ denote the density, the heat capacity and the heat conductivity of the tissue. Moreover, D_{pr} denotes the subset of D which is covered by the RF probe. The Dirichlet boundary conditions (7.4b) - (7.4d) are due to the assumptions that an internally cooled RF probe is used (with here $T_{\text{probe}} = T_{\text{body}}$), that on the outer boundary Γ_{out} of the computational domain D (i.e. far away from the probe) there is no significant heating effect any more, and that at the beginning of an RF ablation the tissue naturally has body temperature.

Discretization in Time and Space: After having presented the time-dependent model for simulating an RF ablation, now (in order to solve the model equations) a discretization of the model in time and space has to be performed.

For reasons of analogy, the following description is restricted to the solution of the heat equation (7.4) (cf. Sect. 2.4.2).

Let us assume the problem to be adjusted to homogeneous Dirichlet boundary conditions in the usual way (see e.g. [17]). The variational (or weak) form in space is obtained by multiplying the heat equation with a test function $v \in H_0^1(D)$. Integrating by parts over D leads to

$$\rho c (\partial_t T, v) + \lambda (\nabla T, \nabla v) + (\nu T, v) = (Q_{\text{rf}}, v) , \quad (7.5)$$

where (\cdot, \cdot) is either the L^2 -scalar product as described in Sect. 2.4.2, or (in case of the first term and the right hand side of (7.5)) a pairing of functions in $H^1(D)^*$ and $H^1(D)$. To this end, we identify (w, v) for $w \in H^1(D)^*$ and $v \in H^1(D)$ with $w[v]$. Note that if both $w[v]$ and $(w, v)_{L^2(D)}$ are defined, this is the same.

Before starting with the description of the applied discretization, some further remarks on the domains of the involved quantities have to be made: Here, (as in Sect. 2.4.2) the potential ϕ and the time-independent temperature $T(t, \cdot)$ lie within the Hilbert space $H^1(D)$, whereas the time-independent heat source $Q_{\text{rf}}(t, \cdot)$ only lies in $H^1(D)^*$ (cf. [8]). Further, the time-derivative $\partial_t T(t, \cdot)$ of the temperature T

as function of the space x , has to lie in $H^1(D)^*$, such that the pairing $(\partial_t T(t, \cdot), v)$ (cf. Eq. (7.5)) is well-defined. Then the time- and space-dependent temperature T is an element of the domain $L^2(I, H^1(D))$, and its time-derivative $\partial_t T$ is an element of $L^2(I, H^1(D)^*)$, where for an arbitrary Banach space X the space $L^2(I, X)$ consists of all functions $f : I \rightarrow X$ with norm

$$\|f\|_{L^2(I, X)} := \left(\int_I \|f(t)\|_X^2 dt \right)^{1/2} < \infty .$$

Both of the above requirements can be combined by the notation

$$T \in H^1(I, H^1(D), H^1(D)^*) , \quad (7.6)$$

i. e. $H^1(I, H^1(D), H^1(D)^*)$ is the space of all functions $f \in L^2(I, H^1(D))$ with derivatives $f' \in L^2(I, H^1(D)^*)$. Further, we have the norm

$$\|f\|_{H^1(I, H^1(D), H^1(D)^*)} := \|f\|_{L^2(I, H^1(D))} + \|f'\|_{L^2(I, H^1(D)^*)} .$$

Analog, the time- and space-dependent heat source density Q_{rf} can be chosen to lie in the domain

$$Q_{\text{rf}} \in L^2(I, H^1(D)^*) . \quad (7.7)$$

For this setting, the existence of a unique temperature distribution T which solves the problem (7.5) with boundary conditions (7.4b) - (7.4d) can be proven, see the example in Großmann and Roos [41]², Chapt. 5, p. 315 and the existence theorem in Zeidler [96].

In a next step, the variational problem (7.5) is discretized in time and space. The discretization in space is performed as described in Sect. 2.4.2, where – again as in Sect. 2.4.2 – the electric field $\nabla\phi$ (which is needed to calculate the heat source Q_{rf}) is determined with central differences after the solution of the potential equation (2.13).

For the discretization in time, the temperature T and the heat source density Q_{rf} are evaluated at selected, equidistant points of time t_k ($k = 0, \dots, N$) only. This yields the following fully discretized (i. e. time- and space-discretized) (linear) problem

$$\rho c M_1 \frac{T(t_{k+1}, x) - T(t_k, x)}{\tau} + (\lambda L + M_\nu) T(t_{k+1}, x) = M_1 Q_{\text{rf}}(t_{k+1}, x)$$

for $k = 0, \dots, N-1$. Here, τ is an equidistant step size in time, i. e. $\tau = \frac{t_f}{N}$. Denoting $T(t_k, x)$ with T^k , as well as $Q_{\text{rf}}(t_k, x)$ with Q_{rf}^k for $k = 0, \dots, N$, and moreover multiplying the above equation with the time step size τ , yields the following formulation of the fully discretized problem:

$$(\rho c M_1 + \tau \lambda L + \tau M_\nu) T^{k+1} = \tau M_1 Q_{\text{rf}}^{k+1} + \rho c M_1 T^k \quad (7.8)$$

²Note that some authors as e.g. Großmann and Roos [41], denote the domain $H^1(I, H^1(D), H^1(D)^*)$ (see (7.6)) as $W_2^1(0, t_f; H^1(D), L^2(D))$, where both denotations refer to the Gelfand triple $H^1(D) \subset L^2(D) \subset H^1(D)^*$.

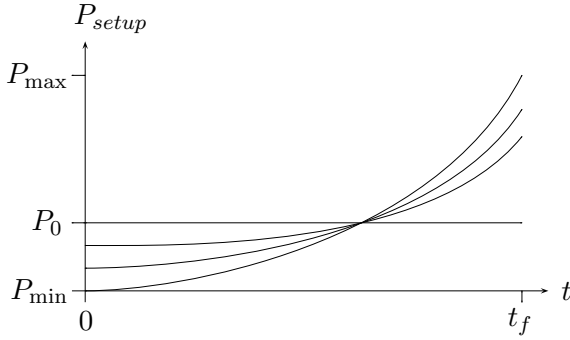


Figure 7.1: Schematic showing the convergence of the generator power P_{setup} to a setting which is P_{min} at the beginning of the RF ablation and P_{max} at the end t_f of the RF ablation. Here, as start setting we have a constant generator power of $P_{\text{setup}}(t) = P_0 \forall t \in I$.

for $k = 0, \dots, N - 1$.

Having defined a model and an appropriate discretization for the space- and time-dependent forward simulation, we now need to develop a suitable objective functional for calculating the optimal control of the generator power P_{setup} .

7.1.3 Modeling and Comparison of Different Objective Functionals

In this section, a (preliminary) objective functional for the calculation of the optimal control of the generator power will be derived in several steps: At first, an initial version of an objective functional is defined. Then, potential disadvantages are examined, and the objective functional is gradually improved.

A First Approach As described in Sects. 3.2 and 3.3, the aim of an RF ablation is to heat up the tumor D_t to a critical temperature T_{crit} at which the tissue cells die, while at the same time, the temperature of the native tissue shall be kept close to body temperature, so that as much native tissue as possible is saved. In a first attempt, the following temperature-based objective functional $f : H^1(I, H^1(D), H^1(D)^*) \rightarrow \mathbb{R}$ has been used in order to find an optimal control of the generator power that yields the desired temperature distribution of the tissue:

$$f(T) := w_{\text{in}} \int_{D_t} \exp(T_{\text{crit}} - T(t_f, x)) dx + w_{\text{out}} \int_{I \times D_n} (T(t, x) - T_{\text{body}})^2 dx dt. \quad (7.9)$$

Here, D_t and D_n are the region of the tumor and native tissue, respectively, and w_{in} and w_{out} are suitable weights for the destruction of the tumor and the saving of native tissue.

Unfortunately, with this objective functional, the calculation of an optimal control of the generator power (by e. g. Alg. 7.1 of Sect. 7.1.4) always converges to a generator power which is zero at the beginning of the ablation, and then monotonously increases until the end t_f of the ablation is reached (cf. Fig. 7.1). This result is probably due to the fact that the simulation stops directly after switching off the generator. Hence, when heating only at the end of the ablation, the simulated temperature increase has no chance to diffuse into the surrounding native tissue, and

consequently, the damage of the native tissue is not taken into account. Obviously, this is not realistic. In practice, the temperature still diffuses into the surrounding tissue after switching off the generator.

This discrepancy shows that considering additional time after switching off the generator is indispensable to determine a realistic optimal control for the generator power.

Consideration of Additional Time Let m be an appropriate amount of additional time for which the temperature diffusion is determined after switching off the generator, such that the damage of the native tissue is detected sufficiently accurate, while the calculating-time does not grow too high. Then the time interval I is extended to $I = [0, t_e]$ with $t_e := t_f + m$.

One idea to keep the calculating-time low is to solve the diffusion of heat after switching off the generator analytically. This can be done, since here the material parameters are modeled to be constant. More specifically, one can try to extend the fundamental solution

$$T(t, x) = \frac{1}{(4\pi\lambda t)^{3/2}} \exp\left(-\frac{|x|^2}{4\lambda t}\right)$$

of the heat equation

$$\partial_t T - \lambda \Delta T = 0 \quad \text{in } I \times \mathbb{R}^3$$

(see e. g. [31]) to solve the heat equation

$$\begin{aligned} \rho c \partial_t T - \lambda \Delta T + \nu T &= \nu T_{\text{body}} & \text{in } I \times \mathbb{R}^3 \\ T(0, x) &= T_{\text{high}}(x) & \text{in } \mathbb{R}^3, \end{aligned}$$

where $T_{\text{high}}(x) = T(t_f, x) \forall x \in \mathbb{R}^3$ is an extension of the current tissue temperature $T(t_f, \cdot)$ in D at the moment the generator is switched off, to the whole \mathbb{R}^3 . Then, using the fundamental solution of the heat equation, one can determine the time t after which the tissue temperature approximately reaches body temperature. The result is the additional amount of time m that is needed to determine the damage of the native tissue.

Generally, the amount of time m that has to be modeled after switching off the generator depends on the tissue properties (i. e. on the relative blood circulation rate, the density, the heat capacity and the heat conductivity), as well as on the tissue temperature $T(t_f, \cdot)$ when switching off the generator. Here, in a first approach, the number of additional time steps m is determined experimentally.

Note that when simulating additional time steps after switching off the generator, i. e. with $P_{\text{setup}}(t) = 0$ for $t \in [t_f, t_e]$, the calculation of the adjoint changes significantly. A detailed description of the calculation of the adjoint will be given in Sect. 7.1.4.

Regrettably, even with the implementation of additional time steps after switching off the generator, the problem described before (cf. Fig. 7.1) remains. More precisely, the generator power still converges to a setting which is $P_{\min} = 0$ at the beginning of the RF ablation and then monotonously increases to the maximum power P_{\max} . This might be due to the fact that, when using the objective functional (7.9), a tissue heating at the beginning of the ablation process has no advantage over a single, strong heating at the end of the ablation. The reason for this is that in order to obtain a high temperature at the end t_f of the ablation, the tissue must be heated again shortly before the end is reached, anyway, because of the heat sink effect due to the perfusion. Thus, for a tissue heating at the beginning of the ablation, the native tissue is affected twice, while for a strong tissue heating at the end of the ablation process, the native tissue is affected only once.

Although minimizing the applied objective functional (7.9) (including additional time steps after switching off the generator), such a power setting cannot be optimal in practice, since for a too strong heating, the tissue temperature reaches boiling temperature which instantaneously leads to the drying out of the tissue (cf. Sect. 7.1.1). In order to obtain a more realistic optimal control of the generator power, the effect of vaporization has to be included into our optimal control problem.

Evading Vaporization Taking into account the vaporization can be performed in several different ways:

- A first possibility is to model the vaporization directly to influence the forward problem and thus, the temperature distribution of the tissue. More specifically, the tissue properties could be modeled to depend on the dehydration state F_D of the tissue, and the right hand side of the heat equation could be implemented to depend on the energy balance Q_{PC} due to the phase changes of water (cf. Sect. 2.2). However, modeling the thermodynamics of phase changes together with the implementation of state dependent material parameters would increase the computational complexity, and thus the calculating-time, considerably.
- Another approach is to prevent the tissue temperature from exceeding the boiling temperature of 373.15 K ($\hat{=} 100^\circ\text{C}$) by implementing a state constraint: $T(t, x) < 373.15 \text{ K}$ for each $(t, x) \in I \times D$. Unfortunately, the incorporation of state constraints into an optimal control process, again is computationally complex and thus not really advisable, here.
- A more efficient solution can be obtained by penalizing a too high tissue temperature ($T(t, x) \geq 373.15 \text{ K}$) within the objective functional. To this end,

definition (7.9) can be extended in the following way:

$$\begin{aligned}
 f(T) := & w_{\text{in}} \int_{D_t} \exp(T_{\text{crit}} - T(t_f, x)) dx + w_{\text{out}} \int_{I \times D_n} (T(t, x) - T_{\text{body}})^2 dx dt \\
 & + w_{\text{all}} \int_{I \times D} \exp(T(t, x) - T_{\text{limit}}) dx dt .
 \end{aligned} \tag{7.10}$$

Here, the upper limit T_{limit} for the temperature T is boiling temperature, i. e. $T_{\text{limit}}(t, x) = 373.15 \text{ K}$ for each $(t, x) \in I \times D$, and the constant w_{all} in front of the third integral is a suitable weight for the penalization of too high tissue temperatures.

Note that using such an additional condition for penalizing excessive tissue temperatures, the optimal control problem is regularized (i. e. the space of possible solutions is restricted).

For the numerical evaluation of the objective functional f , we have to modify the definition of f in (7.10) slightly. This is due to the fact that in case of a very high temperature ($T \gg T_{\text{limit}}$), the third integral in (7.10) cannot be evaluated robustly. More precisely, the temperature T might exceed boiling temperature T_{limit} considerably during the first steps of the iteration, such that the corresponding values of the exponential function grow too high and thus lead to a numerical overflow.

A modification of the expression $\exp(T - T_{\text{limit}})$ in the third integral of (7.10), that mainly retains the desired behavior, but improves the numerical evaluation, is obtained by using the minimum function. Formally, that means we extend the expression $\exp(T - T_{\text{limit}})$ to

$$\exp(\min(T, T_{\text{max}}) - T_{\text{limit}}) , \tag{7.11}$$

where $T_{\text{max}} > T_{\text{limit}}$ is a constant high temperature, which guarantees that the upper boundary $\exp(T_{\text{max}} - T_{\text{limit}})$ of (7.11) is evaluable.³

Unfortunately, the minimum function and thus the argument of the exponential function in (7.11) is not differentiable. However, for $T \leq T_{\text{max}}$ this is the old expression $\exp(T - T_{\text{limit}})$, which we can differentiate as will be described in Sect. 7.1.4. Further, for $T > T_{\text{max}}$ (i. e. for $T \gg T_{\text{limit}}$) the best direction for the gradient descent is clear and can be assumed to be approximately the same as for $T = T_{\text{max}}$. Hence, by using the expression (7.11), we obtain the following robustly evaluable objective functional

$$\begin{aligned}
 f(T) := & w_{\text{in}} \int_{D_t} \exp(T_{\text{crit}} - T(t_f)) dx + w_{\text{out}} \int_{I \times D_n} (T - T_{\text{body}})^2 dx dt \\
 & + w_{\text{all}} \int_{I \times D} \exp(\min(T, T_{\text{max}}) - T_{\text{limit}}) dx dt .
 \end{aligned} \tag{7.10'}$$

³Note that for clarity, sometimes the variable arguments t, x for time and space, will be omitted within formulas and other mathematical expressions.

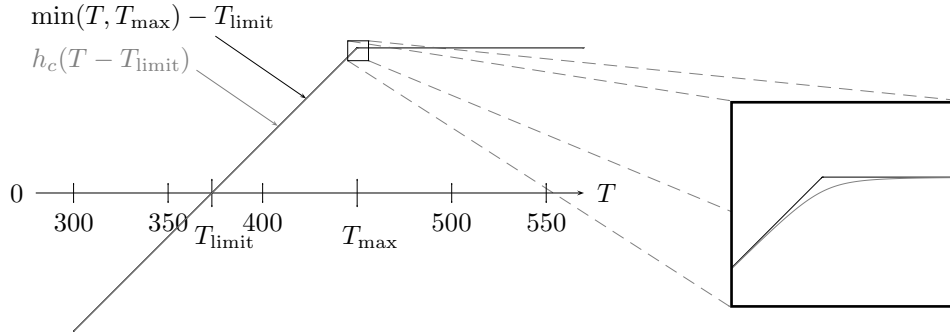


Figure 7.2: Smooth approximation of the function $\min(T, T_{\max}) - T_{\text{limit}}$ (black) by the function $h_c(T - T_{\text{limit}})$ (gray) with $c = T_{\max} - T_{\text{limit}}$ and $h_c = h_{c,1}$ as defined in (7.13). The cutout on the right shows a zoomed view of the relevant region around $T = T_{\max}$, where the black curve has a kink, while the gray shows a smooth bend.

As an alternative to the approach described above, one can also try to find a robustly evaluable and at the same time completely differentiable objective functional. To achieve this, one has to find a smooth approximation for the argument

$$\min(T, T_{\max}) - T_{\text{limit}} \quad (7.12)$$

of the exponential function in (7.11). Such a smooth approximation can be obtained by using e. g. the following definition of functions $h_{c,\varepsilon}, h_\varepsilon : \mathbb{R} \rightarrow \mathbb{R}$,

$$h_{c,\varepsilon}(x) := h_\varepsilon(x - c) + c \quad \text{with} \quad h_\varepsilon(x) := \frac{-x \left(\arctan\left(\frac{x}{\varepsilon}\right) - \frac{\pi}{2} \right) - 1 \cdot \varepsilon}{\pi} \quad (7.13)$$

where $c > 0$ is a constant value and both functions depend on a variable $\varepsilon > 0$. If for each $(t, x) \in I \times D$ we apply the function $h_{c,\varepsilon}$ to the argument $T(t, x) - T_{\text{limit}}(t, x)$ with $c = T_{\max}(t, x) - T_{\text{limit}}(t, x)$, we obtain the desired smooth approximation of (7.12) (see Fig. 7.2, where the variable ε has been set to $\varepsilon = 1$). To prove that $h_{c,\varepsilon}(T - T_{\text{limit}})$ with $c = T_{\max} - T_{\text{limit}}$ is a smooth approximation of $\min(T, T_{\max}) - T_{\text{limit}}$, we have to show that for $\varepsilon \rightarrow 0$ the function $h_{c,\varepsilon}(T - T_{\text{limit}})$ with $c = T_{\max} - T_{\text{limit}}$ converges pointwise to the minimum function $\min(T, T_{\max}) - T_{\text{limit}}$, i. e. we have to show that

$$\lim_{\varepsilon \rightarrow 0} \left| \min(T, T_{\max}) - T_{\text{limit}} - h_{c,\varepsilon}(T - T_{\text{limit}}) \right| \stackrel{!}{=} 0 \quad (7.14)$$

Let us firstly consider the case $T < T_{\max}$. Then we have

$$\begin{aligned}
 & \lim_{\varepsilon \rightarrow 0} \left| \min(T, T_{\max}) - T_{\text{limit}} - h_{c,\varepsilon}(T - T_{\text{limit}}) \right| \\
 & \stackrel{(7.13)}{=} \lim_{\varepsilon \rightarrow 0} \left| T - \cancel{T_{\text{limit}}} - h_{\varepsilon}(T - T_{\max}) - T_{\max} + \cancel{T_{\text{limit}}} \right| \\
 & \stackrel{(7.13)}{=} \lim_{\varepsilon \rightarrow 0} \left| T - \frac{-(T - T_{\max}) \left(\overbrace{\arctan\left(\frac{T - T_{\max}}{\varepsilon}\right) - \frac{\pi}{2}}^{\rightarrow -\frac{\pi}{2}} \right) - \overbrace{1 \cdot \varepsilon}^{\rightarrow 0}}{\pi} - T_{\max} \right| \\
 & = \lim_{\varepsilon \rightarrow 0} \left| T - \frac{-(T - T_{\max})(-\pi)}{\pi} - T_{\max} \right| = 0 .
 \end{aligned}$$

Thus, for the case $T < T_{\max}$ the requirement (7.14) is fulfilled. Now, let us consider the case $T > T_{\max}$. Then we obtain

$$\begin{aligned}
 & \lim_{\varepsilon \rightarrow 0} \left| \min(T, T_{\max}) - T_{\text{limit}} - h_{c,\varepsilon}(T - T_{\text{limit}}) \right| \\
 & \stackrel{(7.13)}{=} \lim_{\varepsilon \rightarrow 0} \left| \cancel{T_{\max}} - \cancel{T_{\text{limit}}} - h_{\varepsilon}(T - T_{\max}) - \cancel{T_{\max}} + \cancel{T_{\text{limit}}} \right| \\
 & \stackrel{(7.13)}{=} \lim_{\varepsilon \rightarrow 0} \left| -\frac{-(T - T_{\max}) \left(\overbrace{\arctan\left(\frac{T - T_{\max}}{\varepsilon}\right) - \frac{\pi}{2}}^{\rightarrow +\frac{\pi}{2}} \right) - \overbrace{1 \cdot \varepsilon}^{\rightarrow 0}}{\pi} \right| = 0 .
 \end{aligned}$$

Hence, also for the case $T > T_{\max}$ the requirement (7.14) is met. The case $T = T_{\max}$ remains to be considered. For this case, the requirement (7.14) can be seen as follows:

$$\begin{aligned}
 & \lim_{\varepsilon \rightarrow 0} \left| \min(T, T_{\max}) - T_{\text{limit}} - h_{c,\varepsilon}(T - T_{\text{limit}}) \right| \\
 & \stackrel{(7.13)}{=} \lim_{\varepsilon \rightarrow 0} \left| \cancel{T_{\max}} - \cancel{T_{\text{limit}}} - h_{\varepsilon}(0) - \cancel{T_{\max}} + \cancel{T_{\text{limit}}} \right| \\
 & \stackrel{(7.13)}{=} \lim_{\varepsilon \rightarrow 0} \left| -\frac{0 \cdot \left(\overbrace{\arctan(0) - \frac{\pi}{2}}^{=0} \right) - \overbrace{1 \cdot \varepsilon}^{\rightarrow 0}}{\pi} \right| = 0 . \quad \square
 \end{aligned}$$

In the remaining part of this chapter the variable ε is chosen to be $\varepsilon = 1$. Moreover, $h_{c,1}$ and h_1 are denoted as h_c and h , respectively. Using the smooth approximation $h_c(T - T_{\text{limit}})$ for $\min(T, T_{\max}) - T_{\text{limit}}$, the objective functional (7.10) can now be modified to become the robustly evaluable and completely differentiable objective functional

$$\begin{aligned}
 f(T) & := w_{\text{in}} \int_{D_t} \exp(T_{\text{crit}} - T(t_f)) dx + w_{\text{out}} \int_{I \times D_n} (T - T_{\text{body}})^2 dx dt \\
 & + w_{\text{all}} \int_{I \times D} \exp(h_c(T - T_{\text{limit}})) dx dt ,
 \end{aligned} \tag{7.10''}$$

where $c = T_{\max} - T_{\text{limit}}$ and $h_c = h_{c,1}$ as defined in (7.13).

In the following explanation, formally, the objective functional (7.10) is used. However, since within the implementation, the objective functional (7.10') and (7.10''), respectively, is applied, the corresponding changes in theory are also explained within the next section, after having derived the adjoint state (see Sect. 7.1.4, p. 142). Moreover, additional time steps t_f, \dots, t_e are added to the time space I , in order to model the heat diffusion after switching off the generator (i. e. with $P_{\text{setup}}(t) = 0$ for $t \in [t_f, t_e]$).

7.1.4 An Algorithm for Solving the Optimal Control Problem

As a first approach towards a calculation of the optimal control of the generator power, a gradient descent method (see Sect. 3.1.1) has been used, together with a projection of the values of the generator power onto the feasible range of $[P_{\min}, P_{\max}]$. Like in Sect. 3.4, the particular ingredients of the gradient descent method are the following (they will be discussed in more detail below):

- **Initial value.** First, an arbitrary setting of the generator power P_{setup} is chosen as an initial guess for the optimal control problem. More precisely, a constant setup power $P_{\text{setup}}(t) = P_0 \ \forall t \in I$ (with $P_0 \in [P_{\min}, P_{\max}]$) is taken as initial setting.
- **Descent direction.** Then, in each iteration step $n \geq 0$, the descent direction w^n is calculated from the current iterate P_{setup}^n as an approximation of $-\nabla_{P_{\text{setup}}} f(P_{\text{setup}}^n)$.
- **Step size.** Next, the step size $s^n > 0$ is determined, such that the resulting new iterate $P_{\text{setup}}^{n+1} = \mathcal{P}(P_{\text{setup}}^n + s^n w^n)$ reduces the value of the objective function $f(P_{\text{setup}}^{n+1}) < f(P_{\text{setup}}^n)$. Using the projection \mathcal{P} ensures that the new values for the setup power $P_{\text{setup}}(t)$, $t \in I$, lie in the interval $[P_{\min}, P_{\max}]$.
- **Stopping criterion.** The iteration stops when the norm of the descent direction $\|w^{n+1}\|_{L^2(I)}$ or the norm of the difference $\|P_{\text{setup}}^{n+1} - P_{\text{setup}}^n\|_{L^2(I)}$ falls below a given threshold θ_1 and θ_2 , respectively.

Descent Direction

Formally, the objective function f can be considered a function of the temperature distribution T , where T is a function of the heat source Q_{rf} , and Q_{rf} is a function of the control parameter P_{setup} . Hence, one can write

$$\begin{aligned} Q_{\text{rf}} &= \mathcal{Q}(P_{\text{setup}}) \ , & \mathcal{Q} : L^\infty(I, [P_{\min}, P_{\max}]) &\rightarrow L^2(I, H^1(D)^*) \ , \\ T &= \mathcal{T}(Q_{\text{rf}}) \ , & \mathcal{T} : L^2(I, H^1(D)^*) &\rightarrow H^1(I, H^1(D), H^1(D)^*) \ . \end{aligned} \tag{7.15}$$

To search for an optimal control of the generator power means we are looking for $P_{\text{setup}} \in L^\infty(I, [P_{\min}, P_{\max}])$ such that $F : L^\infty(I, [P_{\min}, P_{\max}]) \rightarrow \mathbb{R}$, defined by

$F(P_{\text{setup}}) := f \circ \mathcal{T} \circ \mathcal{Q}(P_{\text{setup}})$, becomes minimal. Here, $L^\infty(I, [P_{\min}, P_{\max}])$ is defined as the space of essentially bounded, measurable functions from the interval $I \subset \mathbb{R}$ into the interval $[P_{\min}, P_{\max}] \subset \mathbb{R}$. Formally, for two intervals $A, B \subset \mathbb{R}$ the space $L^\infty(A, B)$ can be written as $L^\infty(A, B) := \{f \in L^\infty(A, \mathbb{R}) \mid f(x) \in B \ \forall x \in A\}$.

Now, to derive the optimal control problem, we have to define a Lagrange function by subtracting all constraints (with appropriate multipliers) from the objective functional. Since here, like in Sect. 3.4, the connection between the electric potential and the heat source Q_{rf} is rather complicated through equations (7.1), we do not insert this constraint into the Lagrange function. Instead, as described above (see (7.15)), we consider the source term Q_{rf} to depend directly on the setup power P_{setup} (i. e. $Q_{\text{rf}} = \mathcal{Q}(P_{\text{setup}})$). Hence, we obtain the following reduced Lagrange function:

$$\begin{aligned} \mathcal{L}(T, P_{\text{setup}}, v) := & f(T) - \rho c \int_I \int_D \partial_t T(t, x) v(t, x) \, dx \, dt \\ & - \lambda \int_I \int_D \nabla T(t, x) \nabla v(t, x) \, dx \, dt \\ & - \int_I \int_D \nu(x) T(t, x) v(t, x) \, dx \, dt \\ & + \int_I \int_D Q_{\text{rf}}(t, x) v(t, x) \, dx \, dt \end{aligned} \quad (7.16)$$

with the Lagrange multiplier $v \in L^2(I, H^1(D), H^1(D)^*)$.

Similar as in Sect. 3.4.1, minimizing the objective functional (7.10) is equivalent to finding solutions of $D_T \mathcal{L}(T, P_{\text{setup}}, v)[\gamma] = 0$ and $D_{P_{\text{setup}}} \mathcal{L}(T, P_{\text{setup}}, v)[\gamma] \geq 0$ for all test functions γ .⁴ Here, the variation $D_T \mathcal{L}(T, P_{\text{setup}}, v)[\gamma]$ is given by

$$\begin{aligned} D_T \mathcal{L}(T, P_{\text{setup}}, v)[\gamma] = & -w_{\text{in}} \int_{D_t} \exp(T_{\text{crit}} - T(t_f, x)) \gamma(t_f, x) \, dx \\ & + 2w_{\text{out}} \int_I \int_{D_n} (T(t, x) - T_{\text{body}}) \gamma(t, x) \, dx \, dt \\ & + w_{\text{all}} \int_I \int_D \exp(T(t, x) - T_{\text{limit}}) \gamma(t, x) \, dx \, dt \\ & - \rho c \int_I \int_D v(t, x) \partial_t \gamma(t, x) \, dx \, dt \\ & - \lambda \int_I \int_D \nabla v(t, x) \nabla \gamma(t, x) \, dx \, dt \\ & - \int_I \int_D \nu(x) v(t, x) \gamma(t, x) \, dx \, dt \end{aligned} \quad (7.17)$$

for all test functions $\gamma \in L^2(I, H^1(D), H^1(D)^*)$. Using this variation, we obtain the *adjoint equation* by setting $D_T \mathcal{L}(T, P_{\text{setup}}, v) = 0$. Removing the integration over

⁴Note that the weakening of the condition $D_u \mathcal{L}(T, u, v)[\gamma] = 0$ (cf. Sect.3.4.1) to a condition $D_{P_{\text{setup}}} \mathcal{L}(T, P_{\text{setup}}, v)[\gamma] \geq 0$ is due to the fact, that here we have box constraints for our optimal control parameter P_{setup} such that the direction γ cannot reach any value in $L^\infty(I, \mathbb{R})$ (cf. Sect.3.1).

7 Ongoing Work

the domain D within the corresponding equation yields:

$$\begin{aligned}
0 = & -w_{\text{in}} \chi_{D_t}(x) e^{T_{\text{crit}} - T(t_f, x)} \gamma(t_f, x) + 2w_{\text{out}} \int_I \chi_{D_n}(x) (T(t, x) - T_{\text{body}}) \gamma(t, x) dt \\
& + w_{\text{all}} \int_I e^{T(t, x) - T_{\text{limit}}} \gamma(t, x) dt - \rho c \int_I v(t, x) \partial_t \gamma(t, x) dt \\
& + \lambda \int_I \Delta v(t, x) \gamma(t, x) dt - \nu \int_I v(t, x) \gamma(t, x) dt ,
\end{aligned} \tag{7.18}$$

where χ_{D_t} and χ_{D_n} are indicator functions which have values 1 and 0 only (depending on whether a point x of the computational domain D belongs to the tumor and native tissue, respectively, or not). To be able to remove the integration over the time space I , as well as the test function $\gamma(t, x)$, we formally split up the time space $I = [0, t_e]$ into the time intervals $[0, t_f]$ and $[t_f, t_e]$, assuming v to jump at t_f . Moreover, we integrate the time integral containing $\partial_t \gamma(t, x)$ by parts:

$$\begin{aligned}
& -\rho c \left(\int_0^{t_f} v(t, x) \partial_t \gamma(t, x) dt + \int_{t_f}^{t_e} v(t, x) \partial_t \gamma(t, x) dt \right) \\
& = -\rho c \left(\gamma(t_f, x) v(t_f - 0, x) - \gamma(0, x) v(0, x) + \gamma(t_e, x) v(t_e, x) - \gamma(t_f, x) v(t_f + 0, x) \right. \\
& \quad \left. - \int_0^{t_f} \gamma(t, x) \partial_t v(t, x) dt - \int_{t_f}^{t_e} \gamma(t, x) \partial_t v(t, x) dt \right) ,
\end{aligned}$$

where $\gamma(0, x) = 0$, since γ is a test function for the temperature T which is defined to be zero in $t = 0$ (see (7.4d)). Moreover, the expressions $v(t_f - 0, x)$ and $v(t_f + 0, x)$ are defined by

$$v(t_f - 0, x) := \lim_{\varepsilon \rightarrow 0} v(t_f - \varepsilon, x) \quad \text{and} \quad v(t_f + 0, x) := \lim_{\varepsilon \rightarrow 0} v(t_f + \varepsilon, x) .$$

Including the result into the above equation (7.18) yields:

$$\begin{aligned}
0 = & \int_I \left(2w_{\text{out}} \chi_{D_n} (T - T_{\text{body}}) + w_{\text{all}} e^{T - T_{\text{limit}}} + \rho c \partial_t v + \lambda \Delta v - \nu v \right) \gamma dt \\
& + \left(-w_{\text{in}} \chi_{D_t} e^{T_{\text{crit}} - T(t_f)} - \rho c v(t_f - 0) + \rho c v(t_f + 0) \right) \gamma(t_f) - \rho c v(t_e) \gamma(t_e) .
\end{aligned}$$

Since this equation has to be met for each test function $\gamma \in H^1(I, H^1(D), H^1(D)^*)$, the term in parentheses within the time integral must be zero, such that we obtain the condition

$$-\rho c \partial_t v - \lambda \Delta v + \nu v = 2w_{\text{out}} \chi_{D_n} (T - T_{\text{body}}) + w_{\text{all}} e^{T - T_{\text{limit}}} \quad \text{a.e. in } I \times D . \tag{7.19}$$

The remaining part then can be written as

$$0 = \left(-w_{\text{in}} \chi_{D_t} e^{T_{\text{crit}} - T(t_f)} - \rho c v(t_f - 0) + \rho c v(t_f + 0) \right) \gamma(t_f) - \rho c v(t_e) \gamma(t_e) ,$$

where this condition still has to be met for each $\gamma \in H^1(I, H^1(D), H^1(D)^*)$. By thinking of e. g. a function γ which is zero in $t = t_f$, but does not vanish for $t = t_e$, it is easy to see that the above condition can only be met by setting $v(t_e) = v(t_e, x) = 0$ for all $x \in D$. Considering a function γ which does not vanish in $t = t_f$, for the remaining part, we obtain the condition

$$v(t_f - 0, x) = v(t_f + 0, x) - \frac{w_{\text{in}}}{\rho c} \chi_{D_t}(x) e^{T_{\text{crit}} - T(t_f, x)} \quad \forall x \in D . \quad (7.20)$$

When combining the conditions (7.19) and (7.20), as well as the condition in $t = t_e$ and on the inner and outer boundary of the computational domain D (cf. (7.4b), (7.4c)), we obtain the PDE system modeling the adjoint state:

$$\begin{aligned} -\rho c \partial_t v(t, x) - \lambda \Delta v(t, x) + \nu v(t, x) &= 2 w_{\text{out}} (T(t, x) - T_{\text{body}}) \chi_{D_n}(x) \\ &+ w_{\text{all}} \exp(T(t, x) - T_{\text{limit}}) \end{aligned} \quad (7.21a)$$

for all $(t, x) \in I \times (D \setminus \overline{D_{\text{pr}}})$, together with the boundary conditions

$$v(t, x) = 0 \quad \text{in } I \times \overline{D_{\text{pr}}} , \quad (7.21b)$$

$$v(t, x) = 0 \quad \text{in } I \times \Gamma_{\text{out}} , \quad (7.21c)$$

$$v(t_e, x) = 0 \quad \text{in } D , \quad (7.21d)$$

$$v(t_f - 0, x) = v(t_f + 0, x) - \frac{w_{\text{in}}}{\rho c} \exp(T_{\text{crit}} - T(t_f, x)) \chi_{D_t}(x) \quad \text{in } D . \quad (7.21e)$$

Note, that the adjoint v is calculated backwards in time. As a result, we have an initial condition in the end t_e of the heat diffusion (see (7.21d) and Fig. 7.3), as well as an initial condition in the end t_f of the active tissue heating (see (7.21e) and Fig. 7.3).

Hence, for the calculation of the adjoint, the temperature T which is calculated forwards in time, has to be stored in each time step. Then the calculation of the adjoint v can be performed by a conjugated gradient (CG) method on a finite element grid, analog to the calculation of the temperature T (cf. Sect. 7.1.2), but with a slight modification of the time-discretization in the obvious way.

Further, note that in the implementation we have to use the objective functional (7.10') or (7.10'') instead of (7.10), because, as already described at the end of

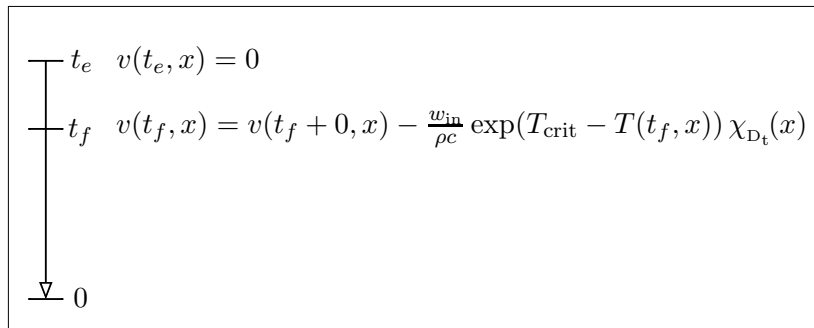


Figure 7.3: Schematic showing the calculation of the adjoint v backwards in time, starting with an initial condition in t_e , as well as in t_f , and proceeding until the start time $t = 0$ is reached.

Sect. 7.1.3, the evaluation of the term $\exp(T - T_{\text{limit}})$ within (7.10) might lead to a numerical overflow. Hence, the calculation of the adjoint state, which is critical for the same reasons (it also includes the evaluation of $\exp(T - T_{\text{limit}})$; see (7.21a)), changes slightly:

- If we use the objective functional (7.10') instead of (7.10) (with $\min(T, T_{\text{max}}) - T_{\text{limit}}$ instead of $T - T_{\text{limit}}$ as argument for the exponential function), we first proceed as described above, i. e. we formally derive the objective functional (7.10) to determine the adjoint state, but then replace the term $T - T_{\text{limit}}$ within the right hand side of (7.21a) by $\min(T, T_{\text{max}}) - T_{\text{limit}}$ as in (7.10'). Thus, we obtain the adjoint equation

$$\begin{aligned} -\rho c \partial_t v - \lambda \Delta v + \nu v &= 2 w_{\text{out}} (T - T_{\text{body}}) \chi_{D_n} \\ &+ w_{\text{all}} \exp(\min(T, T_{\text{max}}) - T_{\text{limit}}) \end{aligned} \quad (7.21a')$$

in $I \times D$, with the boundary conditions (7.21c) - (7.21e) from above.

- If we use the objective functional (7.10'') instead of (7.10) (with $h_c(T - T_{\text{limit}})$, cf. (7.13); $c = T_{\text{max}} - T_{\text{limit}}$) as argument for the exponential function), the right hand side of the adjoint state in (7.21a) has to be extended by the inner derivative of $\exp(h_c(T - T_{\text{limit}}))$, i. e. by

$$\begin{aligned} D_T h_c(T - T_{\text{limit}}) \\ &= D_T h(T - T_{\text{max}}) \\ &= \frac{1}{2} - \frac{1}{\pi} \left(\arctan(T - T_{\text{max}}) + (T - T_{\text{max}})(1 + (T - T_{\text{max}})^2)^{-1} \right) . \end{aligned} \quad (7.22)$$

Consequently, the adjoint equation changes to

$$\begin{aligned} -\rho c \partial_t v - \lambda \Delta v + \nu v &= 2 w_{\text{out}} (T - T_{\text{body}}) \chi_{D_n} \\ &+ w_{\text{all}} \exp(h_c(T - T_{\text{limit}})) D_T h_c(T - T_{\text{limit}}) \end{aligned} \quad (7.21a'')$$

in $I \times D$, with $h_c(T - T_{\text{limit}})$ as defined in (7.13) ($c = T_{\text{max}} - T_{\text{limit}}$) and $D_T h_c(T - T_{\text{limit}})$ as calculated in (7.22). As before, the boundary conditions (7.21c) - (7.21e) stay unmodified.

In the next step, the descent direction has to be defined. To do this, we need the derivative of the Lagrangian with respect to the control parameter P_{setup} . Here, $D_{P_{\text{setup}}} \mathcal{L}(T, P_{\text{setup}}, v)[\gamma]$ is given by

$$D_{P_{\text{setup}}} \mathcal{L}(T, P_{\text{setup}}, v)[\gamma] = \int_I \int_D \frac{\partial}{\partial P_{\text{setup}}} Q_{\text{rf}}(P_{\text{setup}})(t, x) v(t, x) dx \gamma(t) dt \quad (7.23)$$

for all $\gamma \in L^\infty(I, [P_{\text{min}}, P_{\text{max}}])$. Now, one can calculate the gradient in direction of w . Since we search for a steepest descent, this is

$$w(t) := - \int_D \frac{\partial}{\partial P_{\text{setup}}} Q_{\text{rf}}(P_{\text{setup}})(t, x) v(t, x) dx , \quad (7.24)$$

where v is given by the adjoint equation from above and $\frac{\partial}{\partial P_{\text{setup}}} Q_{\text{rf}}(P_{\text{setup}})$ can be calculated analytically as

$$\frac{\partial}{\partial P_{\text{setup}}} Q_{\text{rf}}(P_{\text{setup}})(t, x) = \begin{cases} \frac{1}{P_{\text{total}}} \sigma |\nabla \phi(x)|^2 \frac{4RR_1}{(R+R_1)^2} , & \text{in } [0, t_f] \times D , \\ 0 , & \text{in } [t_f, t_e] \times D . \end{cases} \quad (7.25)$$

Obviously, for the descent direction w defined in (7.24), the variation (7.23) attains its minimal value, namely

$$D_{P_{\text{setup}}} \mathcal{L}(T, P_{\text{setup}}, v)[w] = - \int_I w(t)^2 dt = - \|w\|_{L^2(I)}^2 . \quad (7.26)$$

Step Size

To determine the optimal step size s in each step of the iteration, the equation

$$s = \underset{s > 0}{\operatorname{argmin}} f(\mathcal{P}(P_{\text{setup}} + s w)) \quad (7.27)$$

has to be evaluated. The projection \mathcal{P} restricts a function $g \in L^\infty(I, \mathbb{R})$ to the domain $L^\infty(I, [P_{\text{min}}, P_{\text{max}}])$ by mapping the values $g(t)$, $t \in I$, which leave the feasible interval $[P_{\text{min}}, P_{\text{max}}]$, onto the nearest boundary value P_{min} or P_{max} . For the identification of the optimal step size, a bisection rule similar to Armijo's rule (cf. [34]) can be applied:

First, an initial guess is chosen, which is adapted to the magnitude of the descent direction and the maximum P_{max} for the setup power values $P_{\text{setup}}(t)$, $t \in I$. Then, if necessary, the step size is decreased until the new iterate reduces the objective function value. Note, that the admissibility of the new iterate is already ensured by the projection \mathcal{P} . The choice of an initial guess for the step size is different for the first iteration step and the following ones. For the first iteration step $n = 0$, the initial step size s^0 is chosen such that

$$s^0 \|w^0\|_{L^2(I)} = \frac{1}{2} P_{\text{max}} , \quad \text{i. e.} \quad s^0 = \frac{P_{\text{max}}}{2 \|w^0\|_{L^2(I)}} .$$

The following iteration steps $n > 0$ start with a step size that fulfills

$$s^n \|w^n\|_{L^2(I)} = 2 s^{n-1} \|w^{n-1}\|_{L^2(I)} , \quad \text{i. e.} \quad s^n = 2 s^{n-1} \frac{\|w^{n-1}\|_{L^2(I)}}{\|w^n\|_{L^2(I)}} .$$

After having chosen an initial value for the step size s^n , this value is bisected until the new iterate $P_{\text{setup}}^{n+1} = \mathcal{P}(P_{\text{setup}}^n + s^n w^n) \in L^\infty(I, [P_{\text{min}}, P_{\text{max}}])$ fulfills the inequality $f(P_{\text{setup}}^{n+1}) < f(P_{\text{setup}}^n)$. If this condition is not met after a certain number of bisections, the step size s^n is set to zero and the algorithm stops.

Note that, as described in Sect. 3.4.2, the search for the optimal step size can be accelerated by using a scheme which uses not only bisections, but also divisions by higher powers of two.

Stopping Criterion

Here, we have two different stopping criteria for the calculation of the optimal control of the setup power P_{setup} :

- On the one hand, the iteration stops if the norm of the gradient of the objective function f , i. e. the norm of the descent direction w , falls below a given threshold θ_1 . Descriptively this means, that the shape of the objective function becomes flat. Formally, we obtain the condition

$$\|w^{n+1}\|_{L^2(I)} < \theta_1 . \quad (7.28)$$

- On the other hand, the iteration stops if the norm of the difference between the new and old iterate $P_{\text{setup}}^{n+1} - P_{\text{setup}}^n$ falls below a given threshold θ_2 , i. e. if

$$\|P_{\text{setup}}^{n+1} - P_{\text{setup}}^n\|_{L^2(I)} < \theta_2 . \quad (7.29)$$

Optimal Control Algorithm

In Alg. 7.1 the main steps of the calculation of an optimal control of the generator power P_{setup} are briefly summerized. Since a gradient descent method has been used to find an optimal control for the generator power, the basic framework of the algorithm does not differ significantly from the framework of Alg. 3.1 in Sect. 3.4.4. However, the particular ingredients, such as the modeling of the objective functional and the determination of the time dependent adjoint state via Eqs. (7.21) and (7.21a')/(7.21a''), respectively, obviously are different.

Finally it has to be remarked, that for the problem of finding the optimal control of the generator power, also an implementation of e. g. a Lagrange-Newton (SQP) approach providing superlinear convergence seems reasonable, and will be addressed in a future work.

7.1.5 Results and Discussion

In this section the application of the optimal control algorithm described above to an artificial test scenario is presented as a first approach. For the determination of the optimal control of the generator power, here the objective function (7.10'') (cf. Sect 7.1.3, p. 136-137) is used together with the weights $w_{\text{in}} = 10$, $w_{\text{out}} = 0.5$ and $w_{\text{all}} = 100$ for the destruction of the tumor, the protection of the native tissue, and the penalization of temperature values exceeding boiling temperature, respectively. The temperature T_{crit} at which the tissue is considered destroyed, is modeled to be $T_{\text{crit}} = 333.15 \text{ K}$ ($\hat{=} 60^\circ\text{C}$) (cf. Sect. 6.1, p. 6.12). Moreover, here the computational domain D is of extent $60 \times 60 \times 60$ [mm] with an overlaid Cartesian grid consisting of 60^3 grid cells. The modeled duration of the RF ablation is $t_f = 300$ s and the simulated additional time after switching off the generator is 300 s as well. Hence, the modeled overall time adds up to $t_e = 600$ s. Consequently, we have a time

Algorithm 7.1 Algorithm for the calculation of an optimal control of P_{setup}

```

1: Choose  $P_{\text{setup}}^0$                                 ▷ Initialize start setup power
2:  $n \leftarrow 0$ 
3: repeat
4:    $w^n \leftarrow -\nabla_{P_{\text{setup}}} f(P_{\text{setup}}^n)$       ▷ Compute descent direction
                                                ▷ Initialize step size
5:   if  $n = 0$  then
6:      $s^0 = P_{\text{max}} (2 \|w^0\|_{L^2(I)})^{-1}$ 
7:   else
8:      $s^n = 2 s^{n-1} \|w^{n-1}\|_{L^2(I)} (\|w^n\|_{L^2(I)})^{-1}$ 
9:   end if
                                                ▷ Determine step size
10:   $m \leftarrow 0$ 
11:   $P_{\text{setup}}^{n+1} \leftarrow \mathcal{P}(P_{\text{setup}}^n + s^n w^n)$ 
12:  while  $f(P_{\text{setup}}^{n+1}) > f(P_{\text{setup}}^n)$  do      ▷ Compare objective
                                                function values
13:     $m \leftarrow m + 1$ 
14:    if  $m = m_{\text{max}}$  then
15:      STOP.
16:    end if
17:     $s^n \leftarrow s^n / 2$                                 ▷ Bisect step size
18:     $P_{\text{setup}}^{n+1} \leftarrow \mathcal{P}(P_{\text{setup}}^n + s^n w^n)$ 
19:  end while
20: until  $\|w^{n+1}\|_{L^2(I)} < \theta_1$  or  $\|P_{\text{setup}}^{n+1} - P_{\text{setup}}^n\|_{L^2(I)} < \theta_2$     ▷ Check stop criterion
21:  $\bar{P}_{\text{setup}} \leftarrow P_{\text{setup}}^{n+1}$                     ▷ Save optimal setup power

```

interval of $I = [0 \text{ s}, 600 \text{ s}]$. Further, the considered time step size is 5 s, so altogether, for each forward simulation, the algorithm has to perform 120 time steps. Here, a small ellipsoid with main axis' of length 10 mm, 10 mm and 15 mm, located in the center of D , is used as the tumor region. This tumor is treated with a monopolar probe of radius 0.75 mm and an electrode length of 9 mm. The probe is placed in the center of the tumor and oriented along the main principal axis of the tumor, i. e. the probe's orientation is $d = (0, 0, 1)$. As in Sects. 3.5 and 3.8, here, the heat conductivity is set to $\lambda = 0.5 \text{ W/K m}$ and the electric conductivity is set to $\sigma = 0.21 \text{ S/m}$. Further, the density and heat capacity of the tissue are $\rho = 1050.0 \text{ kg/m}^3$ and $c = 3590.0 \text{ J/kg K}$, respectively (cf. [79]). The perfusion (see Sect. 7.1.2, Eq. (7.3)) is modeled by taking the values $\nu_{\text{vessel}} = 0.05 \text{ s}^{-1}$ and $\nu_{\text{cap}} = 0.01765 \text{ s}^{-1}$ together with $\rho_{\text{blood}} = 1059.0 \text{ kg/m}^3$ and $c_{\text{blood}} = 3850.0 \text{ J/kg K}$. The applied RF generator has an inner resistance of 80Ω and the optimal control algorithm starts with a constant setup power of $P_{\text{setup}}(t) = 0 \text{ W}$ for all $t \in [0, t_f]$. During the whole iteration, the generator power is restricted to the interval $[P_{\text{min}}, P_{\text{max}}]$ (see (7.2)) with $P_{\text{min}} = 0 \text{ W}$

7 Ongoing Work

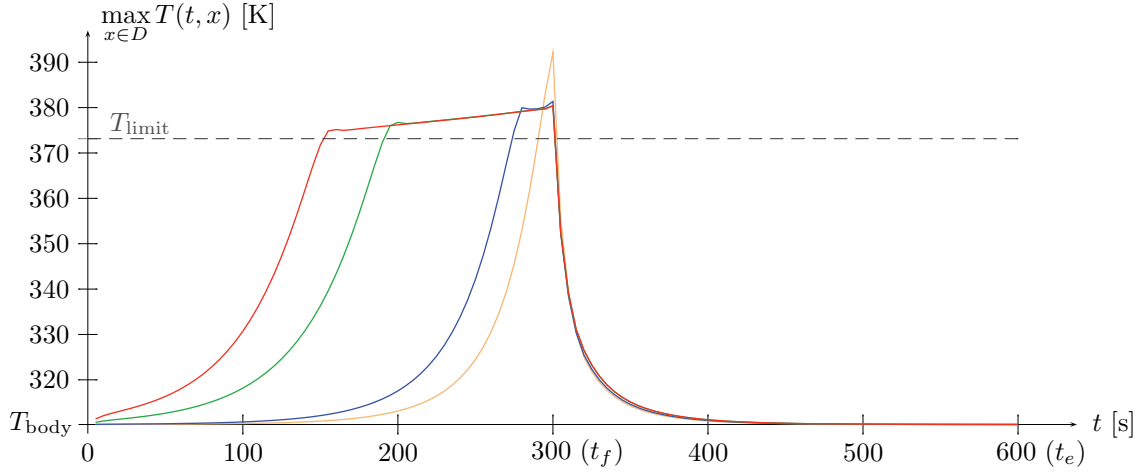


Figure 7.4: Curves showing the maximal temperature values during the RF ablation ($t \in [0\text{s}, 300\text{s}]$) and during the following 5 minutes ($t \in [300\text{s}, 600\text{s}]$) for iteration step 1 (yellow), 10 (blue), 1000 (green), and 3982 (red). Obviously, the highest temperature values are obtained at the end t_f of the ablation.

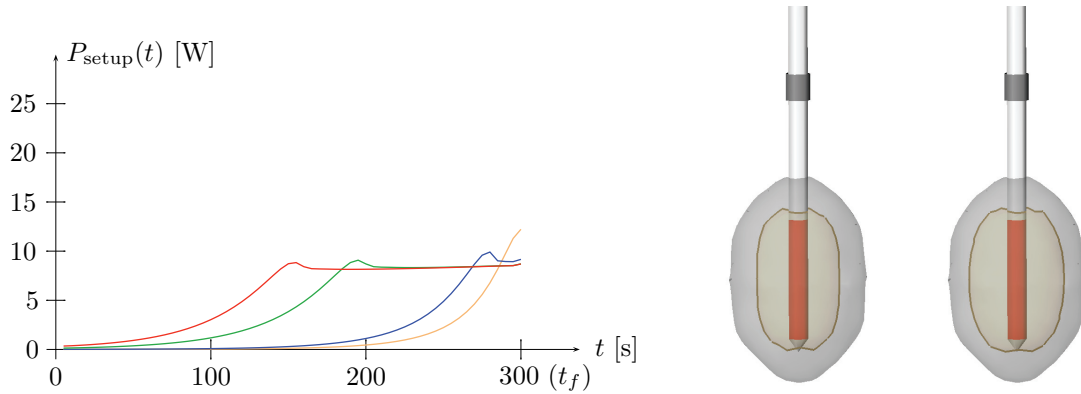


Figure 7.5: Left: Curves showing the setup power P_{setup} during the RF ablation for iteration step 1 (yellow), 10 (blue), 1000 (green) and 3982 (red). Right: 60°C -isosurface of the temperature (transparent yellow) at the end t_f of the ablation for iteration step 1 (left) and iteration step 3982 (right). Moreover, we see an artificial tumor (gray ellipsoid) and a monopolar probe with red electrode.

and $P_{\text{max}} = 200\text{ W}$. For the stopping criterion of the iteration (see (7.28) and (7.29)) the thresholds θ_1 and θ_2 are both set to 10^{-5} .

Some preliminary results of this first approach are presented in Figs. 7.4 and 7.5.

More specifically, Fig. 7.4 shows the curves with the maximal temperature values for different steps of the iteration (step 1, 10, 1000 and 3982) in each time step. That means, for each time step $t \in I = [0\text{s}, 600\text{s}]$, the maximal temperature value $\max_{x \in D} T(t, x)$ over the computational domain D is depicted. Moreover, the diagram on the left of Fig. 7.5 shows the time dependent generator power P_{setup} for the same steps of the iteration as presented in Fig. 7.4. In contrast to the curves with

the maximal temperature values, the curves showing the setup power are visualized only for the first 300 seconds, i. e. until switching off the generator in $t = t_f$, because afterwards the generator power obviously is zero ($P_{\text{setup}}(t) = 0 \text{ W}$ for $t > t_f$). On the right of Fig. 7.5, we see the 60°C -temperature profile (transparent yellow) at the end t_f of the ablation for the first iteration step (left) and for step 3982 of the iteration (right). Further the gray ellipsoids represent the artificial tumor lesion, inside of which the monopolar probe (with red electrode) is placed.

The results show a clear tendency of the setup power converging to an almost constant power of about 8 W (see Fig. 7.5, left). For this power setting, the maximum temperature values seem to converge against the upper limit of $T_{\text{limit}} = 373.15 \text{ K}$ ($\hat{=} 100^\circ\text{C}$) (Fig. 7.4). The 60°C -isosurface of the temperature $T(t_f)$ at the end t_f of the ablation and at the end of the optimization, however, might not cover the tumor completely (cf. Fig. 7.5, right: step 3982 of the optimization). The reason for this is possibly that the penalization for reaching the limit temperature of 100°C is too strong, since in practice even if boiling temperature is reached, the tissue does not dry out directly such that a very strong tissue heating can also be achieved for short time periods with $T > 100^\circ\text{C}$. Hence, a next step can be either decreasing the weight w_{all} within the objective functional (7.10), or trying to incorporate the effect of vaporization directly into the forward model.

A consideration of the 50°C -temperature profile at the end of the ablation



Figure 7.6: 50°C -isosurface of the temperature (transparent yellow) at the end t_f of the ablation and for step 3982 of the optimization.

and for step 3982 of the optimization (see Fig. 7.6) shows that at the end of the optimization, the tumor is heated to a temperature of at least 50°C . Such a tissue temperature can already cause protein coagulation and thus tumor cell destruction, if the time the tissue is exposed to this temperature is long enough. Further, note that shortly before the probe is pulled out of the tissue, the attending physician usually

turns out the internal cooling of the probe, so that the tissue directly surrounding the probe is destroyed and in particular no tumor cells are carried along with the probe.

Since the algorithm for optimizing the setup power currently needs a large number of iteration steps (for the example considered here: more than 3982 steps) and is thus very time consuming, future investigations might deal with the acceleration of the algorithm. A speed-up can probably be achieved by using higher order optimization methods like e. g. more sophisticated Lagrange-Newton (SQP) approaches. Also, the implementation of a multi-grid approach as discussed in Sect. 3.7 might be a promising enhancement to the current algorithm (Alg. 7.1).

Finally, a further improvement would perhaps be to consider the coagulation state F_C of the tissue (see Sect. 2.2, p. 2.9/2.10) instead of the temperature $T(t_f)$ at the end of the ablation within the first integral of the objective functional (7.10).

7.2 Miscellaneous

Within this section, the basic ideas of all current investigations, which can be found only separately within the chapters of this work so far, will be summarized.

First of all, the incorporation of anatomical constraints within the optimization of the RF probe placement, respecting critical structures such as inner organs or large blood vessels that must not be punctured, is a substantial extension to the optimization algorithm, which currently is work in progress. A further issue of current research is the maximization of the confidence for the success of RF ablation in the presence of uncertain tissue properties. Also, an adaptive approach with piecewise multilinear Ansatz-functions for the interpolation in the stochastic space is currently being considered in order to obtain an improved approximation of the stochastic process, i. e. for the optimization process with uncertain tissue parameters. Moreover, a distribution more realistic than a uniform distribution for modeling the uncertainty in material parameters is being searched for (on the one hand by analyzing experimental results, and on the other hand by solving the inverse problem of parameter identification). In contrast to that, also a modeling of the tissue properties as fuzzy parameters, i. e. with unknown stochastic distribution is part of ongoing research. Further, an analytical approximation of the objective functional as function of the probe placement and the uncertain tissue properties (a so-called “response surface approximation” (RSA)) is of current interest, because the optimization of confidence can be performed quite fast on such an approximation (i. e. after having determined a suitable RSA, no further solution of the forward problem is needed). In addition, a final cluster analysis yielding optimal subspaces of probe placements and thus compensating slight deviations from the optimal needle insertion is part of ongoing studies.

Regarding the considerations dealing with the estimation of the heat sink effect of large blood vessels on RF ablation (see Chapt. 5), an extension of the dependencies between the maximal probe-vessel distance, the vessel radius and the thickness of the criticality tube (i. e. the vessel surrounding tubes of vital tissue) by further quantities, such as the critical temperature at which the tissue is considered destroyed, is of current investigation. Moreover, an improvement of the visualization by additionally displaying a movable RF probe and automatically adapting the sizes of criticality tubes to the probe-vessel distance, is part of ongoing work. Instead of criticality tubes, also a dynamic tumor coloring with only two colors indicating destroyed versus not destroyed tumor regions is under investigation, because the visualization of such a coloring is likely to be quite faster than the visualization of dynamic criticality tubes. A rather basic step towards an improvement of the results of the underlying vessel segmentation is the development of a correction model for the segmented vessel radii, based on mathematically and physically founded heuristics.

Considering the problem of searching for an optimal control of the generator power (see previous section) a speed-up of the algorithm by implementing a multi-grid approach (cf. Sect. 3.7) as well as the consideration of a higher order optimization approach is part of current studies.

Finally, for all optimization and optimal control approaches discussed in this work, a more comprehensive evaluation on artificial and real configurations with different tumor shapes and vascular systems is of essential importance and thus might be one of the next steps.

8 Summary and Future Work

In this work, several models have been developed for optimizing the probe placement for radiofrequency ablation using mono- and bipolar probes as well as clusters of probes. Additionally, a method for a fast estimation of the cooling influence of large blood vessels on RF ablation and in particular on the optimal probe placement has been presented. Besides the optimization of the probe placement, also a first approach for the calculation of an optimal control of the generator power has been discussed. In the following, the particular approaches will be summarized and possible enhancements will be shown.

Summary

Radiofrequency (RF) ablation is a widely used, minimally invasive technique preferentially applied for the treatment of liver tumors (Chapt. 1). The success of this method, which places a needle connected to an RF generator into the malignant tissue in order to destroy the tumor by heat, considerably depends on the quality of the probe placement, as well as on the control of the energy supply. The modeling of RF ablation yields a system of partial differential equations for the calculation of the electric potential and the heat distribution in the tissue (Chapt. 2). Both equations can be solved numerically using finite elements.

As objective functional for the optimization of the probe placement e. g. a differentiable approximation of the minimum function as described in Sect. 3.3, is appropriate. For the optimization, a gradient descent method has been used (Sect. 3.4), which needs only very few iteration steps to optimize the probe placement. In contrast to that, a Lagrange-Newton approach is not suitable here, since the Hessian of the Lagrange function is very ill-conditioned for this problem (Sect. 3.4). After first results of the algorithm for optimizing a single monopolar probe had been presented, the algorithm was extended to the application of a cluster of several probes and supplemented by a multi-grid approach that improved the performance considerably.

Since the input parameters for the problem of finding an optimal probe placement, i. e. the individual properties of the human tissue such as the electrical and thermal conductivity, cannot be determined exactly due to their patient- and state-dependence, in a further approach (Chapt. 4) these quantities have been modeled stochastically. It has been assumed that intervals for the tissue parameters and a stochastic distribution of the tissue parameters within these intervals are known (in a first approach this has been assumed to be a unique distribution). The result-

ing stochastic optimization problem has been solved using a stochastic collocation method which, if applied to sufficiently smooth problems, needs less sampling points and thus converges faster than e. g. a Monte Carlo method. With this approach, a first sensitivity analysis for the optimization of the probe placement in dependence of uncertain electrical and thermal conductivity has been performed. Unfortunately, the problem of finding an optimal probe placement or the numerics for solving this problem turned out to be not smooth enough to guarantee convergence of the collocation method. In order to solve this problem, i. e. in order to achieve a better approximation of the stochastic process, in a next step piecewise multilinear functions instead of global polynomials are going to be used for the stochastic interpolation. Anyhow, the results already indicate first tendencies of a stronger dependence of the optimal probe placement with respect to the electric conductivity than with respect to the thermal conductivity, which might be due to a stronger dependence of the system on the electric conductivity in terms of the heat source and effective generator power. Further, it is noticeable that the main deviation of the optimal probe position distributes along the prominent direction of the vessels close to the tumor. Thus, the vascular system seems to have a significant impact on the sensitivity of the optimal probe position with respect to the electrical and thermal conductivity.

Obviously, the success of an RF ablation considerably depends on the cooling effects of large blood vessels. For this reason, a method for a fast estimation of these cooling effects has been developed (Chapt. 5). In more detail, maximum allowable distances between probe and vessels have been determined for a predefined tumor region close by vessels of diameter greater than 3 mm, such that the induced energy suffices to destroy the tumor region under investigation. The basic idea of this approach consists of a changed perspective when considering the Bioheat-Transfer-Equation: Instead of investigating the heat supply via the probe, now the propagation of the cooling effects of large blood vessels are in the focus of investigation. Moreover, short computational time has been achieved by a calculation and storage of all patient-independent data in advance. Those just have to be read out in order to calculate the cooling effects of an individual tumor-vessel configuration. The visualization of the maximum allowable distances of the probe to the vessels has been performed by a tumor coloring and by vessel-surrounding tubes of different thicknesses in dependence on the maximal probe-vessel distances.

Finally, in Chapt. 6 two further approaches for the optimization of the probe placement have been discussed, which extend the algorithm presented in Chapt. 3. One of these approaches deals with the coupled optimization of bipolar probes and a constant generator power. Here, the basic innovation consists of a geometric pre-optimization with an ellipsoidal-shaped region of coagulated tissue, the shape of which is fixed except for the radii which change according to the generator power. The second approach presented in this chapter describes an optimization of the number and placement of several uncoupled probes. As this approach showed a problem of “getting trapped” in local optima, a “simulated annealing” like scheme was applied, which replaced the found solution with a random “nearby” solution after each gradient descent as well as after each optimization.

Besides the probe placement, also the control of the energy supply has a significant influence on the success of an RF therapy. Thus, concludingly, in Chapt. 7 a first approach for calculating an optimal control of the generator power has been presented. The mathematical modeling of RF ablation (which previously had been simplified for the calculation of an optimal probe placement) has been extended to time dependence. In addition, an objective functional has been modeled which considers the propagation of heat into the tissue after switching off the generator (via additional time steps) and moreover penalizes tissue dehydration at high temperature values (above boiling temperature). As algorithm for calculating an optimal control of the generator power, here again the gradient descent method has been tested first, but for this optimal control problem, considerably more iteration steps are needed than for the previously considered probe placement optimization. Hence, in further investigations regarding the problem of finding an optimal control for the generator power, the gradient descent method should be replaced by a more suitable approach such as a Lagrange-Newton (SQP) approach.

Outlook

For future investigations, various extensions and improvements of the presented models and algorithms are planned and actually already are investigated in parts. First, the consideration of anatomical constraints for the probe placement caused by e. g. inner organs, bones, or large blood vessels has to be mentioned. The modeling and observance of such constraints is subject of the current research of Sabrina Haase¹.

Since in practice it will be hard for the attending physician to achieve exactly the computed optimal probe placement, a sensitivity analysis that yields an estimation of the risk of failure of an RF ablation with respect to deviations from the optimal probe positioning would be desirable.

For the improvement of the stochastic approach analyzing the influence of uncertain tissue parameters on the optimal probe placement, a modeling of the stochastic process by using piecewise multilinear functions on hierarchical grids already is under investigation. Further, a modeling of the material parameters as fuzzy-parameters is planned, since their stochastic distribution is unknown, yet. Simultaneously, conclusions on the distribution of the tissue parameters might be drawn from experimental results and from analyzing the inverse problem of parameter identification. The investigation of this problem is part of the current research of Hanne Tiesler². In addition, besides the electrical and thermal conductivity, also the perfusion coefficients (i. e. the relative perfusion rate, as well as the density and heat capacity of blood) might be modeled as stochastically or fuzzy distributed quantities. Moreover, a maximization of the confidence of the success of the RF therapy is aimed.

¹sabrina.haase@ewetel.net; CeVis - University of Bremen

²Hanne.Tiesler@cevis.uni-bremen.de; CeVis and ZeTeM - University of Bremen

In order to improve the estimation of the cooling influence of large blood vessels, a correction model for the segmentation of the vessel radii, based on mathematical and physical heuristics, should be part of future work. In addition, the visualization of the cooling effects might be improved by enabling an interaction with the user. More precisely, the consequences of probe movements performed by the user in future approaches might be visualized by a tumor coloring with only two colors, marking destroyed and vital tumor regions, respectively, and changing automatically according to the probe movements. An extension of the parameters that influence the cooling effects, i. e. an extension of the input parameters of the look-up-table, as well as an experimental validation of the considered approach are subjects to future investigation of a collaboration with the Charité Berlin³.

Finally, for the calculation of an optimal control of the generator power, the application of higher order methods such as Lagrange-Newton (SQP) methods, as well as an implementation of a multi-grid approach (as already performed for the problem of optimizing the probe placement; Sect. 3.7) are planned.

Moreover, for all approaches presented in this work, a comprehensive evaluation on the basis of artificial configurations as well as real patient data with different tumor shapes and vascular systems are required.

³Charité, Campus Benjamin Franklin, Hindenburgdamm 30, 12203 Berlin, Germany; <http://www.charite.de>.

Zusammenfassung und Ausblick

In dieser Arbeit wurden verschiedene Modelle für die Optimierung der Platzierung von mono- und bipolaren Applikatoren sowie von Applikatorclustern bei der Radio-Frequenz (RF) Ablation entwickelt. Darüber hinaus wurde ein Verfahren zur schnellen Bewertung des Kühleinflusses großer Gefäße auf die RF Ablation und insbesondere auf die optimale Applikatorplatzierung, vorgestellt. Neben der Optimierung der Applikatorplatzierung wurde schließlich auch ein erster Ansatz für die optimale Steuerung der Generatorleistung diskutiert. Im Folgenden sollen die einzelnen Ansätze noch einmal zusammengefasst und mögliche Ergänzungen aufgezeigt werden.

Zusammenfassung

Radio-Frequenz (RF) Ablation ist ein weitverbreitetes minimal-invasives Verfahren, welches vorrangig zur Behandlung von Lebertumoren eingesetzt wird (Kapitel 1). Der Erfolg dieses Verfahrens, bei dem eine an einem RF Generator angeschlossene Nadel in den Tumor geführt und dieser dann mittels Hitze zerstört wird, hängt maßgeblich von der Güte der Nadelpositionierung sowie von der Steuerung der Energiezufuhr ab. Die Modellierung der RF Ablation führt auf partielle Differentialgleichungen zur Bestimmung des elektrischen Potentials und der Wärmeverteilung im Gewebe (Kapitel 2). Beide Gleichungen lassen sich z.B. numerisch mit Hilfe von Finiten Elementen lösen.

Als Zielfunktional für die Optimierung der Applikatorplatzierung eignet sich z.B. eine differenzierbare Approximation der Minimum-Funktion wie sie in Kapitel 3.3 vorgestellt wurde. Für die Optimierung wurde hier ein Gradientenabstiegsverfahren verwendet (Kapitel 3.4), welches für das Problem der optimalen Applikatorplatzierung nur recht wenige Iterationsschritte benötigt. Ein Lagrange-Newton Verfahren eignet sich hier dagegen eher nicht, weil die Hessematrix der Lagrange-Funktion für das Problem der optimalen Applikatorplatzierung sehr schlecht konditioniert ist (Kapitel 3.4). Nachdem erste Ergebnisse der entwickelten Methode zur Optimierung eines einzelnen monopolaren Applikators vorgestellt worden sind, wurde der Algorithmus schließlich für die Anwendung auf ein Cluster von mehreren Applikatoren erweitert und um einen Mehrgitter-Ansatz ergänzt, wodurch die Rechenzeit noch erheblich reduziert werden konnte.

Da die Eingangsdaten für das Applikatorplatzierungsproblem, genauer gesagt die individuellen Eigenschaften des menschlichen Gewebes wie z.B. die elektrische und thermische Leitfähigkeit, aufgrund ihrer Patienten- und Zustandsabhängigkeit nicht

exakt bestimmt werden können, wurden diese Daten in einem weiteren Ansatz (Kapitel 4) stochastisch modelliert. Dabei wurde angenommen, dass zumindest die Intervalle bekannt sind, in denen die Gewebeparameter liegen, sowie eine stochastische Verteilung der Gewebeparameter innerhalb dieser Intervalle (im ersten Ansatz eine Gleichverteilung). Das entsprechende stochastische Optimierungsproblem wurde schließlich mit Hilfe eines stochastischen Kollokationsverfahrens gelöst, welches angewandt auf hinreichend glatte Probleme und durch eine geschickte Stützstellenwahl gegenüber einem Monte Carlo Verfahren den Vorteil einer schnelleren Konvergenz aufweist. Schließlich wurde mit diesem Ansatz eine erste Sensitivitätsanalyse für die Optimierung der Applikatorplatzierung in Abhängigkeit von Schwankungen in der elektrischen und thermischen Leitfähigkeit durchgeführt. Leider stellte sich hierbei heraus, dass das Problem der optimalen Applikatorplatzierung oder die Numerik zur Lösung dieses Problems noch nicht glatt genug sind, um die Konvergenz des Kollokationsverfahrens zu gewährleisten. Um dieses Problem zu beheben, d.h. um eine besser Approximation des stochastischen Prozesses zu erzielen, sollen in einem nächsten Schritt stückweise multilineare Funktionen anstelle von Polynomen für die stochastische Interpolation verwendet werden. Gleichwohl deuten die Ergebnisse bereits erste Tendenzen einer stärkeren Abhängigkeit der optimalen Applikatorpositionierung von der elektrischen als von der thermischen Leitfähigkeit an, was darin begründet sein könnte, dass die elektrische Leitfähigkeit das System über die Heizquelle und die effektive Generatorleistung möglicherweise stärker beeinflusst als die thermische Leitfähigkeit. Zudem fällt auf, dass die Hauptauslenkung der optimalen Applikatorposition entlang der Hauptausrichtung der tumornahen Gefäße verläuft. Die Blutgefäße scheinen also einen nicht unerheblichen Einfluss auf die Sensitivität der optimalen Applikatorposition bezüglich der elektrischen und thermischen Leitfähigkeit auszuüben.

Insgesamt hängt der Erfolg einer RF Ablation offensichtlich sehr stark von den durch die Blutgefäße hervorgerufenen Kühleffekten ab. Aus diesem Grund wurde eine Methode zur schnellen Bewertung der Kühleffekte großer Gefäße (von einem Durchmesser über 3 mm) entwickelt (Kapitel 5). Dabei wurde für festgelegte Bereiche des Tumors in der Nähe großer Gefäße bestimmt, wie weit der Applikator höchstens von den Gefäßen entfernt sein darf, damit die zugeführte Heizenergie noch zur Zerstörung der entsprechenden Tumorregionen ausreicht. Die wesentliche Idee dieses Ansatzes besteht aus einem Perspektivenwechsel in der Betrachtung der Wärmeleitungsgleichung von der Wärmezufuhr über den Applikator hin zur Ausbreitung der Kühleffekte ausgehend von den Gefäßen. Die Schnelligkeit des Verfahrens wurde dabei durch eine Vorabberechnung und Abspeicherung aller patientenunabhängigen Daten erzielt, welche dann zur Berechnung der Kühleffekte für eine individuelle Tumor-Gefäß-Konfiguration nur noch ausgelesen werden müssen. Visualisiert wurden die maximal erlaubten Abstände des Applikators zu den Gefäßen durch eine entsprechende Einfärbung der Tumore, sowie durch gefäßumschließende Schläuche unterschiedlicher Dicke in Abhängigkeit vom erlaubten Maximalabstand zwischen dem Applikator und dem jeweiligen Gefäß.

In Kapitel 6 wurden schließlich noch zwei weitere Ansätze zur Optimierung der

Applikatorplatzierung diskutiert, welche den in Kapitel 3 vorgestellten Algorithmus ergänzen. Einer dieser Ansätze befasst sich mit der gekoppelte Optimierung von bipolaren Applikatoren und einer konstanten Generatorleistung. Hierbei besteht die wesentliche Neuerung aus einer geometrischen Vorooptimierung mit einem ellipsoidförmigen Koagulationsarreal, dessen Form bis auf die Radien, die sich mit der Generatorleistung ändern, fest ist. Der zweite in diesem Kapitel vorgestellte Ansatz beschreibt eine Optimierung der Anzahl und Platzierung von mehreren ungekoppelten Applikatoren. Um das hierbei verstärkte Problem der lokalen Optima in den Griff zu bekommen, wird ein dem “Simulated Annealing” ähnliches Verfahren verwendet, welches sowohl nach jedem Gradientenabstieg als auch nach einer kompletten Optimierung an der Lösung rüttelt um so aus möglichen lokalen Optima herauszuführen.

Neben der Applikatorplatzierung hat auch die Steuerung der Energiezufuhr einen erheblichen Einfluss auf den Erfolg der RF Therapie. Abschließend wurde deshalb in Kapitel 7 ein erster Ansatz zur Berechnung einer optimalen Steuerung der Generatorleistung vorgestellt. Die zuvor für die Optimierung der Applikatorplatzierung vereinfachte Modellierung der RF Ablation wurde hierbei wieder um die Zeitabhängigkeit ergänzt. Zudem wurde ein Zielfunktional modelliert, welches (durch die Einführung von Zusatzzeitschritten) die Wärmeausbreitung nach dem Abschalten des Generators mitberücksichtigt und darüber hinaus die Austrocknung des Gewebes bei zu hohen Temperaturen bestraft. Für den Algorithmus zur optimalen Steuerung der Generatorleistung wurde hier zunächst wieder das Gradientenabstiegsverfahren getestet, welches für dieses Optimalsteuerungsproblem jedoch weitaus mehr Iterationsschritte benötigt als für das zuvor betrachtete Applikatorpositionierungsproblem. In weiteren Untersuchungen sollte das Gradientenabstiegsverfahren für das Problem der optimalen Generatorleistungssteuerung somit durch ein geeigneteres Verfahren wie z.B. ein Lagrange-Newton (SQP) Verfahren ersetzt werden.

Ausblick

Für zukünftige Untersuchungen sind zahlreiche Erweiterungen und Verbesserungen der vorgestellten Modelle und Algorithmen geplant und werden teilweise sogar bereits erforscht. Zunächst einmal soll hier die Berücksichtigung von anatomischen Beschränkungen durch z.B. innere Organe, Knochen, oder große Blutgefäße für die Applikatorplatzierung genannt werden. Die Modellierung und Einhaltung solcher Beschränkungen ist Thema einer aktuellen Forschungsarbeit von Sabrina Haase⁴.

Da es in der Praxis für den behandelnden Arzt nicht leicht sein wird, die berechnete optimale Applikatorplatzierung exakt zu treffen, wäre zudem eine Sensitivitätsanalyse wünschenswert, welche eine Abschätzung der Versagenswahrscheinlichkeit einer RF Ablation bei Ungenauigkeiten in der Applikatorpositionierung liefert.

⁴shaase@mevis.de; Institut CeVis der Universität Bremen

Für die Verbesserung des stochastischen Ansatzes zur Untersuchung des Einflusses von ungenauen Gewebeparametern auf die optimale Applikatorplatzierung wird bereits eine Modellierung des stochastischen Prozesses durch stückweise multilineare Funktionen auf hierarchischen Gittern untersucht. Des Weiteren ist eine Modellierung der Materialparameter als Fuzzy-Größen geplant, weil ihre stochastische Verteilung zunächst eigentlich noch unbekannt ist. Mit Hilfe von Experimenten und einer Betrachtung des inversen Problems, bei dem zu einer gegebenen Temperaturverteilung die zugehörigen Gewebeparameter ermittelt werden, soll gleichzeitig versucht werden, Rückschlüsse auf die Verteilung der Gewebeparameter zu ziehen. Die Betrachtung dieser Fragestellung und insbesondere des inversen Problems gehören zum aktuellen Forschungsgebiet von Hanne Tiesler⁵. Schließlich sollen neben der elektrischen und thermischen Leitfähigkeit auch die Perfusionskoeffizienten (d.h. die relative Durchblutungsrate, die Dichte und die Wärmekapazität des Blutes) als stochastische bzw. fuzzyverteilte Größen modelliert werden. Darüber hinaus ist eine Maximierung der Konfidenz für den Erfolg der RF Therapie geplant.

Um die Bewertung des Kühleinflusses großer Gefäße noch weiter zu verbessern, ist ein Korrekturmodell für die Segmentierung der Gefäßradien, basierend auf mathematischen und physikalischen Heuristiken Bestandteil weiterer Forschung. Zudem soll die Visualisierung der Kühleffekte durch die Ermöglichung einer Benutzerinteraktion verbessert werden. Dabei können die Auswirkungen einer vom Benutzer durchgeführten Applikatorverschiebung z.B. anhand von zwei veränderlichen Tumorfärbungen, die zerstörtes bzw. unzerstörtes Tumorgewebe beschreiben, visualisiert werden. Eine Erweiterung der Einflussgrößen innerhalb der Look-up-Tabelle, sowie eine experimentelle Validierung in Zusammenarbeit mit dem Charité Berlin⁶ sind ebenfalls geplant.

Schließlich sind für die Berechnung einer Optimalsteuerung der Generatorleistung die Anwendung von Verfahren höherer Ordnung wie z.B. Lagrange-Newton (SQP) Verfahren, sowie die Implementierung eines Mehrgitterverfahrens (wie bereits für das Applikatorpositionierungsproblem durchgeführt; Kapitel 3.7) geplant.

Darüber hinaus, ist für alle in dieser Arbeit vorgestellten Ansätze eine umfassende Auswertung anhand von sowohl künstlichen Konfigurationen, als auch echten Patientendatensätzen mit verschiedenen Tumorformen und Gefäßsystemen erforderlich.

⁵Hanne.Tiesler@cevis.uni-bremen.de; Institute CeVis und ZeTem der Universität Bremen

⁶Charité, Campus Benjamin Franklin, Hindenburgdamm 30, 12203 Berlin; <http://www.charite.de>.

List of Figures

2.1	Dependencies in the modeling of RF ablation.	8
2.2	Schematic setting of the considered configuration. Note that $D_+ \cup D_- = D_{\pm} \subset D_{pr}$, where all these sets depend on p and d	9
2.3	Left: Equivalent circuit diagram for the calculation of the scaling factor which is needed to convert the unscaled power P into the effective heat source Q_{rf} . Right: The characteristic curve of the generator shows the dependence of the effective power P_{eff} on the impedance R of the tissue, while R_I and P_{setup} are fixed (here: $R_I = 80 \Omega$, $P_{setup} = 200 \text{ W}$).	10
2.4	Dotted curve: Measured values for the electric conductivity. Solid curves: Curves of two fourth order polynomial functions the coefficients of which have been determined to approximate the measured data as good as possible.	15
2.5	Approximation of an electrode of length L and radius R (left) by a concatenation of overlapping charged balls (right).	18
2.6	Schematic setting of the considered configuration. Here, r_i is the distance of a point $x \in D$ from the centerpoint of the i -th ball of radius R and charge Q	19
2.7	Approximation of a bipolar probe of position $p = (p_1, p_2, p_3)$ and direction $d = (d_1, d_2, d_3)$ by a concatenation of overlapping charged balls.	20
3.1	One-dimensional schematic showing the idea of the gradient descent method: A local minimum of an objective function f shall be found by taking steps in direction of the anti-gradient of f	26
3.2	Two different schematics showing disadvantageous scenarios that lead to a slow convergence of the gradient descent method. Left: Zig-zag course to the minimum. Right: Only very small iteration steps.	27
3.3	One-dimensional schematic showing the idea of the Newton method to find a root of a function $F = \nabla f$: An approximation to the root is successively improved by linearising F at this approximation and taking the root of the resulting tangent on F as new approximation to the root of F	28

3.4	2D-optimization of the positioning of a bipolar RF probe for an artificial example with elliptically shaped tumor. The left image shows the target temperature T_{target} , and the small images show from left to right steps 0 (start), 2, 3, and 8 (end) of the optimization. In the top row the energy source Q_{rf} from the probe is depicted, and in the bottom row the steady state of the heat distribution T is shown. . . .	31
3.5	2D-optimization of a bipolar RF probe's positioning for an artificial example with irregular shaped tumor and linear vessel. The left image again shows the target temperature T_{target} , and the small images show from left to right steps 0 (start), 1, 3, and 10 (end) of the optimization. As in Fig. 3.4, in the top row the heat source Q_{rf} is shown, and in the bottom row the steady state of the heat distribution T is presented.	32
3.6	Left: Non-uniform tumor heating (only one hot region inside the tumor) Right: Uniform tumor heating.	34
3.7	Different curves of exponential functions without additional weighting (black) or with a weighting factor in the argument (gray). The steep slope leads to a high penalty for low temperatures.	35
3.8	Light Gray: Slope of the heat source next to the boundary of the probe for $p = (p_1 + \varepsilon, p_2, p_3)$ and $p = (p_1 - \varepsilon, p_2, p_3)$, respectively. Dark Gray: Central difference quotient for approximating the derivative of Q_{rf} with respect to the x -component p_1 of the probe's position. . . .	40
3.9	Optimization of the probe's placement for an artificial example with an ellipsoid-shaped tumor (dark gray) and a linear vessel (black). The pictures show from left to right steps 0 (start), 4, 6, and 9 of the optimization and display the probe (white-gray) and a corresponding iso-surface of the temperature (transparent) as well.	46
3.10	Optimization for an example based on patient data with segmented tumor and surrounding vessels. The pictures show from left to right steps 0, 5, 10 and 15 of the optimization process and display the tumor together with the vascular system, the probe position and a corresponding isosurface of the temperature (cf. Fig. 3.9).	47
3.11	Comparison of the computed optimal probe placement (left) with the probe placement chosen by the responsible physician (right).	48
3.12	Cluster of three monopolar probes together with the optimization parameters: the position p (i.e. the barycenter of the probes' active zones), the direction d and the rotation vector r	49
3.13	Intersection of the probe with a slice of the grid orthogonal to the probe. Here, h_l is the minimal voxel size of the grid \mathcal{G}_l , so the diameter of the probe must be at least $h_l\sqrt{2}$	51

3.14	Left: The progression of the objective function value is shown for the multi-scale optimization algorithm (●) and the standard algorithm (+). In contrast to the standard algorithm, the multi-scale optimization finds a slightly better minimum with a considerably smaller number of iterations on the finest-grid. Right: The progression of the objective function value is shown for the definition of a coarse-grid tumor and vascular domains which involve a thresholding.	51
3.15	Optimization of the probe's placement for an artificial example with an ellipsoid-shaped tumor (dark gray), a linear vessel (black), and a monopolar probe (white-gray). The transparent layer is the corresponding 60°-isosurface of the temperature. A: Steps 0 (start), 1, 2 and 20 of the 1st pre-optimization (coarsest grid). B: Steps 0 and 15 of the 2nd pre-optimization. C: Steps 0 and 11 (end) of the main optimization.	54
3.16	Optimization for an example based on patient data with segmented tumor and surrounding vascular system. Here, we have a fixed cluster of three monopolar probes with the corresponding 60°-isosurface of the temperature. A: Steps 0 (start), 1, 2 and 9 of the 1st pre-optimization (coarsest grid). B: Steps 0 and 9 of the 2nd pre-optimization. C: Steps 0 and 4 (end) of the main optimization.	55
3.17	Comparison of the optimal probe placement found by the optimization algorithm (left) with the probe placement chosen by the responsible physician (right).	56
3.18	Comparison of the 60° C - temperature profiles yield by the different probe placements suggested by the algorithm (left) and applied by the physician (right).	57
4.1	Two essentially different situations for the energy graph of the objective function that lead to similar distributions of the optimal probe placement in dependence of the uncertain tissue parameters. Left: Desired situation of a strong variation of the energy graph in dependence of the optimal probe position and tissue parameters, respectively. Right: Disadvantageous situation of a local insensitivity of the objective function to changes in the optimal probe position. . . .	68
4.2	The sensitivity of the optimal probe location is investigated for the artificial scenario with an ellipsoidal lesion and a linear vessel. Left: The PDF of the optimal probe location with distributed σ is shown with a volume rendering. The transfer function uses the color ramp shown on the left such that likely locations appear orange/red whereas unlikely locations appear green. Right: The ellipsoid shown inside the volume rendering cloud reveals a simpler visualization. It is centered at the mean of the distribution and it is oriented and scaled with the eigenvectors and eigenvalues of the distribution's covariance matrix. Moreover, for better visibility, it is magnified by a factor of 10. . . .	74

4.3	For the artificial scenario the sensitivity of the optimal probe position and orientation w.r.t. variations in the electric conductivity σ is shown. Left: Sensitivity of the optimal probe position visualized through an ellipsoidal representation of the covariance matrix (magnified by a factor of 10). Right: PDF of the optimal probe orientation visualized through a coloring of the sphere. As shown by the color ramp on the right, green colors indicate unlikely orientations, whereas red colors show likely orientations. In both images the RF probe is drawn at the mean of the placement's distribution, the linear vessel D_v is displayed in red and the ellipsoidal shaped tumor lesion D_t is displayed in a transparent gray.	75
4.4	The 60 °C iso-surface of the temperature is shown for the optimal probe placement obtained in collocation point 5 (left), collocation point 16 (middle) and collocation point 23 (right) of the sensitivity analysis of the probe placement w.r.t. uncertainties in σ . In all three cases the lesion is ablated completely.	76
4.5	Approximation of the graph of the objective function $f(x)$ where the position x varies along the eigenvector corresponding to the largest eigenvalue of the covariance matrix (longest principal axis of the ellipsoid).	76
4.6	Visualization of the sensitivity of the optimal probe position through an ellipsoidal representation of the covariance matrix. The sensitivity with respect to the thermal conductivity λ (left), the electric conductivity σ (middle), and both parameters (right), yield by a collocation on level $k = 2$ and scaled by a factor of 10, is shown. The RF probe is drawn at the mean of the placement's distribution. The segmented vascular system D_v is shown in red and the segmented lesion D_t is shown in transparent gray.	78
4.7	Approximation of the energy graph of the objective function $f(x)$ where the position x varies along the eigenvector corresponding to the largest eigenvalue of the covariance matrix (longest principal axis of the ellipsoid).	79
4.8	Two different views of the tumor's surface close to the vessels, together with a zoomed view of the framed area, where tumor and vessel are directly neighboring. Note, that for better visibility in all these figures, the front vessel has been pruned.	80
4.9	The 60 °C iso-surface of the temperature is shown for the optimal probe placement obtained in node 60 (left), node 38 (middle) and node 14 (right) of the sensitivity analysis of the probe location w.r.t. uncertainties in λ and σ , performed with collocation on level $k = 2$. As can be seen in the figure, the shown temperature iso-surfaces for these parameter settings do not always destroy the lesion completely. . . .	80

4.10	One-dimensional PDFs of the optimal probe locations along the three principal axes v_1 , v_2 , and v_3 [mm] of the covariances. PDFs are shown for variations w.r.t. all material parameters (top row), w.r.t. λ (middle row) and w.r.t. σ (bottom row).	81
4.11	The sensitivities of the optimal probe position with respect to the electric conductivity σ yield by a collocation on level $k = 1$ (inner ellipsoid), $k = 2$, $k = 3$ and $k = 4$ (outer ellipsoid) are compared. Here as in Fig. 4.6 the tumor is shown in a transparent gray color.	82
4.12	The sensitivity of the optimal probe orientation with respect to variations in the heat conductivity λ (left), the electric conductivity σ (middle), and both material parameters (right) is shown. As in the artificial example (see Fig. 4.3), the PDFs of the corresponding distributions of the optimal probe orientation are visualized by a coloring of the sphere. Again, green colors indicate unlikely orientations, whereas red colors show likely orientations (see color ramp on the right). The top row and the bottom row show two different viewpoints on the scene. The RF probe is drawn at the mean of the placement's distribution.	83
4.13	The optimization of the position and direction of a mono-polar probe is shown. The 60°C iso-surface of the expectation of the temperature distribution is depicted in a transparent yellow color. The vascular structure D_v is shown in red and the tumor domain D_t is shown in gray. A: Steps 0 (start), 1, 2 and 13 of the 1st pre-optimization (coarsest grid). B: Steps 0 and 12 of the 2nd pre-optimization. C: Steps 0 and 11 (end) of the main optimization.	84
4.14	For the optimization of the probe placement with the stochastic multi-scale algorithm shown in Fig. 4.13 the decay of the energy is displayed. The transitions between different grids are marked with vertical dotted lines.	85
4.15	Left: The optimization of the probe placement for the deterministic model is shown. Again the 60°C iso-surface of the temperature distribution is depicted in a transparent yellow color. The vessel system D_v and tumor D_t are the same as in Fig.4.13. A: Step 11 (end) of the 1st pre-optimization. B: Step 10 (end) of the 2nd pre-optimization. C: Step 16 (end) of the main optimization. Right: Expected optimal probe placement, yield by a collocation on level $k = 1$, with corresponding 60°C iso-surface of the temperature.	86

4.16 Left: Distribution of nodes obtained with the Smolyak algorithm (i. e. at the extreme values of the Chebychev polynomials which are well suited for polynomial interpolation). Middle: Uniform, adaptive distribution of nodes for the stochastic interpolation with piecewise multilinear, hierarchical basis functions Right: First five piecewise linear basis functions h_j for the interpolation approximation of the random field $f(\boldsymbol{\xi}) \approx \sum_{j=1}^q f(\boldsymbol{\xi}_j)h_j(\boldsymbol{\xi})$ (cf. Sect.4.3). 87

5.1 Change of the perspective in considering the heat equation. Left: Previous perspective, i. e. propagation of heat from the probe into the surrounding tissue. Right: New perspective, i. e. propagation of the cooling effects from a blood vessel into the tissue. 92

5.2 Left: Determination of the integral over all orthogonal cross sections through the probe's active zone. Right: Orthogonal cross section through the center of the probe's active zone. (If the probe is bipolar, this cross section passes the isolator and thus the corresponding heating profile along this cross section is unrepresentatively low.) . . . 96

5.3 Thickness d_{vt} of a tube of vital tissue around a vessel V in dependence of the temperature $T = T(R_{bv}, d)$ 97

5.4 Two-dimensional view of the criticality tube C (which in two dimensions is denoted as C') of thickness d_{vt} around a vessel V . (Note, that even if depicted in only two dimensions, the criticality tube C of course is three-dimensional.) 98

5.5 Maximal distance d_{max} between the RF probe and the vessel V , such that the point \vec{x} of the tumor D_t lies on the outer boundary of the criticality tube C . Thus, d_{max} is the maximal distance the probe may have to the vessel V , in order to destroy the point \vec{x} of the tumor. . . 99

5.6 With help of the 2D calculation results of $(d_{vt} \circ T)(R_{bv}, d)$ for different vessel radii R_{bv} and probe-vessel distances d , now one quickly can determine how the maximal distance d_{max} between the probe and a vessel V of radius R_{bv} has to be chosen, such that a considered point \vec{x} of the tumor lies on the outer boundary of the criticality tube C of vital tissue around the vessel V 99

5.7 Commutative diagram showing all compositions of functions for calculating the criticality tubes C and maximum allowable probe vessel distances d_{max} . Red: Functions which are precalculated. Blue: Functions which are evaluated ad hoc for the individual patient. 100

5.8 Considered configuration of a whole vascular tree G with two nearby lying tumors Θ_1 and Θ_2 provided with a color coding, where different colors represent different maximum allowable distances d_{max} between the given RF probe and the respective vessel. The dashed tubes around the large vessels are the criticality tubes corresponding to the coding colors of the tumors. 100

5.9 Left: Schematic of the two-dimensional look-up-table, containing the different thicknesses $f_{ij} = (d_{vt} \circ T)(R_{bv}^i, d^j)$ of tubes of vital tissue in dependence of the vessel radii R_{bv}^i and the probe-vessel distances d^j . Right: Part of the filled look-up-table. Here, all values are given in millimeters [mm]. 103

5.10 Extent of the three-dimensional computational domain D for the calculation of the heat source density Q_{rf} induced into the tissue by the applied RF probe cluster. 103

5.11 Extent of the two-dimensional computational domain D' obtained from D by omitting the z -direction, and used for the calculation of the temperature $T(R_{bv}, d)$ which is needed to calculate the entries of the look-up-table shown in Fig. 5.9. 104

5.12 The curves show the thickness $d_{vt} = d_{vt}(T(R_{bv}, d))$ of the vessel surrounding region of vital tissue, in dependence of the distance d of the applied RF probe cluster from the vessel for different vessel radii. *Dotted Line*: No blood vessel, i. e. only a coding of the distance between an imaginary vessel wall and the coagulated region of tissue around the probe cluster. *Dashed Line*: Curve for a blood vessel of radius 1.0 mm. *Solid Line*: Curve for a blood vessel of radius 7.4 mm. 105

5.13 Example based on real patient data, showing the portal vein of the liver (light red) and three hepatic tumors near to the vessels. Tumor regions which cannot be destroyed if the distance between the applied RF probe cluster and the respective vessels (of radius $R_{bv} > 1.5$ mm) is more than $d_{max} = 5.0$ mm, are colored in dark blue, those regions which cannot be destroyed if the distance is larger than $d_{max} = 10.0$ mm, are colored in light blue, and all remaining tumor regions are colored in yellow. 106

5.14 Different views of the single tumors from Fig. 5.13 next to the vessels of the portal vein, together with the corresponding color coding of the tumors (cf. Fig. 5.13), and criticality tubes (depicted in a transparent blue color) around the vessels, for $d_{max} = 5.0$ mm (left two columns) and $d_{max} = 10.0$ mm (right two columns). The figures in column 2 and 4 are zoomed views of the configurations shown in column 1 and 3. (Note, that slightly deviations of the criticality tubes from the color coding of the tumors are due to visualization artifacts.) 107

5.15 Three different positionings of the RF probe cluster with respect to the considered vessel. Left: Parallel setting. Middle: Skew-orthogonal setting. Right: Direct-orthogonal setting. 108

5.16 Configuration showing a cutout of the hepatic vein and all layers of criticality tubes simultaneously, for a probe-vessel distance of 5.0 mm, 10.0 mm and 12.0 mm. 109

- 6.1 Two-dimensional schematic, showing the determination of the two radii $r_1(w)$ and $r_2(w)$ of the ellipsoid D_{coag} that approximates the rather “peanut-shaped” region $I_{P_{\text{setup}}}$ of coagulated tissue. 114
- 6.2 Radii of an ellipsoidal-shaped approximation of the region of coagulated tissue for a bipolar probe used for the artificial example with a grid of 120^3 grid cells and a voxel size of 0.5 mm^3 . Left: Radius of the latitude. Right: Radius of the longitude. 114
- 6.3 Schematic configuration of the ellipsoidal-shaped, approximative region of coagulated tissue D_{coag} with radii r_1 and r_2 , located in the center $p = (p_1, p_2, p_3)$ of the probe’s active zone, and aligned with the probe’s direction \vec{d} . For each point $x = (x_1, x_2, x_3)$ of the computational domain D , it has to be tested, if x lies in D_{coag} , or not. 115
- 6.4 Schematic of a critical configuration for the location and size of the coagulated tissue region D_{coag} compared to the location and size of the tumor region D_t . Here, the objective functional (6.7) would be an unfavorable choice for an optimization. 116
- 6.5 Region of coagulated tissue D_{coag} , where voxel values are set to 1, together with a small range $D_{\pm\epsilon}$, where the state of coagulation passes into the state of vitality, i. e. where the voxel value 1 from inside the region of coagulated tissue D_{coag} smoothly decreases to the voxel value 0 outside D_{coag} , i. e. on the native tissue $D \setminus D_{\text{coag}}$ 116
- 6.6 Function $1_{D_{\text{coag}}}(s)$, which is 1 for the state of coagulation and 0 for the state of vitality. *Gray Curve*: Jump between coagulated and native tissue (see formula (6.9)). *Black Curve*: ϵ -range of smooth transition between coagulated and native tissue (see formula (6.11)). 117
- 6.7 Optimization of the probe’s placement for an artificial example with an ellipsoid-shaped tumor (dark gray), a linear vessel (black), and a bipolar probe (white-gray). The transparent layer is the corresponding region of coagulated tissue and 60° -isosurface of the temperature, respectively. **A**: Steps 0 (start), 1, 2, 3, 4 and 48 of the (geometrical) pre-optimization with an ellipsoidal-shaped approximation of the region of coagulated tissue. **B**: Steps 0 and 9 of the main optimization with the 60° -isosurface of the temperature. 119
- 6.8 Optimization for an example based on patient data with a segmented tumor and surrounding vascular system. Here, we have a bipolar probe with the corresponding region of coagulated tissue and 60° -isosurface of the temperature, respectively. **A**: Steps 0 (start), 1, 2, 3, 4 and 15 of the (geometrical) pre-optimization with an ellipsoidal-shaped, approximative region of coagulated tissue. **B**: Steps 0 (start) and 10 of the main optimization with the 60° -isosurface of the temperature. 120

6.9	<p>Optimization of the placement and number of monopolar probes for the example known from the previous sections (e. g. Sect. 6.1.1, Fig. 6.8). The optimization starts with a single probe ($\mathbf{A}_1, \mathbf{B}_1, \mathbf{C}_1$) and ends with two probes ($\mathbf{A}_2, \mathbf{B}_2, \mathbf{C}_2$). \mathbf{A}_1: Steps 0 (start) and 25 of optimization (OP) 1, steps 0 and 6 of OP 9 and steps 0 and 7 of OP 16 on the coarsest grid. \mathbf{B}_1: Steps 0 and 5 of the optimization on the next finer grid. \mathbf{C}_1: Steps 0 and 2 (end) of the optimization on the finest grid. \mathbf{A}_2: Steps 0 (start) and 25 of OP 1, steps 0 and 11 of OP 9 and steps 0 and 7 of OP 17 on the coarsest grid. \mathbf{B}_2: Steps 0 and 9 of the optimization on the next finer grid. \mathbf{C}_2: Steps 0 and 2 (end) of the optimization on the finest grid.</p>	126
6.10	<p>Two different views of the optimal probe placement for a single probe and for two uncoupled probes (cf. Fig. 6.9). In the case of a single probe, the tumor region is not completely covered by the 60°C-temperature profile, so that the algorithm decides to use an additional probe. In the case of two probes, one probe moves nearer to the vessels, while the other moves in the opposite direction, resulting in the entire tumor being covered by the 60°C-temperature profile.</p>	127
7.1	<p>Schematic showing the convergence of the generator power P_{setup} to a setting which is P_{min} at the beginning of the RF ablation and P_{max} at the end t_f of the RF ablation. Here, as start setting we have a constant generator power of $P_{\text{setup}}(t) = P_0 \forall t \in I$.</p>	132
7.2	<p>Smooth approximation of the function $\min(T, T_{\text{max}}) - T_{\text{limit}}$ (black) by the function $h_c(T - T_{\text{limit}})$ (gray) with $c = T_{\text{max}} - T_{\text{limit}}$ and $h_c = h_{c,1}$ as defined in (7.13). The cutout on the right shows a zoomed view of the relevant region around $T = T_{\text{max}}$, where the black curve has a kink, while the gray shows a smooth bend.</p>	136
7.3	<p>Schematic showing the calculation of the adjoint v backwards in time, starting with an initial condition in t_e, as well as in t_f, and proceeding until the start time $t = 0$ is reached.</p>	141
7.4	<p>Curves showing the maximal temperature values during the RF ablation ($t \in [0 \text{ s}, 300 \text{ s}]$) and during the following 5 minutes ($t \in [300 \text{ s}, 600 \text{ s}]$) for iteration step 1 (yellow), 10 (blue), 1000 (green), and 3982 (red). Obviously, the highest temperature values are obtained at the end t_f of the ablation.</p>	146
7.5	<p>Left: Curves showing the setup power P_{setup} during the RF ablation for iteration step 1 (yellow), 10 (blue), 1000 (green) and 3982 (red). Right: 60°C–isosurface of the temperature (transparent yellow) at the end t_f of the ablation for iteration step 1 (left) and iteration step 3982 (right). Moreover, we see an artificial tumor (gray ellipsoid) and a monopolar probe with red electrode.</p>	146
7.6	<p>50°C–isosurface of the temperature (transparent yellow) at the end t_f of the ablation and for step 3982 of the optimization.</p>	147

List of Tables

4.1	Number of collocation points for the stochastic dimensions dim and the levels k of approximation used in this study.	73
4.2	Eigenvalues of covariance matrices for the PDF of the probe location for the real RF scenario (values given in millimeters).	78
4.3	Sensitivities of the probe position with respect to the six stochastic quantities. The derivatives are evaluated at the midpoint of the hyper-cuboid in the stochastic space. The values are given in the respective SI units.	82

List of Algorithms

3.1	Basic algorithm for the optimization of the probe placement	45
3.2	Multi-scale algorithm for the optimization of the probe placement	53
4.1	Stochastic multi-scale algorithm for probe placement optimization	72
7.1	Algorithm for the calculation of an optimal control of P_{setup}	145

Bibliography

- [1] R. A. Adams. *Sobolev Spaces*. Academic Press, New York, 1975.
- [2] W. Alt. The lagrange-newton method for infinite-dimensional optimization problems. *Numerical Functional Analysis and Optimization*, 11(3-4):201–224, 1990.
- [3] W. Alt and K. Malanowski. The lagrange-newton method for nonlinear optimal control problems. *Computational Optimization and Applications*, 2:77–100, 1993.
- [4] I. Altrogge, T. Kröger, T. Preusser, C. Büskens, P. L. Pereira, D. Schmidt, A. Weihusen, and H.-O. Peitgen. Towards optimization of probe placement for radio-frequency ablation. *Proc. MICCAI, LNCS*, 4190:486–493, 2006.
- [5] I. Altrogge, T. Preusser, T. Kröger, C. Büskens, P. L. Pereira, D. Schmidt, and H.-O. Peitgen. Multi-scale optimization of the probe placement for radio-frequency ablation. *Academic Radiology*, 14(11):1310–1324, 2007.
- [6] P. Andersson and J. Wren. Radiofrequency thermal ablation of liver tumors - impact of large vessels. In *Proc. ASME 2008, Summer Bioeng. Conf. (SBC2008)*, 2008. <http://www.x-cd.com/sbc08/pdfs/193059.pdf>.
- [7] A. Antoniou and W.-S. Lu. *Practical Optimization - Algorithms and Engineering Applications*. Springer Science, 2007.
- [8] S. N. Antontsev and M. Chipot. The thermistor problem: Existence, smoothness, uniqueness, blowup. *SIAM J. Math. Anal.*, 25(4):1128–1156, 1994.
- [9] S. Arrhenius. Über die Reaktionsgeschwindigkeit bei der Inversion von Rohrzucker durch Säuren. *Z. Phys. Chem.*, 4:226–248, 1889.
- [10] C. Baegert, C. Villard, P. Schreck, and L. Soler. Multi-criteria trajectory planning for hepatic radiofrequency ablation. *Proc. MICCAI, LNCS*, 4792:676–684, 2007.
- [11] C. Baegert, C. Villard, P. Schreck, and L. Soler. Precise determination of regions of interest for hepatic rfa planning. *SPIE Medical Imaging*, 6509, 2007.
- [12] C. Baegert, C. Villard, P. Schreck, L. Soler, and A. Gangi. Trajectory optimization for the planning of percutaneous radiofrequency ablation on hepatic tumors. *Journal of Computer Aided Surgery*, 12(2):82–90, 2007.

- [13] W. U. Batzler, K. Giersiepen, S. Hentschel, G. Husmann, P. Kaatsch, A. Katalinic, J. Kieschke, K. Kraywinkel, M. Meyer, R. Stabenow, C. Stegmaier, J. Bertz, J. Haberland, and U. Wolf. *Cancer in Germany, 2003-2004. Incidence and Trends. Sixth edition.* Robert Koch Institute (ed.) and Association of Population-based Cancer Registries in Germany (ed.), Berlin, 2008.
- [14] E. J. Berjano. Theoretical modeling for radiofrequency ablation: state-of-the-art and challenges for the future. *BioMedical Engineering On-Line*: <http://www.biomedical-engineering-online.com/content/5/1/24>, 5(24), 2006.
- [15] H. Bourquain, A. Schenk, F. Link, B. Preim, G. Prause, and H.-O. Peitgen. Hepavision2: A software assistant for preoperative planning in living-related liver transplantation and oncologic liver surgery. *CARS*, pages 341–346, 2002.
- [16] H. F. Bowman. Heat transfer and thermal dosimetry. *J. Microwave power*, 16(2), 1981.
- [17] D. Braess. *Finite Elemente*. Springer, Berlin, 3rd edition, 2003.
- [18] H.-J. Bungartz and S. Dirnstorfer. Multivariate quadrature on adaptive sparse grids. *Computing*, 71:89–114, 2003.
- [19] C. Büskens and H. Maurer. Sqp-methods for solving optimal control problems with control and state constraints: adjoint variables, sensitivity analysis and real-time control. *Journal of Computational and Applied Mathematics*, 120(1-2):85–108, 2000.
- [20] A.J. Chorin. Hermite expansions in Monte Carlo computation. *J. Comput. Phys.*, 8:471–482, 1971.
- [21] A.J. Chorin. Gaussian fields and random flow. *J. Fluid Mech.*, 63:21–32, 1974.
- [22] Luisa Consiglieri, I. dos Santos, and D. Haemmerich. Theoretical analysis of the heat convection coefficient in large vessels and the significance for thermal ablative therapies. *Phys. Med. Biol.*, 48(24):4125–4134, 2003.
- [23] J. Crezee and J. J. W. Lagendijk. Temperature uniformity during hyperthermia: the impact of large vessels. *Phys. Med. Biol.*, 37(6):1321–1337, 1992.
- [24] L. Crocetti and R. Lencioni. Thermal ablation of hepatocellular carcinoma. *Cancer Imaging*, 8:19–26, 2008.
- [25] M.K. Deb, I.M. Babuška, and J.T. Oden. Solutions of stochastic partial differential equations using Galerkin finite element techniques. *Comput. Methods Appl. Mech. Eng.*, 190:6359–6372, 2001.

- [26] W. Demtröder. *Experimentalphysik 2, Elektrizität und Optik*. Springer, Berlin, 1995.
- [27] P. Deuffhard. *Newton Methods for Nonlinear Problems, Affine Invariance and Adaptive Algorithms*. Springer Series in Computational Mathematics. Springer, 2004.
- [28] P. Deuffhard, M. Weiser, and M. Seebaß. A new nonlinear elliptic multilevel FEM applied to regional hyperthermia. *Comput. Vis. Sci.*, 3(3):115–120, 2000.
- [29] I. dos Santos, D. Correia, A. J. M. Soares, J. A. Goes, A. F. da Rocha, D. Schutt, and D. Haemmerich. A surgical device for radiofrequency ablation of large liver tumors. *Physiol. Meas.*, 29(10):N59–N70, 2008.
- [30] I. dos Santos, D. Haemmerich, C. S. Pinheiro, and A. F. da Rocha. Effect of variable heat transfer coefficient on tissue temperature next to a large vessel during radiofrequency tumor ablation. *Biomed. Eng. Online*, 11:7–21, 2008.
- [31] L. C. Evans. *Partial Differential Equations*, volume 19 of *Graduate Studies in Mathematics*. American Mathematical Society, 1998.
- [32] E. C. Feliberti and L. D. Wagman. Radiofrequency ablation of liver metastases from colorectal cancer. *Cancer Control*, 13(1):48–51, 2006.
- [33] J. Ferlay, P. Autier, M. Boniol, M. Heanue, M. Colombet, and P. Boyle. Estimates of the cancer incidence and mortality in europe in 2006. *Annals of Oncology*, 18(3):581–592, 2007.
- [34] R. Fletcher. *Practical Methods of Optimization*. John Wiley & Sons, 2000.
- [35] A. Frommer. Numerische Methoden der nichtlinearen Optimierung. <http://www.math.uni-wuppertal.de/~frommer/manuscripts/NichtLinOpt.pdf>, 2004.
- [36] C. Geiger and C. Kanzow. *Numerische Verfahren zur Lösung unrestringierter Optimierungsaufgaben*. Springer, 1999.
- [37] S.E. Geneser, R.M. Kirby, and R.S. MacLeod. Application of stochastic finite element methods to study the sensitivity of eeg forward modeling to organ conductivity. *IEEE Transactions on Biomedical Engineering*, In Press, 2007.
- [38] S.E. Geneser, D.B. Xiu, R.M. Kirby, and F.B. Sachse. Stochastic Markovian modeling of electrophysiology of ion channels: Reconstruction of standard deviations in macroscopic currents. *Journal of Theoretical Biology*, 245(4):627–637, 2007.
- [39] R.G. Ghanem and P. Spanos. *Stochastic Finite Elements: A Spectral Approach*. Springer, New York, NY, 1991.

- [40] R. Griesse. Lecture notes: Infinite-dimensional optimization.
- [41] C. Großmann and H.-G. Roos. *Numerische Behandlung partieller Differentialgleichungen*. Teubner, Stuttgart, 3. edition, November 2005.
- [42] W. Hackbusch. *Multi-Grid Methods and Applications*, volume 4 of *Springer Series in Computational Mathematics*. Springer, 1985.
- [43] D. Haemmerich. *Finite Element Modeling of Hepatic Radio Frequency Ablation*. PhD thesis, University of Wisconsin - Madison, 2001.
- [44] D. Haemmerich, A. W. Wright, D. M. Mahvi, F. T. Lee Jr., and J.G. Webster. Hepatic bipolar radiofrequency ablation creates coagulation zones close to blood vessels: a finite element study. *Med. Biol. Eng. Comput.*, 41:317–323, 2003.
- [45] O. Harth. Wasserhaushalt, Stoff und Flüssigkeitstransport. In R. F. Schmidt and G. Thews, editors, *Physiologie des Menschen*. Springer, 1993.
- [46] Jr. J. E. Dennis and R. B. Schnabel. *Numerical Methods for Unconstrained Optimization and Nonlinear Equations*. Prentice-Hall Series in Computational Mathematics. Prentice-Hall, New Jersey, 1983.
- [47] M. K. Jain and P. D. Wolf. A three-dimensional finite element model of radiofrequency ablation with blood flow and its experimental validation. *Ann. Biomed. Eng.*, 28(9):1075–84, 2000.
- [48] J. Kaipio and E. Somersalo. Statistical inverse problems: Discretization, model reduction and inverse crimes. *Journal of Computational and Applied Mathematics*, 1098:493–504, 2007.
- [49] A. Keese. A review of recent developments in the numerical solution of stochastic partial differential equations (stochastic finite elements). Technical Report 2003-06, Technical University Braunschweig, 2003.
- [50] A. Keese. *Numerical Solution of Systems with Stochastic Uncertainties: A General Purpose Framework for Stochastic Finite Elements*. PhD thesis, Technical University Braunschweig, 2004. <http://www.digibib.tu-bs.de/?docid=00001595>.
- [51] Y. S. Khajanchee, D. Streeter, L. L. Swanstrom, and P. D. Hansen. A mathematical model for preoperative planning of radiofrequency ablation of hepatic tumors. *Surgical Endoscopy*, 18(4):696–701, 2004.
- [52] I. S. Khalil-Bustany, C. J. Diederich, E. Polak, and C. Kirjner-Neto. Minmax optimization-based inverse treatment planning for interstitial thermal therapy. *Int. J. Hyperthermia*, 14(4):347–366, 1998.

- [53] S. Kirkpatrick, C. D. Gelatt, and M. P. Vecchi. Optimization by simulated annealing. *Science*, 220(4598):671–680, 1983.
- [54] T. Kröger. Convergence of a temperature based objective functional for optimizing the probe placement in radio-frequency ablation. 2008. in preparation.
- [55] T. Kröger, I. Altrogge, O. Konrad, R. M. Kirby, and T. Preusser. Estimation of probability density functions for parameter sensitivity analyses. In *Proceedings of Simulation and Visualization (SimVis)*, pages 61–74, 2008.
- [56] T. Kröger, I. Altrogge, T. Preusser, P. L. Pereira, D. Schmidt, A. Weihusen, and H.-O. Peitgen. Numerical simulation of radio frequency ablation with state dependent material parameters in three space dimensions. *Proc. MICCAI, LNCS*, 4191:380–388, 2006.
- [57] K. Kunisch and S. Volkwein. Augmented lagrangian-sqp techniques and their approximations. In S. Cox and I. Lasiecka, editors, *Optimization Methods in Partial Differential Equations*, volume 209 of *Proceedings from the 1996 Joint Summer Research Conference*, pages 147–159. American Mathematical Society, June 1996.
- [58] R. Lencioni, D. Cioni, L. Crocetti, and C. Bartolozzi. Percutaneous ablation of hepatocellular carcinoma: State-of-the-art. *Liver Transpl.*, 10(2):91–97, 2004.
- [59] R. Lencioni and L. Crocetti. Radiofrequency ablation of liver cancer. *Tech Vasc Interv Radiol.*, 10(1):38–46, 2007.
- [60] R. Lencioni, C. Della Pina, L. Crocetti, and D. Cioni. Percutaneous ablation of hepatocellular carcinoma. In *Minimally Invasive Tumor Therapies*, volume 167 of *Recent Results in Cancer Research*, chapter 7, pages 91–105. Springer Berlin Heidelberg, 2006.
- [61] X. Ma and N. Zabaras. An adaptive hierarchical sparse grid collocation algorithm for the solution of stochastic differential equations. *Journal of Computational Physics*, 2008. submitted.
- [62] O.P. Le Maître, M. . Reagan, H.N. Najm, R.G. Ghanem, and O.M. Knio. A stochastic projection method for fluid flow II.: random process. *Journal of Computational Physics*, 181(1):9–44, 2002.
- [63] F.H. Maltz and D.L. Hitzl. Variance reduction in Monte Carlo computations using multi-dimensional Hermite polynomials. *J. Comput. Phys.*, 32:345–376, 1979.
- [64] H. Maurer and J. Zowe. First and second-order necessary and sufficient optimality conditions for infinite-dimensional programming problems. *Mathematical Programming*, 16:98–110, 1979.

- [65] W.C. Meecham and D.T. Jeng. Use of Wiener-Hermite expansion for nearly normal turbulence. *J. Fluid Mech.*, (32):225–249, 1968.
- [66] B. Möller and M. Beer. *Fuzzy Randomness*. Springer, Berlin, 2004.
- [67] S. Mulier, Y. Ni, J. Jamart, L. Michel, G. Marchal, and T. Ruers. Radiofrequency ablation versus resection for resectable colorectal liver metastases: Time for a randomized trial? *Annals of Surgical Oncology*, 15(1):144–157, 2007.
- [68] T. Pätz. Composite FE für ein Mehrphasen-Modell zur Simulation von Radiofrequenz-Ablation. Diploma thesis, University of Bremen - Germany, 2008.
- [69] H. H. Pennes. Analysis of tissue and arterial blood temperatures in a resting forearm. *J. Appl. Physiol.*, 1:93–122, 1948.
- [70] P. L. Pereira. Actual role of radiofrequency ablation of liver metastases. *Eur Radiol.*, 17(8):2062–2070, 2007.
- [71] T. Preusser and M. Rumpf. An adaptive finite element method for large scale image processing. In *LNCS: Proceedings of the Second International Conference on Scale-Space Theories in Computer Vision*, volume 1682, pages 223–234. Springer, 1999.
- [72] T. Preusser, A. Weihusen, and H.-O. Peitgen. On the modelling of perfusion in the simulation of RF-ablation. In *Proc. SimVis*, Magdeburg, 2005.
- [73] P. Rossmanith. Simulated annealing. In *Taschenbuch der Algorithmen*, eXamen.press, chapter IV, 43, pages 423–431. Springer Berlin Heidelberg, 2008.
- [74] D. Schmidt, J. Trübenbach, C. W. König, J. Brieger, S. Duda, C. D. Claussen, and P.L. Pereira. Radiofrequenzablation ex-vivo: Vergleich der Effektivität von impedance control mode versus manual control mode unter verwendung einer geschlossen perfundierten cluster-ablationssonde. *RöFo Fortschr. Röntgenstr.*, 175(7):967–972, 2003.
- [75] E. Schreier, D. Radun, H. Neuhauser, and K. Stark. GBE Booklet 15 “Hepatitis C”. Published in June 2003 as part of the series of Federal Health Reporting (“Gesundheitsberichterstattung der Bundes”) by the Robert Koch Institute.
- [76] D. Selle, B. Preim, A. Schenk, and H.-O. Peitgen. Analysis of vasculature for liver surgical planning. *IEEE Trans. Med. Imaging*, 21(11):1344–1357, 2002.
- [77] T. W. H. Sheu, C. W. Chou, S. F. Tsai, and P. C. Liang. Three-dimensional analysis for radio-frequency ablation of liver tumor with blood perfusion effect. *Comp. Meth. Biomech. and Biomed. Eng.*, 8(4):229–240, 2005.
- [78] P. Spellucci. *Numerische Verfahren der nichtlinearen Optimierung*. Birkhäuser, 1993.

- [79] T. Stein. *Untersuchungen zur Dosimetrie der hochfrequenzstrominduzierten interstitiellen Thermotherapie in bipolarer Technik*, volume 22 of *Fortschritte in der Lasermedizin*. Müller and Berlien, 2000.
- [80] A. Suppiah, T. J. White, S. H. Roy-Choudhury, D. J. Breen, J. Cast, A. Maraveyas, J. E. Hartley, and J. R. T. Monson. Long-term results of percutaneous radiofrequency ablation of unresectable colorectal hepatic metastases: Final outcomes. *Dig Surg.*, 24:358–360, 2007.
- [81] V. Thomee. *Galerkin - Finite Element Methods for Parabolic Problems*. Springer, 1984.
- [82] H. Tiesler. Identification of material parameters for thermal ablation. Talk at the workshop “PDE Constrained Optimization - recent challenges and future developments” in Hamburg, Germany (see <http://www.math.uni-hamburg.de/spag/zms/pdeopt>), March 2008.
- [83] F. Tröltzsch. *Optimale Steuerung partieller Differentialgleichungen*. Vieweg, 2005.
- [84] S. Tungjitkusolmun, S. T. Staelin, D. Haemmerich, J.-Z. Tsai, H. Cao, J. G. Webster, F. T. Lee Jr., D. M. Mahvi, and V. R. Vorperian. Three-dimensional finite-element analyses for radio-frequency hepatic tumor ablation. *IEEE Trans. Biomed. Eng.*, 49(1):3–9, 2002.
- [85] C. Villard, L. Soler, and A. Gangi. Radiofrequency ablation of hepatic tumors: simulation, planning, and contribution of virtual reality and haptics. *Comp. Meth. Biomech. & Biomed. Eng.*, 8(4):215–227, August 2005.
- [86] C. Villard, L. Soler, A. Gangi, D. Mutter, and J. Marescaux. Towards realistic radiofrequency ablation of hepatic tumors 3d simulation and planning. *SPIE Medical Imaging 2004: Visualization, Image-Guided Procedures, and Display*, 5367:586–595, February 2004.
- [87] C. Welp. *Simulationsbasierte Untersuchung der hochfrequenten Thermoablation bei Lebertumoren*. PhD thesis, Ruhr-University of Bochum - Germany, 2005.
- [88] C. Welp, S. Siebers, H. Ermert, and J. Werner. Investigation of the influence of blood flow rate on large vessel cooling in hepatic radiofrequency ablation. *Biomed. Tech.*, 51:337–346, 2006.
- [89] World Health Organization (WHO). Fact sheet no.297 “Cancer”. <http://www.who.int/mediacentre/factsheets/fs297>. Published by the WHO in July 2008.
- [90] N. Wiener. The homogeneous chaos. *American Journal of Mathematics*, 60(4):897–936, 1938.

- [91] D.B. Xiu and J.S. Hesthaven. High-order collocation methods for differential equations with random inputs. *SIAM Journal on Scientific Computing*, 27(3):1118–1139, 2005.
- [92] D.B. Xiu and G.E. Karniadakis. Modeling uncertainty in steady state diffusion problems via generalized polynomial chaos. *Comput. Methods Appl. Mech. Eng.*, 191:4927–4948, 2002.
- [93] D.B. Xiu and G.E. Karniadakis. The Wiener-Askey polynomial chaos for stochastic differential equations. *SIAM J. Sci. Comput.*, 24:619–644, 2002.
- [94] D.B. Xiu and G.E. Karniadakis. Modeling uncertainty in flow simulations via generalized polynomial chaos. *J. Comput. Phys.*, 187:137–167, 2003.
- [95] P. J. Yim, H. B. Marcos, P. L. Choyke, J. L. Hvizda, S. K. Libutti, and B. J. Wood. Detection of blood vessels for radio-frequency ablation treatment planning. *Proc. 14th IEEE Symposium on Computer-Based Medical Systems (CBMS'01)*, pages 123–126, 2001.
- [96] E. Zeidler. *Nonlinear functional analysis and its applications*, volume 1-5. Springer, Berlin, 1985-1990.
- [97] U. Zurbuchen and T. Kröger. Ex-vivo studies of temperature dependent electric conductivity in porcine liver. 2009. in preparation.